NAM

Calibration and verification of a nonlinear macro-element for SSI analysis in the Groningen region

Francesco Cavalieri, António A. Correia

MOSAYK

Date April 2019

Editors Jan van Elk & Dirk Doornhof

General Introduction

In this report, a study into the transfer of seismic motion from the soil into the foundation and the structure of buildings, i.e. the soil structure interaction, is described.

Extensive studies have been carried out by Deltares to prepare a detailed map of the shallow subsurface (Ref. 1 to 3). Based on the description of the shallow sub-surface, amplification factors of the ground motion have been derived and included in the ground motion model (GMM) (Ref. 4).

Using representative values of the amplification factor, the response of a selection of buildings to earthquake motion is analysed in this report. The models prepared for the index buildings used in the derivation of fragility functions were used in this study (Ref. 5). The foundation of the buildings is important in the transfer of the ground motion into the buildings. In this study index buildings with shallow foundations as wells as buildings with pile foundations were considered.

References

1. Geological schematisation of the shallow subsurface of Groningen. For site response to earthquakes for the Groningen gas field. part 1 to 3, Pauline Kruiver, Ger de Lange, Ane Wiersma, Piet Meijers, Mandy Korff, Jan Peeters, Jan Stafleu, Ronald Harting, Roula Dambrink, Freek Busschers and Jan Gunnink, Deltares and NAM, June 2015.
2. Modifications of the Geological model for Site response at the Groningen Field, P. Kruiver, Deltares, June 2016.
3. Background document NAM database of subsurface information - Version date of database - 29 March 2018, Pauline Kruiver, Fred Kloosterman, Ger de Lange, Pieter Doornenbal, Deltares, Mar 2018.
4. V5 Ground-Motion Model (GMM) for the Groningen Field - Re-issue with Assurance Letter, Julian J Bommer, Benjamin Edwards, Pauline P Kruiver, Adrian Rodriguez-Marek, Peter J Stafford, Bernard Dost, Michail Ntinalexis, Elmer Ruigrok and Jesper Spetzler, , Mar 2018.
5. Report on the v6 Fragility and Consequence Models for the Groningen Field, Helen Crowley, Rui Pinho and Francesco Cavalieri, March 2019

NAM

Title	Calibration and verification of a nonlinear macro-element for SSI analysis in the Groningen region		Date: April 2019 Initiator: NAM
Autor(s)	Francesco Cavalieri, António A. Correia	Editors	Jan van Elk and Dirk Doornhof
Organisation	MOSAYK	Organisation	NAM
Place in the Study and Data Acquisition Plan	Study Theme: Seismic Response of Buildings (URM) Comment: In this report, a study into the transfer of seismic motion from the soil into the foundation and the structure of buildings, i.e. the soil structure interaction, is described. Extensive studies have been carried out by Deltares to prepare a detailed map of the shallow subsurface (Ref. 1 to 3). Based on the description of the shallow sub-surface, amplification factors of the ground motion have been derived and included in the ground motion model (GMM) (Ref. 4). Using representative values of the amplification factor, the response of a selection of buildings to earthquake motion is analysed in this report. The models prepared for the index buildings used in the derivation of fragility functions were used in this study (Ref. 5). The foundation of the buildings is important in the transfer of the ground motion into the buildings. In this study index buildings with shallow foundations as wells as buildings with pile foundations were considered.		
Directliy linked research	(1) Shake table tests (2) Fragility curves for building typologies (URM) (3) Shallow geology and soil (4) Risk Assessment		
Used data	Experiments		
Associated organisation	NAM		
Assurance	Eucentre		

D14

DELIVERABLE

Project Information

Project Title:	**Modelling of URM buildings in support of damage fragility functions derivation**
Project Start:	February 2017
Duration:	23 months
Technical Point of Contact:	Rui Pinho
Administrative Point of Contact:	Roberto Nascimbene

Deliverable Information

Deliverable Title:	**Calibration and verification of a nonlinear macro-element for SSI analysis in the Groningen region**
Data of Issue:	30th April 2019
Authors:	Francesco Cavalieri, António A. Correia
Reviewer:	Rui Pinho

REVISION: **v1**

Table of Contents

Introduction

Dynamic soil–structure interaction (SSI), involving the coupling of structure, foundation and soil, is a crucial and challenging problem, especially when soil nonlinearity plays an important role. In a previous study by Mosayk (2015) a one-dimensional frequency-independent model (where soil nonlinearity was accounted for only in a simplified manner) was proposed to represent SSI in the development of fragility functions for buildings in the Groningen field (Crowley et al., 2015; Crowley and Pinho, 2017).

This work describes instead the calibration of an explicitly nonlinear SSI macro-element used in the development of the v6 fragility functions for buildings in the Groningen region (Crowley et al., 2019). Further, in order to gain confidence on the former, calibration of two alternative SSI approaches (one-dimensional frequency-independent model and a Lumped Parameter Model) are also carried out, and the results compared in terms of their impact on fragility functions.

The report starts in Chapter 1 with a description of the characterisation of the soil properties in the Groningen region and the selection of representative soil profiles for the subsequent analyses. Chapter 2 summarises the eight typical structural configurations to which the three SSI approaches are applied. This is then followed by the calibration of the input parameters for the nonlinear macro-element approach (Chapter 3) and for the two alternative linear methods (Chapter 4). Finally, in Chapter 5, the comparison in terms of fragility functions is presented.

1 Procedure for the selection of representative soil profile for SSI

In order to account for Soil-Structure-Interaction (SSI) it is first required to define representative soil profiles that may be used for assessment of the input parameters of the different models used (one-dimensional frequency-independent, LPM, macro-element). The representativeness of the soil profile becomes an even more important aspect, given the wide area being considered in this study.

The selection of representative soil profiles takes advantage of the detailed microzonation carried out in recent years for the Groningen region, resulting, among others, in maps of the site response Amplification Factor (AF) for several spectral ordinates (Rodriguez-Marek et al., 2017). The examination of AF distributions shows that in general the patterns of high and low AF are well reflected by the geological zonation model (Bommer et al., 2017). Therefore, the AF represents well the soil behaviour of the shallow deposits, and it can be considered a reliable parameter for the identification of representative soil profiles.

The procedure for the soil profile selection involves several steps listed below and described in more detail in the following sections.

1) Analysis of the Amplification Factor (AF) distribution;
2) Selection of one or more sets of sites around representative values of AF;
3) Selection of the Vs profiles corresponding to the locations with homogeneous AF identified in 2);
4) Evaluation of the mean Vs profiles;
5) Search of the single Vs profile with the best fit in comparison with the mean Vs profile;
6) Extraction of the properties of the single Vs profile;

The data used in this section comes from the enormous amount of multidisciplinary work carried out on the Groningen field area concerning geology, seismic hazard, site response analysis, geotechnical characterization, ground motion model, risk assessment, etc., and documented in numerous publications, such as e.g. Bommer et al. (2015), Bommer et al. (2017), Bommer et al. (2018), Kruiver & de Lange (2015), Kruiver et al. (2017a), Kruiver et al. (2017b), Rodriguez-Marek et al. (2017), Romijn R. (2017).

1.1 Analysis of the Amplification Factor (AF) distribution

The Groningen subsurface consists of up to an 800 m thick sequence of soft unconsolidated sediments that are mainly composed of sand and clay.

TNO – Geological Survey of the Netherlands (TNO-GSN) systematically produces 3D geological models of the Dutch subsurface (Van der Meulen et al., 2013). One of these models is the voxel model called GeoTOP, which describes the geometry and properties of the shallow subsurface to a maximum depth of NAP −50 m (Stafleu et al., 2011, 2012; Maljers et al., 2015; Stafleu & Dubelaar, 2016). GeoTOP schematises the subsurface in a regular grid of rectangular blocks (‘voxels’, ‘tiles’ or ‘3D grid cells’) each measuring 100 m × 100 m × 0.5 m (x, y, z). Each voxel in the model contains estimates of the lithostratigraphical unit and the representative lithological class (including a grain-size class for sand) (Kruiver et al., 2017a).

In order to quantify seismic hazard and risk due to production-induced earthquakes in the Groningen gas field two geological models are available, the first focusing on site response and the second on liquefaction. To derive input parameters for SSI analysis, most of the information came from the first model, which is the ‘Geological model for Site response in Groningen’ (GSG model) (Kruiver et al., 2017a) and is based on the detailed 3D GeoTOP voxel model containing lithostratigraphy and lithoclass attributes mentioned above.

To build the GSG model, Kruiver et al. (2017a) combine the GeoTOP model with information from boreholes, cone penetration tests, regional digital geological and geo-hydrological models to cover the full range from the surface down to the base of the North Sea Supergroup (base Paleogene) at ~800 m depth. The GSG model consists of a microzonation based on geology and a stack of soil stratigraphy for each of the about 140,000 grid cells (100 m × 100 m) to which properties (V_S and parameters relevant for nonlinear soil behaviour) were assigned.

Figure 1.1 shows the Geological zonation of the Groningen field used for the assessment of site amplification (GMPE V4) (Kruiver et al., 2017a). It is constituted by 22 main zones, each of them can be further subdivided into subzones with similar geological characteristics, for a total of more than 150 zones. Each zone is characterized by a code, the first two numbers describe the typical soil column, whereas the last two digits are a sequential number characterising differences for instance in the thickness and/or depth of certain layers. For instance, zones 1011 and 1012 have the same typical soil column of type 10 (see legend of the geological zonation map), but with different thickness and depth sequence, in order to capture the litho-stratigraphic amplification.

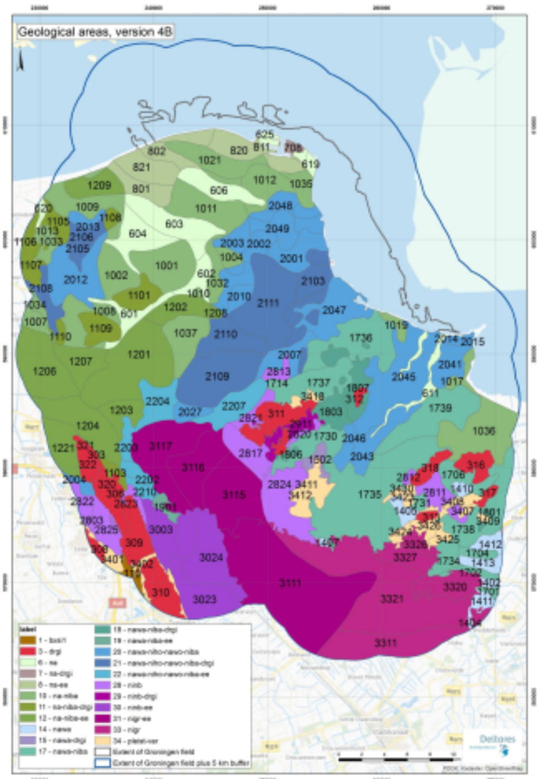

Figure 1.1 Geological zonation of the Groningen field used for the assessment of site amplification (GMPE V4). Similar colours indicate similar geological successions in the shallow depth range (Kruiver et al., 2017a).

For the Groningen field, a regional shear-wave velocity (V_S) model was constructed partially based on the GSG model (Kruiver et al., 2017b). The V_S model extends to a depth of almost 1 km, the detailed V_S profiles are constructed from a combination of three data sets covering different, partially overlapping, depth ranges. The uppermost 50 m of the V_S profiles are obtained from a high-resolution geological model with representative V_S values assigned to the sediments. Field measurements of V_S were used to derive representative V_S values for the different types of sediments. The profiles from 50 to 120 m are obtained from inversion of surface waves recorded (as noise) during deep seismic reflection profiling of the gas reservoir. The deepest part of the profiles is obtained from sonic logging and V_P–V_S relationships based on measurements in deep boreholes (Kruiver et al., 2017b). The interested reader is referred to the latter work for additional information about the shear-wave velocity (V_S) model.

The regional shear-wave velocity (V_S) model described above has been used as a basis for seismic microzonation of the Groningen gas field area, extending more than 1000 km^2. In this framework, the field-wide V_S profiles are subsequently used to define a reference rock horizon—at a depth of about 800 m—and then used in a large number of site response analyses to obtain nonlinear frequency-dependent amplification factors, as described in Rodriguez-Marek et al. (2017).

The site response analysis study (carried out considering 3600 input motions subdivided into ten levels) was performed for a grid of about 140’000 points homogeneously distributed in the Groningen area. Figure 1.2 shows, as an example, the spatial distribution of AF across the Groningen area at 0.01 s periods for Weak input motion (i.e. rank 1-360) and Strong input motion (i.e. rank 3241-3600). Similar data is available for others periods.

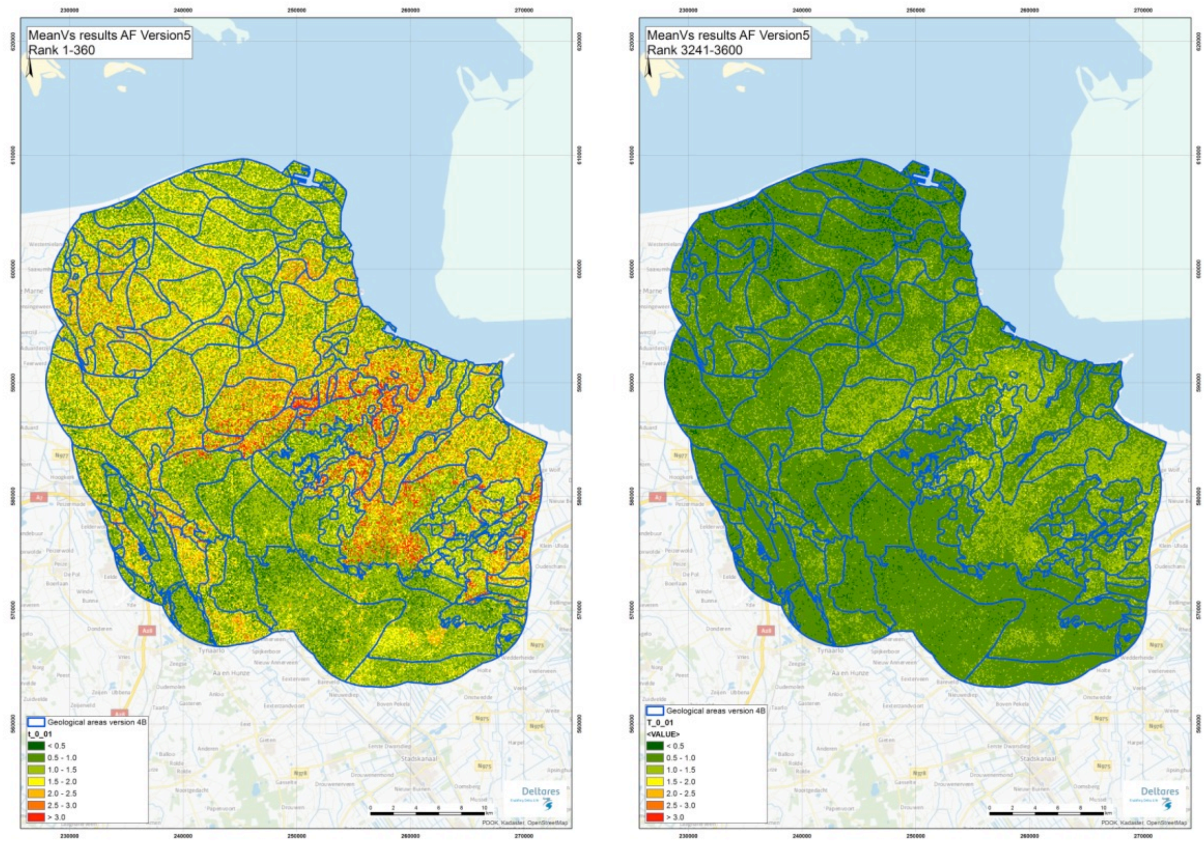

a) b)

Figure 1.2 Amplification Factor (AF) for T=0.01 s: a) Weak motion (rank 1-360); b) Strong motion (rank 3241-3600) (Kruiver, 2018).

The AF data are organized in one file per geological zone. Each file contains the following information: localization the site (i.e. zone code, coordinates); magnitude and distance of the corresponding input motion; the rank of the input motion (with the meaning described below); the spectral acceleration at the reference rock horizon and the corresponding amplification factor (AF) for 23 periods ranging from 0.01 to 5 s; the maximum shear strain; the PGV on bedrock, the PGV at surface and the PGV amplification factor.

The rank characterizes the input motion, with a low rank corresponding to a weak input motion, whereas high rank corresponds to a strong input motion. The 3600 input motions were sorted into 10 groups and one motion per group is used for each coordinate. The weakest motions have rank 1-360 (group 1, Low i.m. in the following), intermediate have rank 1441-1800 (group 5, Medium i.m. in the following) and the strongest have rank 3241-3600 (group 10, High i.m. in the following).

The AF is available for different periods, the analysis of the data has been carried out considering the period of 0.5 s, which is close to the structural period of the buildings considered, and for three different levels of input motion: low, medium and high input motion. Figure 1.3 shows the histograms of the Amplification Factor (AF) for period equal to 0.5 s for the three input motions considered.

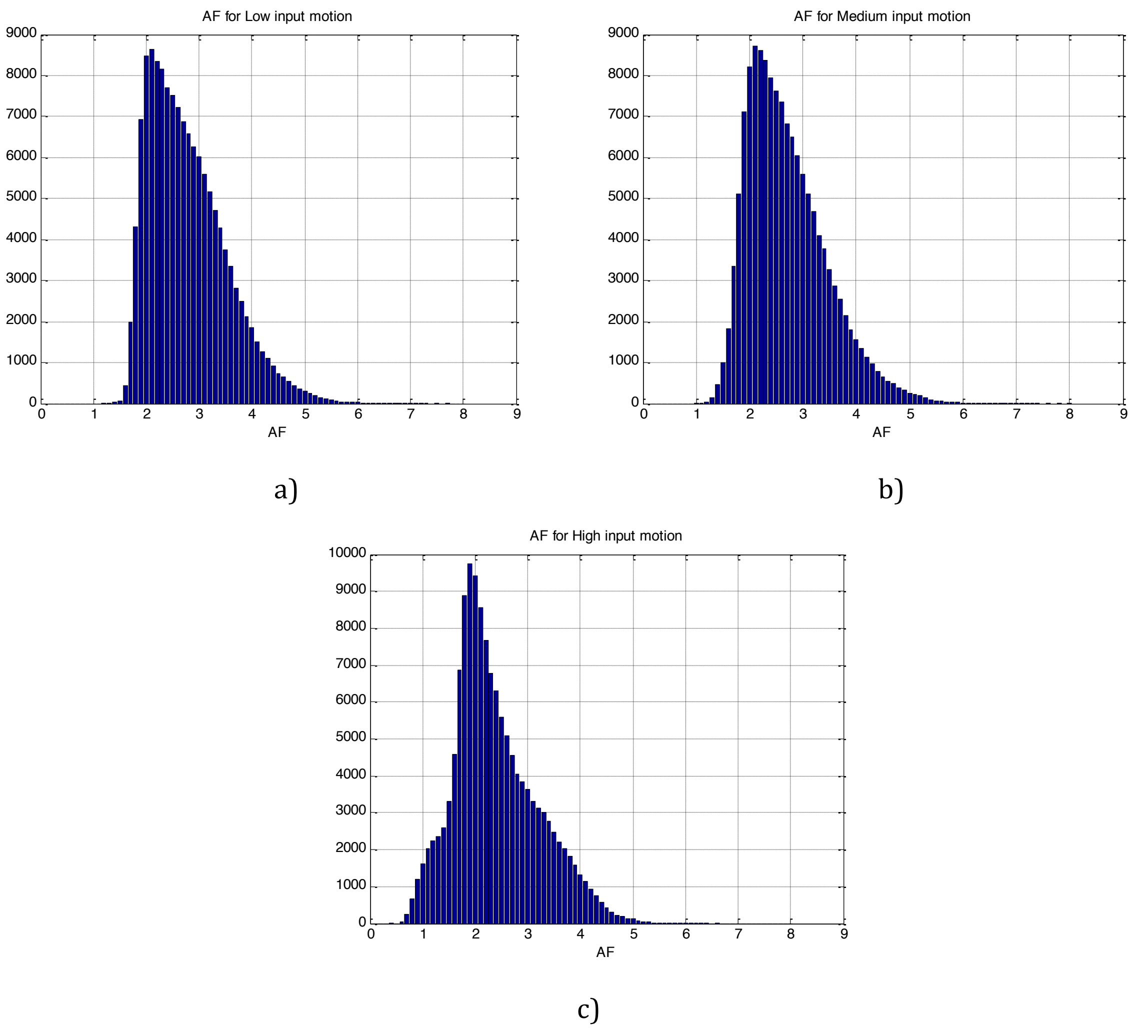

Figure 1.3 Histograms of the Amplification Factor (AF) for period equal to 0.5 s: a) Low i.m.; b) Medium i.m.; c) High i.m.

1.2 Selection of one or more sets of sites around representative values of AF

Due to the non-negative values of the AF, it was assumed that AF follows a lognormal distribution. Assuming μ and σ respectively as the expectation and standard deviation of ln(AF), the following relationship can be defined:

- $e^{\mu} = \mu^*$: median, geometric "mean",
- $e^{\sigma} = \sigma^*$: multiplicative standard deviation

Figure 1.4 shows the typical shape of a lognormal distribution. In accordance with this distribution, about 68% of data are included in the range $(\mu^*/\sigma^*)\div(\mu^*\cdot\sigma^*)$, whereas about 95% of data are included in the range $(\mu^*/\sigma^{*2})\div(\mu^*\cdot\sigma^{*2})$. Based on the lognormal distribution two representative values of AF have been selected, the first is the median (μ^*) while the second is set equal to $\mu^*\cdot\sigma^{*2}$. For each of the two values of AF a set of Vs profiles corresponding to different sites have been analysed. Depending on the AF considered, two different intervals of values have been considered, for the median (μ^*) AF the selected intervals have an amplitude respectively of 0.1 and 0.2, whereas for AF equal to $\mu^*\ \sigma^{*2}$ the amplitude of the intervals considered is larger, i.e. 0.2 and 0.4, due to the reduced frequency around that value.

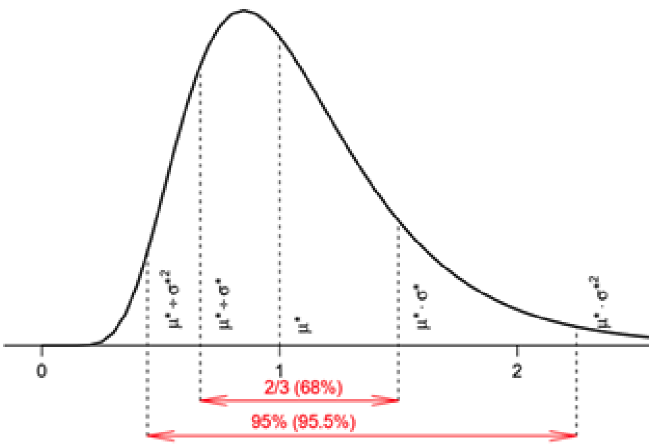

Figure 1.4 Shape of log-normal distribution.

To analyse the AF distribution, the period of 0.5 s has been selected considering its representativeness with respect to the structural period of the building stock of the Groningen area used for derivation of fragility curves. Table 1.1 summarizes the number of sites considered around the two AF values (i.e. μ^* and $\mu^*\cdot\ \sigma^{*2}$) at period equal to 0.5 s, for two amplitude intervals and taking into account three levels of input motion (i.e. Medium, High and Low).

Table 1.1: Number of sites considered around the two AF values at period equal to 0.5 s (i.e. μ^* and $\mu^*\cdot\ \sigma^{*2}$) for two amplitude intervals and taking into account three levels of input motion (i.e. Medium, High and Low).

	Low i.m.	Medium i.m.	High i.m.
N° sites in the interval 0.1 around median AF	6895	7272	7216
N° sites in the interval 0.2 around median AF	13749	14500	14437
N° sites in the interval 0.2 around AF equal to $\mu^*\cdot\ \sigma^{*2}$	1526	1491	888
N° sites in the interval 0.4 around AF equal to $\mu^*\cdot\sigma^{*2}$	3214	3070	1815

Figure 1.5 shows the normalized histograms and corresponding lognormal distribution of the Amplification Factor (AF) for a period equal to 0.5 s, for the three levels of input motion. Table 1.2 summarizes the relevant parameters of the lognormal distribution of the AF at period equal to 0.5 s for the three levels of input motion.

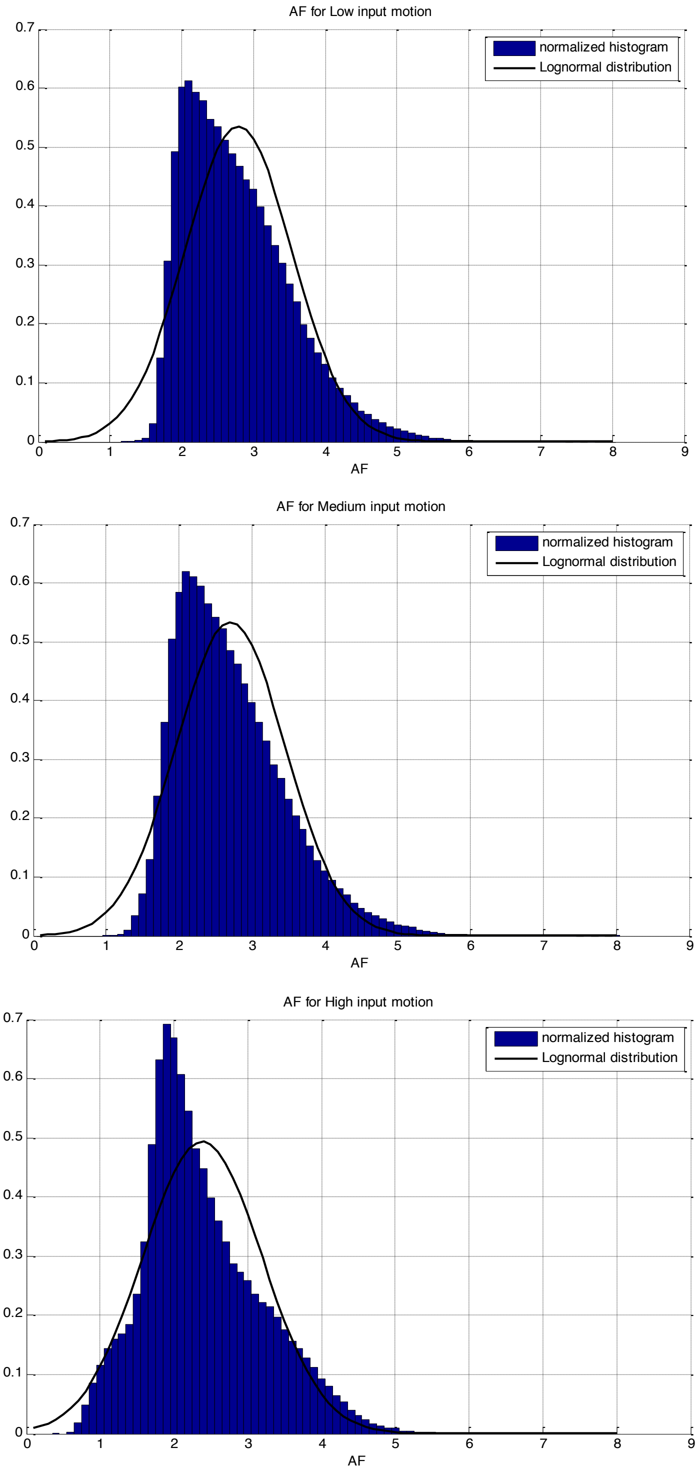

a)
b)
c)

Figure 1.5 Normalized histograms and lognormal distribution of the Amplification Factor (AF) for period equal to 0.5 s: a) Low i.m.; b) Medium i.m.; c) High i.m.

Table 1.2: Relevant parameters of the lognormal distribution of the AF at period equal to 0.5 s for three levels of input motion (i.e. Low, Medium and High).

LOGNORMAL DISTRIBUTION	Low i.m.	Medium i.m.	High i.m.
Mean of ln(AF) ==> μ	0.9925	0.9608	0.8114
Standard deviation of ln(AF) ==> σ	0.2549	0.2643	0.3465
median==> $\mu^*=e^\mu$	2.70	2.61	2.25
$\sigma^*=e^\sigma$	1.29	1.30	1.41
$\mu^*\ \sigma^{*2}$	4.49	4.43	4.50

1.3 Selection of V_s profile corresponding to identified locations with homogeneous AF

The V_s profiles provided by Deltares (Kruiver, 2018) are grouped into 158 files based on the geology zonation. An intermediate step was to separate the different Vs profiles (together with the others attributes) into single files, resulting in 140'821 V_S profiles, each of them characterized by a progressive number.

In section 1.2, a few sets of sites with homogeneous AF were identified. The sites were selected from the "Complete" database that is constituted by a regular grid, covering the whole Groningen area, of about ~140k sites. However, since buildings are not equally spread out throughout the region, a "Reduced" subset of sites has been defined, including about ~34k sites, based on the exposure, i.e. considering only profiles close to buildings.

Figure 1.6 shows a Groningen area map indicating the sites where the V_S profiles are considered and the position of the buildings.

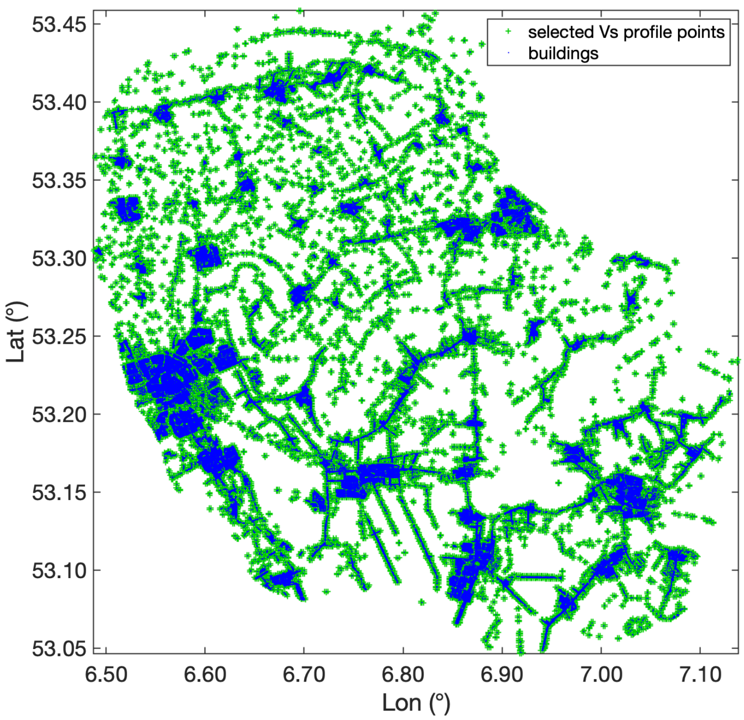

Figure 1.6 Groningen area map in which are indicated the sites where the V_S profiles are considered and the position of the buildings.

In the following, the V_S profiles will be selected considering both the “Complete” and the “Reduced” database, in case the resulting mean V_S profile is not affected by the reduced number of sites considered, the “Reduced” subset has the advantage of considering only soil properties close to the buildings, being therefore more representative for SSI analysis.

The following combination of V_S profiles were extracted for 24 cases:

- two databases of sites: Complete and Reduced depending on exposure;
- three levels of input motion: Low, Medium, High;
- different AF amplitude: μ^* and $\mu^*\sigma^2$;
- for each AF amplitude two different intervals: 0.1 and 0.2 around μ^* and 0.2 and 0.4 around $\mu^*\sigma^2$

The analysis of the V_S profiles has been limited to the first 50m, this depth can be considered sufficiently representative for SSI analysis.

The following figures show the V_S profiles (blue continuous lines) for each group described above. The figures also show the upper and lower envelop (yellow dashed lines). Moreover, in accordance with the considerations discussed in section 1.4, the figures below also show the mean (red dashed line) and mean plus and minus the standard deviations (black dashed lines) V_S profiles.

Complete database

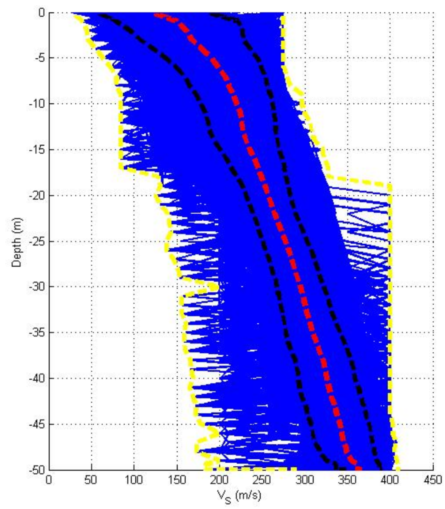

Medium i.m. Interval 0.1 around μ*

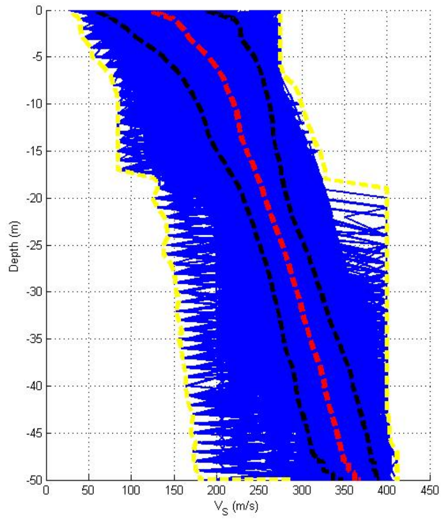

Medium i.m. Interval 0.2 around μ*

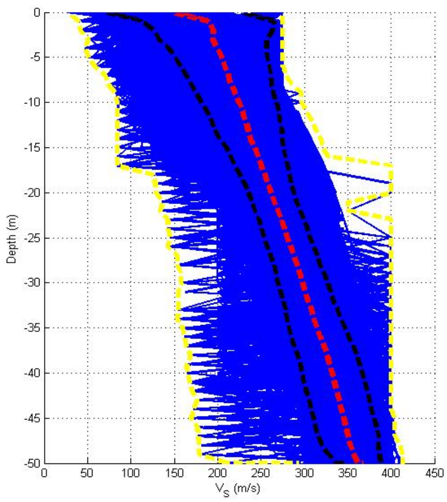

High i.m. Interval 0.1 around μ*

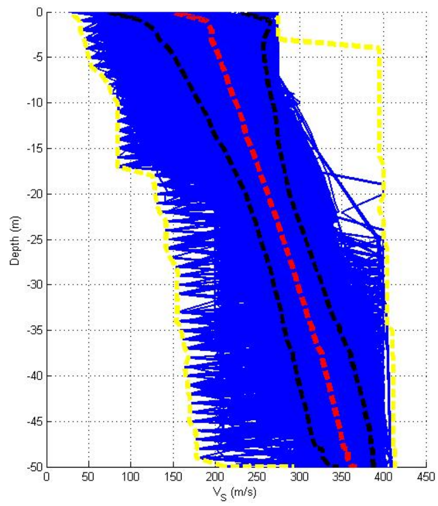

High i.m. Interval 0.2 around μ*

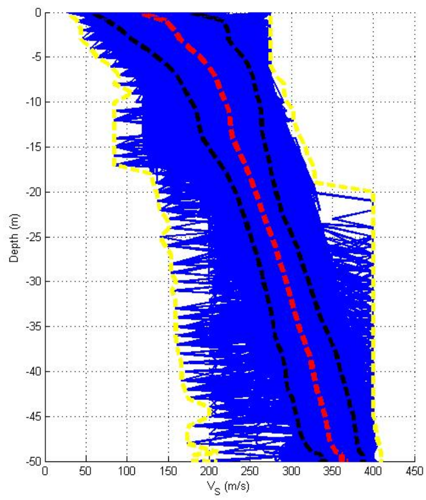

Low i.m. Interval 0.1 around μ*

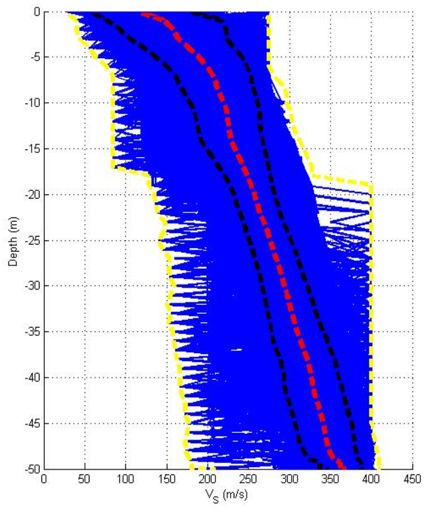

Low i.m. Interval 0.2 around μ*

Figure 1.7 VS profiles for different input motion level (i.e. Medium, High, Low) considering the Complete database of site – Amplitude of the interval around μ*: 0.1 and 0.2.

Reduced database

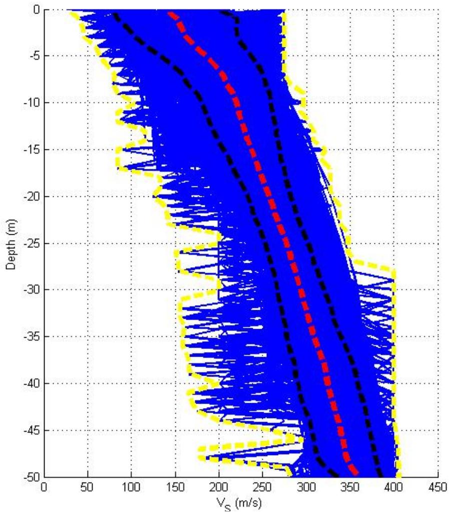

Medium i.m. Interval 0.1 around μ*

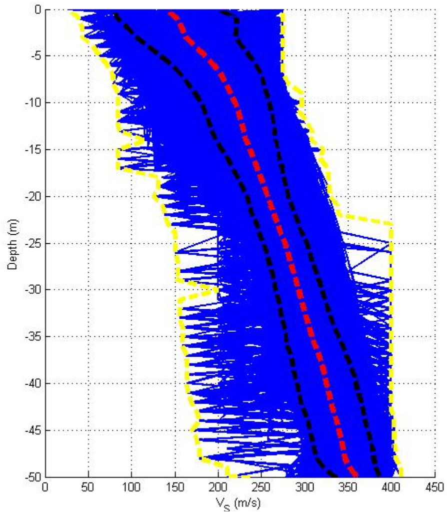

Medium i.m. Interval 0.2 around μ*

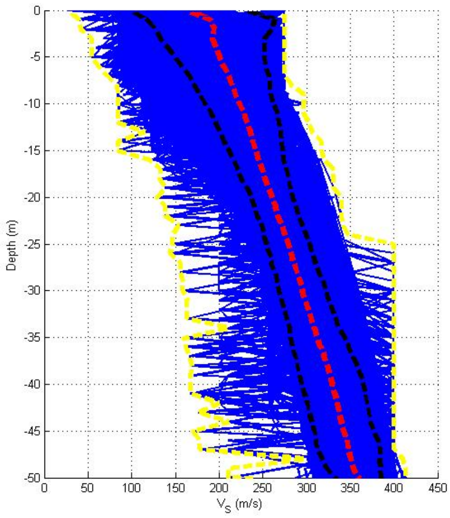

High i.m. Interval 0.1 around μ*

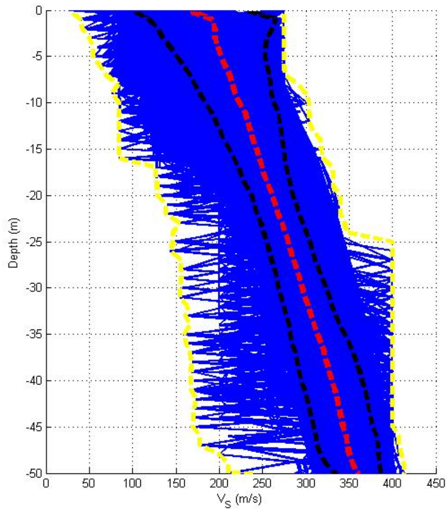

High i.m. Interval 0.2 around μ*

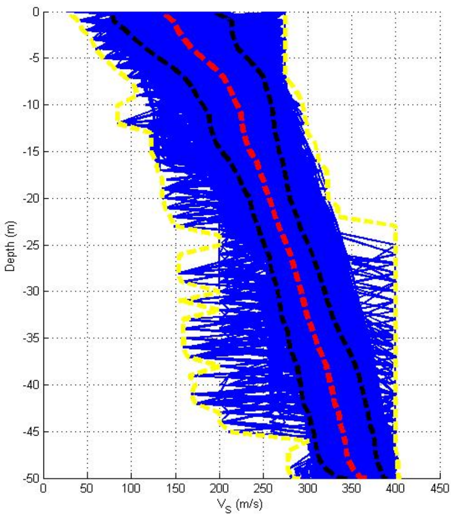

Low i.m. Interval 0.1 around μ*

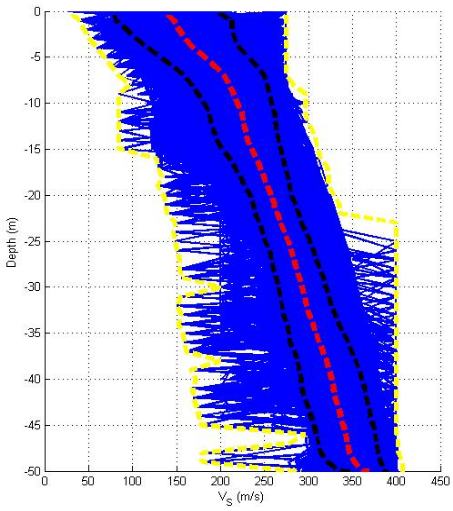

Low i.m. Interval 0.2 around μ*

Figure 1.8 V_S profiles for different input motion level (i.e. Medium, High, Low) considering the Reduced database of site – Amplitude of the interval around μ*: 0.1 and 0.2.

Complete database

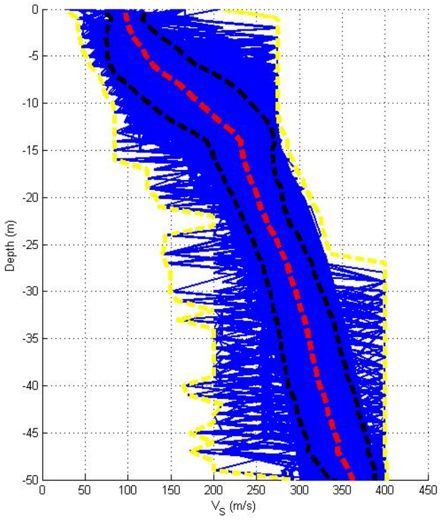

Medium i.m. Interval 0.2 around μ*σ²

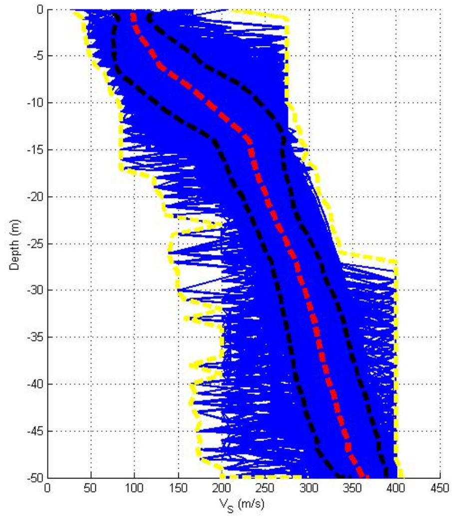

Medium i.m. Interval 0.4 around μ*σ²

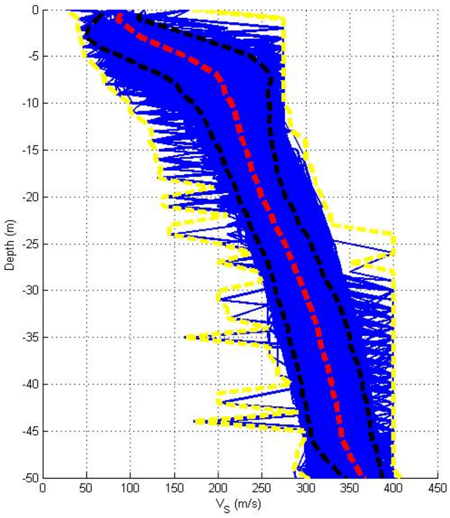

High i.m. Interval 0.2 around μ*σ²

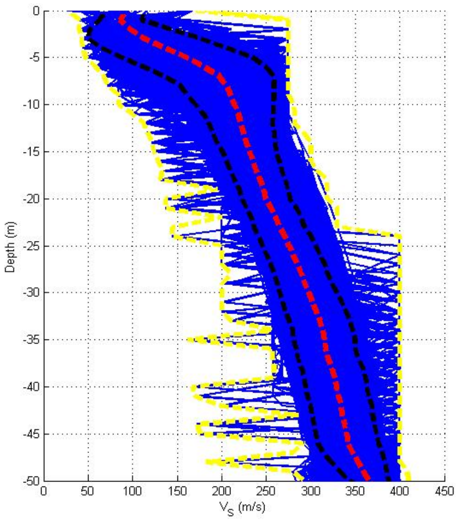

High i.m. Interval 0.4 around μ*σ²

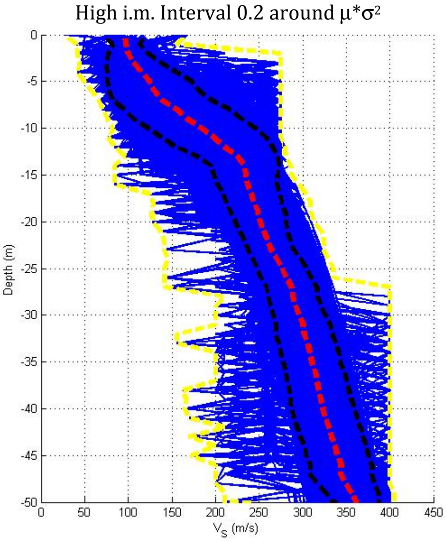

Low i.m. Interval 0.2 around μ*σ²

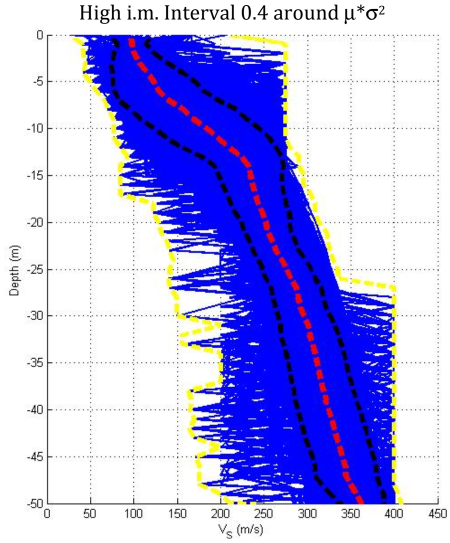

Low i.m. Interval 0.4 around μ*σ²

Figure 1.9 V_S profiles for different input motion level (i.e. Medium, High, Low) considering the Complete database of site – Amplitude of the interval around μ*σ²: 0.2 and 0.4.

Reduced database

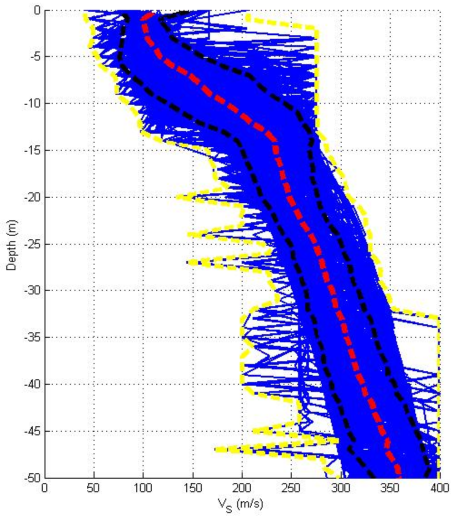

Medium i.m. Interval 0.2 around μ*σ²

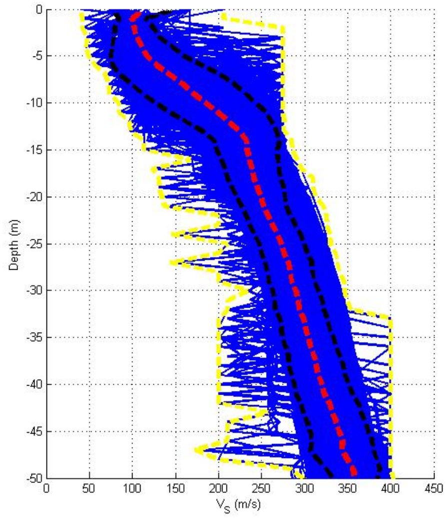

Medium i.m. Interval 0.4 around μ*σ²

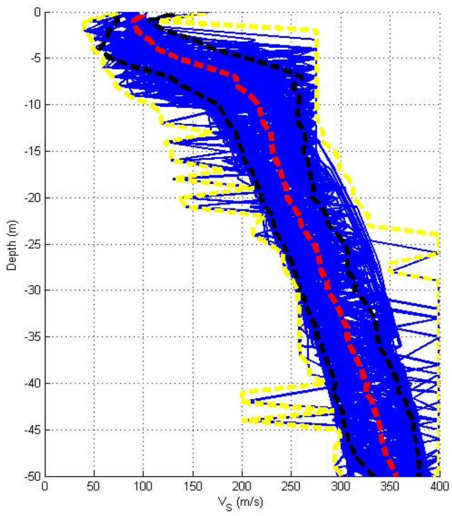

High i.m. Interval 0.2 around μ*σ²

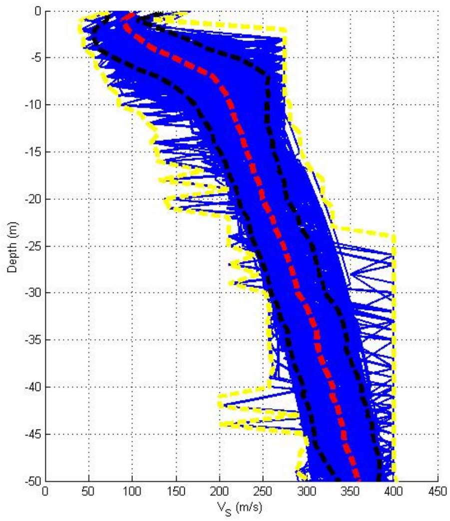

High i.m. Interval 0.4 around μ*σ²

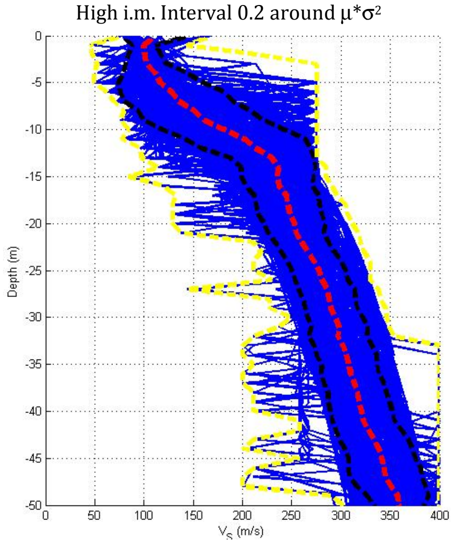

Low i.m. Interval 0.2 around μ*σ²

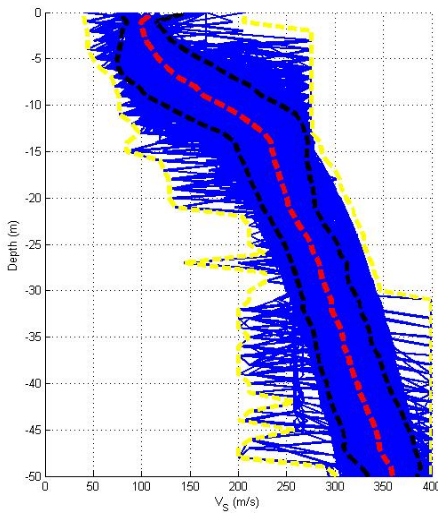

Low i.m. Interval 0.4 around μ*σ²

Figure 1.10 V_S profiles for different input motion level (i.e. Medium, High, Low) considering the Reduced database of site – Amplitude of the interval around μ*σ²: 0.2 and 0.4.

1.4 Evaluation of the mean V_S profiles

In this step, the mean V_S profile and the corresponding standard deviation were evaluated, with the plots of the mean V_S profile (additionally also mean ± standard deviation) for each group considered already shown in section 1.3 (see Figure 1.7, Figure 1.8, Figure 1.9, Figure 1.10). It is worth noting that the dispersion around the mean V_S profiles is generally limited.

In the following, the different parameters, namely type of database, input motion level, value of AF, etc., considered for the evaluation of mean V_S profiles are compared. The comparisons of V_S profiles are limited to the first 20 m depth because those soil layers are the ones mostly affecting SSI. Although it is not shown, the V_S profiles in the lower part (>20 m) are almost coincident.

Figure 1.11 shows the mean V_S profiles for the three input motion levels (i.e. Medium, High, Low) and the two databases (i.e. total and reduced). The analysis is carried out considering the sites with AF amplitude in the interval around μ* equal to 0.1. For both databases, Low and Medium input motions have similar V_S profiles (red continuous and black dashed lines), while the V_S profile corresponding to the High input motion slightly diverges in the upper part (about 6-7m) (blue continuous line).

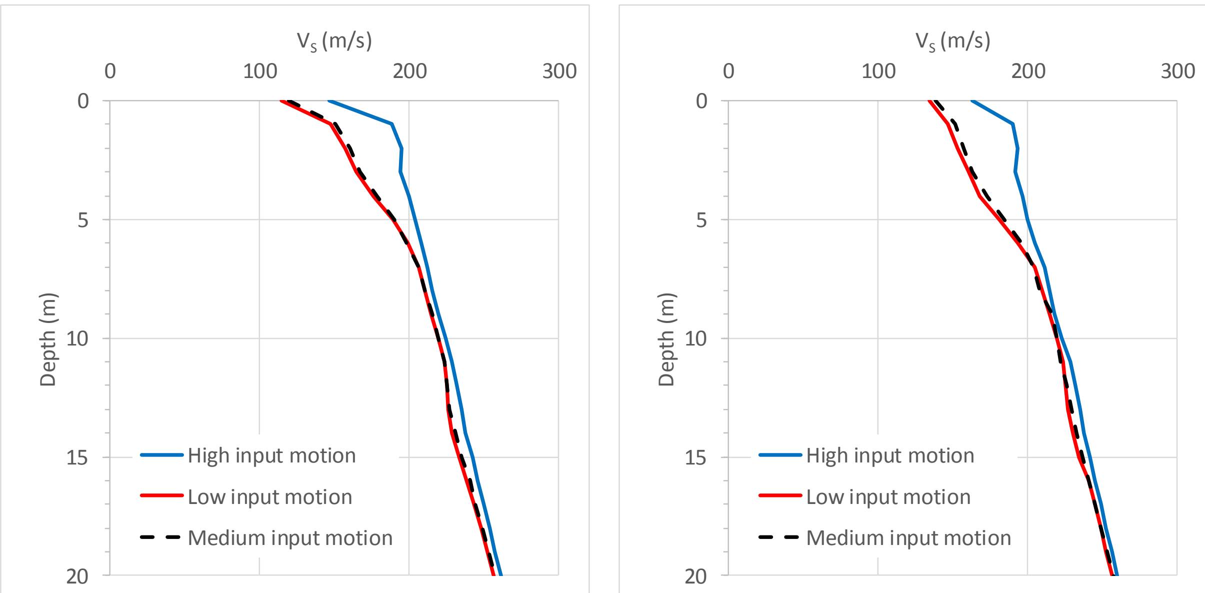

a) b)

Figure 1.11 Mean V_S profiles for three input motion levels (i.e. Medium, High, Low) considering the sites with AF amplitude in the interval around μ* equal to 0.1: a) Complete database; b) reduced database.

Figure 1.12 shows the influence of the amplitude of the interval considered around the selected AF, and in particular around μ*, the comparison is limited to the Complete database. The comparison shows that independently from the input motion level (i.e. Medium, High, Low) the effect of the amplitude of the interval considered (i.e. 0.1 or 0.2) is negligible.

Figure 1.13 shows the influence of the database used (i.e. Complete vs Reduced) for the median AF (μ*), the comparison is limited to the interval around the selected AF equal to 0.2. The comparison shows that independently from the input motion level (i.e. Medium, High, Low) the effect of the database (i.e. Complete vs Reduced) is limited not influencing the mean V_S profile. This result supports the use of the reduced database, which is filtered based on exposure including V_S profiles close to buildings.

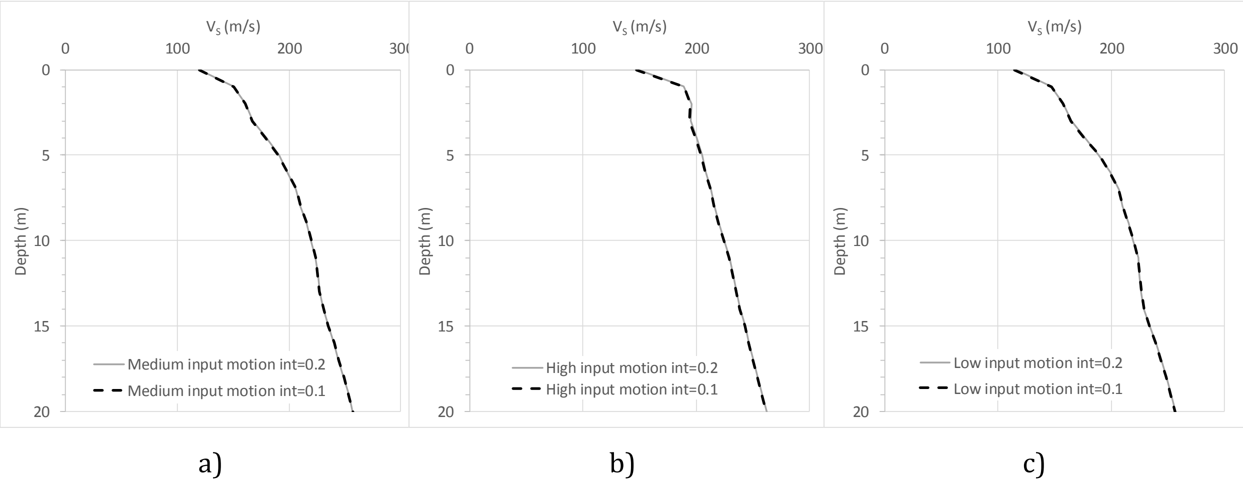

Figure 1.12 Comparison between the mean V_S profiles obtained considering the Complete database and sites with AF amplitude in the interval around μ* equal to 0.1 and 0.2: a) Medium i.m.; b) High i.m.; c) Low i.m.

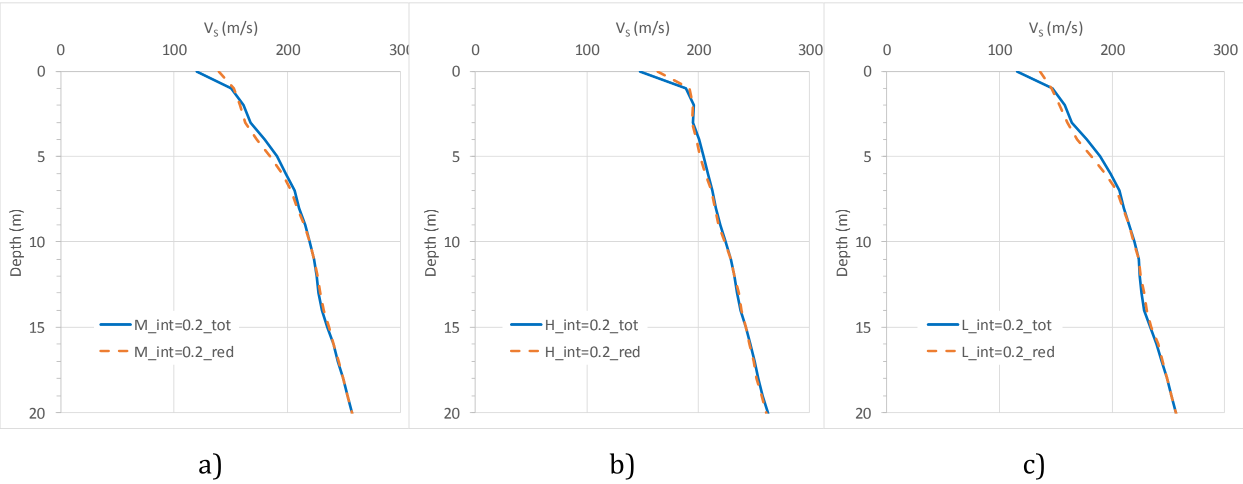

Figure 1.13 Comparison between the mean V_S profiles obtained considering sites with AF amplitude in the interval around μ* equal to 0.2 for Complete and Reduced database: a) Medium i.m.; b) High i.m.; c) Low i.m.

Figure 1.14 shows the mean V_S profiles for the three input motion levels (i.e. Medium, High, Low) and the two databases (i.e. total and reduced) considering the sites with AF amplitude in the interval around $\mu^*\sigma^2$ equal to 0.2. For both databases (i.e. total and reduced), Low and Medium input motions have similar V_S profiles (red continuous and black dashed lines), while the V_S profile corresponding to the High input motion slightly diverges in the upper part between 2 and 13m (blue continuous line).

The trend of V_S profiles for the two AF considered (i.e. μ* and $\mu^*\sigma^2$) is similar for the three i.m. (see Figure 1.11 and Figure 1.14), but the depth at which there are differences between Low/Medimum i.m. and High i.m. is larger for AF equal to $\mu^*\sigma^2$.

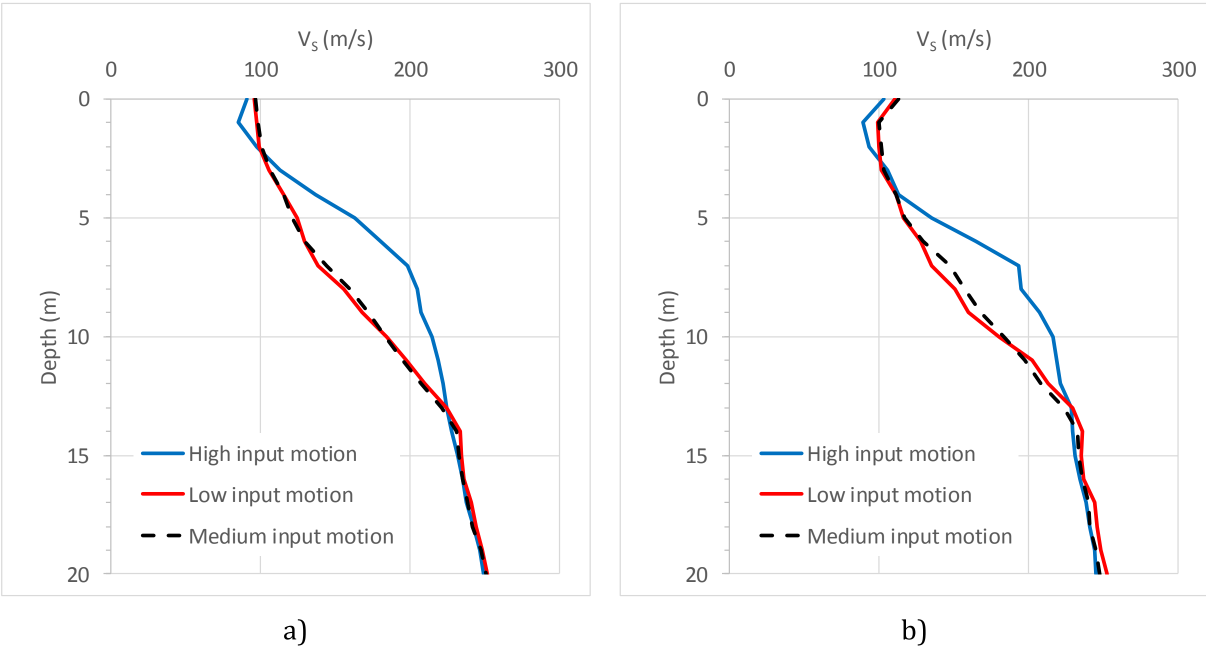

Figure 1.14 Mean V_S profiles for three input motion levels (i.e. Medium, High, Low) considering the sites with AF amplitude in the interval around $\mu^*\sigma^2$ equal to 0.2: a) Complete database; b) Reduced database.

Figure 1.15 shows the influence of the amplitude of the interval considered around the selected AF, and in particular around $\mu^*\sigma^2$, with the comparison limited to the Complete database. The comparison shows that independently from the input motion level (i.e. Medium, High, Low) the effect of the amplitude of the interval considered (i.e. 0.2 or 0.4) is negligible.

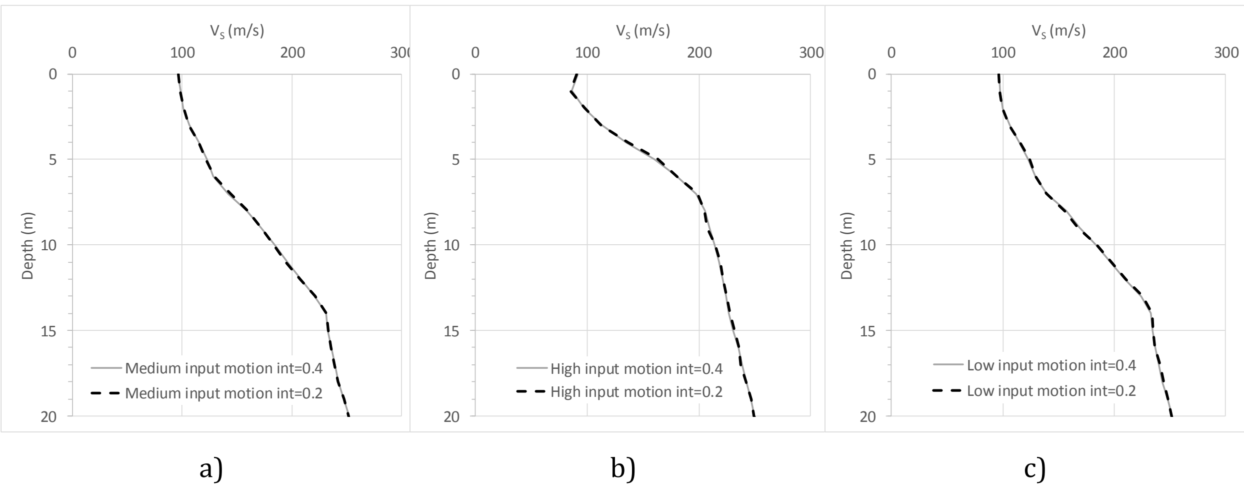

Figure 1.15 Comparison between the mean V_S profiles obtained considering the Complete database and sites with AF amplitude in the interval around $\mu^*\sigma^2$ equal to 0.2 and 0.4: a) Medium i.m.; b) High i.m.; c) Low i.m.

Figure 1.16 shows the influence of the database used (i.e. Complete vs Reduced) for the median AF ($\mu^*\sigma^2$), the comparison is limited to the interval around the selected AF equal to 0.4. The comparison shows that independently from the input motion level (i.e. Medium, High, Low) the effect of the database (i.e. Complete vs Reduced) is limited, not influencing the mean V_S profile. This result supports the use of the reduced database, which is filtered based on exposure including V_S profiles close to buildings.

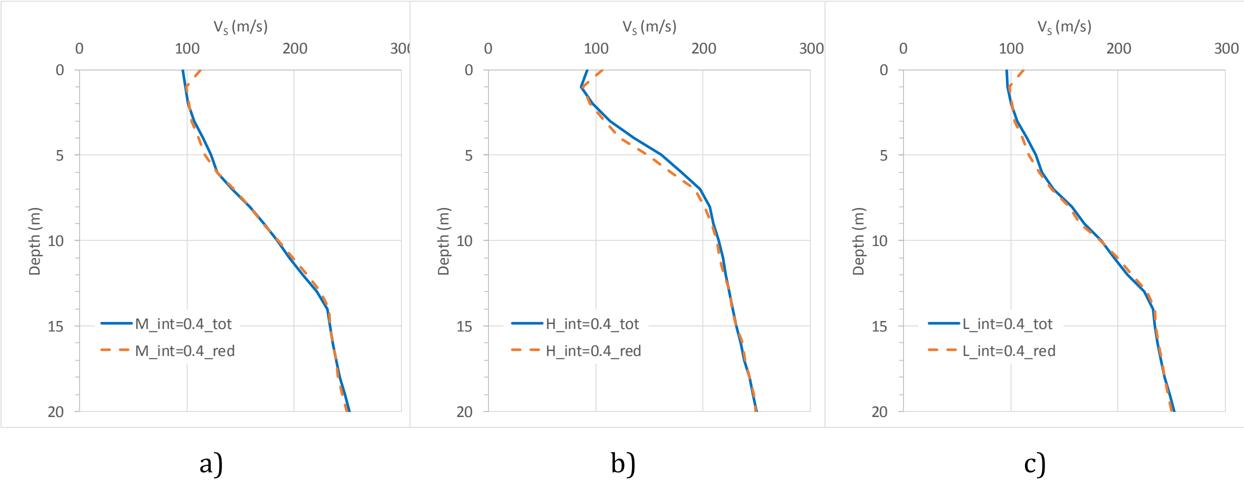

Figure 1.16 Comparison between the mean V_S profiles obtained considering sites with AF amplitude in the interval around $\mu*\sigma^2$ equal to 0.4 for Complete and Reduced database: a) Medium i.m.; b) High i.m.; c) Low i.m.

From the above considerations it results that neither the database (i.e. total vs reduced) nor the amplitude of the interval around the selected AF, affect the mean V_S profiles.

1.5 Search of single V_s profile with best fit with respect to mean V_s profile

In the previous steps, mean V_s profiles for different conditions (i.e. characterized by different AF value and related amplitude interval, type of database, level of input motion) have been calculated. However, V_s is not the only parameter of interest for SSI; a precise stratigraphy, and related parameters, needs to be associated to the V_s profile. The simplest way to perform this operation is to identify a real stratigraphy, i.e. one of the about 140k sites considered (at which a stratigraphy and soil parameters are associated), compatible with the computed mean V_s profile. This can be done evaluating the deviation between the mean V_s profile and one of the V_s profiles belonging to the group considered (i.e. characterized by the AF value and related amplitude interval, type of database, level of input motion). The deviation can be computed using the following formula:

$$\delta_j = \sqrt{\frac{1}{N}\sum_{i=1}^{N}\left[\frac{V_{S,j}(z_i)-V_{S,mean}(z_i)}{V_{S,mean}(z_i)}\right]^2} \tag{1.1}$$

where δ_j is the deviation between the mean V_s profile and the j-ith V_s profile considered in the corresponding group. The deviation represents a quantitative measure of how much the single V_s profile deviates from the reference mean Vs profile. N is the number of levels at which the comparison between the single V_s profile and the mean V_s profile is computed; $V_{S,j}(z_i)$ is the value of $V_{S,j}$ at level z_i; $V_{S,mean}(z_i)$ is the value of $V_{S,mean}$ at level z_i. δ_j has been evaluated within a depth of 50 m.

Based on the value of the minimum deviation, for each mean V_S profile computed a real stratigraphy has been associated. Figure 1.17 shows the comparison between the mean V_S profiles and the V_S profiles with minimum deviation δ_j for 6 cases. Only the reduced database of sites has been considered, in accordance with the conclusions of section 1.4, thus allowing to include in the group of sites only V_S profiles close to buildings. Two AF values were considered, including only the case with larger amplitude resulting in the following combinations: AF around μ^* - Interval 0.2 / AF around $\mu^*\sigma^2$ - Interval 0.4. The three different input motion levels were considered (i.e. Medium, High, Low).

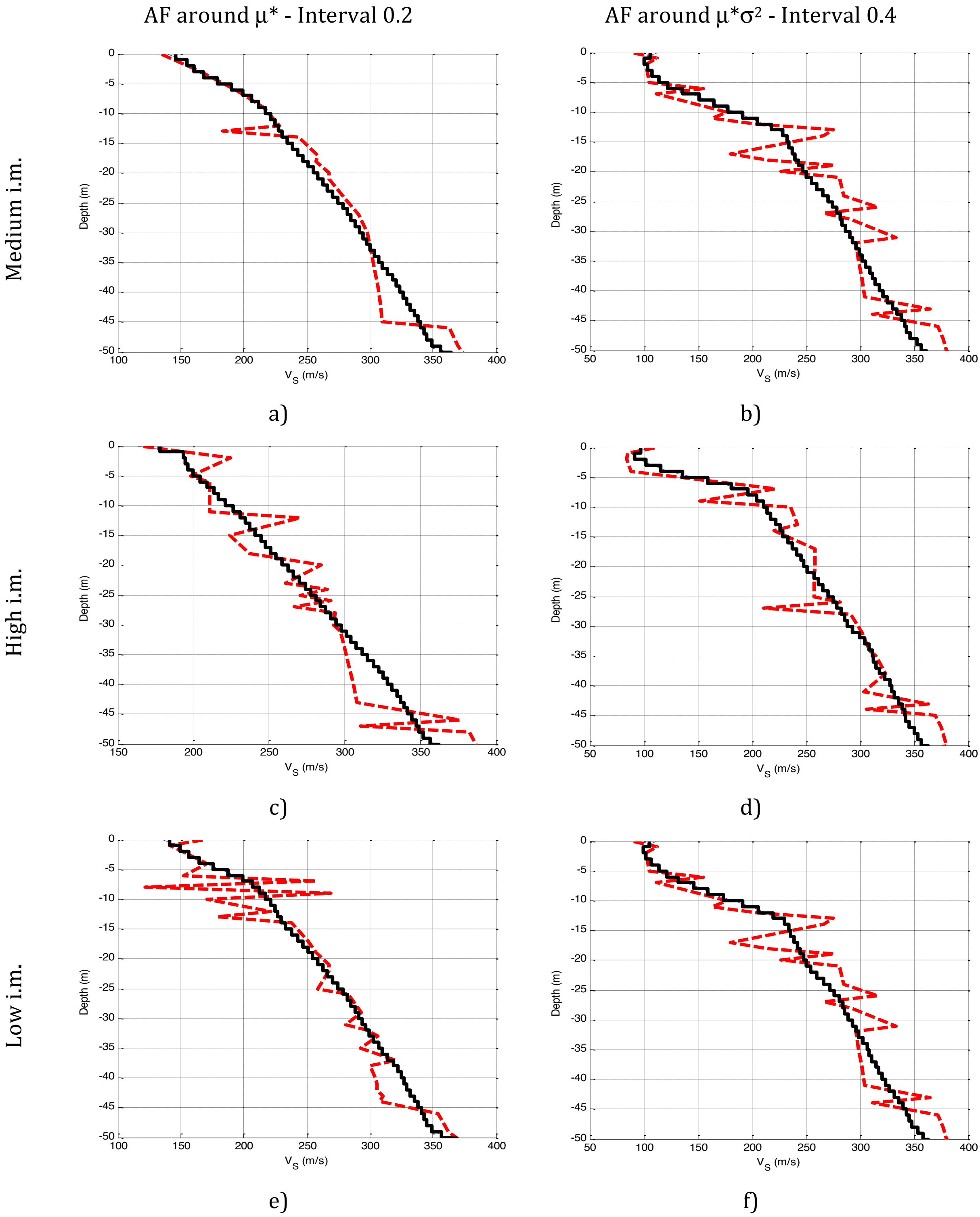

Figure 1.17 Comparison between the mean V_S profiles and the V_S profiles with minimum deviation δ considering the following combination: Reduced database of site; different input motion levels (i.e. Medium, High, Low); two combinations of AF and amplitude interval (AF around μ^* - Interval 0.2 / AF around $\mu^*\sigma^2$ - Interval 0.4).

Section 1.4 showed that the mean V_S profiles have, in general, similar trends independently of the input motion levels; however, in the upper part, there are some differences between the cases of Low/Medium i.m. (that are practically coincident) and High input motion. Among the two levels of input motion, the High i.m. was considered more representative for the development of fragility curves in relation to the spectral acceleration levels considered.

Figure 1.18 shows the response spectrum at bedrock and surface, for High input motion level and reduced database for the two sites in the AF range considered (i.e. μ^* and $\mu^*\sigma^2$), whose V_S profile has the minimum deviation with respect to the mean V_S profile evaluated in section 1.4. For the two cases mentioned above, Figure 1.19 shows the Amplification Factor (AF) evaluated as the ratio of the response spectrum at surface and bedrock. This kind of plot provides a rough idea of the frequency where the maximum amplifications occurs. The data are extracted from the results of site response analysis V5 provided by Kruiver (2018).

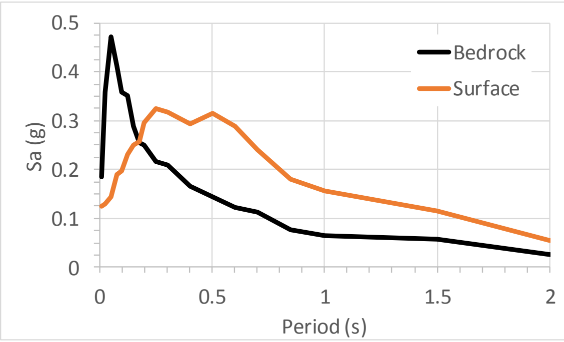

a)

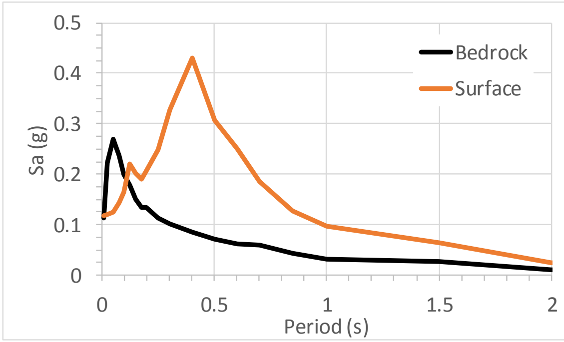

b)

Figure 1.18 Response spectrum at bedrock and surface considering Reduced database and High i.m.: a) site with V_S profile with minimum deviation from the mean V_S profile corresponding to AF equal to μ^* - interval 0.2; b) site with V_S profile with minimum deviation from the mean V_S profile corresponding to AF equal to $\mu^*\sigma^2$ - interval 0.4.

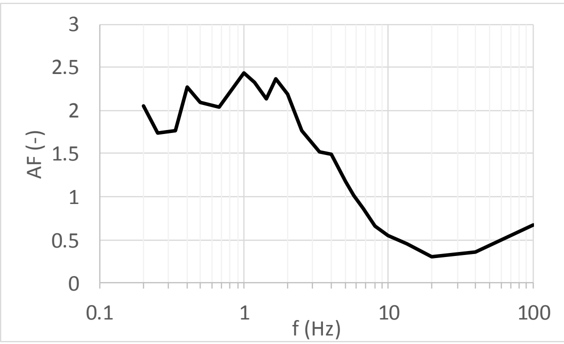

a)

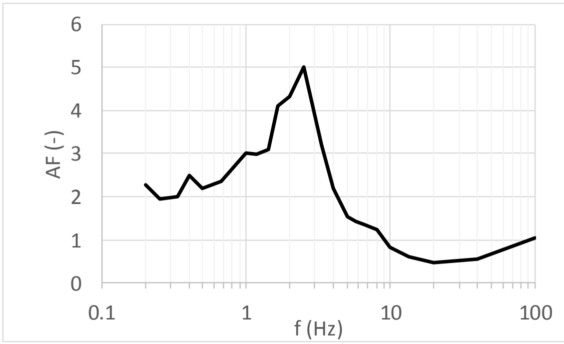

b)

Figure 1.19 Amplification Factor (AF) evaluated as the ratio of the response spectrum at surface and bedrock considering Reduced database and High i.m.: a) site with V_S profile with minimum deviation from the mean V_S profile corresponding to AF equal to μ^* - interval 0.2; b) site with V_S profile with minimum deviation from the mean V_S profile corresponding to AF equal to $\mu^*\sigma^2$ - interval 0.4.

1.6 Extraction of the properties of the single Vs profile

Based on the considerations carried out in the previous sections, two representative soil profiles to account for SSI were identified corresponding to the following combination:

- **Profile Type A**: Reduced database of sites; sites with AF around μ* and interval amplitude 0.2; High input motion level.
- **Profile Type B**: Reduced database of sites; sites with AF around μ*σ² and interval amplitude 0.4; High input motion level.

For each of the two profiles identified above, it is possible to extract besides V_S profile and soil stratigraphy also other geotechnical parameters used for site response analysis. In particular, a set of geomechanical parameters used to describe the dynamic soil behaviour in terms of the modulus reduction and damping curves. For clay, these parameters are the overconsolidation ratio (OCR), the plasticity index (IP), the undrained shear strength (S_u) and the total unit weight, which allows to define modulus reduction and damping curves in accordance with Darendeli (2001) relationships. For sand, these parameters are the median grain size (D_{50}), the coefficient of uniformity (C_u) and the total unit weight, which allows defining modulus reduction and damping curves in accordance with Menq (2003) relationships. See Kruiver et al. (2017a) and Rodriguez-Marek et al. (2017) for more details on the derivation of these parameters.

Among the available parameters for cohesive material (e.g. clay, silt, etc.) there is the undrained shear strength. Conversely, for cohesionless material (e.g. sand, etc.) there is no information on soil strength, therefore further considerations need to be added to define proper strength parameters.

1.6.1 Profile type A

Profile type A corresponds to a site (coordinates 234550, 580650) extracted from the reduced database, taking into account sites with AF around the median value (μ*) and interval amplitude equal to 0.2, and considering the AF obtained with High input motion level.

Table 1.3 shows the stratigraphy and the available geotechnical parameters within 30 m depth for soil type A, the deposit is constituted by an alternation of fine sand and cohesive (i.e. clayey sand and sandy clay) layers. Figure 1.20a) shows the stratigraphy (blue cohesionless layers; red cohesive layers) and undrained shear strength profile for cohesive material, whereas Figure 1.20b) shows the shear wave velocity profile.

Table 1.3: Stratigraphy and geotechnical parameters within 30m depth for soil type A, corresponding to a site with AF around the median value (μ*).

Depth	Thickness	Lithology	V_S	γ	PI	OCR	C_u	D_{50}	k_0	S_u
m	m	-	m/s	kN/m^3	-	-	-	-	-	kPa
0	2	Fine Sand	167.1	18.4	0	1.0	5.53	0.08	0.5	nan
2	3		224.5	19.4	0	1.0	1.94	0.12	1	nan
5	1	Clayey sand and sandy clay	197.9	16.9	50	4.8	nan	nan	1.1	87.5
6	3		211.0	16.7	15	4.9	nan	nan	1.2	101.0
9	2		211.0	16.7	15	5.0	nan	nan	1.2	117.7
11	1		211.0	16.7	10	5.0	nan	nan	1.2	127.7
12	3	Fine Sand	270.8	19.6	0	1.0	1.84	0.12	1	nan
15	3	Clayey sand and sandy clay	224.0	18.1	30	5.3	nan	nan	1.2	142.6
18	2		237.1	18.1	30	5.2	nan	nan	1.2	155.0
20	3	Fine Sand	284.3	19.6	0	1.0	1.84	0.12	1	nan
23	1	Clayey sand and sandy clay	261.0	18.1	30	5.0	nan	nan	1.2	180.1
24	1	Fine Sand	288.4	19.6	0	1.0	1.84	0.12	1	nan
25	1	Clayey sand and sandy clay	270.5	18.1	30	4.9	nan	nan	1.2	191.0
26	1	Fine Sand	290.8	19.6	0	1.0	1.84	0.12	1	nan
27	1	Clay	266.5	17.6	50	4.8	nan	nan	1.1	241.1
28	2	Fine Sand	293.6	19.6	0	1.0	1.84	0.12	1	nan

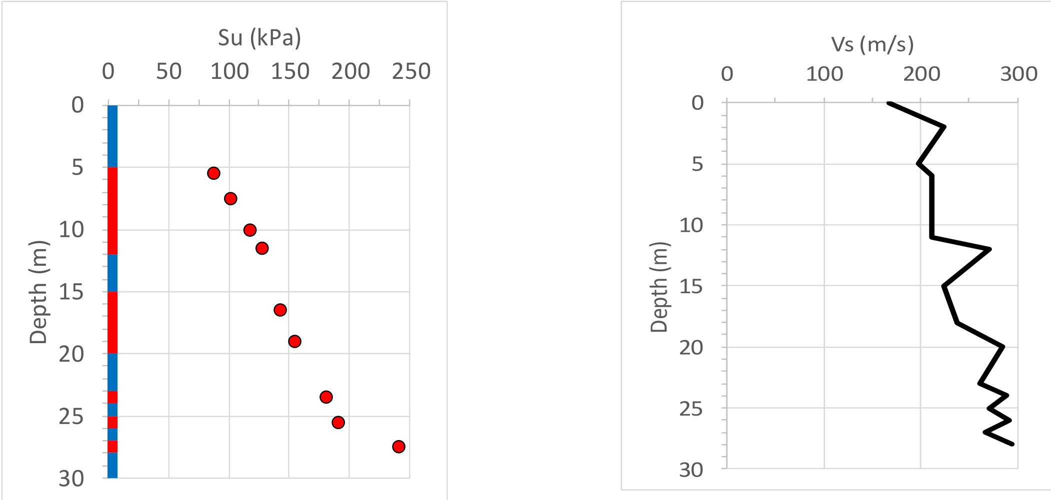

a) b)

Figure 1.20 Soil profile type A: a) Stratigraphy (blue cohesionless layers; red cohesive layers) and undrained shear strength profile for cohesive material; b) Shear wave velocity profile.

As described in more detail in Section 3.1.1, SSI analysis involves modelling the foundations through the macro-element approach, which requires as input parameters the capacity of the foundation. The shallow water table level requires that the computation of the bearing capacity be performed under undrained conditions, consequently proper strength parameters need to be defined.

The 5 m of fine sand in the upper part of the stratigraphy mostly affects the bearing capacity calculation of the shallow foundations. Section 3.1.1.1 describes the main features of the shallow foundations, which are typically characterized by a width of about 60 cm and foundation level rather limited. The two aspects mentioned above make that the depth at which the strength parameters under undrained conditions need to be evaluated is rather shallow, corresponding mostly to the fine sand layer.

Unfortunately, for fine sand, strength parameters were not defined in the framework of site response analysis calculation (see Table 1.3); moreover, results of laboratory tests are not available. Consequently, strength parameters for fine sand were defined based on literature information, trying to constrain the selected values based on available information (i.e. V_S profile, C_u and D_{50}) and engineering judgement.

The assessment of constant-volume friction angle (ϕ'_{cv}), as well as other critical state parameters, has thus been carried out based on literature information. In the following, results of laboratory tests on cohesionless material are collected from literature; particularly Table 1.4 summarizes the characteristics of the sands used by Bolton (1986), Table 1.5 summarizes the characteristics of the sands used by Negussey et al. (1988), Table 1.6 summarizes the characteristics of the sands used by Fear & Robertson (1995), whereas Table 1.7 and Table 1.8 summarize the characteristics of the sands used by Santamarina & Cho (2001). Finally, also the data included in the work of Prearo (2015) has been considered. The laboratory tests results include both classification tests, for instance grain size distribution related parameters such as C_U and D_{50}, as well as critical state parameters, such as ϕ'_{cv}, Γ and λ_{ln}.

Table 1.4: Characteristics of the sands used by Bolton (1986).

Identification	Name	d_{60}: mm	d_{10}: mm	e_{min}	e_{max}	ϕ'_{crit}	Reference		C_U
A	Brasted river	0·29	0·12	0·47	0·79	32·6	Cornforth (1964, 1973)	A	2.42
B	Limassol marine	0·11	0·003	0·57	1·18	34·4	Cornforth (1973)	B	36.67
C	Mersey river	≈0·2	≈0·1	0·49	0·82	32·0	Rowe (1969) Rowe & Barden (1964)	C	1.00
D	Monterey no. 20	≈0·3	≈0·15	0·57	0·78	36·9	Marachi, Chan, Seed & Duncan (1969)	D	2.00
E	Monterey no. 0	≈0·5	≈0·3	0·57	0·86	37·0	Lade & Duncan (1973)	E	1.67
F	Ham river	0·25	0·16	0·59	0·92	33·0	Bishop & Green (1965)	F	1.56
G	Leighton Buzzard 14/25	0·85	0·65	0·49	0·79	35·0	Stroud (1971)	G	1.31
H	Welland river	0·14	0·10	0·62	0·94	35·0	Barden *et al.* (1969)	H	1.40
I	Chattahoochee river	0·47	0·21	0·61	1·10	32·5	Vesic & Clough (1968)	I	2.24
J	Mol	0·21	0·14	0·56	0·89	32·5	Ladanyi (1960)	J	1.50
K	Berlin	0·25	0·11	0·46	0·75	33·0	De Beer (1965)	K	2.27
L	Guinea marine	0·41	0·16	0·52	0·90	33·0	Cornforth (1973)	L	2.56
M	Portland river	0·36	0·23	0·63	1·10	36·1	Cornforth (1973)	M	1.57
N	Glacial outwash sand	0·9	0·15	0·41	0·84	37·0	Hirschfield & Poulos (1964)	N	6.00
P	Karlsruhe medium sand	0·38	0·20	0·54	0·82	34·0	Hettler (1981)	P	1.73
R	Sacramento river	0·22	0·15	0·61	1·03	33·3	Lee & Seed (1967)	R	1.47
S	Ottawa sand	0·76	0·65	0·49	≈0·8	30·0	Lee & Seed (1967)	S	1.17

Table 1.5: Characteristics of the sands used by Negussey et al. (1988).

TABLE 1. Materials tested and their relevant physical properties

Material	Composition	G_s	e_{max}	e_{min}	D_{50} (mm)	Shape
Ottawa sand ASTM C-109 (medium)	100% quartz	2.67	0.82	0.50	0.4	Rounded
Ottawa sand (fine)	100% quartz	2.67	0.86	0.56	0.2	Rounded
Tailings sand (Brenda Mine)	~65% feldspar ~35% quartz	2.70	1.060	0.688	0.4	Angular
Tailings sand (Lornex Mine)	~63% feldspar ~33% quartz	2.70			0.4	Angular
Granular copper (coarse)		8.92			1.0	Rounded
Granular copper (fine)		8.92			0.6	Cylindrical
Lead shots		11.35			1.4	Spherical
Glass beads		2.50			0.4	Spherical

TABLE 2. Values of ϕ_{cv} for materials tested

Material	ϕ_{cv} (deg)
Ottawa sand (C-109)	29.9
Ottawa sand (fine)	30.2
Lornex Mine tailings	35.1
Brenda Mine tailings	34.7
Granular copper (coarse)	32.9
Granular copper (fine)	32.0
Lead shots	33.0
Glass beads	24.3

Table 1.6: Characteristics of the sands used by Fear & Robertson (1995).

Sand	ϕ'_{ss}	Γ	λ_{ln}	A	B
Ottawa and Alaska sand (Cunning 1994) and Ottawa sand with added kaolinite fines (R. Skirrow, personal communication)					
Ottawa	30.5	0.926	0.032	385.5[a]	261.8
Alaska	36.5	1.485	0.117	319.5[b]	178.7
Ottawa + 5% fines	29.5	0.809	0.029	c	c
Ottawa + 7.5% fines	29.6	0.835	0.052	c	c
Ottawa + 10% fines	29.4	0.930	0.103	c	c
Kaolin[d]	25	1.92	0.181	c	c
Other sands (Sasitharan et al. 1994)					
Erksak	30.9	0.82	0.013	c	c
Toyoura (p'_{ss} < 100 kPa)	30.9	0.938	0.004	c	c
Lornex	35	1.1	0.022	c	c
Brenda	35.9	1.112	0.042	c	c
Syncrude	29.8	0.847	0.017	c	c
Nerlerk	30	0.885	0.014	c	c
Leighton Buzzard	29.8	1	0.035	c	c

[a]Range of 371–397 m/s.
[b]Range of 314–326 m/s.
[c]Use global values of A = 363 m/s (range of 340–380 m/s) and B = 235 m/s.
[d]ϕ'_{ss} cited by Atkinson (1993); λ_{ln} and Γ based on PI = 32%, Gs = 2.70, and formulae in Atkinson (1993).

Table 1.7: Tested materials—properties (from Santamarina and Cho, 2001).

Material	e_{max}	e_{min}	D_{50} (mm)	D_{10} (mm)	C_u
ASTM graded sand	0.820	0.500	0.35	0.23	1.65
Blasting sand	1.025	0.698	0.71	0.42	1.94
Glass beads	0.720	0.542	0.32	0.24	1.37
Granite powder	1.296	0.482	0.089	0.017	6.18
Ottawa 20–30	0.742	0.502	0.72	0.65	1.15
Ottawa F-110 sand	0.848	0.535	0.12	0.081	1.62
Sandboil sand	0.790	0.510	0.36	0.17	2.41
Ticino sand	0.937	0.574	0.58	0.44	1.38

Table 1.8: Simple CS test results—Critical state parameters for several soils (from Santamarina & Cho, 2001).

Material	Friction Angle, ϕ_{cs}	Intercept of CSL at 1 kPa in e-log p'	Slope of CSL in e-log p'
ASTM graded sand	30°	0.869	0.080
Blasting sand	34° (32°)	1.074 (1.099)	0.068 (0.069)
Glass beads	21°	0.807	0.039
Granite powder	34°	1.124	0.070
Ottawa 20–30	28° (27°)	0.806 (0.802)	0.053 (0.047)
Ottawa F-110 sand	31°	0.937	0.077
Sandboil sand	33° (33°)	0.791 (0.785)	0.049 (0.051)
Ticino sand	33° (34°*)	1.006 (0.946*)	0.074 (0.04*)

The critical state angle of shearing resistance of soil, which is shearing at constant volume, is principally a function of mineralogy (Bolton, 1986), and is independent from relative density and mean effective stress. The suggested values of φ'_{cv} of the British Standard 8002:2015 on Earth retaining structures are: 31° for rounded material; 33° for subangular material; 35° for angular material. Based on this literature data, the value of the constant-volume friction angle (ϕ'_{cv}) is assumed equal to 30°.

Fear & Robertson (1995) proposed a framework for estimating the ultimate undrained steady-state shear strength of sand (S_u) from in situ tests, which combines the theory of critical state soil mechanics with shear wave velocity measurements, the latter being available in detail for the Groningen area.

Within the critical state soil mechanics framework, it is possible to calculate S_u for a soil with a given void ratio when loaded in undrained shear, assuming no pore pressure redistribution and therefore no change in void ratio. The concept is that a sand which has an initial state given by (p', q, e) and is loaded in undrained shear will reach the same S_u as the point on its steady state line (SSL) with the same void ratio (p'_{ss}, q_{ss}, e) (Fear & Robertson, 1995). Therefore, S_u can be determined as follows:

$$S_u = \frac{1}{2} M \left[\frac{p'}{\exp\left(\frac{\psi}{\lambda_{\ln}}\right)} \right] \tag{1.2}$$

where

$$M = \frac{q_{ss}}{p'_{ss}} = \frac{6 \sin \phi'_{ss}}{3 - \sin \phi'_{ss}} \tag{1.3}$$

$$p' = \frac{1}{3}(\sigma'_1 + 2\,\sigma'_3) \tag{1.4}$$

$$q = \sigma'_1 - \sigma'_3 \tag{1.5}$$

ϕ'_{ss} or ϕ'_{cv} is the steady state friction angle;

λ_{ln} is the slope of the SSL in e-ln p' space;

$\psi = e - e_{ss}$ is the initial state parameter (Been & Jefferies, 1985);

e is the initial void ratio; and

e_{ss} is the void ratio of the point on the SSL with the same p' as the initial state.

The ultimate steady state line (SSL) in the e-p' plane can be defined by two parameters, Γ and λ_{ln}. Γ is the void ratio on the SSL at p' = 1 kPa, and λ_{ln} is the slope of the SSL when the p' axis is plotted on a natural logarithm scale. The SSL in e-ln p' space is therefore defined as follows:

$$e = \Gamma - \lambda_{\ln} \ln(p') \tag{1.6}$$

Cunning et al. (1995) have demonstrated that soil state can be estimated from shear wave velocity measurements using the following formula:

$$\psi = \left(\frac{A}{B} - \Gamma\right) - \left\{\frac{V_{s1}}{B(K_o)^{na}} - \lambda_{\ln} \ln\left[\frac{\sigma'_v}{3}(1 + 2K_o)\right]\right\} \tag{1.7}$$

where V_{s1} is normalized shear wave velocity, in m/s

$$V_{s1} = V_s \left(\frac{P_a}{\sigma'_v}\right)^{na+nb} \tag{1.8}$$

P_a is 100 kPa and $n_a = n_b = 0.125$, typically; A and B are constants for a given sand, both in m/s; K_o is the ratio of horizontal to vertical effective stresses; and σ'_v is the vertical effective stress.

The state parameter is therefore a function of soil type (A, B, Γ, and λ_{ln}), K_o, σ'_v and V_{s1}. Combining eq. (1.2) with eq. (1.7) results in the following equation relating S_u to V_{s1}:

$$S_u = \frac{M}{2} \exp\left\{\frac{1}{\lambda_{\ln}}\left[\frac{V_{s1}}{B(K_o)^{na}} - \left(\frac{A}{B} - \Gamma\right)\right]\right\} \tag{1.9}$$

where V_{s1} is in m/s and λ_{ln} has units of l/ln(kPa).

Similarly, combining eq. (1.2), properly rearranged as S_u/p', and (1.7) results in the following equation relating S_u/p' to V_{s1}:

$$\frac{S_u}{p'} = \frac{M}{2}\frac{\exp\left[\frac{V_{s1}}{B(K_o)^{na}} - \lambda_{ln}\ln\left(\frac{\sigma'_v}{3}(1+2K_o)\right)\right]}{\exp\left(\frac{A}{B}-\Gamma\right)} \tag{1.10}$$

Replacing p' in the left side of eq. (1.10) by the expression given in eq. (1.4) (substituting σ'_v and $K_o\,\sigma'_v$ for σ'_1, and σ'_3 respectively) results in a similar equation relating S_u/σ'_v to V_{s1}:

$$\frac{S_u}{\sigma'_v} = \frac{M}{6}\left\{\frac{\exp\left[\frac{V_{s1}}{B(K_o)^{na}} - \lambda_{ln}\ln\left(\frac{\sigma'_v}{3}(1+2K_o)\right)\right]}{\exp\left(\frac{A}{B}-\Gamma\right)}\right\}(1+2K_o) \tag{1.11}$$

Examining eq. (1.9), it is clear that for a given material under a particular direction of undrained loading (constant A, B, n_a, M, Γ, and λ_{in}) and for a given K_o, S_u is uniquely a function of V_{s1}. However, eqs. 1.10 and 1.11 show that neither S_u/p' nor S_u/σ'_v are a unique function of V_{s1}, even for a given material and K_o. Rather, S_u/p' and S_u/σ'_v remain a function of σ'_v as well (Fear and Robertson, 1995).

The Fear and Robertson (1995) formulation was used to define the undrained shear strength of the fine sand deposit. To define the required critical state parameters, data available in literature was collected in Table 1.9 defining reasonable ranges of variation (mean and standard deviation). Within the defined ranges of variation, the following values were selected: Γ equal to 0.9 and λ_{ln} equal to 0.05. The A and B parameters have been selected based on Fear & Robertson (1995) suggestion; A equal to 363 m/s, B equal to 235 m/s. Figure 1.21 shows the resulting undrained shear strength versus the depth of the cohesionless layers in the upper part of the deposit.

Table 1.9: Collection of sand parameters from Fear & Robertson (1995), Prearo (2015) and Santamarina & Cho (2001).

	φ'_{ss}	Γ	λ_{ln}	D_{50}	C_u	Source
mean	31.4	0.923	0.0436			
st.dev	2.2	0.096	0.0253			
Ottawa	30.5	0.926	0.032			Fear & Robertson (1995)
Ottawa +5% fines	29.5	0.809	0.029			Fear & Robertson (1995)
Ottawa +7.5% fines	29.6	0.835	0.052			Fear & Robertson (1995)
Ottawa +10% fines	29.4	0.93	0.103			Fear & Robertson (1995)
Erksak	30.9	0.82	0.013			Fear & Robertson (1995)
Toyura (p's<100kPa)	30.9	0.938	0.004			Fear & Robertson (1995)
Lornex	35	1.1	0.022			Fear & Robertson (1995)
Brenda	35.9	1.112	0.042			Fear & Robertson (1995)
Syncrude	29.8	0.847	0.017			Fear & Robertson (1995)
Nerlek	30	0.885	0.014			Fear & Robertson (1995)
Leighton Buzzard	29.8	1	0.035			Fear & Robertson (1995)
Toyura	31	0.934	0.019	0.22-0.18	1.31-1.52	Prearo (2015)
Ticino	34	0.923	0.046	0.53	1.3	Prearo (2015)
ASTM graded sand	30	0.869	0.08	0.35	1.65	Santamarina & Cho (2001)
Blasting sand	34	1.074	0.068	0.71	1.94	Santamarina & Cho (2001)
Ottawa 20–30	28	0.806	0.053	0.72	1.15	Santamarina & Cho (2001)
Ottawa F-110 sand	31	0.937	0.077	0.12	1.62	Santamarina & Cho (2001)
Sandboil sand	33	0.791	0.049	0.36	2.41	Santamarina & Cho (2001)
Ticino sand	34	1.006	0.074	0.58	1.38	Santamarina & Cho (2001)

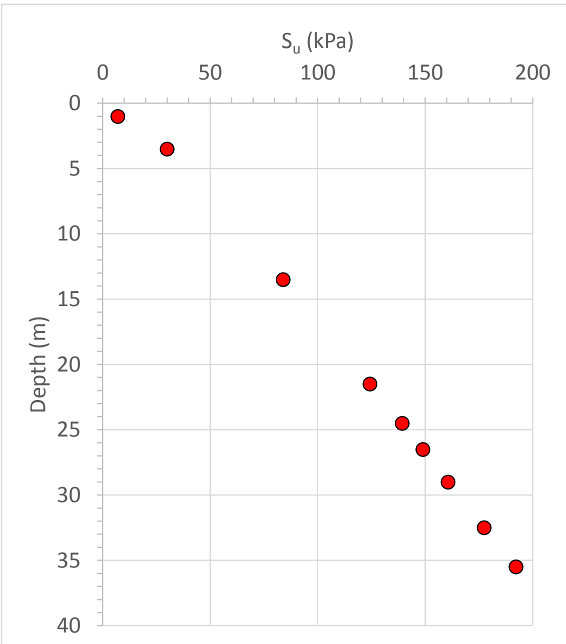

Figure 1.21 Undrained shear strength of sand for Soil profile type A derived using the approach proposed by Fear & Robertson (1995) considering ϕ'_{cv} equal to 30°, Γ equal to, 0.9 and λ_{ln} equal to 0.05, A equal to 363 m/s, B equal to 235 m/s.

1.6.2 Profile type B

Profile type B corresponds to a site (coordinates 242150; 574550) extracted from the reduced database, taking into account sites with AF around the $\mu*\sigma^2$ value and interval amplitude equal to 0.4, and considering the AF obtained with High input motion level.

Table 1.10 shows the stratigraphy and geotechnical parameters within 30 m depth for soil type B; the deposit is constituted by an alternation of cohesive layers (i.e. clayey sand and sandy clay, peat, clay) and cohesionless layers (i.e. fine sand and moderately coarse sand in the bottom part). Figure 1.22a) shows the stratigraphy (blue cohesionless layers; red cohesive layers; yellow peat layer) and undrained shear strength profile for cohesive material, whereas Figure 1.22b) shows the shear wave velocity profile.

Table 1.10: Stratigraphy and geotechnical parameters within 30 m depth for soil type B, corresponding to a site with AF around the median value ($\mu*\sigma^2$).

Depth	Thickness	Lithology	V_S	γ	PI	OCR	C_u	D_{50}	k_0	S_u
m	m	-	m/s	kN/m^3	-	-	-	-	-	kPa
0	1	Clayey sand and sandy clay	110.0	16	50	2.0	nan	nan	0.5	47.9
1	1	Clay	85.0	14.1	50	2.0	nan	nan	0.5	15.6
2	2	Peat	84.6	11.4	nan	4.6	nan	nan	1.1	15.3
4	3		88.2	11.4	nan	4.6	nan	nan	1.1	17.2
7	2	Fine Sand	222.3	19.4	0	1.0	2.34	0.12	1	nan
9	1	Clay	151.8	14.4	50	4.7	nan	nan	1.1	57.2
10	3	Fine Sand	236.1	19.4	0	1.0	2.34	0.12	1	nan
13	1		242.6	19.4	0	1.0	2.34	0.12	1	nan
14	3	Clayey sand and sandy clay	220.5	16.9	50	5.0	nan	nan	1.1	128.0
17	3		258.6	17.2	40	5.1	nan	nan	1.3	149.0
20	2		258.6	17.2	40	5.2	nan	nan	1.3	167.0
22	3	Fine Sand	257.5	19.4	0	1.0	1.76	0.11	1	nan
25	1		257.5	19.4	0	1.0	1.76	0.11	1	nan
26	1	Moderately coarse sand	281.9	20.6	0	1.0	1.86	0.24	1	nan
27	1	Clayey sand and sandy clay	211.0	16.7	15	5.5	nan	nan	1.2	225.1
28	3	Moderately coarse sand	291.8	20.6	0	1.0	1.86	0.24	1	nan

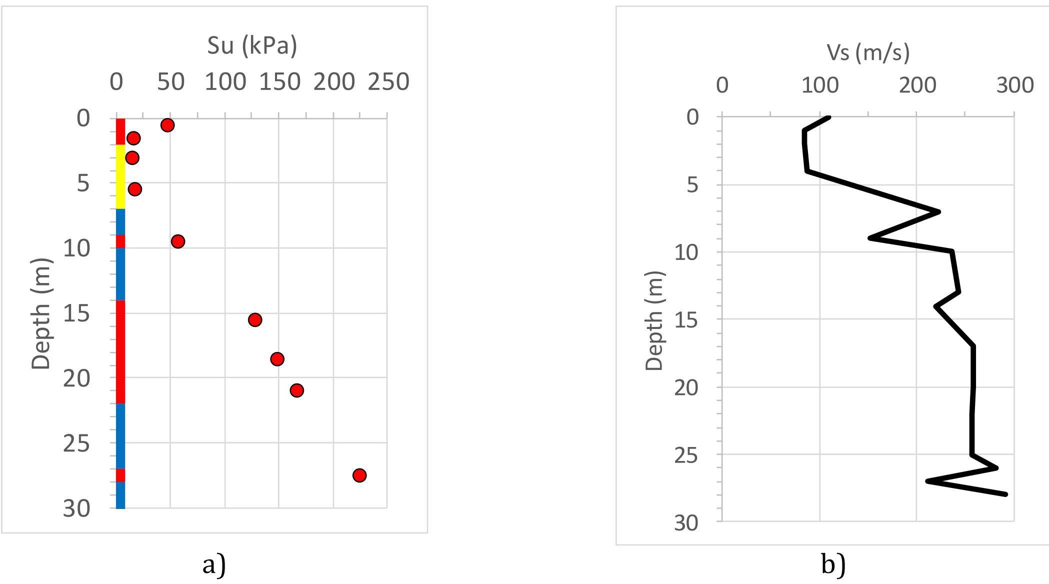

Figure 1.22 Soil profile type B: a) Stratigraphy (blue cohesionless layers; red cohesive layers; yellow peat) and undrained shear strength profile for cohesive material; b) Shear wave velocity profile.

2 Investigated index buildings

Eight different index buildings modelled by Arup (2017; 2019) and featuring either shallow or pile foundations have been considered herein, with the characteristics summarised in Table 2.1 and Table 2.2. These residential buildings are either detached, terraced (with units varying from 2 to 8), aggregate units or apartment blocks and, depending on their age, they are constructed with timber or concrete floors, and solid or cavity URM walls (see Figure 2.1 and Figure 2.2).

Table 2.1: Summary of the URM index buildings with shallow foundations.

Index Building Name	System type	Floor type	Wall type	Number of storeys	Mass (tonnes)	Period (s)
Zijlvest	Terraced	Concrete	Cavity	2 + attic	219	0.34
Kwelder	Detached	Concrete	Cavity	1 + attic	96	0.08
Badweg	Detached	Timber	Cavity	1 + attic	44	0.13
Dijkstraat	Aggregate unit	Timber	Solid	1 + attic	185	0.363
De Haver (barn house)	Detached	Timber	Solid	1 + attic	159	0.125

Table 2.2: Summary of the URM index buildings with pile foundations.

Index Building Name	System type	Floor type	Wall type	Number of storeys	Mass (tonnes)	Period (s)
Drive-in	Apartment block	Concrete	Cavity	Garage + 2	764	0.178
Koeriersterweg (K-Flat)	Apartment block	Concrete	Cavity	3 + 2 attics	1493	0.362
Georg van Saksenlaan	Apartment block	Concrete	Cavity	4	1140	0.199

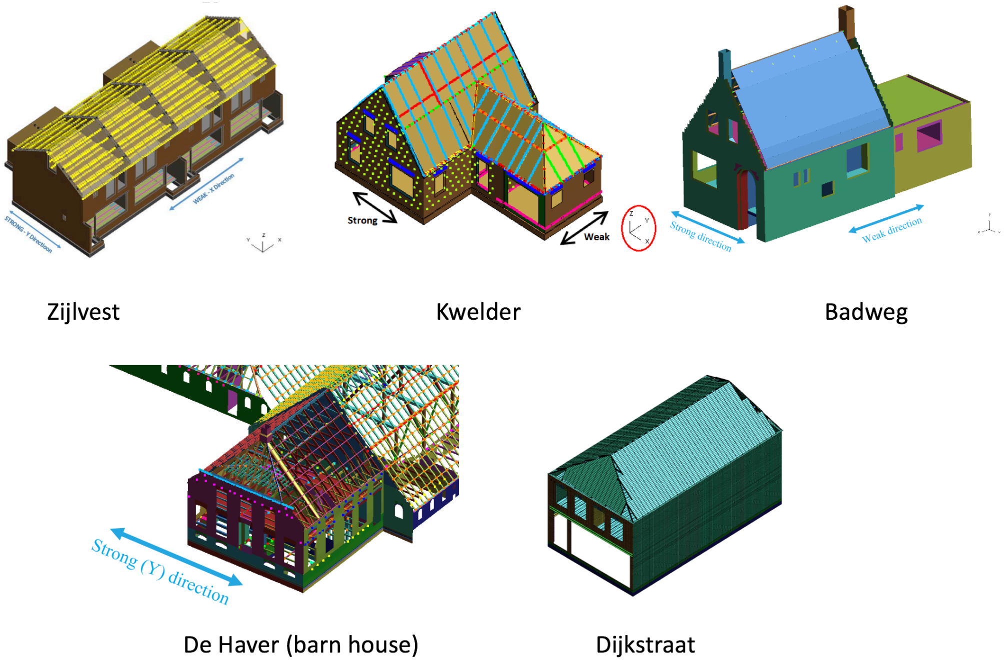

Figure 2.1 Screenshots of LS-DYNA models of buildings assumed to have shallow foundations

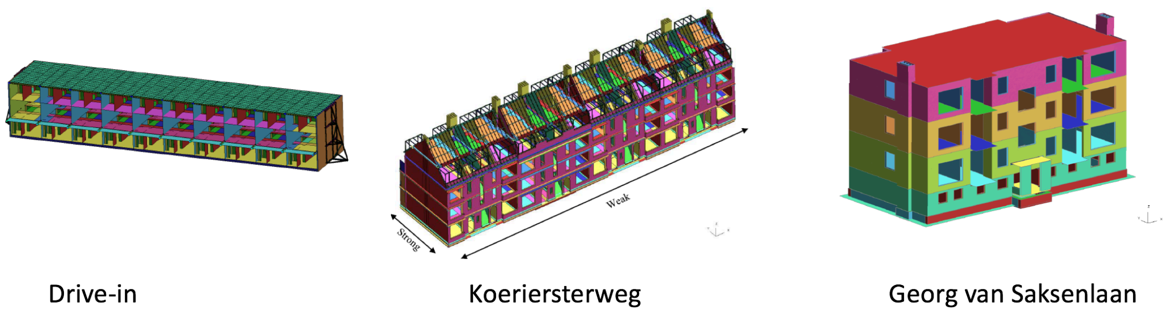

Figure 2.2 Screenshots of LS-DYNA models of buildings assumed to have pile foundations

3 Nonlinear macro-element approach

The concept of macro-elements has been developed by the earthquake engineering community for SSI analysis during the last 20 years. Nowadays it is frequently adopted in research studies for the reliable estimation of soil displacements, despite the complex and highly nonlinear behaviour of the foundation soil and the difficulty in assessing SSI effects (Correia, 2011; 2013).

The macro-element approach belongs to the class of hybrid methods, combining the features of sub-domain decomposition and finite element modelling, including soil nonlinearities. The basic idea of the method is to divide the soil medium in far-field and near-field regions. The far-field is governed by the propagation of seismic waves and modelled with frequency-independent linear springs and dashpots, representing the dynamic impedances. On the other hand, the near-field takes into account all the nonlinearities occurring in the system: geometrical nonlinearities like foundation sliding or uplift for shallow foundations, and material nonlinearities due to soil yielding under the foundation (Pecker et al., 2014). The entire soil-foundation system is condensed into a single nonlinear element at the base of the superstructure, also accounting for energy dissipation through radiation damping (see Figure 3.1).

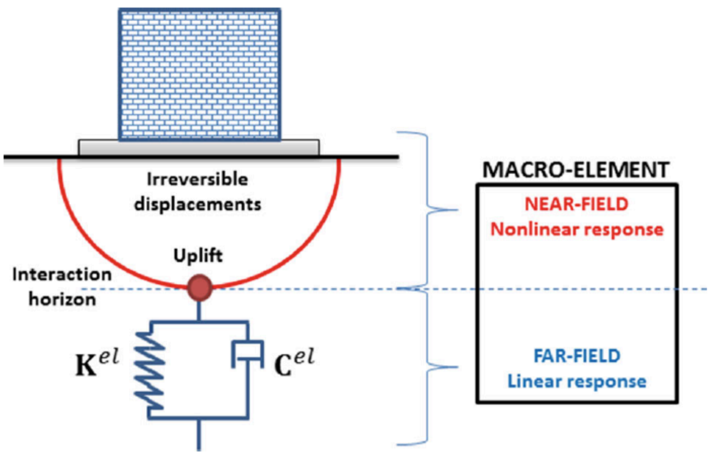

Figure 3.1: Concept of macro-element (Pecker et al., 2014).

3.1 Shallow foundation macro-element

Macro-element models for shallow foundations have previously shown to be a cost-effective and reliable tool for such type of analysis, since they suitably represent both the nonlinear soil behaviour at the near-field and the ground substratum dynamic characteristics at the far-field, as well as the interaction with the seismic response of the structure. Hence, all aspects of elastic and inelastic behaviour of the foundation system are encompassed into one computational entity and are described by the behaviour of a single point at the centre of the foundation. Their application to seismic design is straightforward, leading to a more efficient design and to higher confidence in the predicted structural response.

The macro-element model by Correia & Paolucci (2019) builds upon the innovative concepts and formulations of the models by Chatzigogos et al. (2011) and by Figini et al. (2012). Nevertheless, it incorporates relevant improvements, namely addressing inconsistencies regarding the formulation of the participating mechanisms and extending their scope to three-dimensional loading cases. Moreover, this macro-element introduces an enhanced uplift model, based on a nonlinear elastic-uplift response that also considers the degradation of the contact at the soil/footing interface due to irrecoverable changes in its geometry. An improved bounding surface plasticity model and return mapping algorithms were also adopted in order to reproduce a more general and realistic behaviour, which correctly takes into account the simultaneous elastic-uplift and plastic nonlinear responses. Within the framework of the present endeavour, this model has been implemented in SeismoStruct and herein employed for nonlinear SSI analyses.

Following the parametric study by Pianese (2018), the five calibration parameters of the macro-element became well-constrained, allowing for the dynamic response to be obtained with high confidence. The remaining parameters correspond to: (i) the footing dimensions; (ii) the six initial elastic frequency-independent values of the diagonal impedance matrix, which can be easily obtained from literature, and which represent the far-field response; (iii) the six bearing capacity values, which can be derived from classical formulae, and which represent the near-field failure conditions. In between these two extreme types of response, the macro-element gradually evolves from the initial elastic response to the plastic flow at failure through the bounding surface plasticity model, incorporating the uplift and contact degradation phenomena.

The adopted system for nonlinear dynamic analyses, as modelled in SeismoStruct, composed of a nonlinear structural SDOF and a footing macro-element, is shown in Figure 3.2. The structural SDOF mass, stiffness and damping coefficient are indicated with m_s, k_s and c_s, respectively, in Figure 3.2. In order to capture the inertial interaction between the superstructure and the foundation (with mass m_f), the superstructure mass is placed above the ground at the building centroid height, H_{eff}, and is connected to the interface node by a rigid link. In this way, the rigid displacement of the superstructure mass due to the foundation rotation θ_f, and equal to $H_{eff} \cdot \theta_f$, is taken into account within the nonlinear dynamic analyses, and then subtracted from the total displacement. The seismic acceleration, $a(t)$, is actually input to the system as an inertia force history, $f(t)$, applied to the superstructure mass: this approach properly considers the inertial components in the presence of the structure (structure and foundation masses and their interaction), resulting in a response in terms of relative displacements with respect to the ground motion.

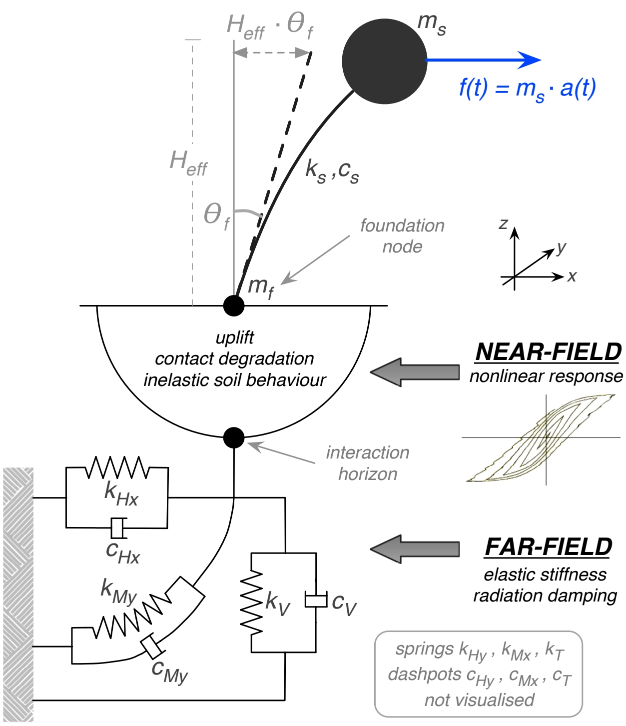

Figure 3.2: Adopted system with structural SDOF and footing macro-element, for dynamic analyses.

The three springs and dashpots represented in the 2D view of Figure 3.2 model the macro-element elastic behaviour in the far-field. Their constants correspond to the stiffness and damping in the vertical direction (k_V, c_V), horizontal x-direction (k_{Hx}, c_{Hx}) and rotational direction around the y-axis (k_{My}, c_{My}). For simplicity, the remaining three springs and dashpots are not visualised in the 2D scheme: however, such elements are present in the macro-element implementation and play an active role in the dynamic analyses, being the macro-element behaviour fully coupled in the six directions.

3.1.1 Assessment of input parameters for shallow foundation macro-element

This paragraph describes the input parameters for shallow foundation macro-elements to be used for the calibration step of MDOF models of the buildings. At this stage, the parameters are derived only for soil type A, being the median AF characterizing soil type A the most representative. The parameters definition is preceded by the description of the foundation typologies.

3.1.1.1 Foundation typologies

The typical foundations of the buildings considered consist of a grid of continuous beams oriented in two orthogonal directions, of either unreinforced masonry or concrete.

Figure 3.3 shows the schemes of foundations considered for bearing capacity calculation by Crux Engineering for both unreinforced masonry and concrete foundations. The typical width is 600mm, whereas the foundation level range between 0.2 and 1m. This type of foundation has been considered for both Detached and Terraced buildings type.

A typical unreinforced masonry foundation (URM) is a strip foundation that is achieved by a widening of the load bearing walls; a representative foundation section is shown in Figure 3.4a). The inertia characteristics of the foundation were evaluated considering, a rectangular section 660mm wide, characterized by the same moment of inertia of the section showed in Figure 3.4a). The resulting height of the equivalent square section is equal to 221mm.

A typical reinforced concrete foundation is a strip foundation with width 600mm and height 330mm; only in some cases, for non-bearing walls of terraced buildings, a square cross section 330mm wide has been considered.

For both unreinforced masonry and concrete, a foundation level at 600mm depth has been considered.

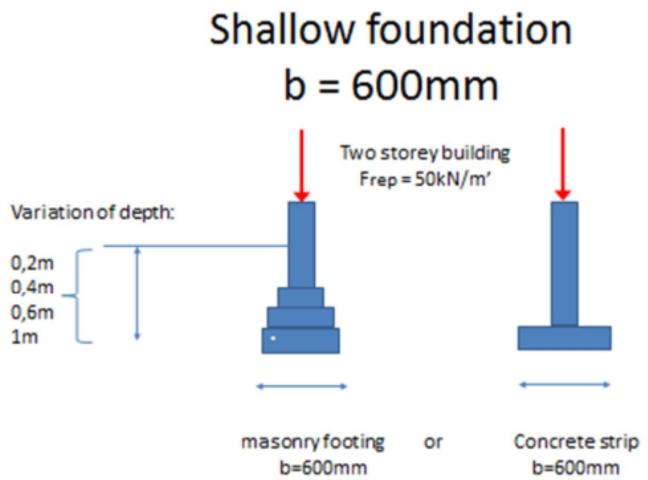

Figure 3.3 Appendix C Crux Engineering BV Reports (229746/032.0/REP102)

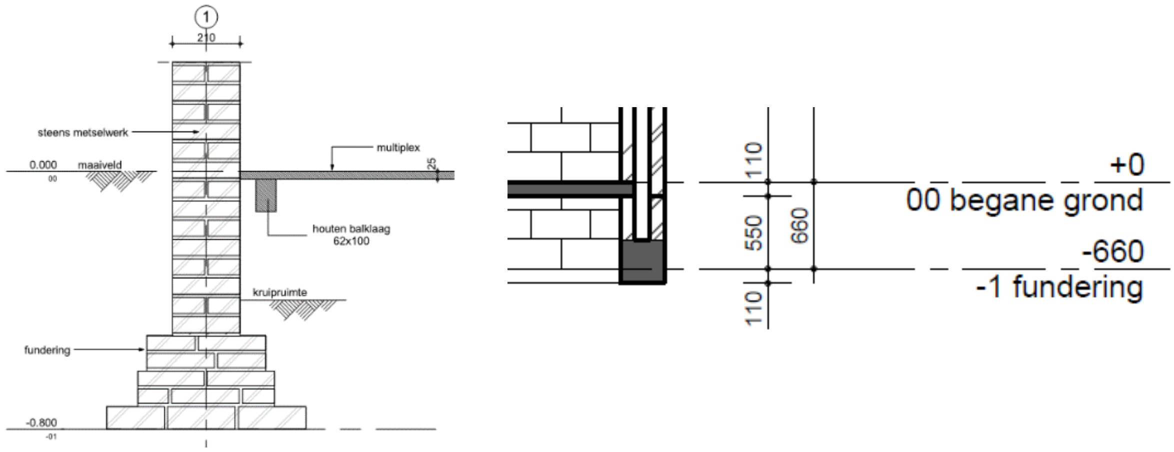

a) b)

Figure 3.4: a) Typical masonry foundation (from Arup 2015b); b) Typical concrete foundation.

3.1.1.2 Macro-element parameters

This paragraph describes the definition of the parameters for macro-elements of shallow foundations to be used for MDOF model. Four cases were considered which are characterized by different foundation layout. Table 3.1 shows the main characteristics of the buildings considered.

Table 3.1: Main characteristics of the buildings considered.

Index Building	Characteristics	Macro-element code
Zijlvest	4 unit 2 storey terraced	ME1
Kwelder	detached 1 storey	ME2
Badweg	detached 1 storey	ME3
Dijkstraat	single unit 2 storey town house	ME4
De Haver	detached 1 storey	ME5

The input parameters of the macro-elements can be subdivided into three main groups described in the following: foundation capacity, foundation stiffness and model specific parameters.

Foundation capacity.

The bearing capacity of shallow foundation under combined loading is represented as a surface in the space of the resultant forces (V, vertical load; H horizontal load; M, bending moment) acting on the foundation (see Figure 3.5).

Butterfield & Gottardi (1994) used to fit to the data for cohesionless dry soil the form shown in Figure 3.5a), in which a symmetrical parabola intersects the V axis, at slope t, at the origin and at V_{max}, where V_{max} is the central vertical load capacity of the footing. Such parabolas have the equations:

$$H/t_h = V\,(V_{max} - V)/V_{max} \tag{3.1}$$

$$M/Bt_{\mathrm{m}} = V\,(V_{\max} - V)/V_{\max} \tag{3.2}$$

When V is much smaller than V_{max}, equation (3.1) reduces to H = V/t_h, and therefore t_h is related to the footing-soil friction. From the simple observation that the eccentricity ratio (e/B = M/BV) of any vertical load cannot exceed 0.5, this is the maximum possible value, at small V, of t_m; the parameter t_m in equation (3.2) is equal to 0.33 according to Meyerhof theory (1953) and to 0.48 according to Vesic's correction (1975). The maximum values of H and M are attained at V/V_{max} equal to 0.5.

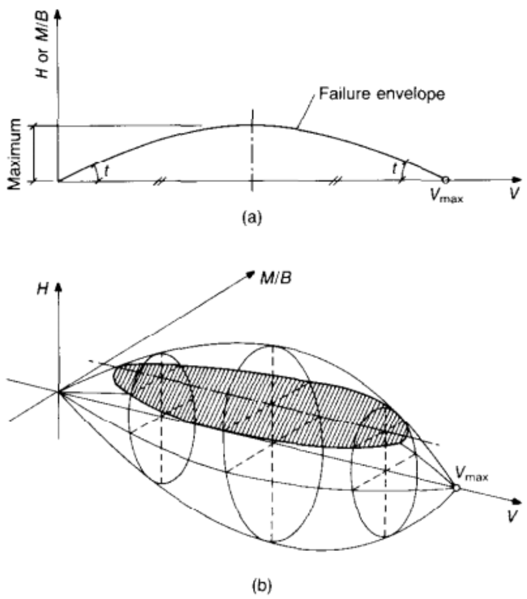

Figure 3.5 Failure envelopes relating (V, H), (V, M/B) and (V, H, M/B) (from Butterfield & Gottardi, 1994)

Due to the high water table level, the bearing capacity was considered under undrained conditions and with a slightly different failure envelope at low values of the vertical load, reflecting the effect of the cohesion (Correia & Paolucci, 2019).

Finally, the strength parameters characterizing the surface of ultimate loads are defined as follows:

- the maximum centred vertical load capacity, V_{max}=q_{lim} B, that corresponds to the ultimate static bearing capacity of the foundation characterized by a width equal to B, and can be evaluated by standard superposition formula (e.g. Brinch-Hansen,1970):

$$q_{\mathrm{lim}} = s_u N_c s_c^o d_c^o i_c^o b_c^o g_c^o + q \tag{3.3}$$

In which for vertical centred load, the only not null correcting factor is related to the foundation shape (B<L are the foundation dimensions):

$$s_c^o = 1 + 0.2\frac{B}{L} \tag{3.4}$$

where S_u is the undrained shear strength, assumed at the depth of interest equal to 12 kPa based on the considerations carried out in section 1.6.

- the maximum base shear capacity, H_{max}, and maximum base moment capacity M_{max}, which can be calibrated based either on material parameters (e.g. soil-foundation friction resistance) or on theoretical values. In the following analyses for undrained conditions:

$$\mathrm{H}_{\max} = s_u \mathrm{A} \tag{3.5}$$

$$\frac{M_{max}}{V_{max} \cdot B} = 0.12 \tag{3.6}$$

where A is the foundation area.

Foundation stiffness.

The foundation elastic impedances can be evaluated by using standard formulas, e.g. Gazetas (1991) proposed closed form solutions for dynamic stiffness and dashpot coefficients for arbitrary shaped foundations on homogenous half-space surface. Impedance formulas are derived for an arbitrarily-shaped foundation mat, with foundation–soil contact surface area (A_b) obtained from a circumscribed rectangle with dimension 2L x 2B (L>B, B and L are semi-width and semi length of the circumscribed rectangle) (see Figure 3.6). The other input parameters for computation of the impedances in the six modes of vibration are:

- moments of inertia about x, y (I_{bx}, I_{by});
- polar moment of inertia about z (J_t) of the actual soil foundation contact surface;
- ω is the cyclic frequency (in rad/s) of interest;
- shear modulus (G);
- Poisson's ratio (ν);
- the shear wave velocity (V_S);
- "Lysmer's analog" wave velocity (V_{La}), i.e. the apparent propagation velocity of compression–extension waves under a foundation and related to V_S according to:

$$V_{\mathrm{La}} = \frac{3.4}{\pi(1-\nu)} V_{\mathrm{s}} \tag{3.7}$$

The static stiffness for the six modes of vibration for rectangular foundations on homogenous half-space proposed by Gazetas (1991) are summarized in the following formula:

Vertical, z
$$K_z = \frac{2GL}{1-\nu}\left[0.73 + 1.54\left(\frac{B}{L}\right)^{0.75}\right] \tag{3.8}$$

Horizontal, y (transverse direction)
$$K_y = \frac{2GL}{2-\nu}\left[2 + 2.5\left(\frac{B}{L}\right)^{0.85}\right] \tag{3.9}$$

Horizontal, x (longitudinal direction)
$$K_x = K_y - \frac{0.2\,GL}{0.75-\nu}\left[1 - \frac{B}{L}\right] \tag{3.10}$$

Rocking rx, (around x axis)
$$K_{rx} = \frac{G}{1-\nu} I_{bx}^{0.75}\left(\frac{L}{B}\right)^{0.25}\left[2.4 + 0.5\frac{B}{L}\right] \tag{3.11}$$

Rocking ry, (around y axis) $$K_{ry} = \frac{G}{1-\nu} I_{by}^{0.75} 3 \left(\frac{L}{B}\right)^{0.15} \quad (3.12)$$

Torsional $$K_t = G\, J_t^{0.75} \left[4 + 11\left(1-\frac{B}{L}\right)^{10}\right] \quad (3.13)$$

where J_t (= I_{bx}+I_{by}) is the polar moment of inertia of the foundation-soil contact surface.

The impedance of a foundation, representing its force-displacement or moment-rotation ratio, is represented in the form expressed by equation 4.2. The radiation damping contribution in equation 4.2, for the six modes of vibration for rectangular foundations on homogenous half-space proposed by Gazetas (1991) are summarized in the following formula:

Vertical, z $$C_z = (\rho V_{La} A_b)\bar{c}_z \quad (3.14)$$
With $\bar{c}_z$ ploted in graph c of Figure 3.6

Horizontal, y (lateral direction) $$C_y = (\rho V_S A_b)\bar{c}_y \quad (3.15)$$
With $\bar{c}_y$ ploted in graph d of Figure 3.6

Horizontal, x (longitudinal direction) $$C_x \cong (\rho V_S A_b) \quad (3.16)$$

Rocking rx, (around x axis) $$C_{rx} = (\rho V_{La} I_{bx})\bar{c}_{rx} \quad (3.17)$$
With $\bar{c}_{rx}$ ploted in graph e of Figure 3.6

Rocking ry, (around y axis) $$C_{ry} = (\rho V_{La} I_{by})\bar{c}_{ry} \quad (3.18)$$
With $\bar{c}_{ry}$ ploted in graph f of Figure 3.6

Torsional $$C_t = (\rho V_S J_t)\bar{c}_t \quad (3.19)$$
With $\bar{c}_t$ ploted in graph g of Figure 3.6

For soil type A, the stiffness and damping coefficients of the foundations have been evaluated considering the relationships described above, taking into account a homogeneous soil profile, since only a shallow depth is involved in the response of the footings, characterized by V_S equal to 190 m/s, γ equal to 18.4 kN/m^3 and ν equal 0.45. The corresponding shear modulus is equal to 67.7 MPa.

The radiation damping coefficient depend on $a_o = 0.5\,\omega B/V_s$ (see Figure 3.6), with the frequency (*f*) for computation of the circular frequency ω (=2 π f) assumed for soil type A equal to 1.67 Hz (i.e. 0.6s). This value was selected taking into account both the period of the structures to be considered and the AF trend shown in Figure 1.19a), the latter has peaks, of almost equal value, between 0.4 and 1.67 Hz. Assuming B equal to 0.6 m, the resulting a_o is equal to 0.017.

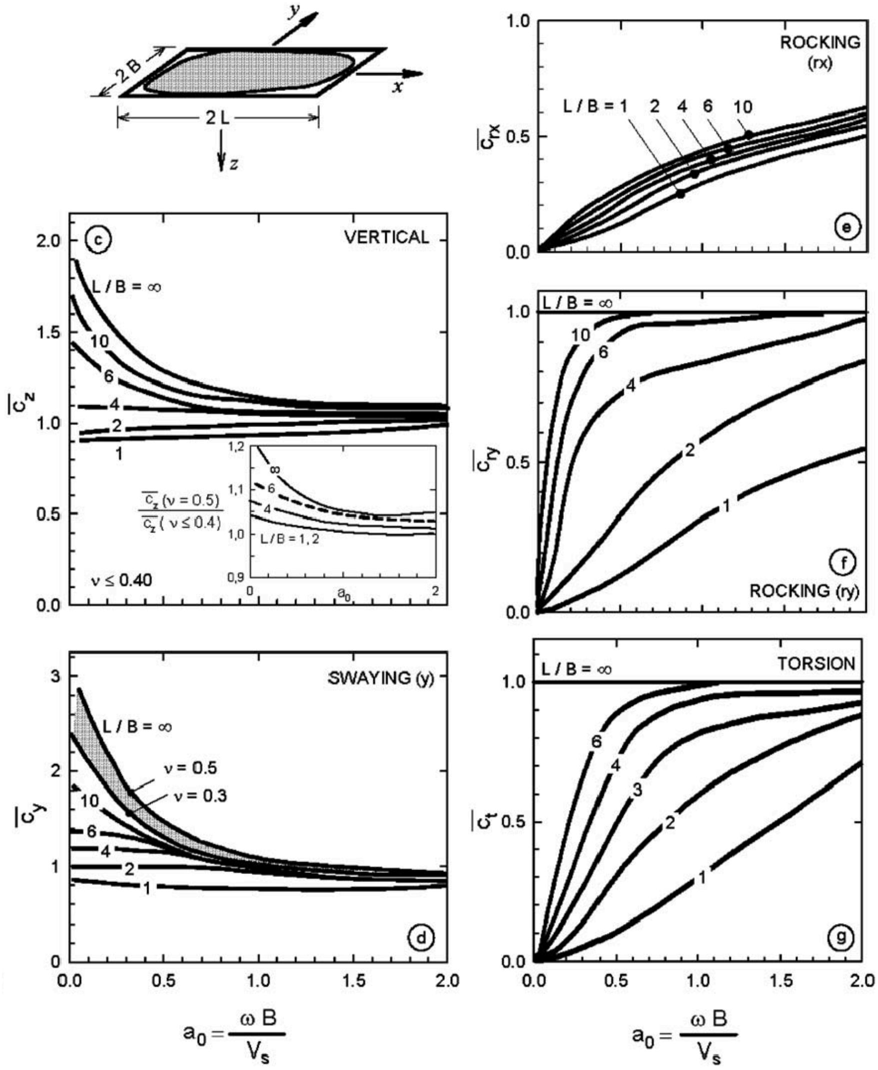

Figure 3.6 Dynamic dashpot coefficients on homogenous half-space (from Mylonakis et al., 2006).

Model specific parameters.

The macro-element model specific parameters are the following:

- the uplift initiation parameter (α) is only dependent on the assumed stress distribution of vertical stresses underneath the foundation and its value can be determined from simple static considerations. In the following analysis, it is set equal to 3, by assuming a linear distribution of vertical stresses underneath the foundation for the soil at the beginning of the analysis;
- the soil/footing contact degradation (d_{mg}) that takes into account the decrease of the contact area due to inelastic rocking, is evaluated based on calibration to experimental results. In the following analyses it is set equal to 0.1;
- reference plastic modulus (h_0), set equal to 0.2;
- the exponent for loading history in unloading/reloading (n_{UR}), set equal to 1;
- plastic potential parameter (χ_g), set equal to 2;
- bounding surface type (rugby ball; scallop shape; ellipsoid), in the following analysis the "scallop" shape was considered, which is suitable for modelling the undrained response.

The definition of the macro-element model parameters takes advantage of the calibration work carried out by Pianese (2018).

3.1.1.3 Terraced house "Zijlvest"

Figure 3.7 shows the position of the 27 foundation beams of the Zijlvest index building, where each beam is modelled by a macro-element. Zijlvest building is a 4 units terraced house, with the foundations of the main walls constituted by 60 cm continuous concrete footings, while the ones of the secondary partition walls (i.e. beams n° 20, 22, 24 and 26 in Figure 3.7) are 33 cm wide.

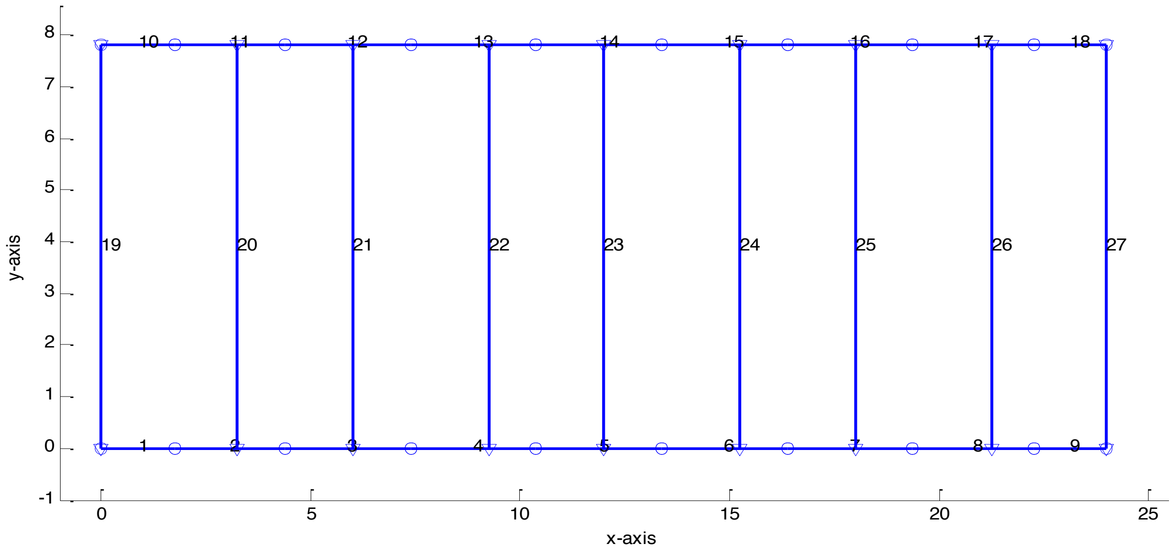

Figure 3.7 Terraced house " Zijlvest" – position of beams representing single macro-elements.

For each of the macro-elements considered, Table 3.2 summarizes their initial stiffness, Table 3.3 summarizes the foundation capacities and Table 3.4 summarizes the radiation damping equivalent dashpot coefficients.

Table 3.2: Initial stiffness of the macro-elements of Zijlvest index building.

Beam	Vertical K_z MN/m	Horizontal along X K_x MN/m	Rotational around Y K_{ry} MNm/rad
1	305.883	203.847	161.489
2	400.364	265.360	427.329
3	439.644	291.310	588.766
4	439.644	291.310	588.766
5	439.644	291.310	588.766
6	439.644	291.310	588.766
7	439.644	291.310	588.766
8	426.612	282.681	531.597
9	305.883	203.847	161.489
10	305.883	203.847	161.489
11	400.364	265.360	427.329
12	439.644	291.310	588.766
13	439.644	291.310	588.766
14	439.644	291.310	588.766
15	439.644	291.310	588.766
16	439.644	291.310	588.766
17	426.612	282.681	531.597
18	305.883	203.847	161.489
19	916.845	777.626	130.723
20	838.809	739.277	39.263
21	916.845	777.626	130.723
22	838.809	739.277	39.263
23	916.845	777.626	130.723
24	838.809	739.277	39.263
25	916.845	777.626	130.723
26	838.809	739.277	39.263
27	916.845	777.626	130.723

Table 3.3: Foundation capacity of the macro-elements of Zijlvest index building.

Beam	Centred vertical bearing strength QQ_N_MAX MN	Maximum base shear capacity along X QQ_HX_MAX MN	Maximum base moment capacity around Y QQ_MY_MAX MNm
1	0.081	0.013	0.017
2	0.119	0.019	0.037
3	0.135	0.022	0.049
4	0.135	0.022	0.049
5	0.135	0.022	0.049
6	0.135	0.022	0.049
7	0.135	0.022	0.049
8	0.130	0.021	0.045
9	0.081	0.013	0.017
10	0.081	0.013	0.017
11	0.119	0.019	0.037
12	0.135	0.022	0.049
13	0.135	0.022	0.049
14	0.135	0.022	0.049
15	0.135	0.022	0.049
16	0.135	0.022	0.049
17	0.130	0.021	0.045
18	0.081	0.013	0.017
19	0.345	0.056	0.025
20	0.189	0.031	0.007
21	0.345	0.056	0.025
22	0.189	0.031	0.007
23	0.345	0.056	0.025
24	0.189	0.031	0.007
25	0.345	0.056	0.025
26	0.189	0.031	0.007
27	0.345	0.056	0.025

Table 3.4: Radiation damping dashpot coefficients of the macro-elements of Zijlvest index building.

C_x ton/s	C_{ry} ton*m2/s
374.2	9.4
561.3	31.7
641.5	47.3
641.5	47.3
641.5	47.3
641.5	47.3
641.5	47.3
614.7	41.7
374.2	9.4
374.2	9.4
561.3	31.7
641.5	47.3
641.5	47.3
641.5	47.3
641.5	47.3
641.5	47.3
614.7	41.7
374.2	9.4
3669.2	13.8
2018.1	2.3
3335.6	13.8
2018.1	2.3
3335.6	13.8
2018.1	2.3
3335.6	13.8
2018.1	2.3
3669.2	13.8

3.1.1.4 Detached house "Kwelder"

Figure 3.8 shows the position of the 16 foundation beams of the Kwelder index building, where each beam is modelled by a macro-element. The foundations of the main walls are constituted by 60 cm continuous concrete footings.

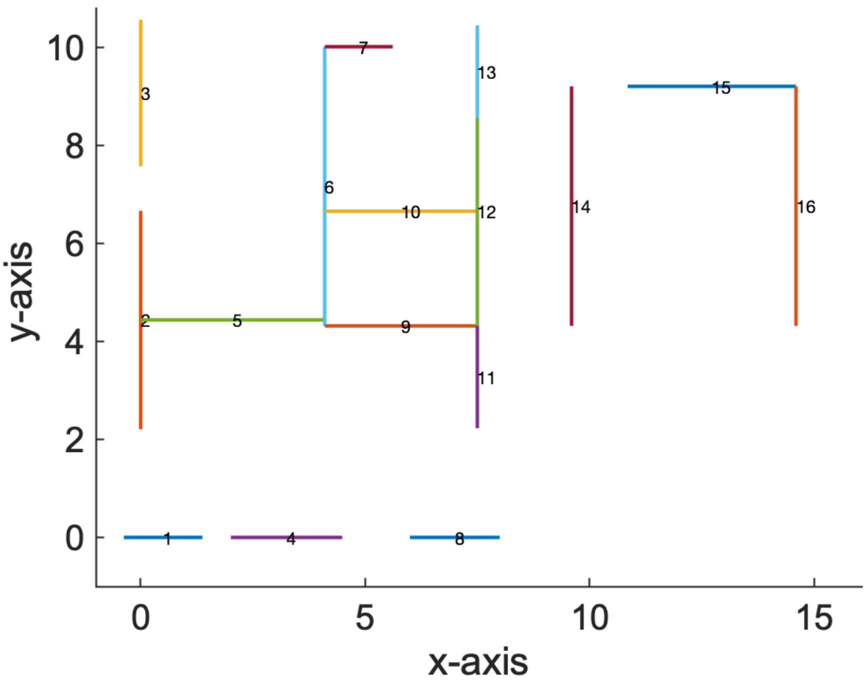

Figure 3.8 Detached house "Kwelder" – position of beams representing single macro-elements.

For each of the macro-elements considered, Table 3.5 summarizes their initial stiffness, Table 3.6 summarizes the foundation capacities and Table 3.7 summarizes the radiation damping equivalent dashpot coefficients.

Table 3.5: Initial stiffness of the macro-elements of Kwelder index building.

Beam	Vertical K_z MN/m	Horizontal along X K_x MN/m	Rotational around Y K_{ry} MNm/rad
1	305.883	203.847	161.489
2	588.559	478.119	75.630
3	438.604	344.555	51.382
4	385.015	255.272	372.852
5	552.300	366.578	1246.044
6	711.859	589.757	96.084
7	279.504	186.975	114.246
8	333.393	221.600	222.497
9	480.993	318.806	795.063
10	480.993	318.806	795.063
11	343.180	261.575	36.537
12	610.601	497.979	79.259
13	321.900	243.389	33.320
14	631.568	516.913	82.723
15	516.794	342.740	1005.836
16	631.568	516.913	82.723

Table 3.6: Foundation capacity of the macro-elements of Kwelder index building.

	Centred vertical bearing strength	Maximum base shear capacity along X	Maximum base moment capacity around Y
	QQ_N_MAX	QQ_HX_MAX	QQ_MY_MAX
Beam	MN	MN	MNm
1	0.081	0.013	0.017
2	0.199	0.032	0.014
3	0.135	0.022	0.010
4	0.113	0.018	0.034
5	0.183	0.030	0.090
6	0.253	0.041	0.018
7	0.071	0.011	0.013
8	0.092	0.014	0.022
9	0.153	0.024	0.062
10	0.153	0.024	0.062
11	0.096	0.015	0.007
12	0.209	0.034	0.015
13	0.087	0.014	0.006
14	0.218	0.035	0.016
15	0.168	0.027	0.076
16	0.218	0.035	0.016

Table 3.7: Radiation damping dashpot coefficients of the macro-elements of Kwelder index building.

C_x	C_{ry}
ton/s	ton*m2/s
374.2	9.4
1525.8	5.6
831.1	1.9
530.3	26.7
876.7	120.8
2193.8	7.2
323.9	6.1
427.6	14.0
727.0	68.9
727.0	68.9
491.6	1.3
1601.1	5.9
445.7	1.2
1672.9	6.2
801.8	92.4
1672.9	6.2

3.1.1.5 Detached house "Badweg"

Figure 3.9 shows the position of the 13 foundation beams of the Badweg index building, each beam being modelled by a macro-element. The foundations of the main walls are constituted by 60 cm continuous unreinforced masonry footings.

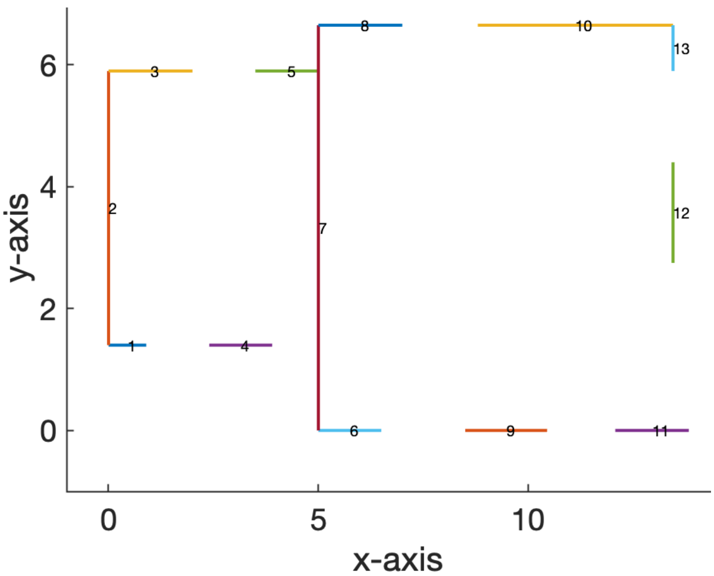

Figure 3.9 Detached house "Badweg" – position of beams representing single macro-elements.

For each of the macro-elements considered, Table 3.8 summarizes their initial stiffness, Table 3.9 summarizes the foundation capacities and Table 3.10 summarizes the radiation damping equivalent dashpot coefficients.

Table 3.8: Initial stiffness of the macro-elements of Badweg index building.

Beam	Vertical K_z MN/m	Horizontal along X K_x MN/m	Rotational around Y K_{ry} MNm/rad
1	206.740	141.474	32.737
2	592.573	481.732	76.290
3	333.393	221.600	222.497
4	277.800	185.891	111.550
5	277.800	185.891	111.550
6	277.800	185.891	111.550
7	805.067	674.893	111.754
8	333.393	221.600	222.497
9	327.930	218.063	209.380
10	607.600	403.877	1685.540
11	305.883	203.847	161.489
12	294.727	220.387	29.279
13	187.653	133.262	14.433

Table 3.9: Foundation capacity of the macro-elements of Badweg index building.

Beam	Centred vertical bearing strength QQ_N_MAX MN	Maximum base shear capacity along X QQ_HX_MAX MN	Maximum base moment capacity around Y QQ_MY_MAX MNm
1	0.044	0.006	0.005
2	0.201	0.032	0.014
3	0.092	0.014	0.022
4	0.070	0.011	0.013
5	0.070	0.011	0.013
6	0.070	0.011	0.013
7	0.295	0.048	0.021
8	0.092	0.014	0.022
9	0.090	0.014	0.021
10	0.207	0.033	0.116
11	0.081	0.013	0.017
12	0.076	0.012	0.006
13	0.037	0.005	0.003

Table 3.10: Radiation damping dashpot coefficients of the macro-elements of Badweg index building.

C_x ton/s	C_{ry} ton*m^2/s
192.4	0.5
1539.5	5.7
427.6	14.0
320.7	5.9
320.7	5.9
320.7	5.9
2559.5	8.4
427.6	14.0
417.0	13.0
994.3	352.5
374.2	9.4
370.4	1.0
152.3	0.2

3.1.1.6 Detached house “Dijkstraat”

Figure 3.10 shows the position of the 8 foundation beams of the Dijkstraat index building, with each beam modelled by a macro-element. The foundations of the main walls are constituted by 60 cm continuous concrete footings.

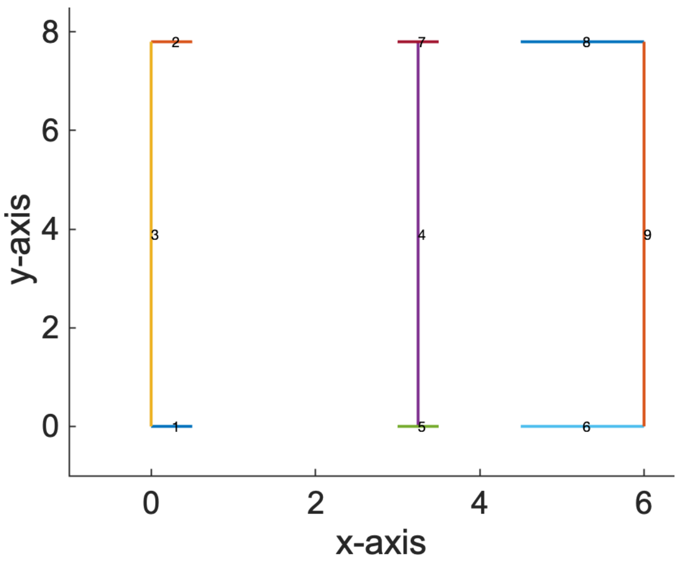

Figure 3.10 Detached house “Dijkstraat” – position of beams representing single macro-elements.

For each of the macro-elements considered, Table 3.11 summarizes their initial stiffness, Table 3.12 summarizes the foundation capacities and Table 3.13 summarizes the radiation damping equivalent dashpot coefficients.

Table 3.11: Initial stiffness of the macro-elements of Dijkstraat index building.

Beam	Vertical K_z MN/m	Horizontal along X K_x MN/m	Rotational around Y K_{ry} MNm/rad
1	248.964	167.666	72.017
2	333.393	221.600	222.497
3	814.829	545.054	4122.694
4	248.964	167.666	72.017
5	333.393	221.600	222.497
6	814.829	545.054	4122.694
7	1789.963	1593.224	282.478
8	1789.963	1593.224	282.478

Table 3.12: Foundation capacity of the macro-elements of Dijkstraat index building.

	Centred vertical bearing strength QQ_N_MAX	Maximum base shear capacity along X QQ_HX_MAX	Maximum base moment capacity around Y QQ_MY_MAX
Beam	MN	MN	MNm
1	0.059	0.009	0.009
2	0.092	0.014	0.022
3	0.299	0.049	0.242
4	0.059	0.009	0.009
5	0.092	0.014	0.022
6	0.299	0.049	0.242
7	0.746	0.122	0.054
8	0.746	0.122	0.054

Table 3.13: Radiation damping dashpot coefficients of the macro-elements of Dijkstraat index building.

C_x	C_{ry}
ton/s	ton*m^2/s
267.3	3.4
427.6	14.0
1443.3	1078.3
267.3	3.4
427.6	14.0
1443.3	1078.3
7997.0	30.0
7997.0	30.0

3.1.1.7 Detached house "De Haver"

Figure 3.11 shows the position of the 28 foundation beams of the De Haver index building, where each beam is modelled by a macro-element. The foundations of the main wall are constituted by 60 cm continuous unreinforced masonry footings.

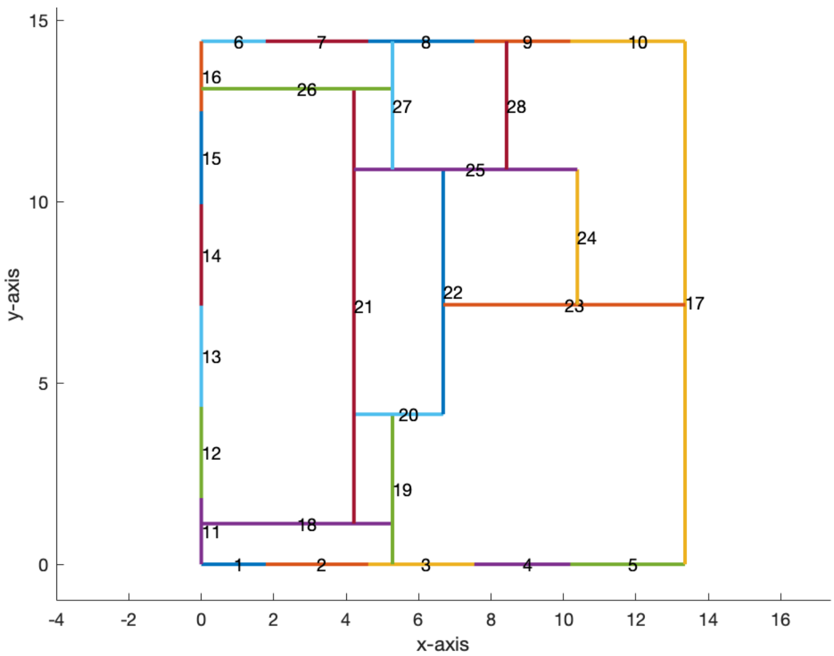

Figure 3.11 Detached house "De Haver" – position of beams representing single macro-elements.

For each of the macro-elements considered, Table 3.14 summarizes their initial stiffness, Table 3.15 summarizes the foundation capacities and Table 3.16 summarizes the radiation damping equivalent dashpot coefficients.

Table 3.14: Initial stiffness of the macro-elements of De Haver index building.

Beam	Vertical K_z MN/m	Horizontal along X K_x MN/m	Rotational around Y K_{ry} MNm/rad
1	308.990	205.844	167.760
2	421.749	279.465	511.195
3	432.353	286.480	556.332
4	403.001	267.096	437.162
5	457.021	302.844	670.767
6	308.990	205.844	167.760
7	421.749	279.465	511.195
8	432.353	286.480	556.332
9	403.001	267.096	437.162
10	457.021	302.844	670.767
11	314.466	237.070	32.207
12	388.543	300.764	43.518
13	417.533	326.062	48.054
14	418.345	326.773	48.182
15	393.496	305.073	44.289
16	325.850	246.754	33.914
17	1547.178	1364.856	239.855
18	670.334	446.408	2286.512
19	555.836	448.730	70.269
20	383.421	254.227	367.462
21	1317.376	1149.612	199.755
22	814.536	683.570	113.354
23	808.387	540.639	4026.609
24	514.553	411.827	63.555
25	757.693	505.947	3317.879
26	670.334	446.408	2286.512
27	494.737	394.192	60.355
28	494.737	394.192	60.355

Table 3.15: Foundation capacity of the macro-elements of De Haver index building.

	Centred vertical bearing strength	Maximum base shear capacity along X	Maximum base moment capacity around Y
	QQ_N_MAX	QQ_HX_MAX	QQ_MY_MAX
Beam	MN	MN	MNm
1	0.082	0.013	0.017
2	0.128	0.020	0.043
3	0.132	0.021	0.047
4	0.120	0.019	0.038
5	0.143	0.023	0.054
6	0.082	0.013	0.017
7	0.128	0.020	0.043
8	0.132	0.021	0.047
9	0.120	0.019	0.038
10	0.143	0.023	0.054
11	0.084	0.013	0.006
12	0.114	0.018	0.008
13	0.126	0.020	0.009
14	0.126	0.020	0.009
15	0.116	0.018	0.008
16	0.089	0.014	0.006
17	0.633	0.104	0.046
18	0.235	0.038	0.149
19	0.185	0.030	0.013
20	0.112	0.018	0.033
21	0.527	0.086	0.038
22	0.299	0.049	0.022
23	0.296	0.048	0.237
24	0.167	0.027	0.012
25	0.273	0.044	0.202
26	0.235	0.038	0.149
27	0.159	0.025	0.011
28	0.159	0.025	0.011

Table 3.16: Radiation damping dashpot coefficients of the macro-elements of De Haver index building.

C_x	C_{ry}
ton/s	ton*m2/s
380.2	9.9
604.8	39.7
626.5	44.1
566.6	32.6
677.3	55.7
380.2	9.9
604.8	39.7
626.5	44.1
566.6	32.6
677.3	55.7
429.8	1.2
644.9	1.6
775.0	1.8
777.2	1.8
656.9	1.6
454.2	1.2
6781.4	18.2
1129.0	516.1
1326.2	2.6
527.1	26.3
5637.9	15.1
2596.8	8.5
1429.2	1047.0
1116.0	2.4
1318.4	822.0
1129.0	516.1
1057.9	2.2
1057.9	2.2

3.1.2 Calibration of the equivalent footing macro-element

The employed footing macro-element models the soil under a single footing or foundation beam. However, given that in the development of fragility functions a simplified SDOF system approach is used to represent the structural systems (Crowley et al., 2019), the derivation of an "equivalent" macro-element for an entire building was needed.

3.1.2.1 Terraced index building

In order to derive an equivalent macro-element, the first step was to build a multiple-degrees-of freedom (MDOF) model for the considered index building (Figure 3.12), Zijlvest, a two-storey unreinforced masonry (URM) terraced index building with four units. Masonry piers and spandrels are introduced as columns and beams, respectively, to model the transverse walls (*y*-direction) and approximately model the sequence of openings in the two façades along the *x*-

direction. Such façades are not identical, but were modelled with the same geometry for simplicity, in the assumption that small changes in the geometry do not affect the characterisation of the equivalent macro-element. The rigid reinforced concrete slabs are modelled with two rigid diaphragms linking the column nodes at the two floor levels.

A total of 27 footing macro-elements are introduced at the base of the model (where grey blocks are located in Figure 3.12), in correspondence to the centroid of masonry piers. Reinforced concrete foundation beams connect the upper nodes of the macro-elements. Both masonry and reinforced concrete were considered as linear elastic materials, in the MDOF models, with the actual values for the elastic modulus and density. The total mass of the models, given by the superstructure mass plus the foundation mass, naturally equates to the actual total mass values used for the equivalent single macro-element properties.

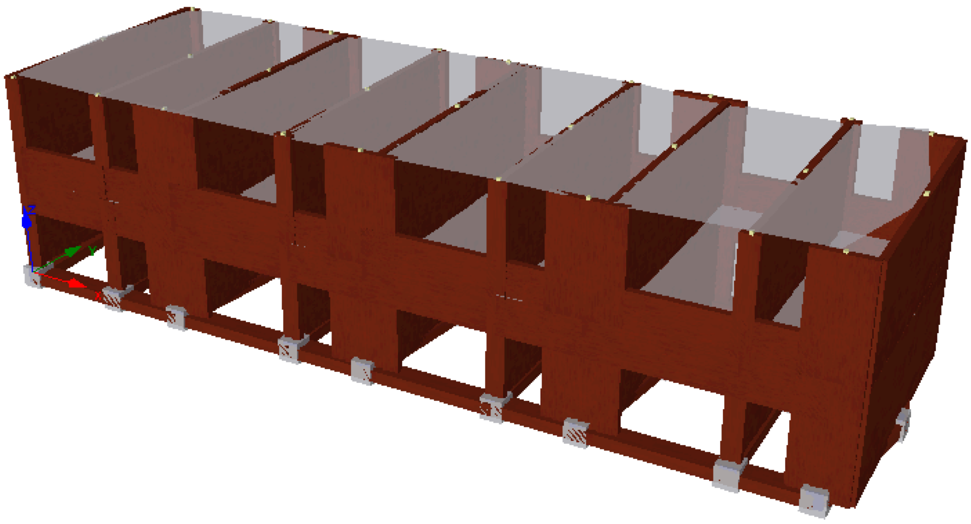

Figure 3.12: The MDOF model used for the terraced index buildings.

The equivalent macro-element calibration requires the computation of the (elastic) stiffnesses, bearing capacity and damping coefficients along the six directions. Most of the parameters were computed analytically starting from the foundation geometry and properties of the single macro-elements, while the remaining ones required the output from the model. The model output parameters needed for the calibration are the vertical reactions of the macro-elements and the base shear capacities in the two horizontal directions x and y: both output results were obtained from two pushover analyses, along x and y. The latter were carried out pushing the structure in load control with point forces located at the floor levels, according to a triangular distribution.

The vertical stiffness, k_V, as well as the horizontal stiffness in the two directions, k_{Hx} and k_{Hy}, were obtained by simply summing up the stiffness values of the single macro-elements, assuming a rigid behaviour of the foundation plane. The torsional stiffness, k_T, does not play a role in the fragility curve derivation since the models represent the response in a single vertical plane. For the rotational stiffness in the two directions, k_{Mx} and k_{My}, the lower bound would be simply the sum over the single macro-elements, as done for the other stiffness components, while adopting the upper bound would mean accounting for both the rotational stiffness of each macro-element and their vertical stiffness contribution for a rigid rotation of the foundation plane. For the case at hand, it was decided to employ the rotational stiffness upper bound, although sensitivity studies demonstrated the small influence of this stiffness in the overall response of these buildings, as discussed below. The rotational stiffness around the generic horizontal direction, k_M, was thus retrieved for a unit rotation as follows:

$$k_M = \sum_{i=1}^{nME} k_{V,i} \cdot d_i^2 + \sum_{i=1}^{nME} k_{M,i} \tag{3.20}$$

where the index i spans all the nME single macro-elements in the model (i.e., 27 in the terraced building model), while d_i is the distance of the i-th macro-element from the foundation centroid.

Since the dynamic behaviour of these buildings on shallow foundations is driven more by sliding than by rocking, this choice should not lead to important variations in the results. To verify this, the fragility curves were also retrieved by using a reduced rotational stiffness, in between the two extreme values. In particular, based on expert judgement, rather than rigorous mechanical considerations, one tenth of the upper bound was adopted, a value that is of course larger than the lower bound. For all the considered buildings, this reduced stiffness led to small to negligible variations in the fragility curve with respect to the one obtained with the upper bound, as expected.

Concerning the bearing capacity, the vertical component, N_{max}, was computed as the sum over the single macro-elements, while for the other components the fully coupled behaviour of the macro-element in the six directions was used for defining the size of its bounding surface. In particular, the bearing capacity in the horizontal direction, H_{max}, was obtained as follows:

$$H_{max} = \frac{\sum_{i=1}^{nME} Q_{NH,i} \cdot H_{max,i}}{Q_{NH}} \tag{3.21}$$

where $H_{max,i}$ is the maximum horizontal capacity of each macro-element in the direction considered, and Q_{NH} and $Q_{NH,i}$ are function of the applied vertical load, for the equivalent macro-element and for each of the single macro-elements, respectively. This function of the applied vertical load relates the maximum horizontal capacity of the macro-element with its actual horizontal shear capacity. In undrained conditions with zero base suction, such function assumes a "scallop shape" and depends on the value of Q_N, which is the ratio between the total vertical reaction of the building and its vertical bearing capacity.

$$Q_{NH} = \begin{cases} [4Q_N(1-Q_N)]^{0.95}, Q_N > 0.5 \\ [1-(1-2Q_N)^{10}], Q_N \leq 0.5 \end{cases} \tag{3.22}$$

Further details on the involved quantities can be found in Correia & Paolucci (2019).

In order to obtain the rotational bearing capacity, M_{max}, the 3D vertical-horizontal-rotational interaction surface for the capacity was used to derive the following expression:

$$M_{max} = \frac{\sum_{k=1}^{N_S} F_{u,k} \cdot h_k}{Q_{NM} \sqrt{1 - \left(\frac{H_u}{Q_{NH} \cdot H_{max}}\right)^2}} \tag{3.23}$$

where $F_{u,k}$ is the ultimate horizontal force at the k-th floor level, obtained from a pushover analysis in the relevant horizontal direction and considering a triangular distribution along the building height, N_s is the number of storeys, h_k is the height of the k-th floor level, and H_u is the sum of $F_{u,k}$ for all storeys and corresponds to the ultimate base shear value. Q_{NH} was already defined, while Q_{NM} is also a function of the applied vertical load that relates the maximum rotational moment capacity of the macro-element with its actual moment capacity. The torsional capacity is of no interest for the 2D analyses performed.

The equivalent dashpot coefficients modelling the radiation damping in the soil along the six directions were computed by summing up the values of the single macro-elements. In what concerns the rocking response this corresponds to a lower bound assumption. Nonetheless, as mentioned above, the response of the buildings considered is mainly dominated by sliding and not by rocking.

Finally, the "model specific parameters" (see final sub-section of Section 3.1.1.2) for the equivalent footing macro-element in SeismoStruct were set equal to those of the single footing macro-elements. The latter assumed values consistent with the calibration procedure done in the work by Pianese (2018). The scallop shape was assumed for the bounding surface, since the dynamic analysis is performed under undrained conditions.

3.1.2.2 Detached index buildings

Three MDOF models (see Figure 3.13, Figure 3.14, Figure 3.15, and Figure 3.16) were created to derive the equivalent footing macro-element for the four considered detached index buildings; Kwelder, Badweg, Dijkstraat and De Haver. The same modelling strategy adopted for the terraced building was used here. The total number of footing macro-elements included in the models is 16 for Kwelder (one-storey), 13 for Badweg (one-storey), 8 for Dijkstraat (two-storey), and 28 for De Haver (one-storey).

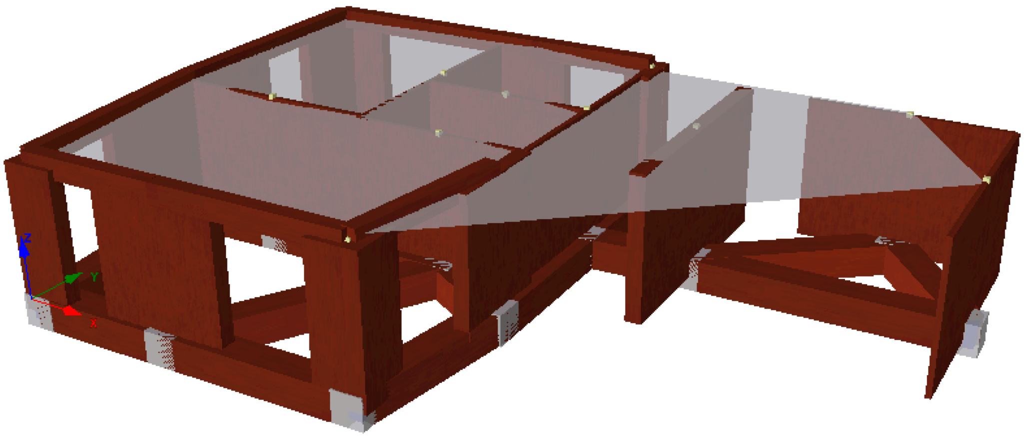

Figure 3.13: The MDOF model used for Kwelder detached index building.

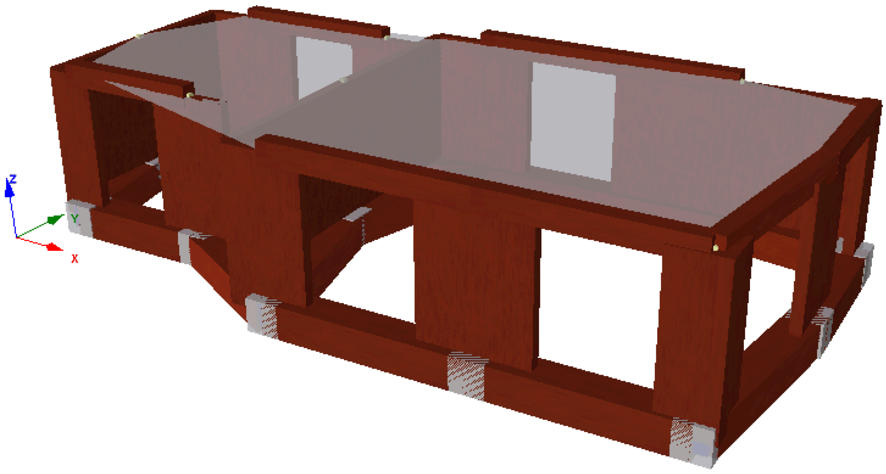

Figure 3.14: The MDOF model used for Badweg detached index building.

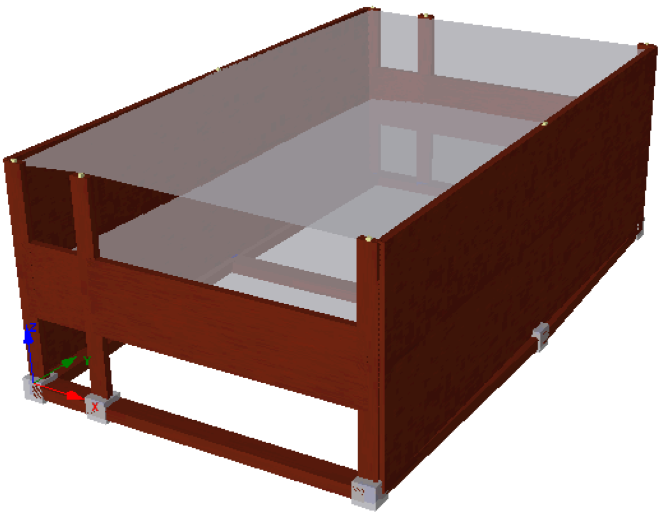

Figure 3.15: The MDOF model used for Dijkstraat detached index building.

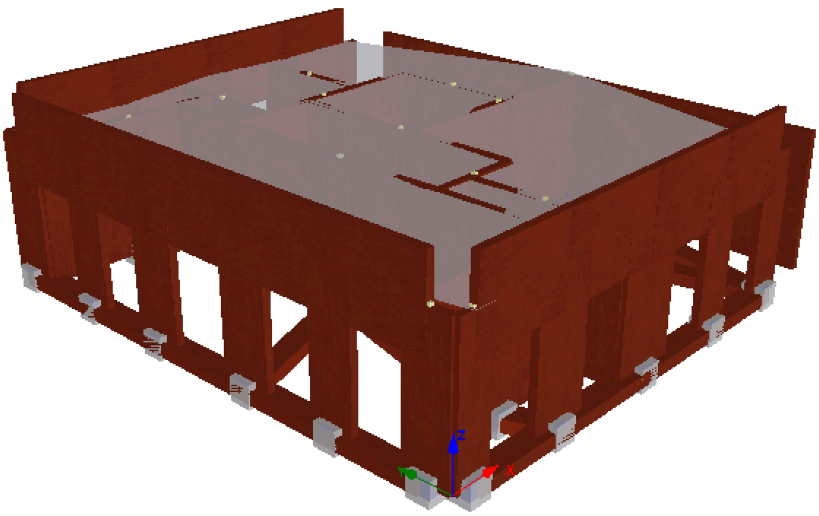

Figure 3.16: The MDOF model used for De Haver detached index building.

The mixed analytical and model-based procedure adopted for the equivalent macro-element calibration is the same used for the terraced index building. The only difference for the first two and fourth models (Figure 3.13, Figure 3.14 and Figure 3.16) is that the number of stories, N_s, is equal to 1, and thus the ultimate horizontal forces in the two horizontal directions coincide with the ultimate base shear values obtained from pushover analyses.

3.1.3 Properties of the equivalent footing macro-elements

The following tables, from Table 3.17 to Table 3.21, report the retrieved properties of the equivalent footing macro-elements for all terraced and detached index buildings, in terms of initial stiffness, foundation capacity and radiation damping equivalent dashpot coefficients.

Table 3.17: Properties of the equivalent macro-element for Zijlvest index building.

k_V (kN/m)	k_{Hx} (kN/m)	k_{My} (kNm/rad)
1.521E+07	1.167E+07	8.514E+08
N_{max} (kN)	$H_{max,x}$ (kN)	$M_{max,y}$ (kNm)
4.653E+03	6.634E+02	2.188E+04
	c_{Hx} (ton/s)	c_{My} (ton*m^2/s)
	3.568E+04	7.356E+02

Table 3.18: Properties of the equivalent macro-element for Kwelder index building.

k_V (kN/m)	k_{Hx} (kN/m)	k_{My} (kNm/rad)
7.613E+06	5.664E+06	1.480E+08
N_{max} (kN)	$H_{max,x}$ (kN)	$M_{max,y}$ (kNm)
2.429E+03	3.739E+02	7.219E+03
	c_{Hx} (ton/s)	c_{My} (ton*m^2/s)
	1.522E+04	4.427E+02

Table 3.19: Properties of the equivalent macro-element for Badweg index building.

k_V (kN/m)	k_{Hx} (kN/m)	k_{My} (kNm/rad)
4.828E+06	3.478E+06	1.123E+08
N_{max} (kN)	$H_{max,x}$ (kN)	$M_{max,y}$ (kNm)
1.425E+03	2.192E+02	4.709E+03
	c_{Hx} (ton/s)	c_{My} (ton*m^2/s)
	8.417E+03	4.364E+02

Table 3.20: Properties of the equivalent macro-element for Dijkstraat index building.

k_V (kN/m)	k_{Hx} (kN/m)	k_{My} (kNm/rad)
6.374E+06	5.055E+06	1.585E+08
N_{max} (kN)	$H_{max,x}$ (kN)	$M_{max,y}$ (kNm)
2.392E+03	2.967E+02	6.415E+03
	c_{Hx} (ton/s)	c_{My} (ton*m²/s)
	2.027E+04	2.251E+03

Table 3.21: Properties of the equivalent macro-element for De Haver index building.

k_V (kN/m)	k_{Hx} (kN/m)	k_{My} (kNm/rad)
1.533E+07	1.147E+07	2.969E+08
N_{max} (kN)	$H_{max,x}$ (kN)	$M_{max,y}$ (kNm)
5.145E+03	7.619E+02	3.582E+03
	c_{Hx} (ton/s)	c_{My} (ton*m²/s)
	3.456E+04	3.352E+03

3.2 Pile foundation macro-element

The pile-head macro-element developed by Correia & Pecker (2019) may be regarded as a lumped model located at the base of the superstructure that intends to represent the behaviour of the entire soil-foundation system. With the aim of realistically simulating the seismic response of the structure, the main sources of nonlinearity for laterally loaded piles, related to soil and pile inelastic response, including gap opening and closure, are considered.

The macro-element adopted herein is thus based on the three fundamental features of the response of laterally loaded piles: initial elastic behaviour, gap opening/closure effects and failure conditions. These three characteristic behaviours are all made compatible by using an inelastic model that accounts for the evolution from initial nonlinear elastic behaviour to full plastic flow at failure. Such inelastic model is based on a bounding surface plasticity theory formulation that ensures a smooth transition from the initial elastic pile-head response up to nonlinear behaviour and collapse.

This pile-head macro-element model represents the lateral behaviour of single vertical piles, subjected to a horizontal load and a moment, from the initial stages of loading up until reaching failure. The effects of vertical loading are not directly considered in this model except for its influence on the plastic moment of the pile cross-section. Otherwise, it is considered that the upper zone of the soil profile, until the depth at which the plastic hinge will form, only contributes to the lateral load resistance. The vertical load is assumed to be transferred to the surrounding soil below that depth, where there is no influence of gap opening effects.

The adopted system for nonlinear dynamic analyses, as modelled in SeismoStruct, composed of a nonlinear structural SDOF and a pile macro-element, is shown in Figure 3.17. The same superstructure-related remarks made in the case of footing macro-element apply in this case. All the springs and dashpots present in the macro-element implementation are visualised in the 2D scheme, apart from the torsional ones, which do not play a role in the analyses of interest.

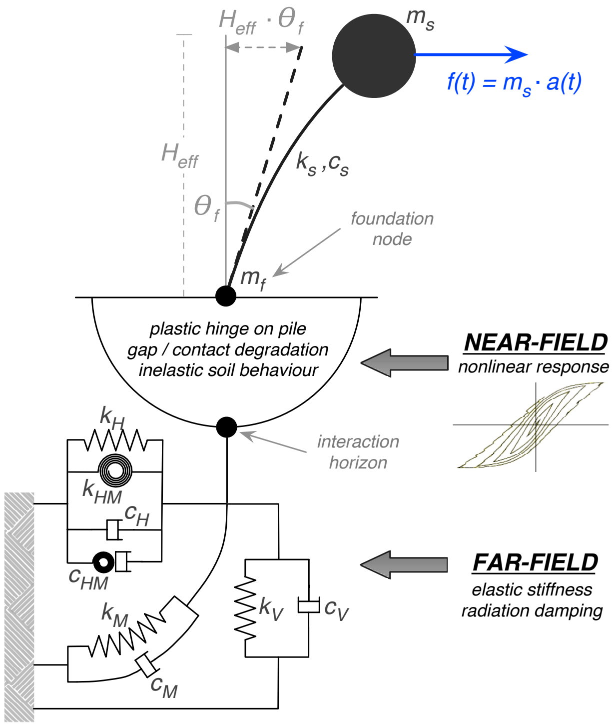

Figure 3.17: Adopted system with structural SDOF and pile macro-element, for dynamic analyses.

3.2.1 Assessment of input parameters for pile foundation macro-element

This section describes the input parameters for pile macro-elements to be used for the calibration step of MDOF models of the buildings. At this stage, the parameters are derived only for soil type A, being the median AF characterizing soil type A the most representative. The parameters definition is preceded by the description of the foundation typologies.

Three different cases have been considered combining two types of piles (see section 3.2.1.1) and three buildings characterized by different properties and loads. Figure 3.18 shows, for half of the model, the pile distribution assumed for the Apartment index buildings. The foundations of all the buildings have the same number (i.e. 67) and position of the piles, as shown in Figure 3.19. Table 3.22 shows the main characteristics of the foundations considered.

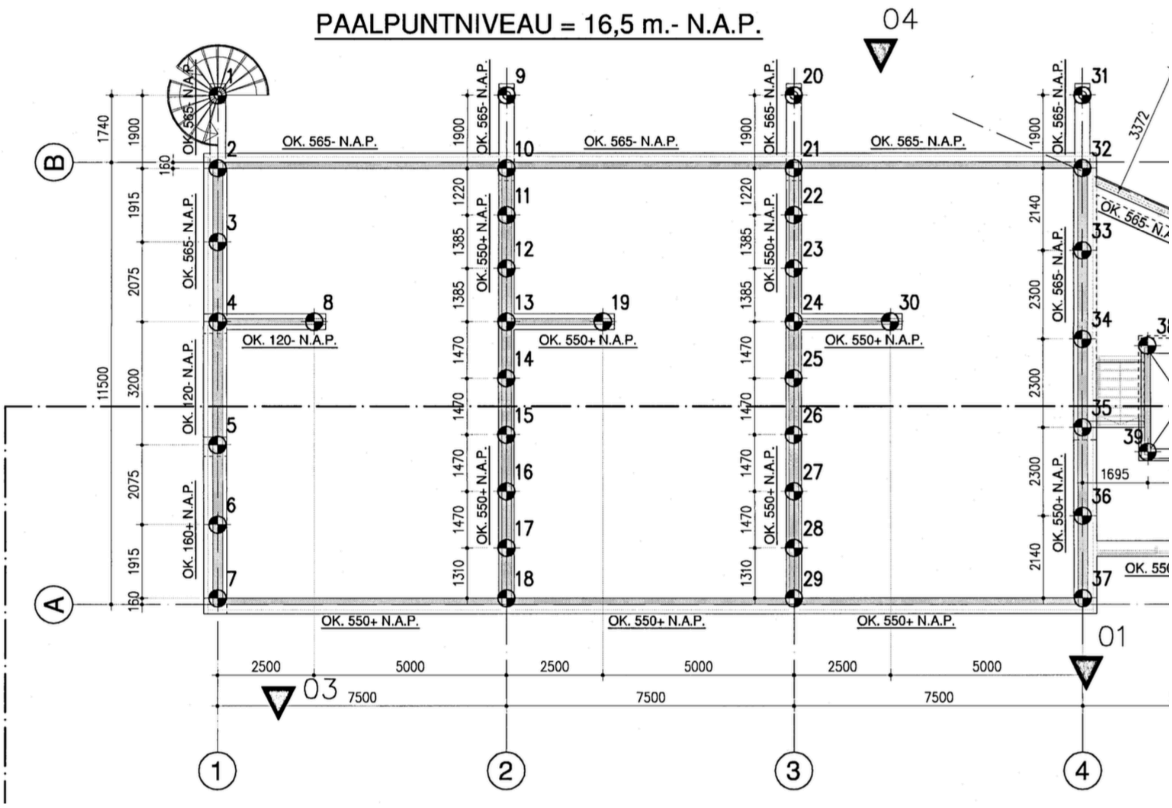

Figure 3.18 Typical pile distribution in an Apartment building (note: modelled index buildings feature twice a number of spans, hence the pile pattern shown herein has been doubled - see Figure 3.19).

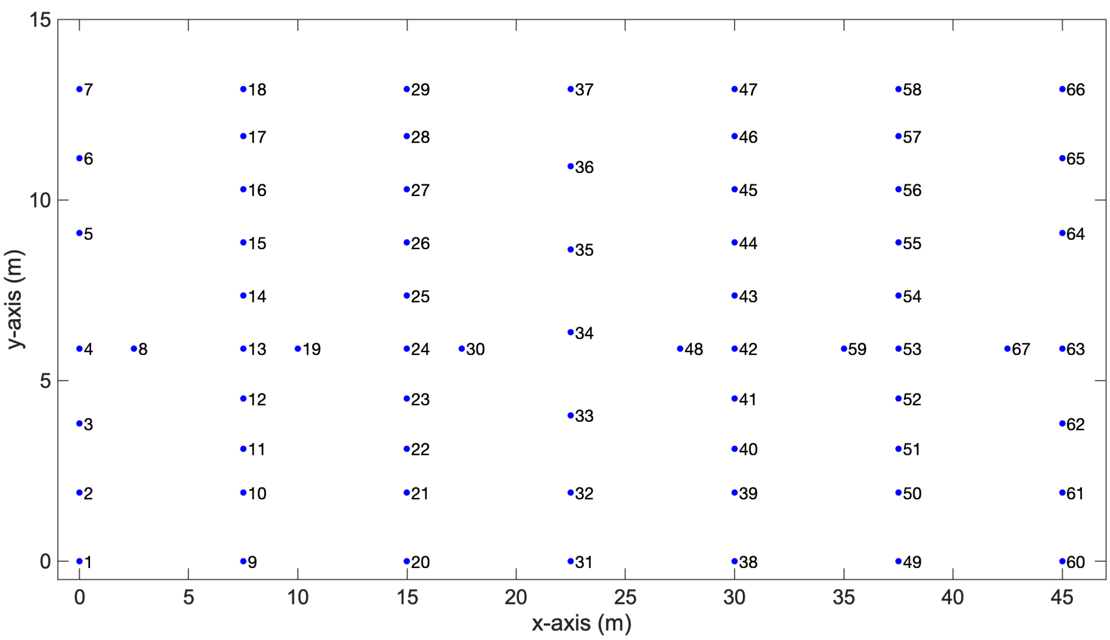

Figure 3.19: The foundation plan used for all apartment index buildings, with pile numbering.

Table 3.22: Main characteristics of the pile foundations considered.

Index Building	Vertical load (kN)	N pile	Pile type	Section	Size (cm)
Drive in	7640	67	Driven	Square	25
K-Flat	14930	67	Bored	Circular	45
Georg van S	11400	67	Bored	Circular	45

3.2.1.1 Foundation typologies

The pile foundations of two of the Apartment index buildings ("K-flat" and "Georg van S") consist of 450 mm solid circular concrete bored piles. The piles' length is equal to 16 m and they are connected by reinforced concrete (RC) capping beams with height equal to 600mm, and a width of 450 mm or 650 mm depending on the beam position (e.g. perimeter, internal). A detail of the foundation is shown in Figure 3.20.

Figure 3.21 shows the detailing of the pile with the characteristics of its materials and reinforcement. The concrete is a B25 type, which is assumed equivalent to C25/30, and for which is assumed a Young's modulus of 31 GPa. The main reinforcement is constituted by 5ϕ12 mm, the transversal reinforcement is constituted ϕ8 mm@250 mm hoops. The steel type is FeB500.

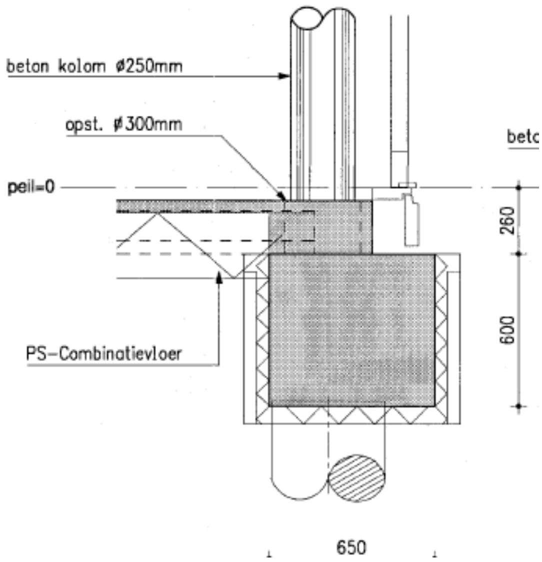

Figure 3.20: Typical detail of circular pile foundation head.

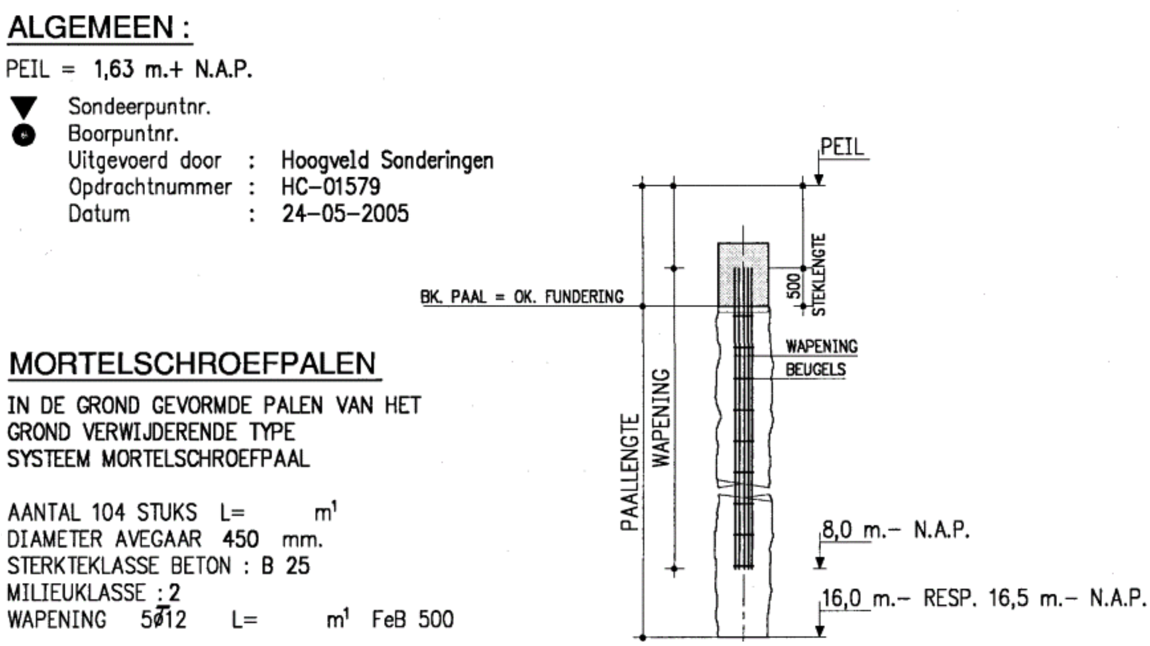

Figure 3.21 Typical material properties and reinforcement of the circular pile with diameter 45 cm.

For the “Drive-in” index building, instead, an alternative pile typology was considered, consisting of 250x250 mm square section concrete piles. The piles' length is equal to 16 m, with a B25 concrete type, which is assumed equivalent to C25/30, and with an assumed Young’s modulus of 31 GPa. The main reinforcement is constituted by 4ϕ12 mm, the transversal reinforcement is constituted ϕ8 mm@250 mm hoops. The steel type is FeB500.

3.2.1.2 Macro-element parameters

Soil-structure interaction of pile foundations was analysed using the macro-element approach proposed by Correia (2011) and Correia & Pecker (2019), which is described above. This Section describes the definition of the parameters for macro-elements of pile foundations to be used in the MDOF model. The input parameters of the macro-elements can be subdivided into three main groups described in the following sections: foundation capacity, foundation stiffness and model specific parameters.

Foundation capacity.

Correia (2011) has determined the failure surface and mechanism for laterally loaded piles (i.e. a soil passive wedge failure at shallow depths and flow-around failure at larger depths, with a possible gap formation on the back of the pile, see Figure 3.22b) through the kinematic approach of yield design theory. Under seismic conditions, a saturated soil deposit is considered, which is assumed to be impervious. Consequently, it responds with undrained behaviour and the Tresca failure criterion may be adopted. Figure 3.22a) shows the two simplified geotechnical scenarios in terms of undrained shear strength (S_u) considered by Correia (2011), which includes constant or linear distribution along the depth of the soil deposit.

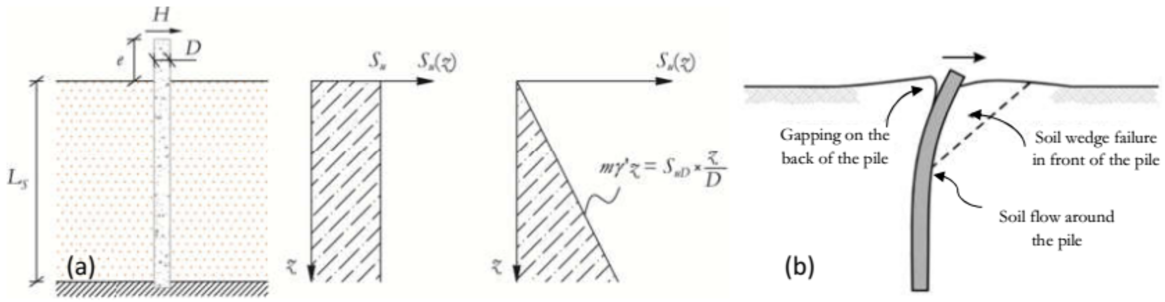

Figure 3.22 a) Geotechnical scenarios: constant and linear undrained shear strength profiles; b) soil response for pile-head lateral loading (Correia, 2011).

Figure 3.23 shows the undrained shear strength evaluated in the shallow part of the deposit of soil type A obtained in section 1.6.1, the values can be interpolated by linear relationship, for such reason the evaluation of the capacity of the macro-element has been estimated considering the linear S_u distribution proposed by Correia (2011).

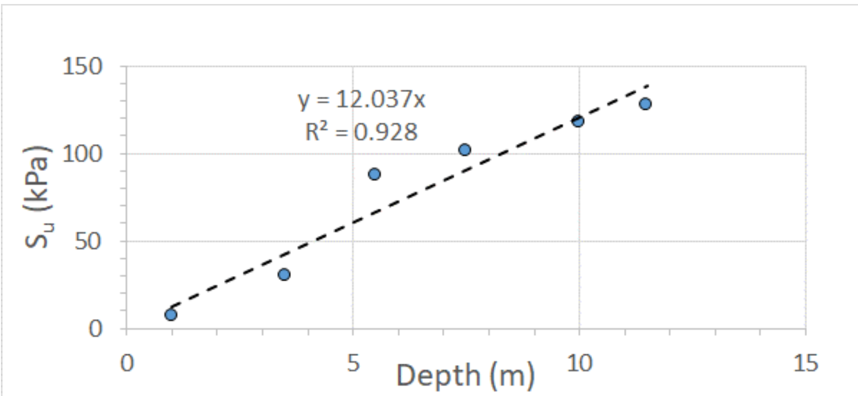

Figure 3.23 Undrained shear strength evaluated in the shallow part of the deposit of soil type A.

The capacity input parameters of the macro-elements are:

- the maximum horizontal pile head force (Q_{Hmax}), calculated for the case of no eccentricity of the horizontal force;
- the pile yield moment ($Q_{Mmax}=M_y$);
- the flexural stiffness of the pile section (E_pI_p).

The last two parameters have been calculated through a moment-curvature analysis using the software CUMBIA (Montejo & Kowalsky, 2007).

The soil-pile plastic mechanism parameters developed by Correia (2011) adopts a wedge-type of mechanism based on the one proposed by Klar & Randolph (2008), modified in order to include a possible gap opening in the back of the pile and/or an active conical wedge of soil. The wedge thickness is identified by the depth z_w. Correia (2011) considers piles invariably classified as long or flexible piles, the least upper bound was always obtained with the deformed shape that includes a plastic hinge, forming at a depth z_h, with almost rigid behaviour of the remaining pile length. Soil inertia effects were also allowed for, although they were shown not to have a significant influence on the least upper bound value (Correia, 2011).

Correia (2011) developed a nonlinear constrained optimisation procedure in order to determine the minimum upper-bound failure mechanism parameters. The optimization procedure uses dimensionless parameters and equations, where D, S_u, and γ_s are considered as fundamental quantities. A dimensional analysis showed that the independent variables were the normalised load eccentricity, $e_n = e/D$, pile yield moment, $M_{yn} = M_y / S_u D^3$, and soil unit weight, $\gamma_n = \gamma_s D / S_u$.

For a straightforward numerical implementation of the plasticity formulation, the pile-head failure surface was approximated by a rounded curve corresponding to a distorted superellipse. Figure 3.24 shows a normalized superellipse described by the following equation:

$$\left|\frac{H_u}{H_{u,e=0}} - \gamma \frac{M_u}{M_y}\right|^{n_H} + \left|\frac{M_u}{M_y}\right|^{n_M} = 1 \tag{3.24}$$

The parameters γ, n_H and n_M are discussed later in the section about model specific parameters.

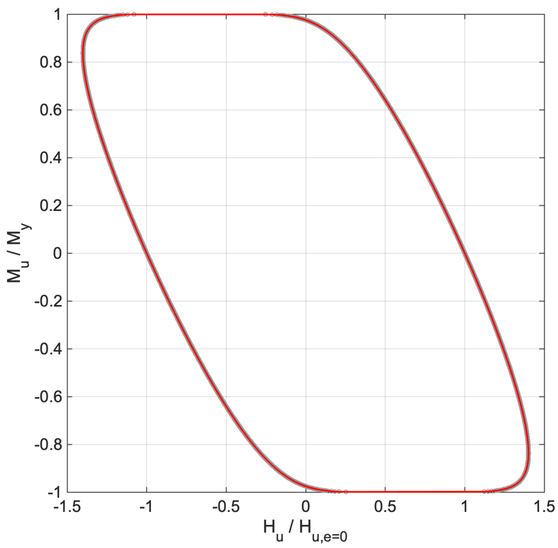

Figure 3.24 Normalized superellipse.

The evolution of the maximum normalised horizontal pile-head load can be related with the normalised yield moment and with the normalised load eccentricity through the following equation, with coefficients listed in Table 3.23.

$$H_{un} = \frac{H_u}{S_u D^2} = \frac{M_{yn}}{e_n + \frac{a_1 M_{yn}\hat{}\left(a_2 - \frac{a_3}{(e_n+1)^{a_4}}\right)}{(e_n+1)^{a_5}}} \tag{3.25}$$

Table 3.23: Coefficients for H_{un} fitting function

a_1	a_2	a_3	a_4	a_5
0.4422	0.4235	0.0960	0.5179	0.3926

The soil wedge normalised depth (z_{wn}) is described by the following equation with coefficients listed in Table 3.24.

$$z_{wn} = \frac{z_w}{D} = \frac{M_{yn}^{a_1}}{a_2(e_n+a_3)^{a_4}+a_5 M_{yn}^{a_6}} \tag{3.26}$$

Table 3.24: Coefficients for z_{wn} fitting function

a_1	a_2	a_3	a_4	a_5	a_6
0.5490	0.1936	3.1504	0.7530	0.2774	0.5309

Foundation stiffness.

Gazetas (1991) made a complete survey of foundation vibration problems and included detailed design charts and equations for direct computation of the pile-head lateral and axial stiffness and damping coefficients. The expressions presented in Gazetas (1991) were obtained through calibration of numerical results and are widely used in equivalent-linear analyses of soil-pile-structure-interaction. His expressions for pile-head static stiffness have been adopted, with slight modifications, in EC 8 – Part 5 (2004). The approximate expressions for pile-head equivalent-linear impedances proposed by Gazetas (1991) and adopted in EC8 – Part 5 (2004), were assumed to be valid for representing the initial elastic dynamic stiffness of the macro-element. These formulas are valid for soil profiles with constant, linear or parabolic increase of soil stiffness with depth. Figure 3.25 represents the soil stiffness evolution with depth in such idealised soil profiles.

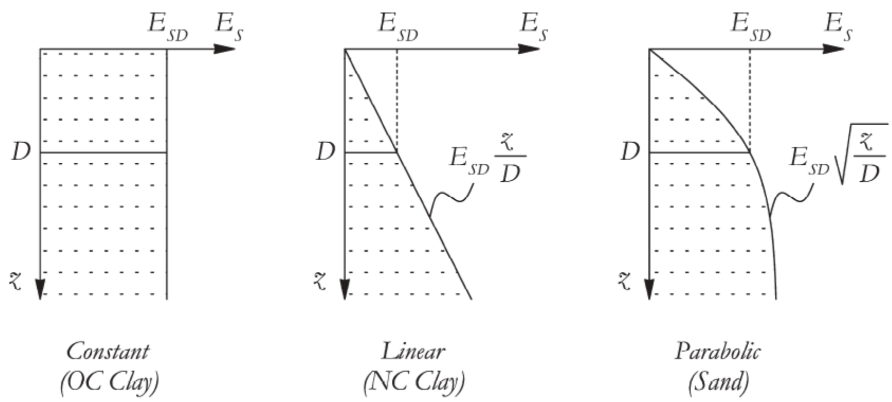

Figure 3.25 Idealized soil stiffness profiles (from Correia, 2011).

The Gazetas (1991) formulas are valid for flexible or long piles and are summarised in Table 3.25. It also presents the pile active length for lateral loading in inertial response, which is somewhat greater than its static counterpart, defining the minimum pile length for the pile to be considered flexible. In those expressions, D is the pile diameter, E_{SD} is the Young' modulus of the soil a depth equal to the pile diameter and E_p is the Young's modulus of the pile material (Correia, 2011). The pile-head stiffness matrix components follow the sign convention expressed in Figure 3.26.

Table 3.25: Pile-head static stiffness coefficients and active length for flexible piles (after EC8 – Part 5, 2004).

Soil stiffness profile	$\frac{K_{HH}}{E_{SD}D}$	$\frac{K_{MM}}{E_{SD}D^3}$	$\frac{K_{HM}}{E_{SD}D^2}$	$\frac{L_a}{D}$
Constant $E_S = E_{SD}$	$1.08\left(\frac{E_p}{E_{SD}}\right)^{0.21}$	$0.16\left(\frac{E_p}{E_{SD}}\right)^{0.75}$	$-0.22\left(\frac{E_p}{E_{SD}}\right)^{0.50}$	$2\left(\frac{E_p}{E_{SD}}\right)^{0.25}$
Linear $E_S = E_{SD}\,z/D$	$0.60\left(\frac{E_p}{E_{SD}}\right)^{0.35}$	$0.14\left(\frac{E_p}{E_{SD}}\right)^{0.80}$	$-0.17\left(\frac{E_p}{E_{SD}}\right)^{0.60}$	$2\left(\frac{E_p}{E_{SD}}\right)^{0.20}$
Parabolic $E_S = E_{SD}\sqrt{z/D}$	$0.79\left(\frac{E_p}{E_{SD}}\right)^{0.28}$	$0.15\left(\frac{E_p}{E_{SD}}\right)^{0.77}$	$-0.24\left(\frac{E_p}{E_{SD}}\right)^{0.53}$	$2\left(\frac{E_p}{E_{SD}}\right)^{0.22}$

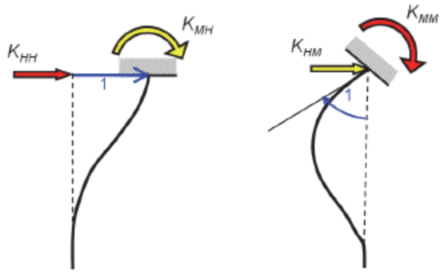

Figure 3.26 Sign convention for pile-head loading (from Correia, 2011).

Gazetas (1991) has also presented the corresponding pile-head damping coefficients, which are computed for each frequency (f) according to the expressions in Table 3.26. These correspond only to the radiation damping component. Moreover, they are only valid for frequencies above the fundamental frequency of vibration of the soil deposit, since, if the bedrock is assumed to be rigid, no radiation damping exists below that frequency. The soil deposit fundamental frequencies (f_S) associated to each idealised soil profile are also given in Table 3.26, with L_S being the soil deposit depth and V_{SD} and V_{SLs} being the shear wave velocity at a depth of one pile diameter and at the bottom of the soil profile, respectively. In the formulas of Table 3.26, the frequency f is assumed for soil type A equal to 1.67 Hz (i.e. 0.6s), taking into account both the period of the structures to be considered and the AF trend shown in Figure 1.19, the latter having peaks of almost equal value between 0.4 and 1.67 Hz.

Table 3.26: Pile-head radiation damping coefficients for flexible piles and fundamental frequencies of soil deposit (after Gazetas, 1991).

Soil stiffness profile	$\frac{\xi_{HH} V_{SD}}{f D}$	$\frac{\xi_{MM} V_{SD}}{f D}$	$\frac{\xi_{HM} V_{SD}}{f D}$	$\frac{f_S L_S}{V_{SL}}$
Constant $E_S = E_{SD}$	$1.10\left(\frac{E_p}{E_{SD}}\right)^{0.17}$	$0.35\left(\frac{E_p}{E_{SD}}\right)^{0.20}$	$0.85\left(\frac{E_p}{E_{SD}}\right)^{0.18}$	0.25
Linear $E_S = E_{SD}\, z/D$	1.80	0.40	1.00	0.19
Parabolic $E_S = E_{SD}\sqrt{z/D}$	$1.20\left(\frac{E_p}{E_{SD}}\right)^{0.08}$	$0.35\left(\frac{E_p}{E_{SD}}\right)^{0.10}$	$0.70\left(\frac{E_p}{E_{SD}}\right)^{0.05}$	0.223

The radiation damping equivalent dashpot coefficients in Table 3.26 are non-dimensional; the corresponding dimensional form can be retrieved using the following expressions:

$$C_{HH} = \frac{2\, K_{HH} \cdot \xi_{HH}}{\omega} \tag{3.27}$$

$$C_{MM} = \frac{2\, K_{MM} \cdot \xi_{MM}}{\omega} \tag{3.28}$$

$$C_{HM} = \frac{2\, K_{HM} \cdot \xi_{HM}}{\omega} \tag{3.29}$$

Figure 3.27 shows the shear wave velocity profile of soil type A. Within the pile length (16m), the V_s profile, and consequently also the Young and shear modulus, are rather constant. Therefore, the pile-head stiffness and damping were selected considering the constant profile.

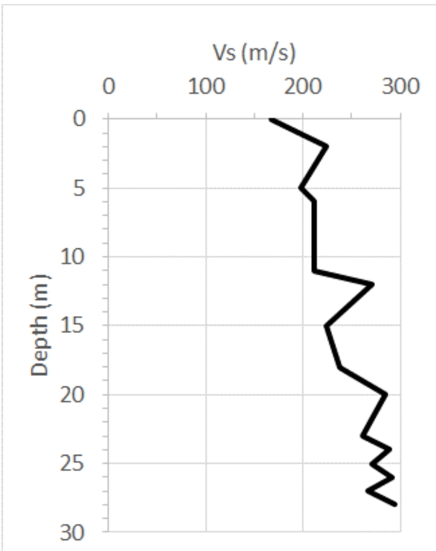

Figure 3.27 Shear wave velocity profile of soil type A.

For the vertical stiffness component, in the case of a pile in a homogenous layer, the solution of the governing equilibrium equation yields the vertical stiffness K atop the pile (see for instance Mylonakys & Gazetas, 1998):

$$K = E_{\mathrm{p}} A_{\mathrm{p}} \lambda \frac{\Omega + \tanh(h\lambda)}{1 + \Omega \tanh(h\lambda)} \tag{3.30}$$

in which Ω and λ stand for the dimensionless pile-base stiffness and load transfer (Winkler) parameter respectively:

$$\Omega \equiv \frac{K_{\mathrm{b}}}{E_{\mathrm{p}} A_{\mathrm{p}} \lambda} \tag{3.31}$$

$$\lambda \equiv \sqrt{\left(\frac{\delta G_{\mathrm{s}}}{E_{\mathrm{p}} A_{\mathrm{p}}}\right)} \tag{3.32}$$

From the simple method of Randolph & Wroth (1978), it follows that the soil around a pile shaft can be represented by distributed springs (Winkler assumption), the stiffness of which (per unit length of pile) can be written as:

$$k_z = \delta G_{\mathrm{s}} \tag{3.33}$$

where:

$$\delta = \frac{2\pi}{\ln\left(\frac{2r_{\mathrm{m}}}{d}\right)} \tag{3.34}$$

and r_m is a threshold radius beyond which soil settlement is vanishingly small. In the general case of an inhomogeneous soil, r_m is given by:

$$r_{\mathrm{m}} \approx \chi_1 \chi_2 L (1 - \nu_{\mathrm{s}}) \tag{3.35}$$

in which χ_1 and χ_2 are empirical factors accounting for soil inhomogeneity.

In accordance with Gazetas (1991) the axial radiation dashpot coefficient for constant soil modulus can be evaluated with the following formula:

$$\begin{aligned} C_{VV} &\cong a_o^{-1/5} \rho V_S \pi D L r_d \quad for\ f > 1.5 f_r \\ &with \quad r_d \cong 1 - e^{-(E_p/E_s)(L/D)^{-2}} \end{aligned} \tag{3.36}$$

$C_{VV} \cong 0 \qquad\qquad for\ f \leq f_r$

Where $f_r \cong \bar{V}_{La}/4H$, with $\bar{V}_{La}$ is the average V_{La} over the stratum depth H, $a_o = \omega D/V_s$. Linear interpolation is required for $f_r<f<1.5f_r$.

Model specific parameters.

The pile macro-element accounts for the three major features of the response of laterally loaded piles: initial elastic behaviour, gap influence and failure conditions. These three characteristic behaviours are all made compatible by using an inelastic model, which accounts for the evolution from initial elastic behaviour to full plastic flow at failure. Such inelastic model is based on bounding surface plasticity theory, for monotonic as well as cyclic pile-head loading conditions (Correia, 2011). A more detailed description of the theoretical aspects regarding the formulation of the pile macro-element can be found in Correia & Pecker (2019).

This section describes the model specific parameters that characterize the pile macro-element. The parameters γ, n_H and n_M describe the shape of the distorted superellipse that approximates the pile-head failure surface. n_H is equal to 7.04 for linear undrained shear strength profile, n_M is always equal to 2, and γ is equal to -0.667 for linear undrained shear strength profile.

The parameters β and η are two calibration parameters describing the gapping model, β is equal to 1, whereas η is taken equal to 0.001.

The parameters H_0^{pl}, n_{UR} and δ_{lim} describe the evolution of the plastic modulus during cyclic response, H_0^{pl} is the reference plastic modulus parameter and is equal to 0.2, n_{UR} is the exponent for plastic modulus evolution and is equal to 1, δ_{lim} is the lower limit value for the similarity ratio δ between the loading and bounding surfaces in unloading/reloading and is equal to 0.33.

3.2.1.3 Apartment block "Drive-in"

The Drive-in index building is founded on square driven piles of width 25 cm; an equivalent diameter of 28.2 cm has thus been computed for the assessment of macro-element parameters, using a criterion of equal cross-section area. Material parameters of the piles are described in section 3.2.1.1.

The initial stiffness parameters of the macro-element have been computed considering a soil profile with constant Young's modulus assuming V_{sD} equal to 215 m/s, density ρ equal to 1670 kg/m^3, and ν equal to 0.45.

An estimate of the load on each pile, to be used for the computation of the moment–curvature relationship, is evaluated dividing the total load by the number of piles; the resulting vertical load is equal to 114 kN. The ensuing moment-curvature plot (obtained using the software Cumbia) is shown in Figure 3.28.

The eccentricity of the horizontal load (e) corresponds to the height of the equivalent SDOF model and is equal to 4.51 m.

The macro-element parameters for each pile were evaluated based on the formulas described in section 3.2.1.2. Table 3.27 summarizes the macro-element parameters for the piles of the Drive-in building.

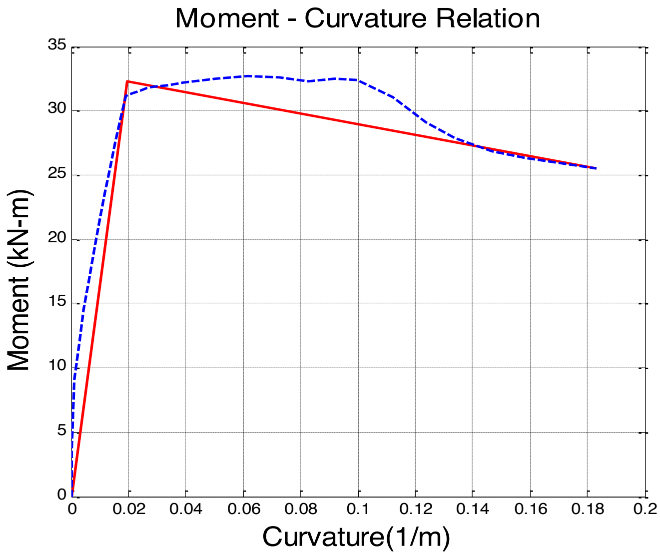

Figure 3.28 Moment-curvature relationship and corresponding bi-linear approximation for pile square section B=25cm for vertical load equal to 114 kN.

Table 3.27: Pile-head macro-element parameters for Drive-in building.

Symbol	Unit	Description	Value
D	m	Pile diameter	0.282
K_{VV}	kN/m	Vertical pile head stiffness	430,957
K_{HH}	kN/m	Horizontal pile head stiffness	192,087
K_{MM}	kN m	Rotational pile head stiffness	32,458
K_{HM}	kN	Hor.-rot. off-diagonal pile head stiffness	- 46,120
QQ_H_MAX	kN	Maximum horizontal pile head force with no eccentricity	35.7
QQ_M_MAX	kNm	Pile head yield moment	32.3
n_H	[-]	Exponent for horizontal force in the superellipse BS	7.04
n_M	[-]	Exponent for moment in the superellipse BS	2
γ	[-]	Distortion of the superellipse BS	-0.667
Z_W	m	Maximum gap depth (soil wedge depth)	0
E_pI_p	kN m2	Pile flexural stiffness	1638.1
β	[-]	Gap evolution parameter	1
η	[-]	Minimum gap depth evolution parameter	0.001
H_0^{pl}	[-]	Reference plastic modulus parameter	0.2
n_{UR}	[-]	Exponent for plastic modulus evolution	1
δ_{LIM}	[-]	Lower limit value for DELTA in unloading/reloading.	0.33
C_{VV}	[N s /m] o [kg/s]	Vertical radiation damping	505,606
C_{HH}	[N s /m] o [kg/s]	Horizontal damping	204,047
C_{MM}	[N m s] o [kg m2/s]	Rotational damping	12,720
C_{HM}	[N s] o [kg m/s]	Hor.-rot. off-diagonal damping	- 39,771
Q_s	[kN]	Shaft capacity	568.3

3.2.1.4 Apartment block "K-flat"

The K-flat index building is founded on circular bored piles of 45 cm diameter; the material parameters of the piles are described in section 3.2.1.1. The initial stiffness parameters of the macro-element were computed considering a soil profile with constant Young's modulus assuming V_{SD} equal to 215 m/s, density ρ equal to 1670 kg/m^3, and ν equal to 0.45.

An estimate of the load on each pile, to be used for the computation of the moment–curvature relationship, is evaluated dividing the total load by the number of piles; the resulting vertical load is equal to 222.8 kN. The ensuing moment-curvature plot (obtained using the software Cumbia) is shown in Figure 3.29.

The eccentricity of the horizontal load (e) corresponds to the height of the equivalent SDOF model and is equal to 6.28 m. The macro-element parameters for each pile were evaluated based on the formulas described in section 3.2.1.2; Table 3.28 summarizes the macro-element parameters for the piles of the K-flat building.

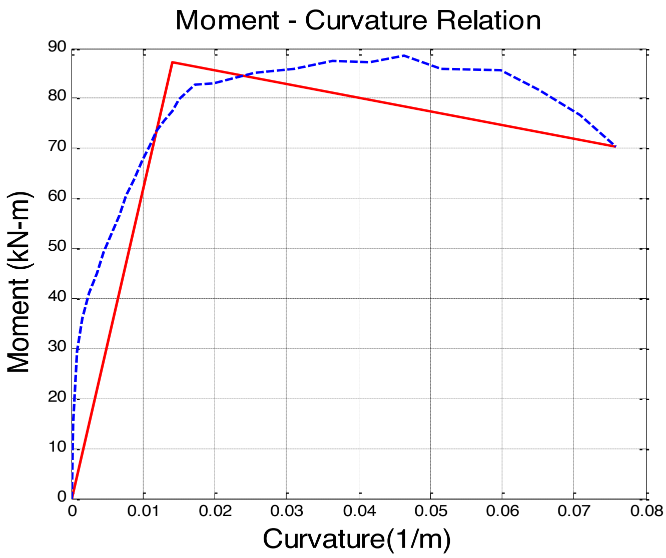

Figure 3.29 Moment-curvature relationship and corresponding bi-linear approximation for pile circular section D=45cm for vertical load equal to 222.8 kN.

Table 3.28: Pile-head macro-element parameters for K-flat building.

Symbol	Unit	Description	Value
D	m	Pile diameter	0.450
K_{VV}	kN/m	Vertical pile head stiffness	713,858
K_{HH}	kN/m	Horizontal pile head stiffness	306,419
K_{MM}	kN m	Rotational pile head stiffness	131,758
K_{HM}	kN	Hor.-rot. off-diagonal pile head stiffness	- 117,361
QQ_H_MAX	kN	Maximum horizontal pile head force with no eccentricity	80.5
QQ_M_MAX	kNm	Pile head yield moment	87.3
n_H	[-]	Exponent for horizontal force in the superellipse BS	7.04
n_M	[-]	Exponent for moment in the superellipse BS	2
γ	[-]	Distortion of the superellipse BS	-0.667
Z_W	m	Maximum gap depth (soil wedge depth)	0
E_pI_p	kN m2	Pile flexural stiffness	6176.9
β	[-]	Gap evolution parameter	1
η	[-]	Minimum gap depth evolution parameter	0.001
H_0^{pl}	[-]	Reference plastic modulus parameter	0.2
n_{UR}	[-]	Exponent for plastic modulus evolution	1
δ_{LIM}	[-]	Lower limit value for DELTA in unloading/reloading.	0.33
C_{VV}	[N s /m] o [kg/s]	Vertical radiation damping	1,809,033
C_{HH}	[N s /m] o [kg/s]	Horizontal damping	519,237
C_{MM}	[N m s] o [kg m2/s]	Rotational damping	82,365
C_{HM}	[N s] o [kg m/s]	Hor.-rot. off-diagonal damping	- 161,441
Q_s	[kN]	Shaft capacity	796.1

3.2.1.5 Apartment block "Georg van S"

The Georg van S index building is founded on circular bored piles of 45 cm diameter; material parameters of the piles are described in section 3.2.1.1. The initial stiffness parameters of the macro-element were computed considering a soil profile with constant Young's modulus assuming V_{sD} equal to 215 m/s, density ρ equal to 1670 kg/m^3, and ν equal to 0.45.

An estimate of the load on each pile, to be used for the computation of the moment–curvature relationship, is evaluated dividing the total load by the number of piles; the resulting vertical load is equal to 170.1 kN. The ensuing moment-curvature plot (obtained using the software Cumbia) is shown in Figure 3.30.

The eccentricity of the horizontal load (e) corresponds to the height of the equivalent SDOF model and is equal to 7.75 m. The macro-element parameters for each pile were evaluated based on the formulas described in section 3.2.1.2; Table 3.29 summarizes the macro-element parameters for the piles of the Georg van S building.

Table 3.29: Pile-head macro-element parameters for Georg van S building.

Symbol	Unit	Description	Value
D	m	Pile diameter	0.450
K_{VV}	kN/m	Vertical pile head stiffness	713,858
K_{HH}	kN/m	Horizontal pile head stiffness	306,419
K_{MM}	kN m	Rotational pile head stiffness	131,758
K_{HM}	kN	Hor.-rot. off-diagonal pile head stiffness	- 117,361
QQ_H_MAX	kN	Maximum horizontal pile head force with no eccentricity	77.0
QQ_M_MAX	kNm	Pile head yield moment	81.7
n_H	[-]	Exponent for horizontal force in the superellipse BS	7.04
n_M	[-]	Exponent for moment in the superellipse BS	2
γ	[-]	Distortion of the superellipse BS	-0.667
Z_W	m	Maximum gap depth (soil wedge depth)	0.001
E_pI_p	kN m2	Pile flexural stiffness	5691.3
β	[-]	Gap evolution parameter	1
η	[-]	Minimum gap depth evolution parameter	0.001
H_0^{pl}	[-]	Reference plastic modulus parameter	0.2
n_{UR}	[-]	Exponent for plastic modulus evolution	1
δ_{LIM}	[-]	Lower limit value for DELTA in unloading/reloading.	0.33
C_{VV}	[N s /m] o [kg/s]	Vertical radiation damping	1,809,033
C_{HH}	[N s /m] o [kg/s]	Horizontal damping	519,237
C_{MM}	[N m s] o [kg m2/s]	Rotational damping	82,365
C_{HM}	[N s] o [kg m/s]	Hor.-rot. off-diagonal damping	- 161,441
Q_s	[kN]	Shaft capacity	796.1

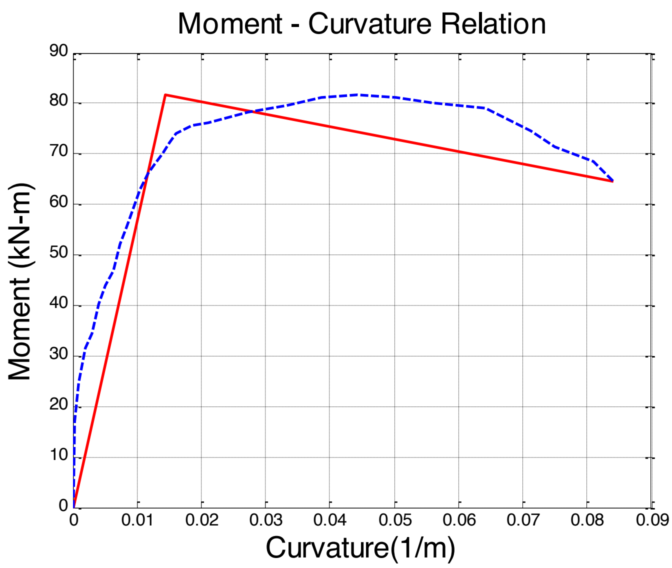

Figure 3.30 Moment-curvature relationship and corresponding bi-linear approximation for pile circular section D=45cm for vertical load equal to 170.1 kN.

3.2.2 Calibration of the equivalent pile macro-element

As discussed already for the buildings on shallow foundations, given that the development of fragility functions is based on dynamic analyses of SDOF systems (Crowley et al., 2019), the calibration of an equivalent pile macro-element was needed also for this second set of index buildings. As for the other index buildings, the first step was thus to create a MDOF model in SeismoStruct for each index building. Apartment buildings have a layout that is similar to that of the terraced buildings, but compared to the latter they are taller (three or four stories) and more massive. Given the similarity of geometric properties for all the considered index buildings, the foundation plane was assumed to be same for all of them, comprising a total of 67 piles distributed along the perimeter and five transversal axes along the *y*-direction (see Figure 3.19).

Also, again considering the similar geometric properties for the three-storey URM apartment index buildings included in this study, namely Drive-in, K-Flat and Georg van S, the same MDOF model (displayed in Figure 3.31) was used for all of them, only changing the total mass accordingly.

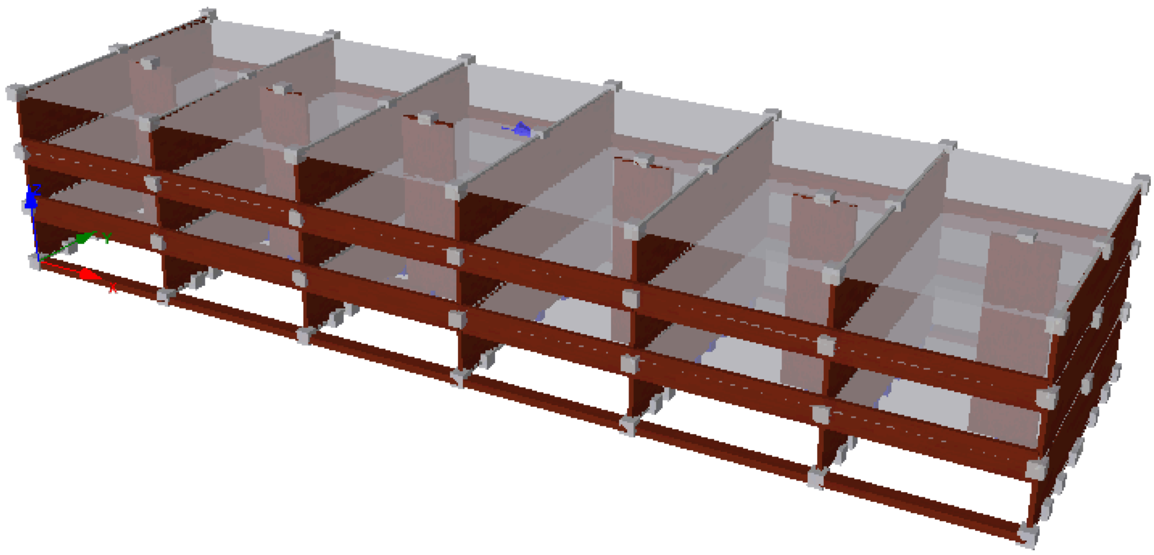

Figure 3.31: The three-storey MDOF model used for Drive-in, K-Flat and Georg van S apartment index buildings.

As for terraced and detached buildings, masonry piers and spandrels are introduced as columns and beams, respectively, to model the transverse walls (*y*-direction) and approximately model the sequence of openings in the two identical façades along the *x*-direction. A total of 67 pile macro-elements are introduced at the base of the model, in correspondence to the pile positions (see Figure 3.19). Similarly to terraced and detached buildings, the analyses were performed along the (weaker) x-direction of the buildings.

Three types of pile alignments are present, and in each of them piles have different distances between each other. In order to model the vertical masonry piers in the *y*-direction without introducing overlapping or openings between them, instead of creating a masonry pier on the top of each macro-element, as done for terraced and detached buildings, the following modelling strategy was adopted. For each pile row, a centroid node at zero elevation was created, not restrained and connected to the upper nodes of the macro-elements through a rigid link. In this way, only one pier per storey was created on the top of this centroid node. Then, to be able to introduce the beams, two lateral nodes at each storey and for each pile row were created, connected via rigid links to the centroid wall nodes.

The rigid reinforced concrete slabs are modelled with rigid diaphragms linking the column and beam nodes at the floor levels. Reinforced concrete foundation beams connect the upper nodes of the macro-elements. Both masonry and reinforced concrete were introduced as linear elastic materials, with the actual values for the elastic modulus and density. The total mass of the model, given by the superstructure mass plus the foundation mass, is approximately equal to the actual total mass, which was used in the derivation of the single macro-element properties.

Two variants of the described MDOF model were produced. The first one, whose output is needed to retrieve one stiffness component (as explained below), has an additional rigid diaphragm at the foundation level connecting the upper nodes of the macro-elements. The latter nodes have their rotations restrained and a relatively small horizontal force (to stay in the initial elastic domain) along x applied. The second variant of the model, whose output is needed to retrieve the rotational bearing capacity, is for pushover analysis along the x-direction, i.e. the only direction of interest for pile macro-elements (which work in only one direction); the pushover was carried out pushing the structure in load control with forces located at the centroids of floor levels, according to a triangular distribution.

The equivalent macro-element calibration requires the computation of the stiffness, capacity and damping along several directions. Most of the parameters were computed analytically starting from the foundation geometry and properties of the single macro-elements, while the remaining ones required the output from the model.

The vertical stiffness, k_V, as well as the horizontal stiffness, k_H, were obtained by simply summing up the stiffness values of the single macro-elements, assuming a rigid behaviour of the foundation plane. The torsional stiffness, k_T, does not play a role in the fragility curve derivation since the models represent the response in a single vertical plane.

For the rotational stiffness, k_M, a more rigorous approach than the one followed for terraced and detached buildings was adopted, since the dynamic behaviour of apartment buildings is driven more by rocking than by sliding: this is basically because they are taller than terraced and detached buildings. The approach consisted in comparing the initial rotational stiffness of the MDOF model with the one of the simplified system composed of a nonlinear structural SDOF and an equivalent pile macro-element (see Figure 3.17 above). The following steps were implemented:

- A pushover analysis is carried out on the MDOF model;
- The average displacement of the foundation plane and of the upper floors are computed at an early stage of loading, so to be in the macro-element linear elastic phase;
- An equivalent floor displacement is computed summing up the single floor displacements squared and then dividing by the sum of floor displacements, assuming equal floor masses;
- The equivalent drift ratio is obtained by subtracting the base displacement from the equivalent floor displacement and dividing by the building centroid height;
- Another pushover analysis is carried out on the simplified SDOF system;
- At the same early stage of loading, the SDOF drift ratio is obtained by subtracting the foundation node displacement from the structural mass displacement and dividing by the building centroid height;

- The equivalent drift ratio (retrieved from the MDOF model) and the SDOF drift ratio are compared, and consequently the SDOF rotational stiffness, k_M, is changed iteratively until the two drifts are close enough.

The described approach gives the analyst an idea of the error due to using the upper or lower bounds for the rotational stiffness, and is a guide to select the most suitable value.

Finally, using the first variant of the MDOF model, the horizontal-rotational off-diagonal stiffness, k_{HM}, corresponds to the sum of reaction moments in the rotation-restrained upper nodes of macro-elements divided by the horizontal displacement of the base rigid plane.

Concerning the bearing capacity, the horizontal component, H_{max}, was computed as the sum over the single macro-elements, while for the rotational component, M_{max}, the following procedure was employed.

The pile-head failure surface is approximated by a rounded curve corresponding to a distorted superellipse (shown in Figure 3.24), of equation (Correia et al., 2012):

$$\left|\frac{H_u}{H_{max}} - \gamma \frac{M_u}{M_{max}}\right|^{n_H} + \left|\frac{M_u}{M_{max}}\right|^{n_M} = 1; \quad \text{with } M_u = \sum_{k=1}^{N_s} F_{u,k} \cdot h_k \tag{3.37}$$

where H_u is the ultimate base shear obtained from the pushover analysis, $F_{u,k}$ is the ultimate horizontal force at the k-th floor level, obtained considering a triangular distribution along the building height, while n_H, n_M and γ were set to 7.04, 2 and -0.667 (assumption of linear variation of undrained shear strength), respectively. In Eq. (3.37), the only unknown is M_{max}: the latter is derived from the ratio M_u / M_{max}, which is obtained by interpolation in correspondence of the actual H_u / H_{max} value.

Concerning the radiation damping coefficients for the equivalent macro-element, they are defined in the vertical (c_V), horizontal (c_H) and rotational (c_M) directions. Similarly to the stiffness, a horizontal-rotational off-diagonal damping coefficient, c_{HM}, is also included in the set of damping parameters and requires a physical damper with coupled behaviour between the horizontal force and moment. Since in the case of SeismoStruct such coupled element was not available at the time of running the analyses, an equivalent set of uncoupled (horizontal and rotational) dampers must be introduced, as follows (Correia, 2011):

$$\begin{cases} C_{HH}^* = C_{HH} \\ C_{MM}^* = C_{MM} - C_{HM}^2 / C_{HH} \end{cases} \tag{3.38}$$

where all coefficients were computed by summing up the values of the single macro-elements. Such set defines an equivalent diagonal damping matrix, which must be eccentric in order to be equivalent to the damping coefficients at the pile-head. The eccentricity, corresponding to the length of a rigid lever arm connecting the macro-element head to the two dampers, is computed as the following depth:

$$z_{damp} = -C_{HM} / C_{HH} \tag{3.39}$$

The "model specific parameters" (see final sub-section of Section 3.2.1.2) for the equivalent pile-head macro-element in SeismoStruct were set equal to those of the single pile-head macro-elements.

3.2.3 Properties of the equivalent pile macro-elements

Table 3.30, Table 3.31 and Table 3.32 report the retrieved properties of the equivalent pile-head macro-elements for the considered apartment index buildings, in terms of initial stiffness, foundation capacity and radiation damping equivalent dashpot coefficients. Although only one MDOF model was built, three different equivalent pile-head macro-elements were calibrated for the three apartment buildings considered, starting from the same MDOF model and varying the actual total weight of the building (which affects the moment capacity of the single piles).

Table 3.30: Properties of the equivalent macro-element for Drive-in index building.

k_V (kN/m)	k_H (kN/m)	k_M (kNm/rad)	k_{HM} (kN)
2.887E+07	1.287E+07	2.610E+06	-3.090E+06
H_{max} (kN)	M_{max} (kNm)		
2.391E+03	9.979E+05		
c_H (ton/s)	c_M (ton*m^2/s)	c_{HM} (ton*m/s)	
1.367E+04	8.522E+02	-2.665E+03	

Table 3.31: Properties of the equivalent macro-element for K-Flat index building.

k_V (kN/m)	k_H (kN/m)	k_M (kNm/rad)	k_{HM} (kN)
4.783E+07	2.053E+07	8.828E+06	-7.863E+06
H_{max} (kN)	M_{max} (kNm)		
5.396E+03	2.388E+06		
c_H (ton/s)	c_M (ton*m^2/s)	c_{HM} (ton*m/s)	
3.479E+04	5.518E+03	-1.082E+04	

Table 3.32: Properties of the equivalent macro-element for Georg van S index building.

k_V (kN/m)	k_H (kN/m)	k_M (kNm/rad)	k_{HM} (kN)
4.783E+07	2.053E+07	8.828E+06	-7.863E+06
H_{max} (kN)	M_{max} (kNm)		
5.160E+03	2.826E+06		
c_H (ton/s)	c_M (ton*m^2/s)	c_{HM} (ton*m/s)	
3.479E+04	5.518E+03	-1.082E+04	

4 Linear substructure approach

In this work, SSI was also analysed by the linear substructure approach, which allows splitting kinematic and inertial interaction in different sub-steps and considering their combined effects using the principle of superposition (Mylonakis et al., 2006).

Kinematic interaction causes a modification of the free-field motion due to the geometry and stiffness of the foundation, on which a different motion is applied, called Foundation Input Motion (FIM). In practical applications, structural engineers commonly neglect the effects of kinematic interaction (Dezi et al., 2010). Arup (2015a, 2015b) also determined kinematic interaction to be negligible in the response of the simplified models used for definition of fragility curves. As a consequence, the free-field motion was used as input motion for the nonlinear dynamic analyses in this study.

Inertial interaction includes the dynamic response of the coupled soil-foundation-structure system due to the input motion and is characterised predominantly by a shift of structural frequencies to lower soil-structure frequencies, due to soil compliance, and by an increase of damping, due to radiation damping. Within the coupled system, the soil is replaced by a lumped parameter model (including a set of springs and dashpots, as well as masses in some cases) at the foundation level, representing the foundation dynamic impedance. The latter is a complex-valued frequency function, whose real and imaginary parts depend on the stiffness and on the energy dissipation properties of the soil substratum, respectively.

Two different models following the substructure approach were implemented in SeismoStruct for derivation of fragility functions, namely a one-dimensional frequency-independent model and a herein called Lumped-Parameter Model (LPM) accounting for frequency-dependence of the impedance functions. These models, described in Sections 4.4 and 4.5, require the definition of the impedance functions of the equivalent foundations of the buildings (see Sections 4.2 and 4.3). Impedance functions were evaluated only for soil Type A (see Section 1) using the software DYNA6.1 (GRC, 2015) for both shallow and pile foundations, as briefly outlined in Section 4.1.

4.1 Overview of the software code for calculation of impedance functions

DYNA6.1 computes the frequency-dependent stiffness and damping constants of either surface foundations, embedded foundations or piles, as well as pile interaction in a pile group and other features. The program returns the response of rigid foundations to different types of dynamic loads; for rigid footings, all six degrees of freedom are considered as coupled.

The computation of impedance functions for shallow footings is evaluated using simplified approaches, which consider three categories of idealized soil profiles (Figure 4.1):

a) half-space;
b) uniform stratum on rigid base;
c) layer on top of a half-space (composite medium).

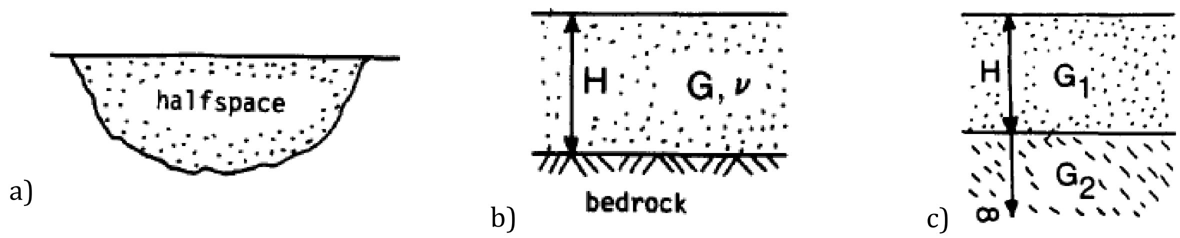

Figure 4.1: Soil profiles: a) half-space; b) uniform stratum on rigid base; c) layer on top of a half-space (from DYNA6.1 User's manual).

Moreover, for a composite medium the soil profile can be either uniform or non-uniform in accordance with the schematization shown in Figure 4.2. These models represent a wide spectrum of actually encountered soil profiles.

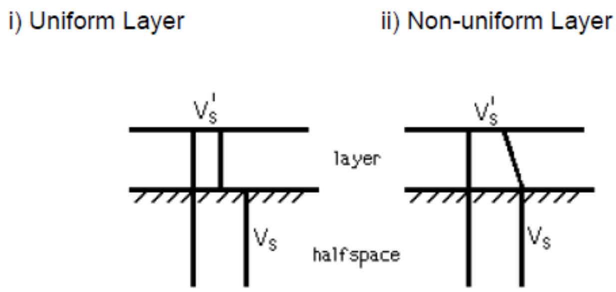

Figure 4.2: Soil velocity profile for composite medium (from DYNA6.1 User's manual)

For pile foundations it is possible to consider a layered medium, for each layer the following input parameters being required: thickness, shear wave velocity, soil unit weight, Poisson's ratio, damping ratio.

4.1.1 Software constraints

The software includes some limitations that shall be taken into account for definition of the input parameters. For composite medium, the impedance functions are exact for the ratio of layer thickness to half-width of the square footing (H/a) equal to 0.5, 1, 2, 3 and 4 for uniform layers and equal to 2, 3, 4, 5 and 10 for non-uniform layers. If the ratio (H/a) doesn't coincide with one of the above values the program chooses the closest (H/a) ratio available, interpolation is not implemented because of the strong non-monotonic variations at high frequencies.

In the composite-medium option, accurate values of stiffness and damping are used at frequencies equal to 0.10, 0.25, 0.50..., 4.75 and 5.0 times ($V_{s,in}$/a) where $V_{s,in}$ is the shear wave velocity at footing base level (see Figure 4.3) and "a" is half width of the square base (or the equivalent square base). For a frequency less than 0.10 $V_{s,in}$/a, the program uses the minimum value (0.10 $V_{s,in}$/a) and for frequencies in the range (0.10÷5.0) $V_{s,in}$/a, a linear interpolation is implemented. If the frequency is greater than 5 ($V_{s,in}$/a) the program uses the maximum value of 5 ($V_{s,in}$/a).

For composite medium, Poisson's ratio of the half-space is assumed equal to 0.33. Material damping of soil is assumed 0.03 and 0.05 for the layer and the half-space, respectively. Two values for Poisson's ratio of the layer are available 0.33 and 0.45. If a different value is entered the program sets it to the closest one (interpolation is not implemented in the program because of non-monotonic variations). Three values of the ratio between the shear wave velocity at footing base and at half-space are available 0.8, 0.6, and 0.3 (see Figure 4.3), if a different value is entered the program sets it to the closest one. The ratio of unit weight of the half-space to that of the layer is assumed 1.13.

Finally, for rectangular shallow foundations the code provides equal values of horizontal dynamic stiffness in x and y direction.

4.2 Impedance functions for shallow foundations

The foundations of the buildings considered consist of a grid of continuous beams oriented in two orthogonal directions. Conversely, the structural model used for definition of the fragility curves is a SDOF system in which the contact with the soil is limited to a single point. The geometry of grid foundations does not allow a simple and unique definition of equivalent dimensions for impedance function calculation. In fact, the latter depends on the degree of freedom analysed (e.g. translational or rotational) or on the component under consideration (i.e. stiffness or damping), and consequently the characteristics of the real foundation to be preserved are different (contact area, inertia, etc.). For such reason, in order to properly consider the real foundation geometry, the definition of the equivalent footing dimensions for impedance calculation made use of the calibration step carried out for the macro-element (see Section 3.1.2), which employs a 3D MDOF model of the buildings. For each building, equivalent dimensions were evaluated independently for stiffness and damping, as well as for the translational and rotational degrees of freedom, in order to reproduce the static stiffness and damping evaluated for the equivalent macro-element of the SDOF system described in Section 3.1.2.

Five index building were considered for impedance functions calculation, one terraced building with 4 units (Zijlvest), and four detached buildings (Kwelder, Badweg, Dijkstraat and De Haver).

4.2.1 Soil model

The soil model selected for the computation of the impedance functions of shallow foundations is the composite medium (i.e. soil layer with defined thickness on top of a half-space). Because the reference shear wave velocity profile has an increment that is rather linear in the upper part, the non-uniform soil profile is preferred to the uniform in order to avoid impedance functions dominated by the main frequency of the uniform soil. A composite medium with non-uniform shear wave velocity profile is characterized by a linear shear wave velocity profile in the layer and constant value on the half space; particularly, there are a set of fixed ratios between the initial shear wave velocities of the layer and half-space (see Section 4.1.1 and Figure 4.3). The model allows considering also a different shear wave velocity for the embedment; however, this is neglected due to its limited thickness.

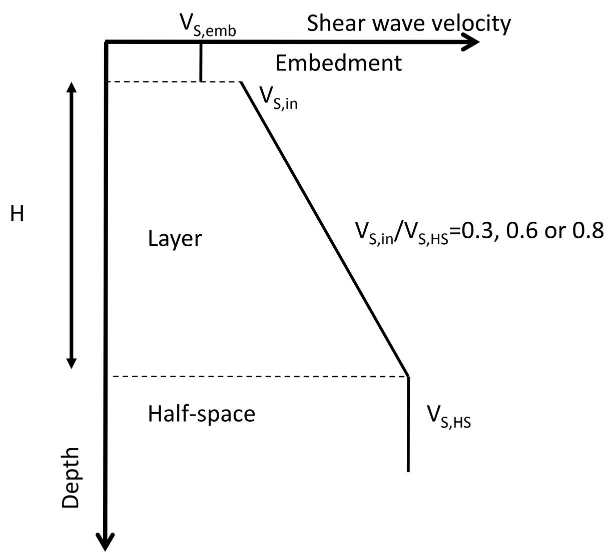

Figure 4.3: Shear wave velocity profile input parameters for composite medium.

The layer properties (e.g. thickness, shear wave velocity) were defined taking into account the software limitations (see section 4.1.1), which considers fixed values of the ratio of layer thickness (H) to the half-width of the equivalent square footing (a). Moreover, the fitting of the shear wave velocity profile was carried out for a ratio between the shear wave velocity at the base of the footing ($V_{s,in}$) and at the half-space ($V_{s,HS}$) equal to 0.6. Given the different equivalent dimensions considered for stiffness and damping, as well as for different degrees of freedom, the V_S profile fitting needs to be repeated for each of the four cases accounted for. The resulting parameters of the fitting procedure are summarized in the following sections.

The impedance functions depend on the shear modulus G; in order to account for its non-linearity, a reasonable approximation of the impedance functions may be obtained from the available linear viscoelastic solutions, provided that the "effective" values of G (i.e. the secant modulus estimated based on the strain level reached during strong motion) is used (Mylonakis et al., 2006).

Based on the results of site response analysis (Rodriguez-Marek et al., 2017, Kruiver et al., 2017a) a procedure was developed to obtain the V_S scaling factor versus PGA. For different levels of strong motion considered, associated to the related PGA values, the shear strain level is evaluated below the foundation depth. In particular, for soil Type A there are 5 m of fine sand, which is subdivided into two sublayers, characterized by different degradation curves of the shear modulus. Considering 1 m in sublayer 1 and 2 m in sublayer 2, the average shear strain is evaluated for different levels of PGA. For each of these values of shear strain the G/G_{max} is estimated, with Figure 4.4 showing the obtained values.

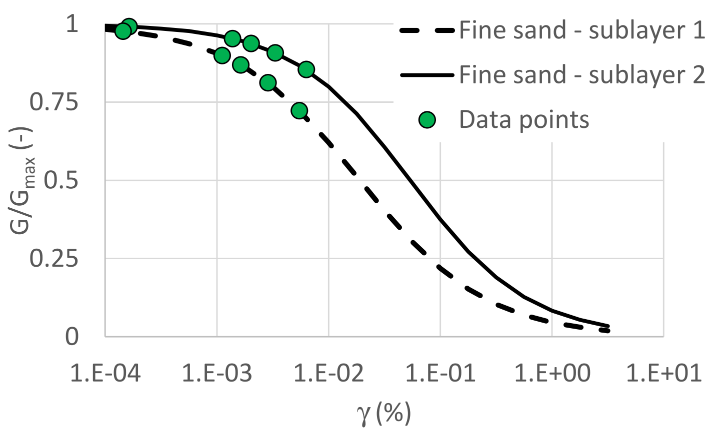

Figure 4.4 G/G_{max} scaling factors obtained from site response analysis for different levels of shear strain in the fine sand layer of soil type A characterised by two shear modulus degradation curves (Raw results from site response analyses provided by Deltares, 2019).

The G/G_{max} scaling factors are converted into V_S scaling factors considering the relationship:

$$G_{max} = \rho \cdot V_S^2 \tag{4.1}$$

For each of the two sublayers, the V_S scaling factors were interpolated using an exponential relationship, as shown in Figure 4.5.

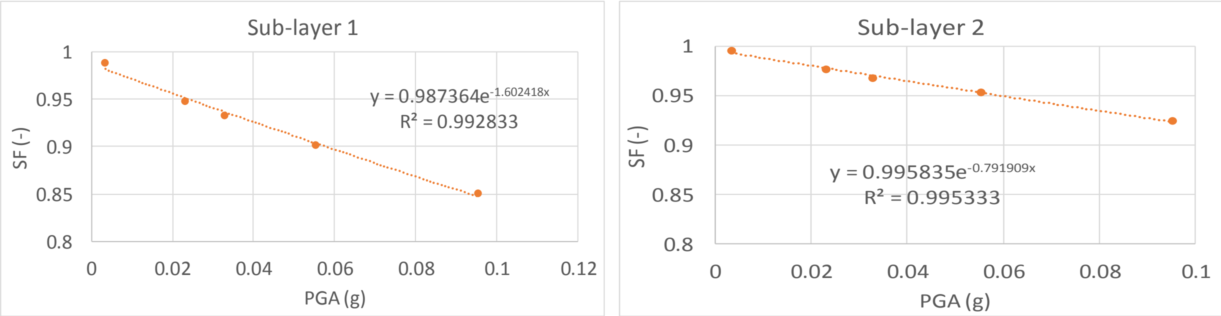

Figure 4.5 Relationship between PGA and V_S scaling factors for soil type A: a) Sublayer 1; b) Sublayer 2.

Five PGA levels ranging from 0.05 g to 0.43 g were considered in the derivation of impedance functions. For these PGA values, the exponential relationships shown in Figure 4.5 were used for the computation of the corresponding V_S scaling factors. Finally, the V_S profiles were scaled considering the mean V_S scaling factor of the two sublayers considered, with the resulting values summarized in Table 4.1.

Table 4.1: V_S scaling factors for soil type A obtained using the exponential relationship shown in Figure 4.5.

PGA (g)	Sub-layer 1	Sub-layer 2	mean SF
0.05	0.911	0.957	**0.934**
0.14	0.789	0.891	**0.840**
0.22	0.694	0.837	**0.765**
0.29	0.620	0.791	**0.706**
0.43	0.496	0.708	**0.602**

4.2.2 Procedure for impedance functions calculation

As described above, the foundations of the buildings considered consist of a grid of continuous beams oriented in two orthogonal directions. With reference to the equivalent SDOF used for fragility analysis, the geometry of the grid foundations does not allow a simple and unique definition of equivalent dimensions for impedance function calculation. In order to properly consider the real foundation geometry, the definition of the equivalent footing dimensions for impedance calculation made use of the calibration step carried out for the macro-element (see Sections 3.1.2 and 3.2.2), which employs a 3D MDOF model of the buildings. For each building, equivalent dimensions were evaluated independently for stiffness and damping, as well as for the translational and rotational degrees of freedom, in order to reproduce the static stiffness and damping evaluated for the equivalent macro-element of the SDOF system described in Sections 3.1.2 and 3.2.2.

Impedance functions are evaluated for rigid and massless foundations and considering a Poisson's ratio equal to 0.45 due to the high-water table level. Considering the limited embedment of the footings, the coupling swaying-rocking term is neglected. The software DYNA 6.1, for the composite medium (i.e. layer over half-space), considers fixed values of material damping, equal to 0.03 for the upper layer and 0.05 for the half-space.

The impedance of a foundation, representing its force-displacement or moment-rotation ratio, is a complex number typically represented in the form:

$$K^* = K + i\omega C \tag{4.2}$$

in which both K and C are, in general, functions of frequency. The spring constant K, termed dynamic stiffness, reflects the stiffness and inertia of the supporting soil; its dependence on frequency relates solely to the influence that frequency exerts on inertia, since soil material properties are to a good approximation frequency-independent. The dashpot coefficient C reflects the two types of damping (radiation and material) generated in the system; the former due to energy carried by the waves spreading away from the foundation, and the latter due to energy dissipated in the soil through hysteretic action (Mylonakis et al, 2006).

The effect of material damping is approximately (this approximation is accurate at low dimensionless frequency) taken into account by multiplying the complex stiffness evaluated from a solution derived without consideration of material damping by the factor (1+i2β), where β represents the material damping coefficient:

$$K^* = (k + i\omega c)(1 + i2\beta) = k - 2\beta c + i\omega\left(c + \frac{2\beta k}{\omega}\right) \tag{4.3}$$

from which it is possible to separate the real and imaginary part of the impedance function:

$$K = k - 2\beta c \tag{4.4}$$

$$C = c + \frac{2\beta k}{\omega} \tag{4.5}$$

Where k is the static stiffness, c is the constant of equivalent viscous damping and ω is the circular frequency.

Eq. (4.5) allows to separate the contribution of material and radiation damping, and is used for the definition of the equivalent dimension of the foundation, because the damping defined for the macro-element included only the radiation damping contribution.

For the reasons explained above, the computation of the impedance functions is performed independently for stiffness and damping, as well as for horizontal translation and rocking, resulting in four independent calculations.

An iterative procedure was developed to fit the impedance evaluated for the macro-element and obtained through the calibration using the MDOF model of the buildings; such model considers the real geometry of the foundation beams.

For each of the four cases considered, the first step was the definition of equivalent dimensions of the footing considering a closed-form solution for half-space, in order to reproduce the impedance used for the macro-element.

For the stiffness terms (horizontal translation and rocking) the formulas proposed by Gazetas (1991) for rectangular foundations were used (see above); conversely, for damping terms a closed-form solution for circular footings was adopted, particularly for the horizontal translation component the Veletsos and Verbic (1973) solution, whereas for the rotational component the Veletsos and Wei (1971) solution. The fragility study analysed the response in one direction only, therefore the use of a circular foundation shape does not affect the results.

As already mentioned, the impedance functions calculated by DYNA6.1 for composite medium are exact for fixed values of the ratio of layer thickness (H) to half-width of the square footing (a) (see Figure 4.3). Based on the preliminary equivalent dimensions estimated using closed-form solutions, the V_s profile is fitted considering the available H/a and $V_{S,in}/V_{S,HS}$ ratios. Based on the input parameters described above, the impedance functions were evaluated using DYNA6.1 considering the composite medium, with the obtained values being compared with the set obtained for the macro-element. Afterwards, an iteration is performed in the calculation, scaling the footing dimensions by the ratio between the impedance evaluated by the closed-form solution and DYNA6.1 (although some differences may arise due to the different soil models considered). With respect to damping, the radiational contribution was separated from DYNA6.1 results making use of Eq. (4.5). In accordance with section 2, a frequency of 1.667Hz was considered. It is worth to notice that this frequency value does not affect too much the evaluation of damping.

The following sections, for each building considered, summarize the input parameters considered, as well as the resulting impedance functions.

4.2.3 Terraced house "Zijlvest"

The scheme of the foundations of this terraced index building with 4 units is shown in Figure 3.7. Impedance functions were evaluated in accordance with the procedure described in section 4.2.2. Table 4.2 summarizes the input parameters used for impedance calculations in DYNA6.1, with four cases being considered because stiffness and damping, as well as horizontal translation and rocking, are evaluated independently. Figure 4.6 shows, for a scaling factor equal to 1, the fitting of the V_s profile obtained considering the limitations of the software DYNA6.1, which considers fixed values of the ratios H/a and $V_{S,in}/V_{S,HS}$ (with the meaning of the symbols described in section 4.2.1).

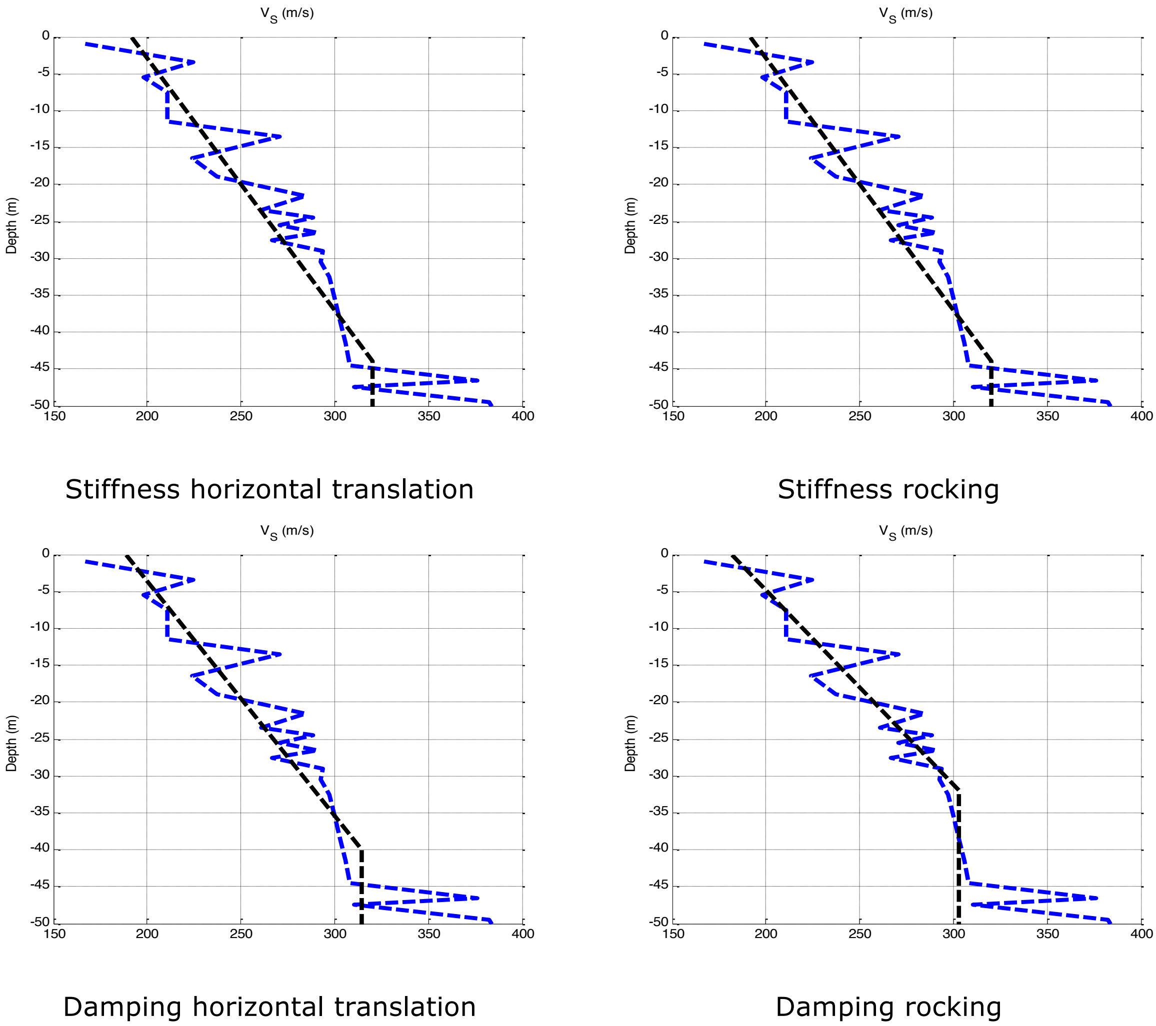

Figure 4.6 Terraced house "Zijlvest": Fitting of the shear wave velocity profile type A using the composite medium (i.e. layer over half-space) depending on the degree of freedom considered (i.e. horizontal translation or rocking) and component (i.e. stiffness and damping) for a scaling factor equal to 1 (SF0).

Table 4.2: Terraced house "Zijlvest" - input parameters for DYNA6.1 considering soil type A: soil model and equivalent footing dimensions for different scaling factors.

Terraced 4 unit - Zijlvest			Stiffness horizontal				Stiffness Rocking				Damping horizontal			Damping rocking		
Soil model: Composite medium with linear velocity			L_x (m)	L_y (m)	Eq. Dim. (m)	H_{layer} (m)	L_x (m)	L_y (m)	Eq. Dim. (m)	H_{layer} (m)	R (m)	Eq. Dim. (m)	H_{layer} (m)	R (m)	Eq. Dim. (m)	H_{layer} (m)
ν =0.45	$V_{S,in}$ /$V_{S,HS}$=0.6	γ=18.4 kN/m^3	77.9	25.3	22.1	44	30.8	10.0	8.8	44	9.1	8.1	40	3.6	3.2	32
PGA (g)	Scaling factor (-)		$V_{S,in}$ (m/s)				$V_{S,in}$ (m/s)				$V_{S,in}$ (m/s)			$V_{S,in}$ (m/s)		
0	SF0	1	192				192				188.7			181.9		
0.05	SF1	0.934	179.3				179.3				176.3			169.9		
0.14	SF2	0.840	161.3				161.3				158.5			152.8		
0.22	SF3	0.765	146.9				146.9				144.4			139.2		
0.29	SF4	0.706	135.5				135.5				133.3			128.4		
0.43	SF5	0.602	115.6				115.6				113.6			109.5		

The following figures show the impedance functions (in terms of frequency-dependent stiffness and damping) of horizontal translation and rocking considering the soil profile type A, taking into account the five scaling factors summarized in Table 4.1.

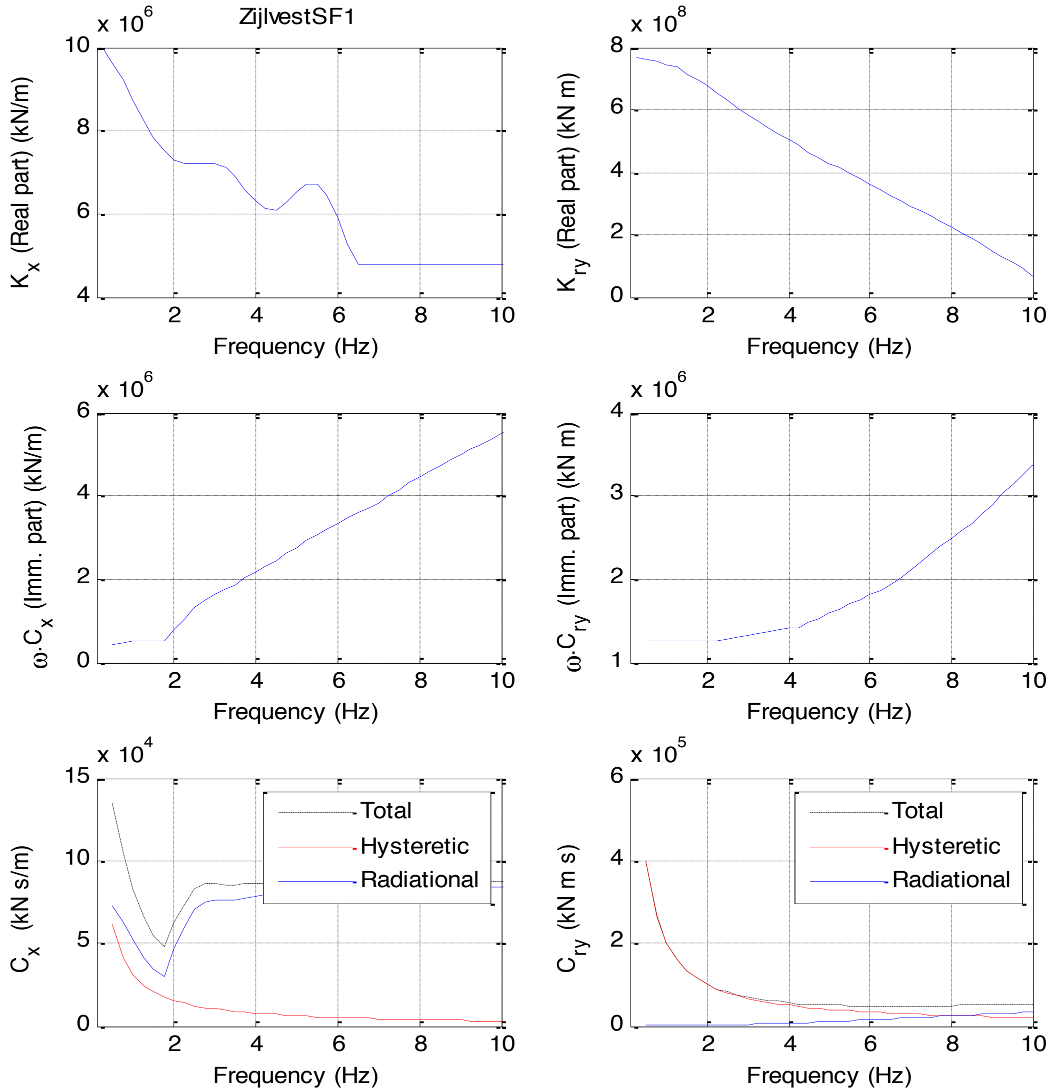

Figure 4.7 Impedance functions for Terraced house "Zijlvest": horizontal translation and rocking – Soil type A, Scaling factor SF1.

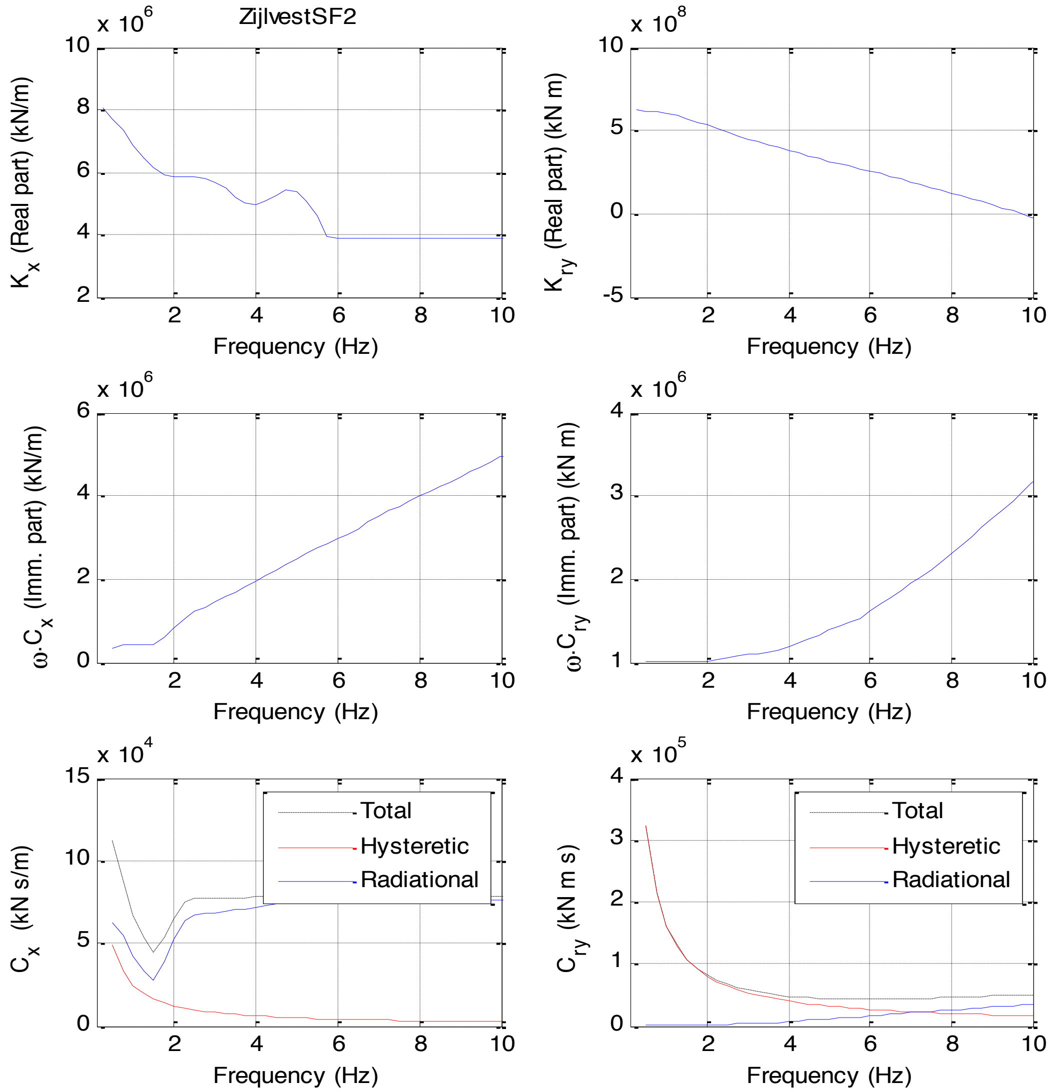

Figure 4.8 Impedance functions for Terraced house "Zijlvest": horizontal translation and rocking – Soil type A, Scaling factor SF2.

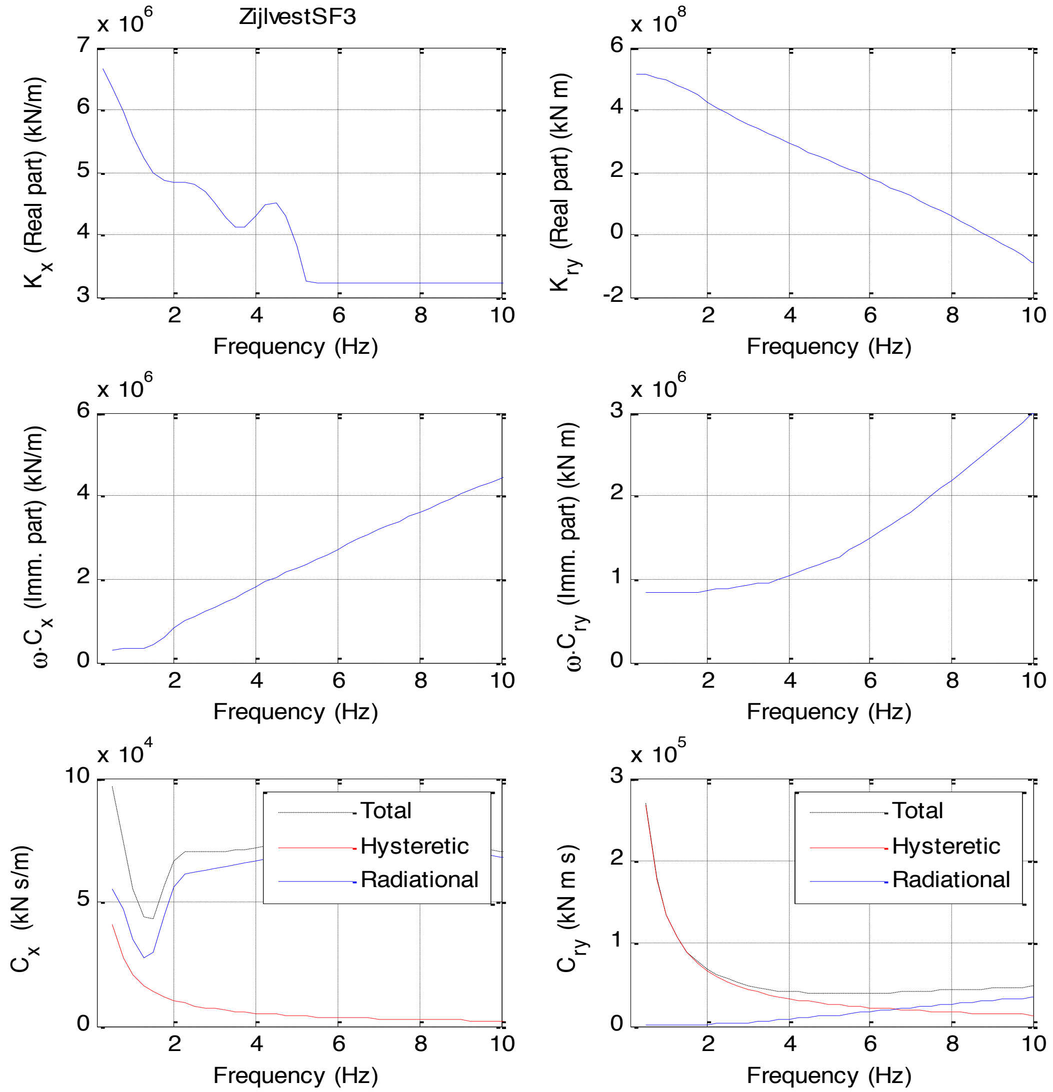

Figure 4.9 Impedance functions for Terraced house "Zijlvest": horizontal translation and rocking – Soil type A, Scaling factor SF3.

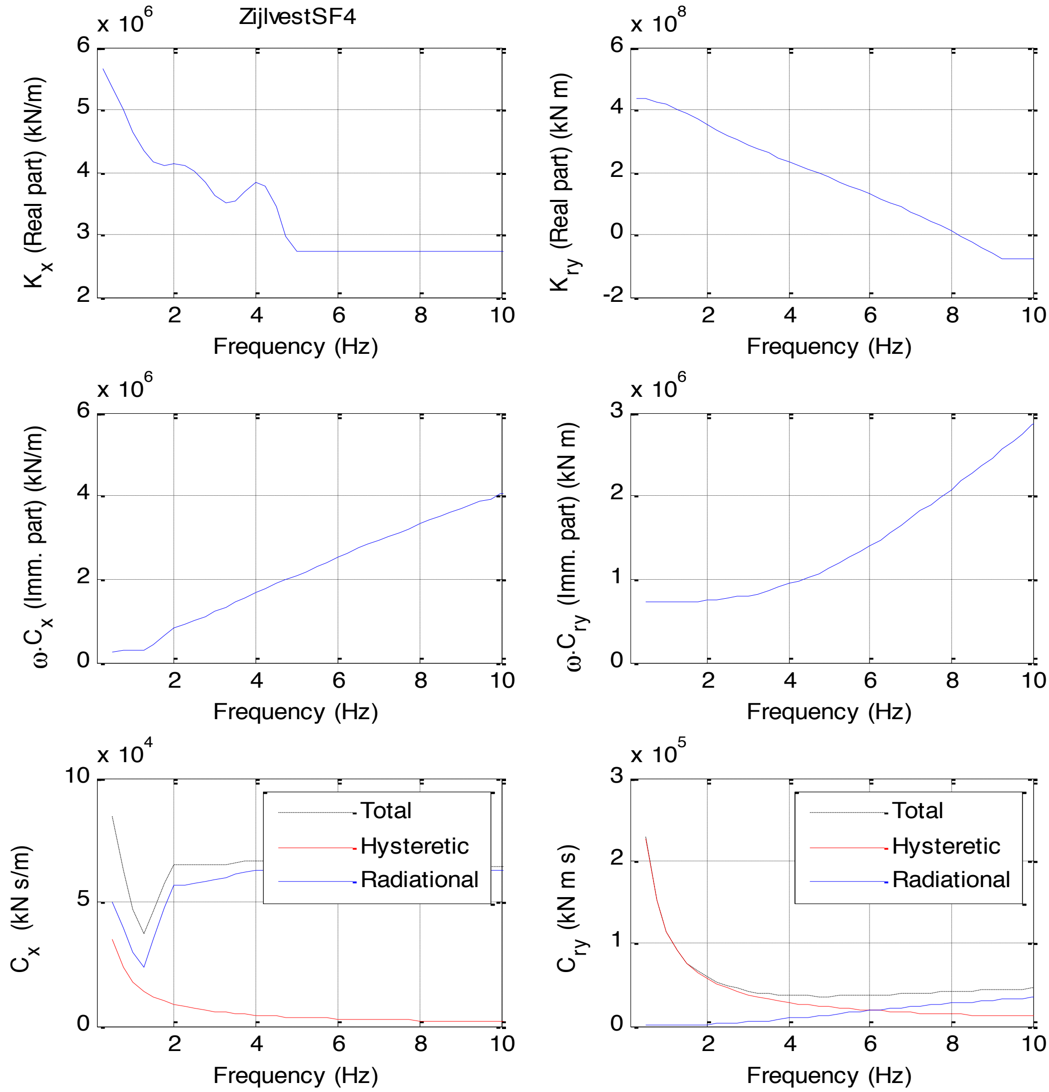

Figure 4.10 Impedance functions for Terraced house "Zijlvest": horizontal translation and rocking – Soil type A, Scaling factor SF4.

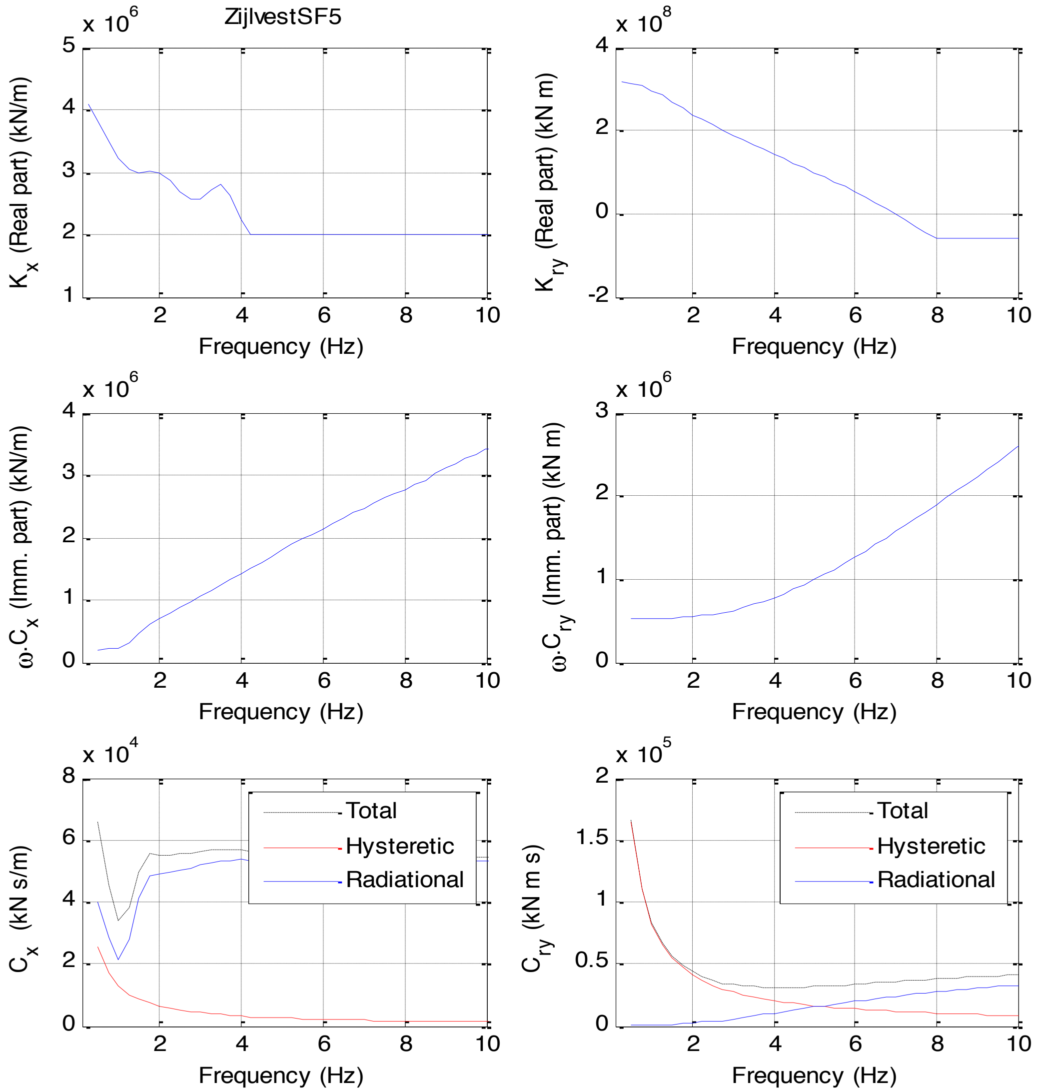

Figure 4.11 Impedance functions for Terraced house "Zijlvest": horizontal translation and rocking – Soil type A, Scaling factor SF5.

4.2.4 Detached house "Kwelder"

The scheme of the foundations of the detached "Kwelder" index building is shown in Figure 3.8. Impedance functions were evaluated in accordance with the procedure described in section 4.2.2. Table 4.3 summarizes the input parameters used for impedance calculations in DYNA6.1, with four cases being considered because stiffness and damping, as well as horizontal translation and rocking, are evaluated independently. Figure 4.12 shows, for a scaling factor equal to 1, the fitting of the V_s profile obtained considering the limitations of the software DYNA6.1, which considers fixed values of the ratios H/a and $V_{S,in}/V_{S,HS}$ (with the meaning of the symbols described in section 4.2.1).

Table 4.3: Detached house "Kwelder" - input parameters for DYNA6.1 considering soil type A: soil model and equivalent footing dimensions for different scaling factors.

Detached - Kwelder			Stiffness horizontal				Stiffness Rocking				Damping horizontal			Damping rocking		
Soil model: Composite medium with linear velocity			L_x (m)	L_y (m)	Eq. Dim. (m)	H_{layer} (m)	L_x (m)	L_y (m)	Eq. Dim. (m)	H_{layer} (m)	R (m)	Eq. Dim. (m)	H_{layer} (m)	R (m)	Eq. Dim. (m)	H_{layer} (m)
ν =0.45	$V_{S,in}$ /$V_{S,HS}$=0.6	γ=18.4 kN/m^3	27.0	18.5	11.2	45	14.8	10.2	6.1	30	4.7	4.2	42	3.1	2.8	28
PGA (g)	Scaling factor (-)		$V_{S,in}$ (m/s)				$V_{S,in}$ (m/s)				$V_{S,in}$ (m/s)			$V_{S,in}$ (m/s)		
0	SF0	1	193.5				180.8				190.8			177		
0.05	SF1	0.934	180.8				168.9				178.2			165.3		
0.14	SF2	0.840	162.6				151.9				160.3			148.7		
0.22	SF3	0.765	148.1				138.3				146			135.9		
0.29	SF4	0.706	136.6				127.7				134.7			125		
0.43	SF5	0.602	116.5				108.9				114.9			106.5		

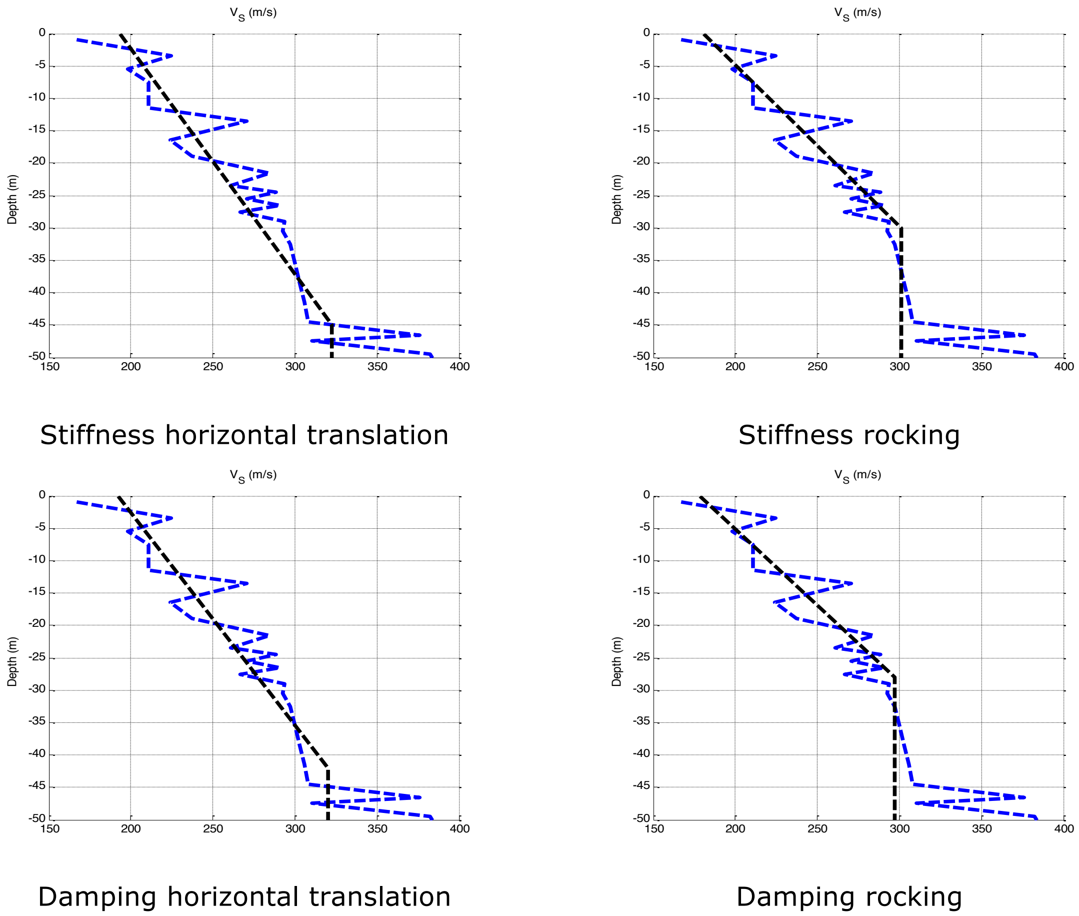

Figure 4.12 Detached house "Kwelder": Fitting of the shear wave velocity profile type A using the composite medium (i.e. layer over half-space) depending on the degree of freedom considered (i.e. horizontal translation or rocking) and component (i.e. stiffness and damping) for a scaling factor equal to 1.

The following figures show the impedance functions (in terms of frequency-dependent stiffness and damping) of horizontal translation and rocking considering the soil profile type A, taking into account the five scaling factors summarized in Table 4.1.

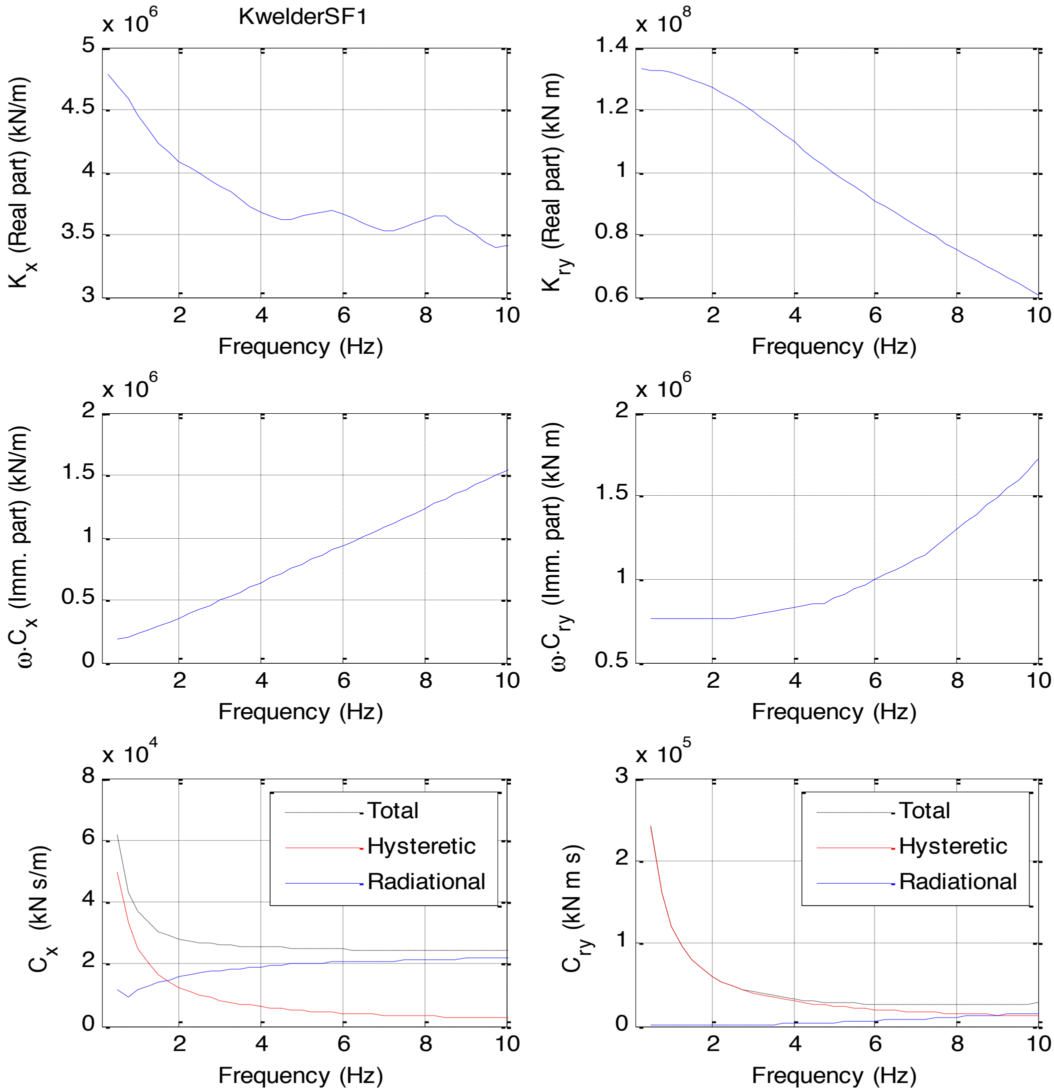

Figure 4.13 Impedance functions for Detached house "Kwelder": horizontal translation and rocking – Soil type A, Scaling factor SF1.

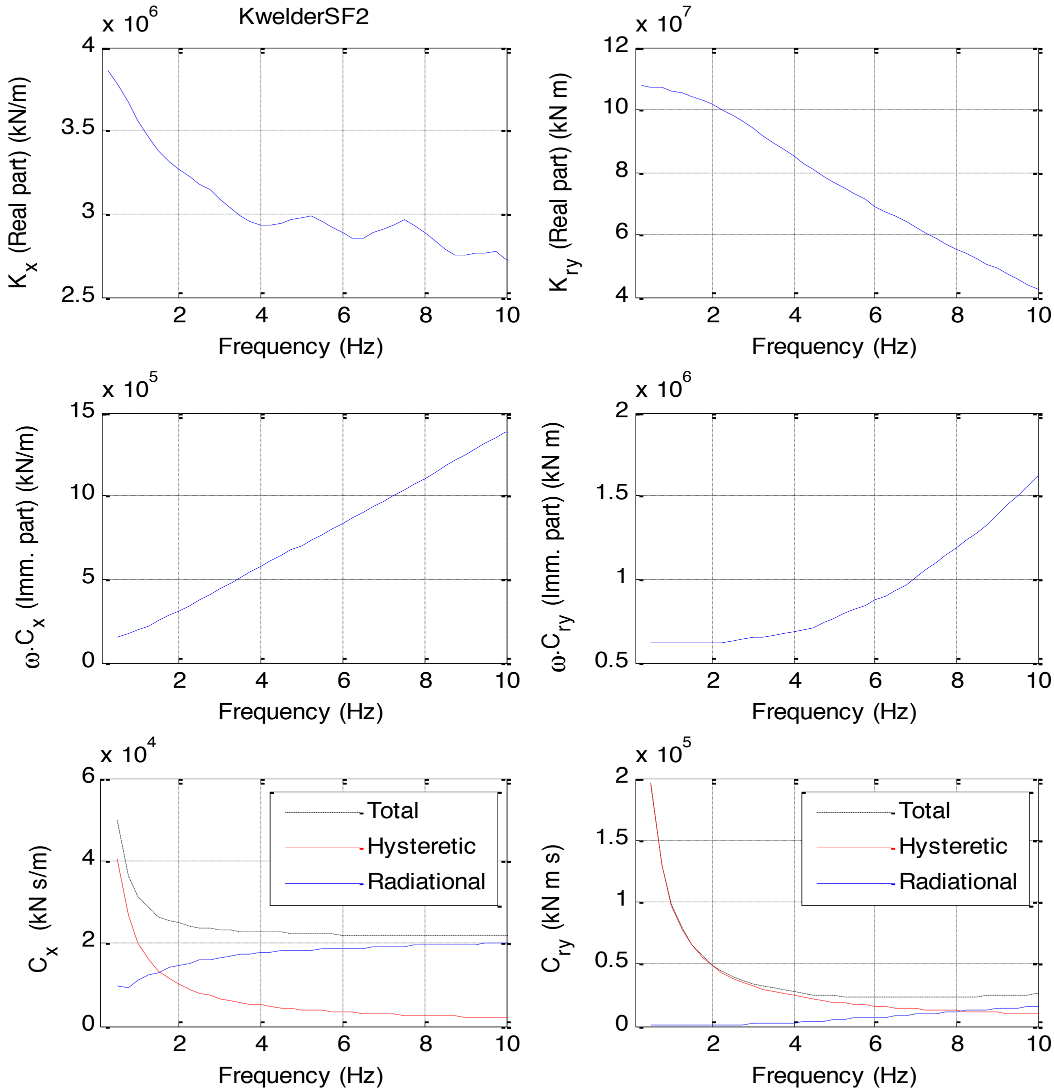

Figure 4.14 Impedance functions for Detached house "Kwelder": horizontal translation and rocking – Soil type A, Scaling factor SF2.

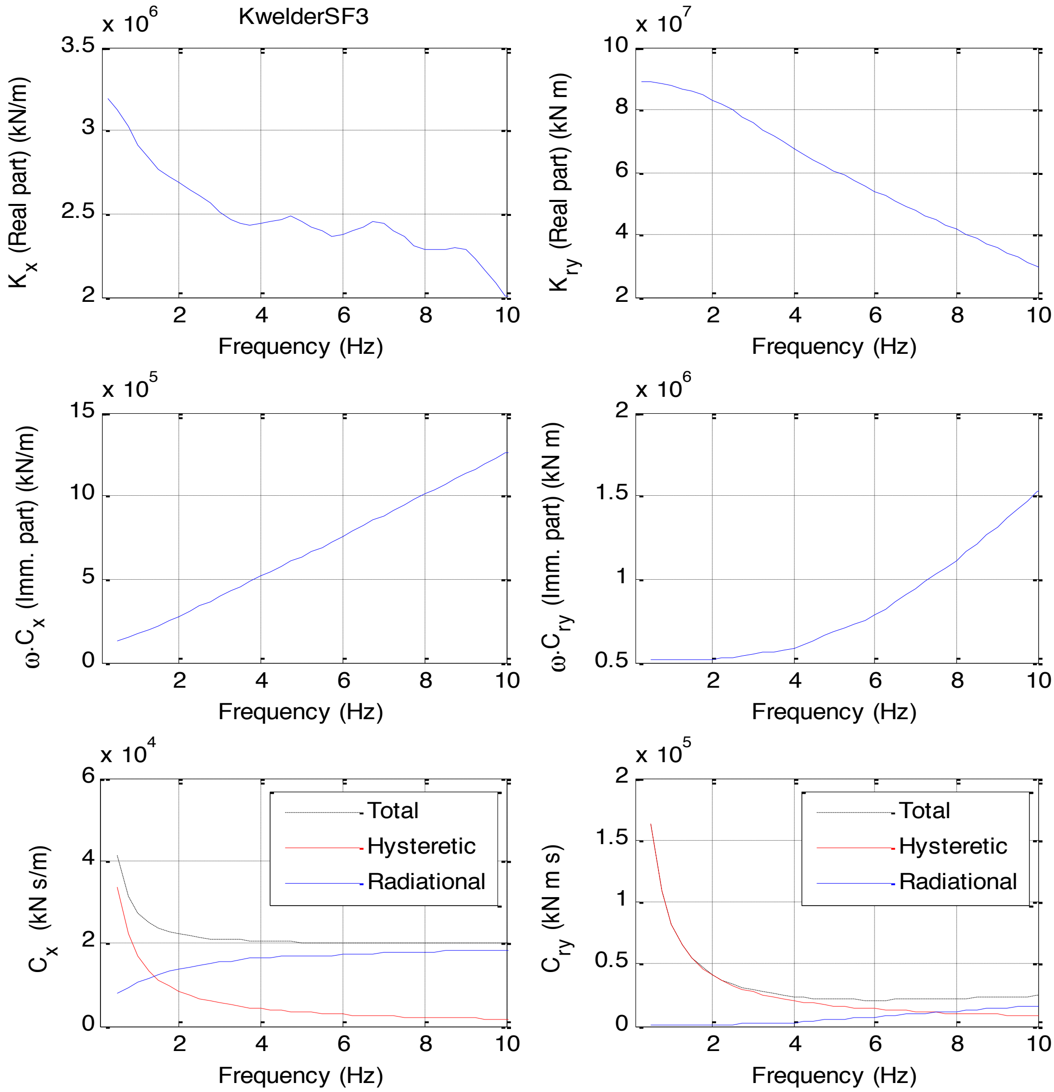

Figure 4.15 Impedance functions for Detached house "Kwelder": horizontal translation and rocking – Soil type A, Scaling factor SF3.

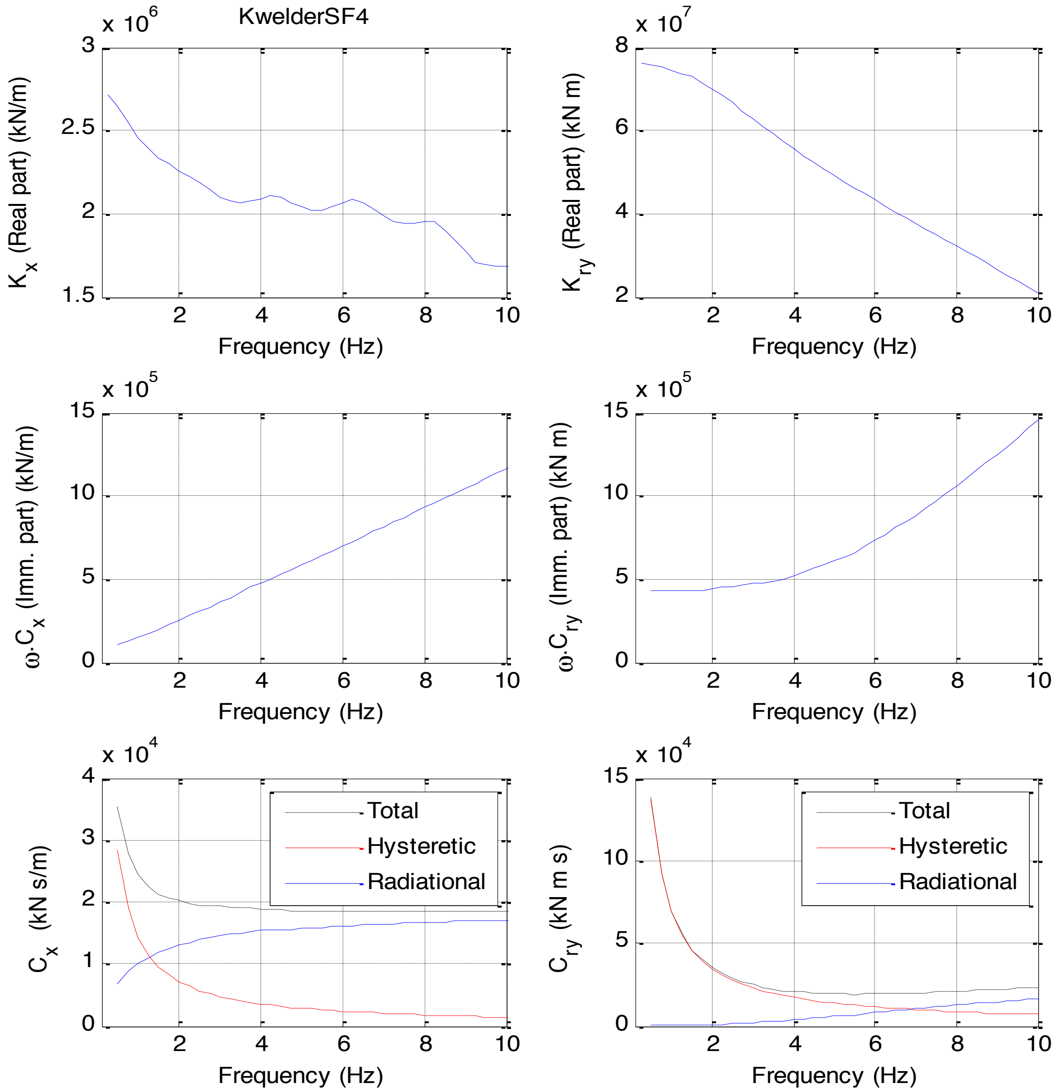

Figure 4.16 Impedance functions for Detached house "Kwelder": horizontal translation and rocking – Soil type A, Scaling factor SF4.

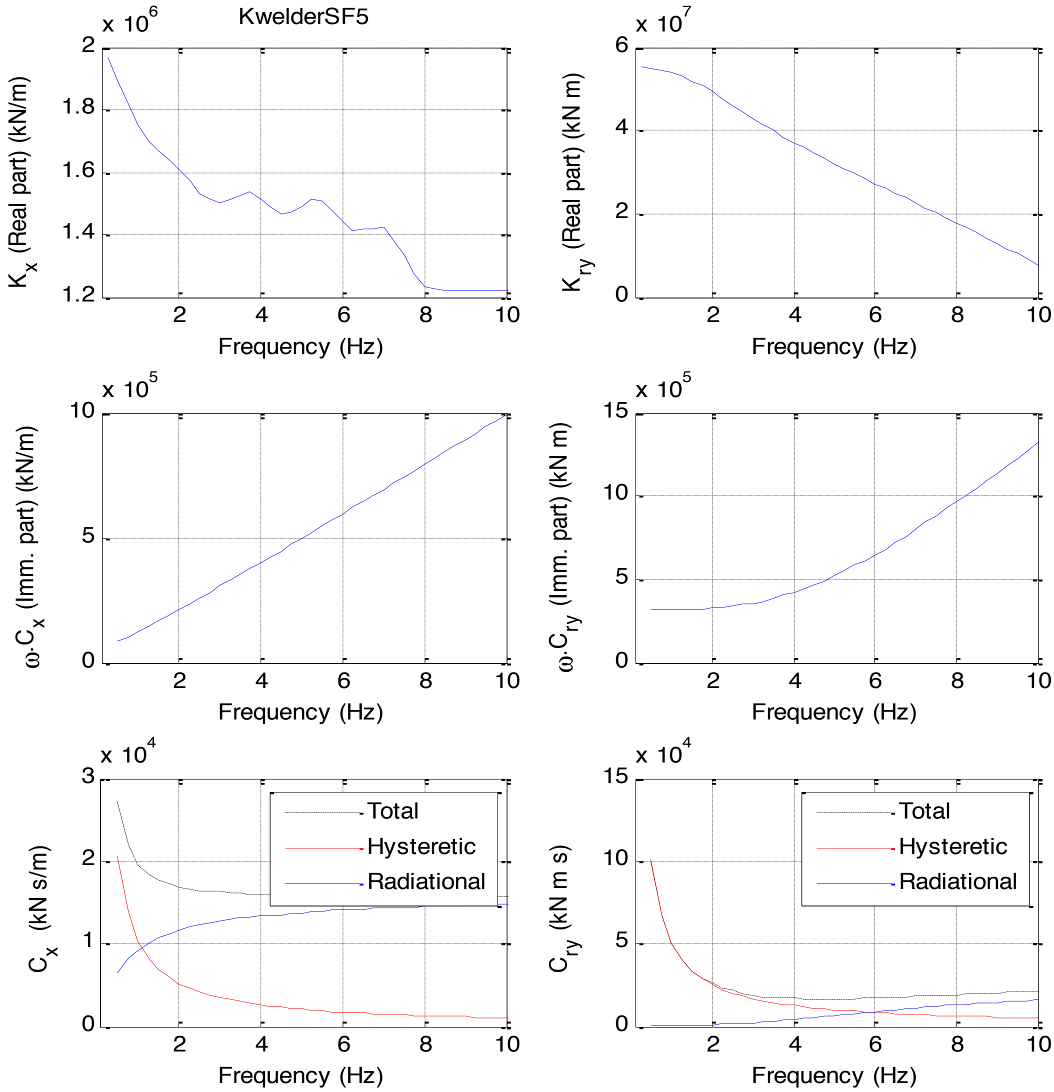

Figure 4.17 Impedance functions for Detached house "Kwelder": horizontal translation and rocking – Soil type A, Scaling factor SF5.

4.2.5 Detached house "Badweg"

The scheme of the foundations of the detached "Badweg" index building is shown in Figure 3.9. Impedance functions were evaluated in accordance with the procedure described in section 4.2.2. Table 4.4 summarizes the input parameters used for impedance calculations in DYNA6.1, with four cases being considered because stiffness and damping, as well as horizontal translation and rocking, are evaluated independently. Figure 4.18 shows, for a scaling factor equal to 1, the fitting of the V_s profile obtained considering the limitations of the software DYNA6.1, which considers fixed values of the ratios H/a and $V_{S,in}/V_{S,HS}$ (with the meaning of the symbols described in section 4.2.1).

Table 4.4: Detached house "Badweg" - input parameters for DYNA6.1 considering soil type A: soil model and equivalent footing dimensions for different scaling factors.

Detached - Badweg			Stiffness horizontal				Stiffness Rocking				Damping horizontal			Damping rocking		
Soil model: Composite medium with linear velocity			L_x (m)	L_y (m)	Eq. Dim. (m)	H_{layer} (m)	L_x (m)	L_y (m)	Eq. Dim. (m)	H_{layer} (m)	R (m)	Eq. Dim. (m)	H_{layer} (m)	R (m)	Eq. Dim. (m)	H_{layer} (m)
ν =0.45	$V_{S,in}$ /$V_{S,HS}$=0.6	γ=18.4 kN/m^3	21.9	10.8	7.7	39	14.4	7.1	5.1	25	3.7	3.3	33	3.1	2.7	27
PGA (g)	Scaling factor (-)		$V_{S,in}$ (m/s)				$V_{S,in}$ (m/s)				$V_{S,in}$ (m/s)			$V_{S,in}$ (m/s)		
0	SF0	1	188.1				175.2				182.9			177.1		
0.05	SF1	0.934	175.7				163.6				170.9			165.4		
0.14	SF2	0.840	158				147.1				153.6			148.8		
0.22	SF3	0.765	143.9				134				139.9			135.5		
0.29	SF4	0.706	132.8				123.7				129.1			125		
0.43	SF5	0.602	113.3				105.4				110.1			106.6		

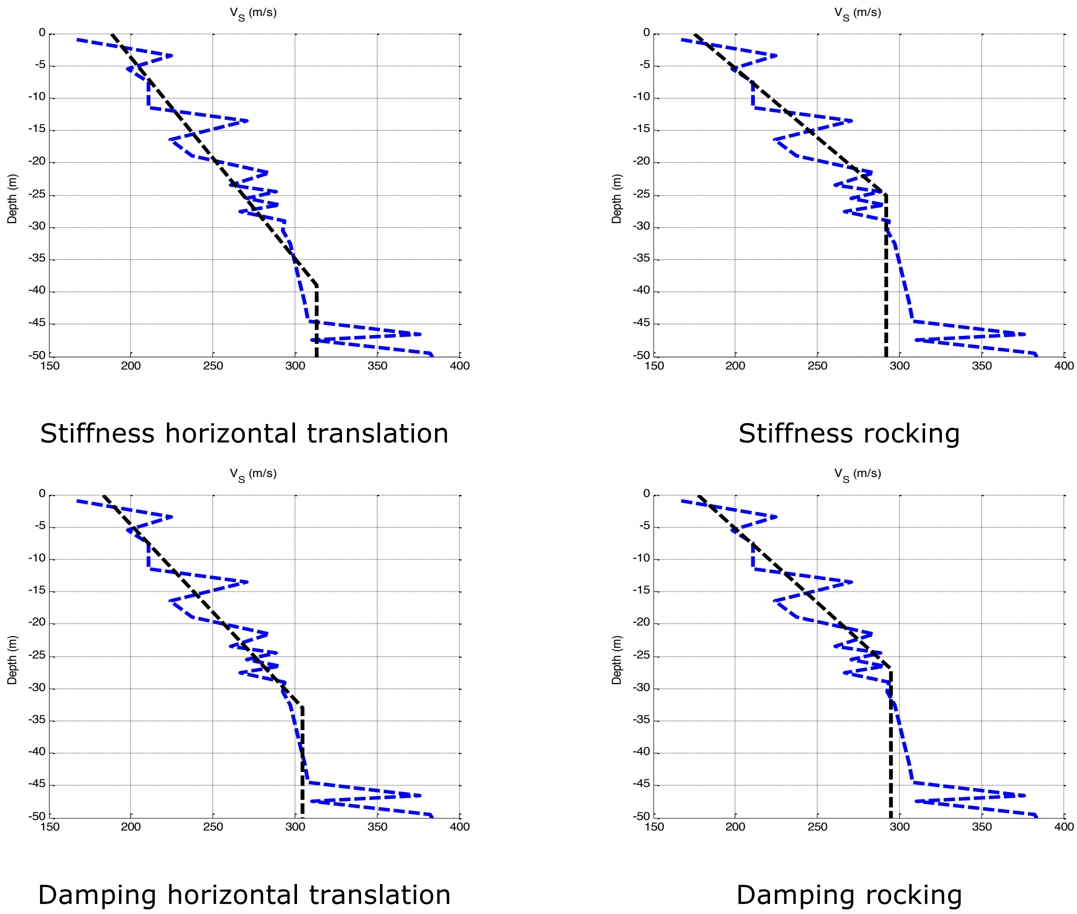

Figure 4.18 Detached house "Badweg": Fitting of the shear wave velocity profile type A using the composite medium (i.e. layer over half-space) depending on the degree of freedom considered (i.e. horizontal translation or rocking) and component (i.e. stiffness and damping) for a scaling factor equal to 1.

The following figures show the impedance functions (in terms of frequency-dependent stiffness and damping) of horizontal translation and rocking considering the soil profile type A, taking into account the five scaling factors summarized in Table 4.1.

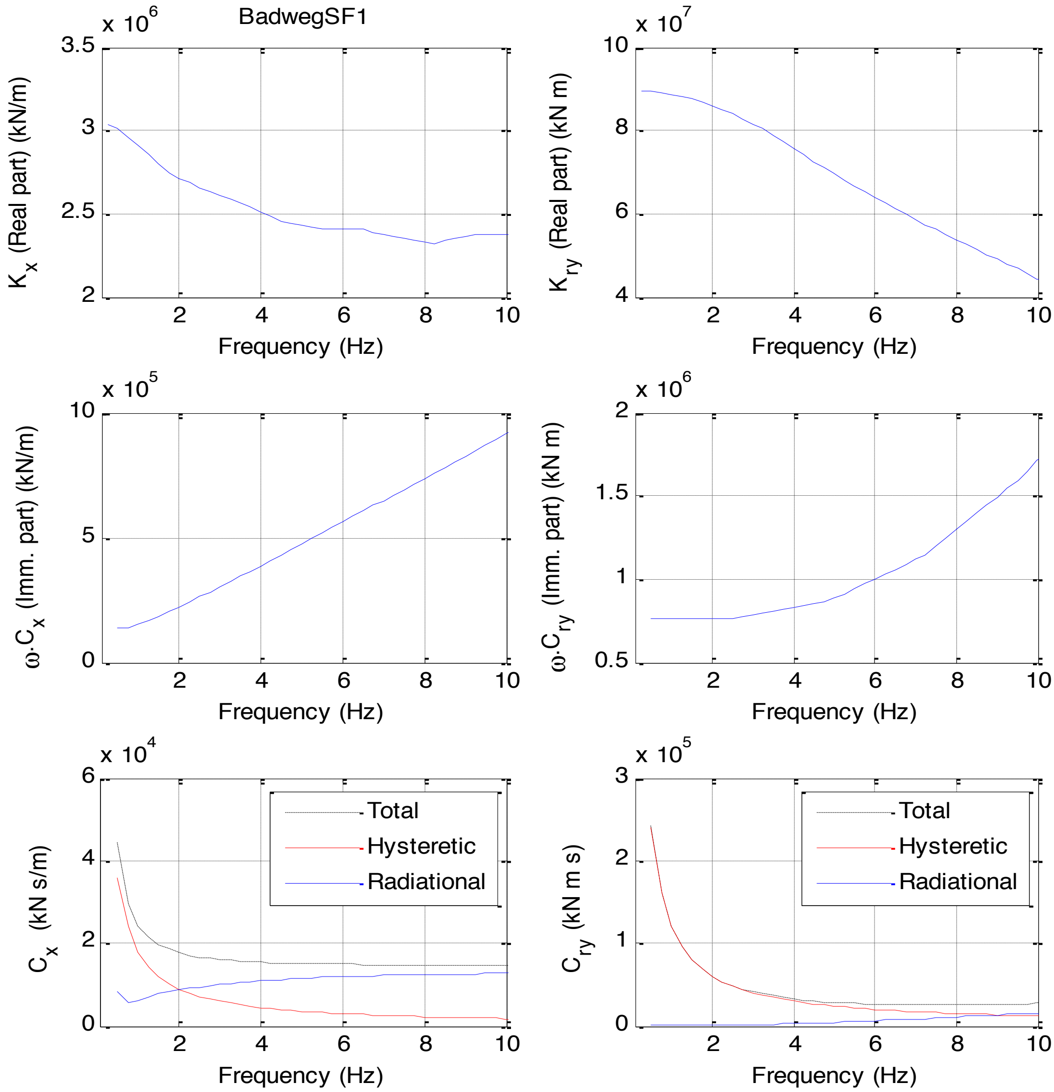

Figure 4.19 Impedance functions for Detached house "Badweg": horizontal translation and rocking – Soil type A, Scaling factor SF1.

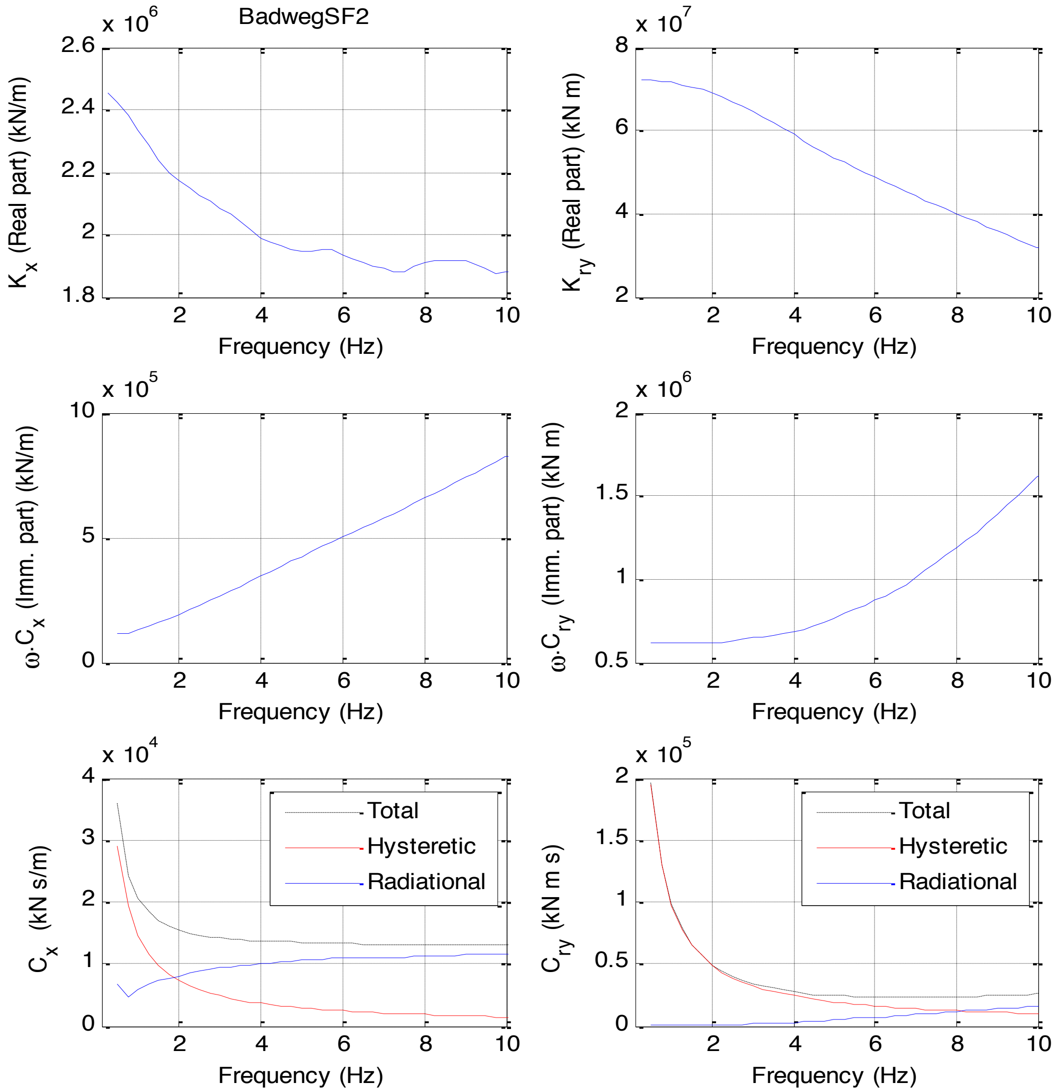

Figure 4.20 Impedance functions for Detached house "Badweg": horizontal translation and rocking – Soil type A, Scaling factor SF2.

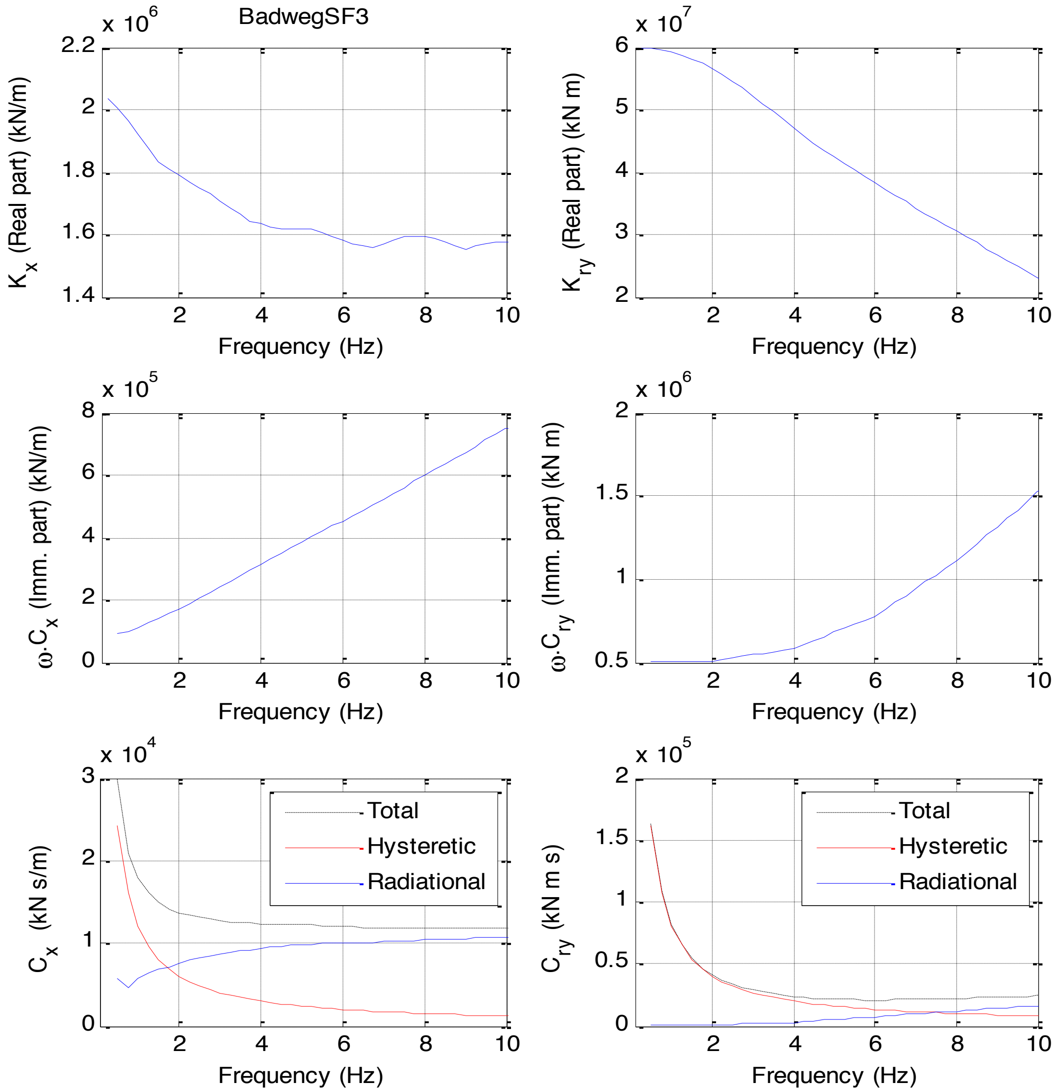

Figure 4.21 Impedance functions for Detached house "Badweg": horizontal translation and rocking – Soil type A, factor SF3.

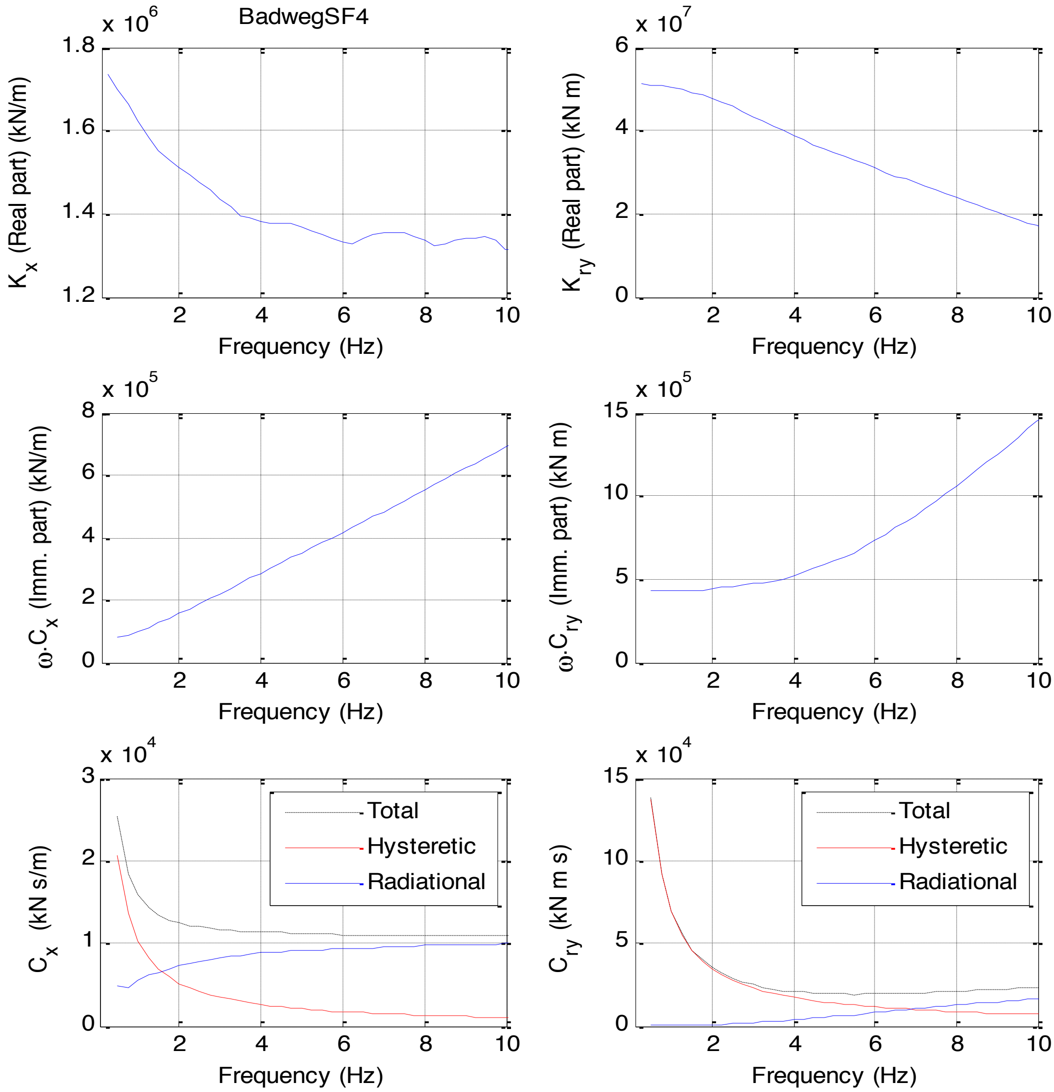

Figure 4.22 Impedance functions for Detached house "Badweg": horizontal translation and rocking – Soil type A, Scaling factor SF4.

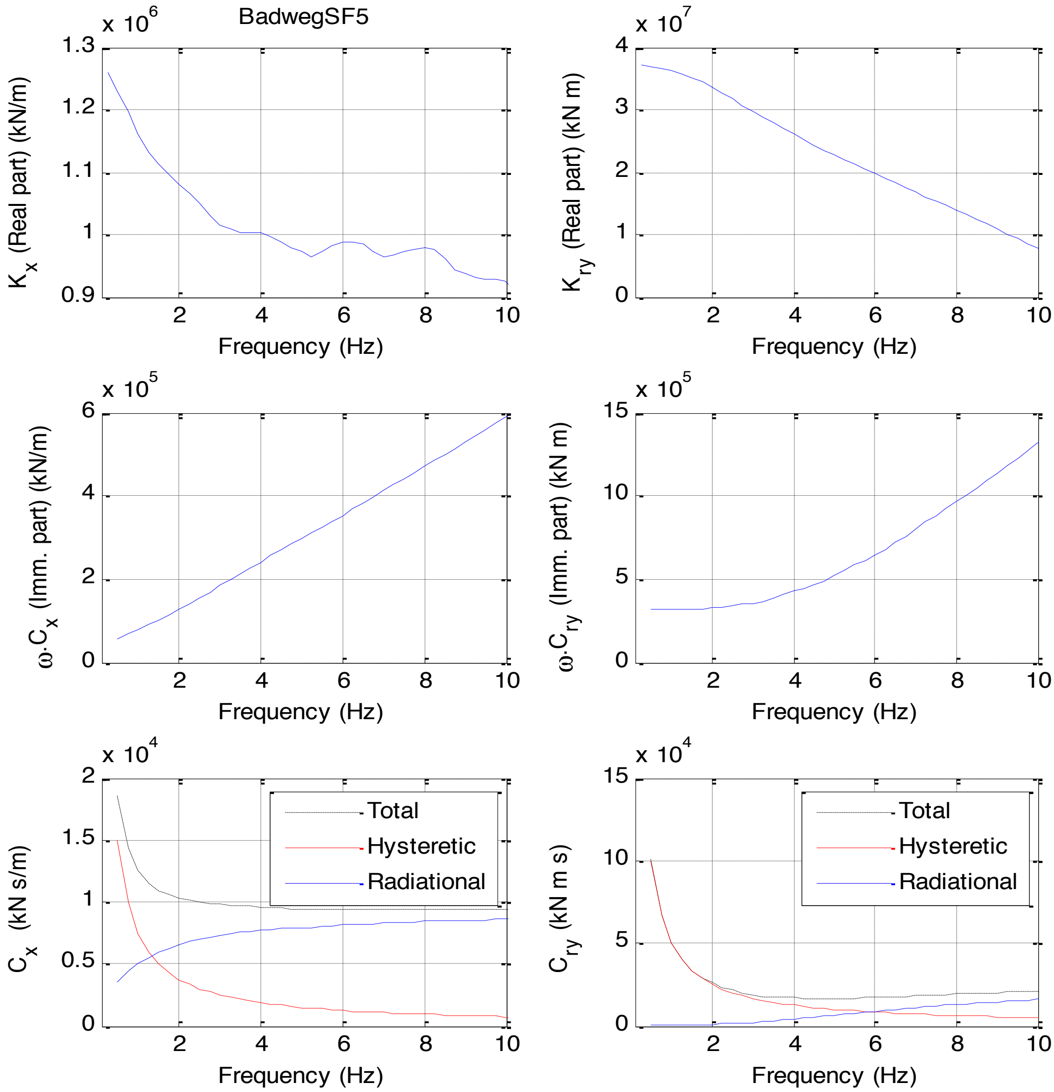

Figure 4.23 Impedance functions for Detached house "Badweg": horizontal translation and rocking – Soil type A, Scaling factor SF5.

4.2.6 Detached house "Dijkstraat"

The scheme of the foundations of the detached "Dijkstraat" index building is shown in Figure 3.10. Impedance functions were evaluated in accordance with the procedure described in section 4.2.2. Table 4.5 summarizes the input parameters used for impedance calculations in DYNA6.1, with four cases being considered because stiffness and damping, as well as horizontal translation and rocking, are evaluated independently. Figure 4.24 shows, for a scaling factor equal to 1, the fitting of the Vs profile obtained considering the limitations of the software DYNA6.1, which considers fixed values of the ratios H/a and $V_{S,in}/V_{S,HS}$ (with the meaning of the symbols described in section 4.2.1).

Table 4.5: Detached house "Dijkstraat" - input parameters for DYNA6.1 considering soil type A: soil model and equivalent footing dimensions for different scaling factors.

Detached - Dijkstraat			Stiffness horizontal				Stiffness Rocking				Damping horizontal			Damping rocking		
Soil model: Composite medium with linear velocity			L_x (m)	L_y (m)	Eq. Dim. (m)	H_{layer} (m)	L_x (m)	L_y (m)	Eq. Dim. (m)	H_{layer} (m)	R (m)	Eq. Dim. (m)	H_{layer} (m)	R (m)	Eq. Dim. (m)	H_{layer} (m)
ν =0.45	$V_{S,in}/V_{S,HS}$=0.6	γ=18.4 kN/m^3	16.3	27.6	10.6	42	12.2	20.7	7.7	39	5.3	4.7	47	5.0	4.5	45
PGA (g)	Scaling factor (-)		$V_{S,in}$ (m/s)				$V_{S,in}$ (m/s)				$V_{S,in}$ (m/s)			$V_{S,in}$ (m/s)		
0	SF0	1	190.8				188.1				195.4			193.5		
0.05	SF1	0.934	178.2				175.7				182.5			180.8		
0.14	SF2	0.840	160.3				158				164.1			162.6		
0.22	SF3	0.765	146				143.9				149.5			148.1		
0.29	SF4	0.706	134.7				132.8				137.9			136.6		
0.43	SF5	0.602	114.9				113.3				117.6			116.5		

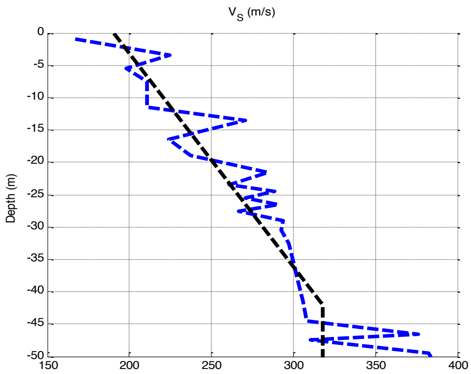

Stiffness horizontal translation

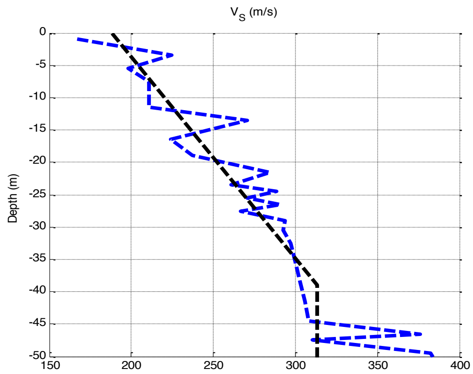

Stiffness rocking

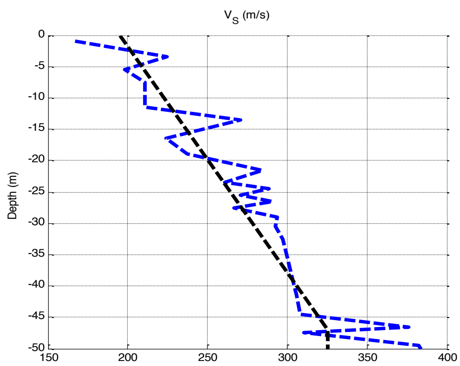

Damping horizontal translation

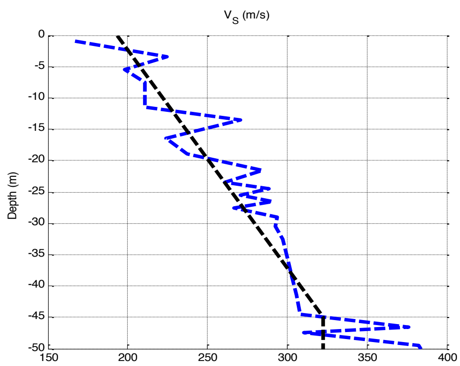

Damping rocking

Figure 4.24 Detached house "Dijkstraat": Fitting of the shear wave velocity profile type A using the composite medium (i.e. layer over half-space) depending on the degree of freedom considered (i.e. horizontal translation or rocking) and component (i.e. stiffness and damping) for a scaling factor equal to 1.

The following figures show the impedance functions (in terms of frequency-dependent stiffness and damping) of horizontal translation and rocking considering the soil profile type A, taking into account the five scaling factors summarized in Table 4.1.

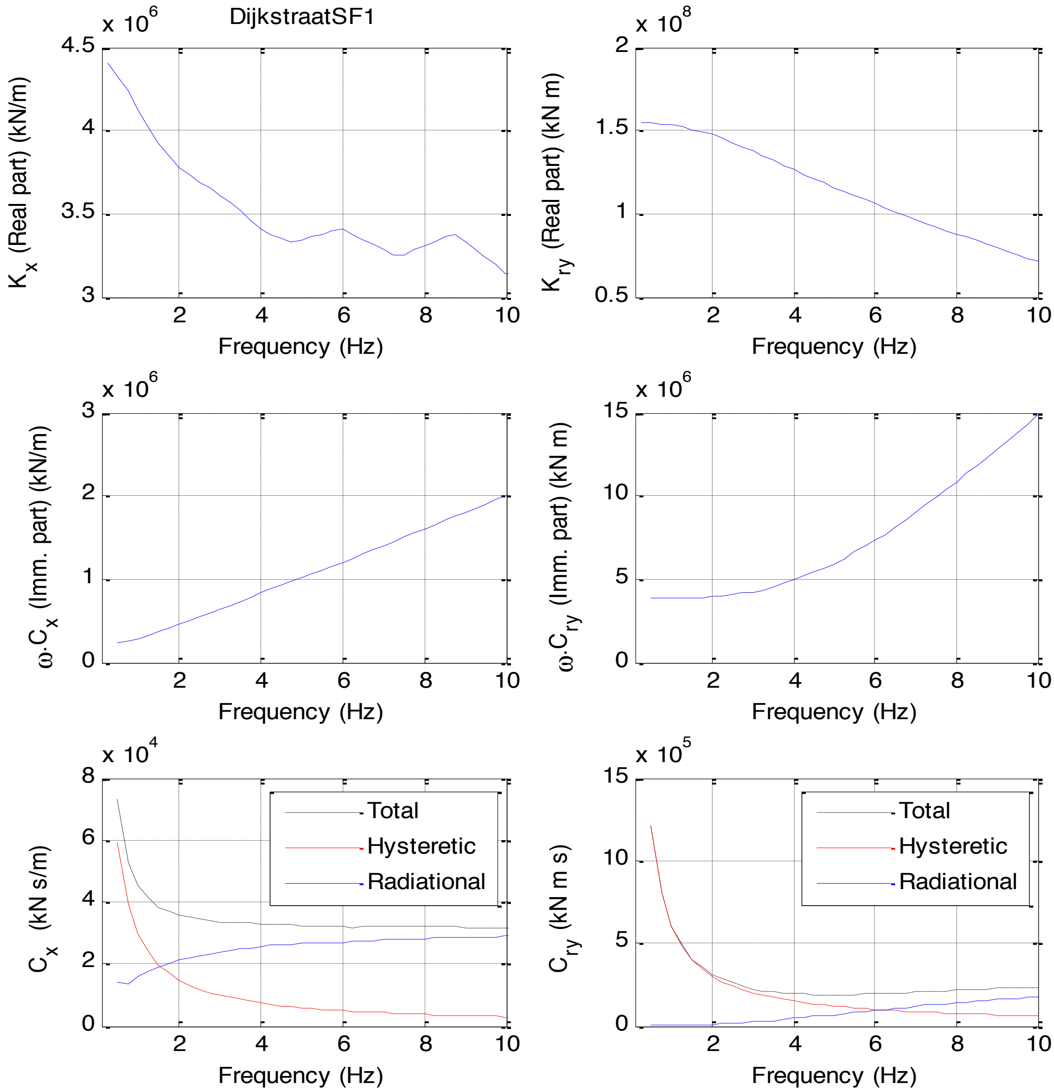

Figure 4.25 Impedance functions for Detached house "Dijkstraat": horizontal translation and rocking – Soil type A, Scaling factor SF1.

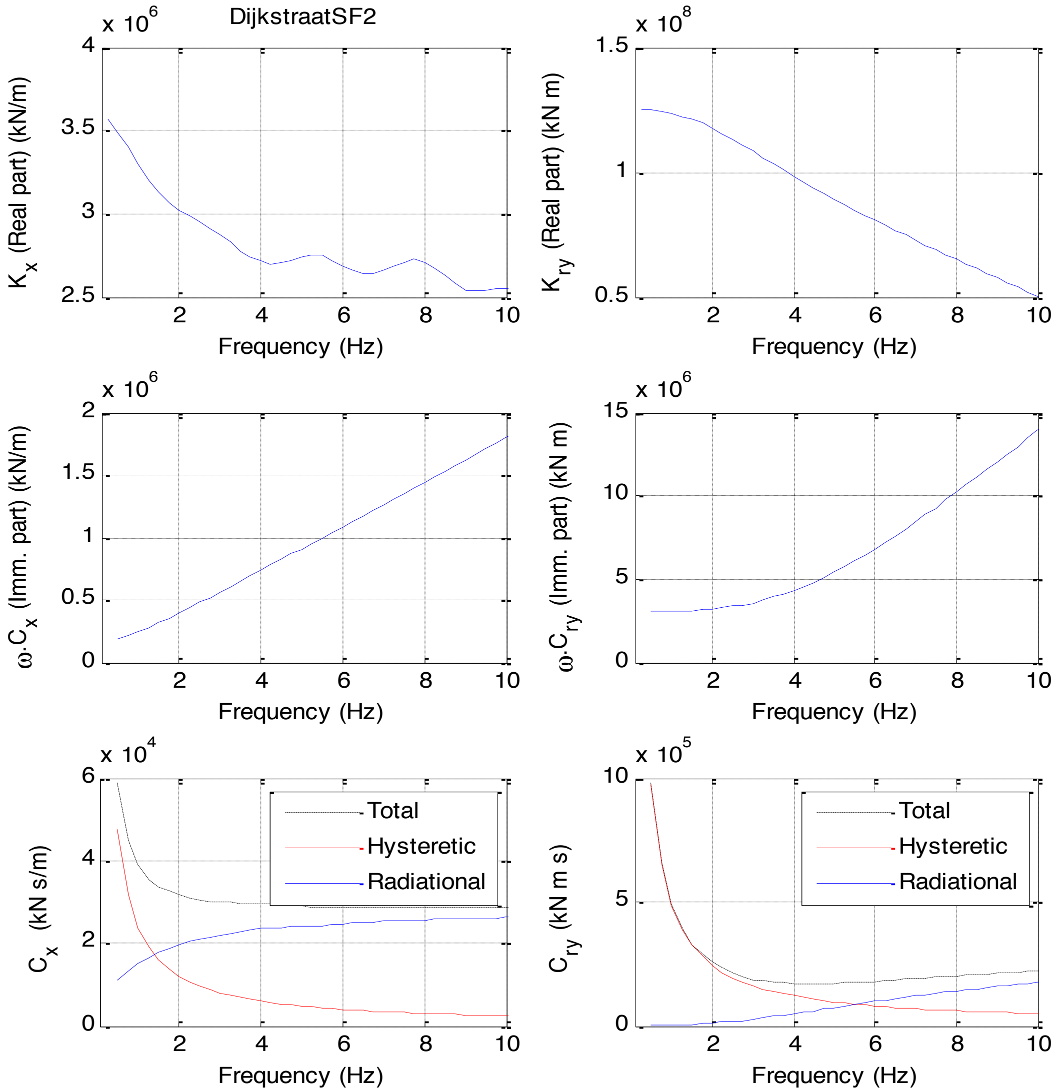

Figure 4.26 Impedance functions for Detached house "Dijkstraat": horizontal translation and rocking - Soil type A, Scaling factor SF2.

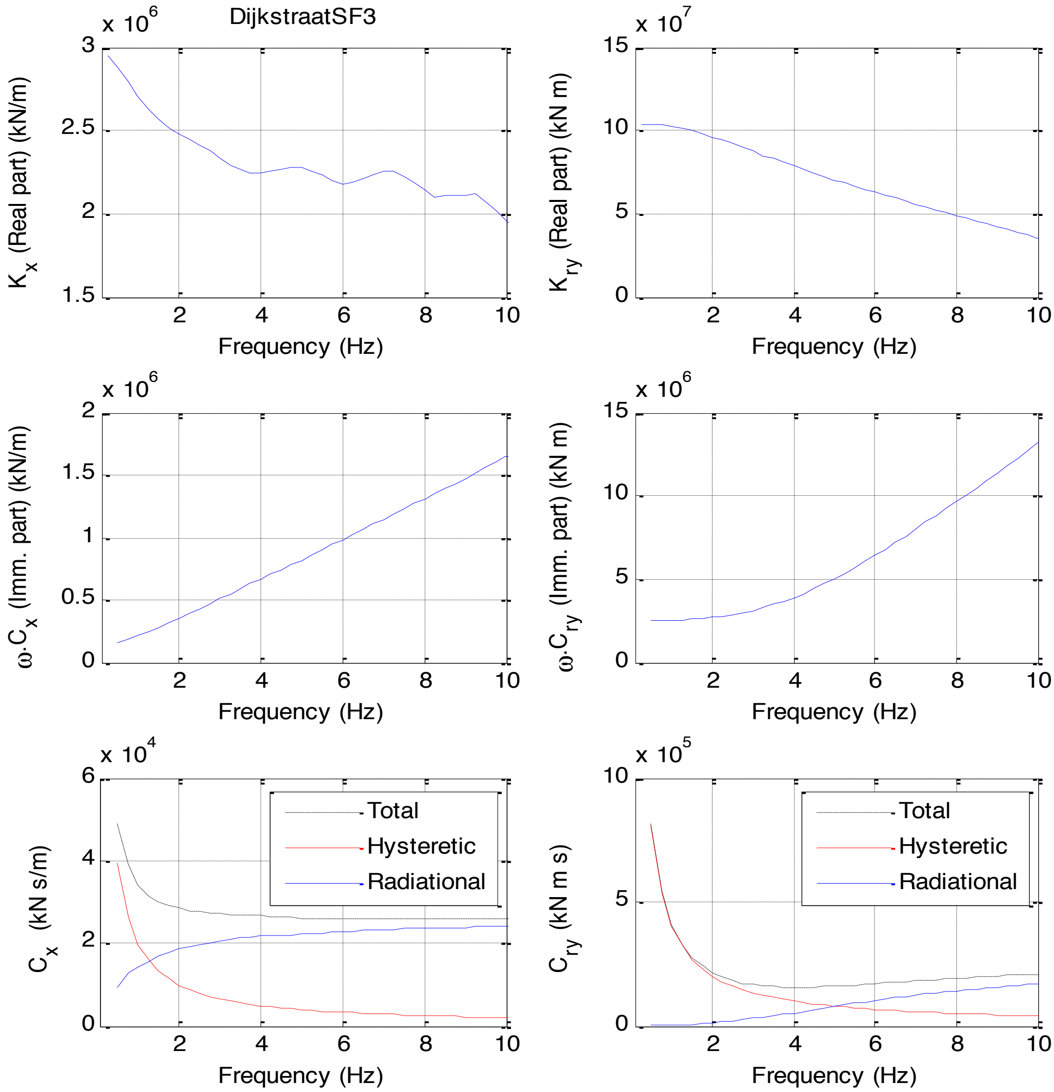

Figure 4.27 Impedance functions for Detached house "Dijkstraat": horizontal translation and rocking – Soil type A, Scaling factor SF3.

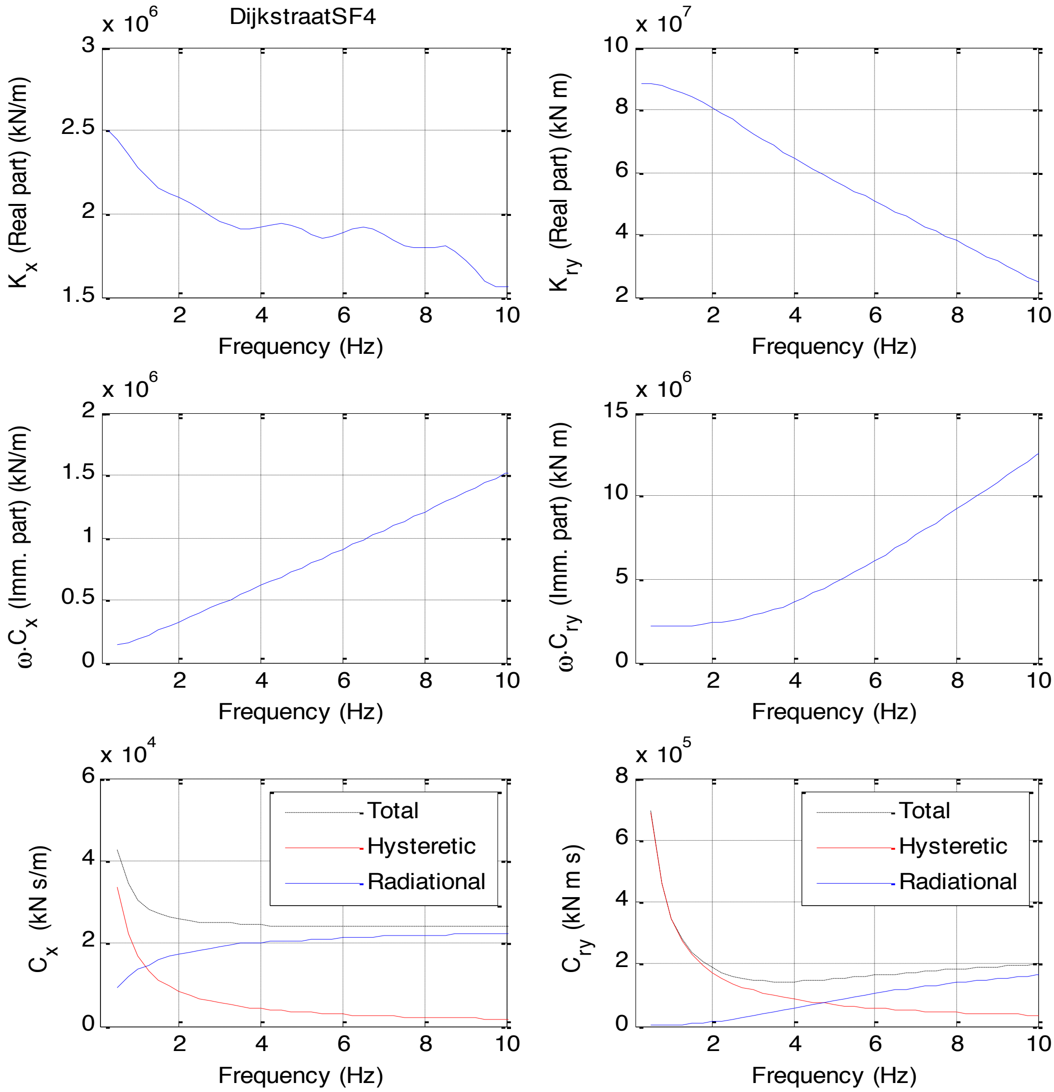

Figure 4.28 Impedance functions for Detached house "Dijkstraat": horizontal translation and rocking – Soil type A, Scaling factor SF4.

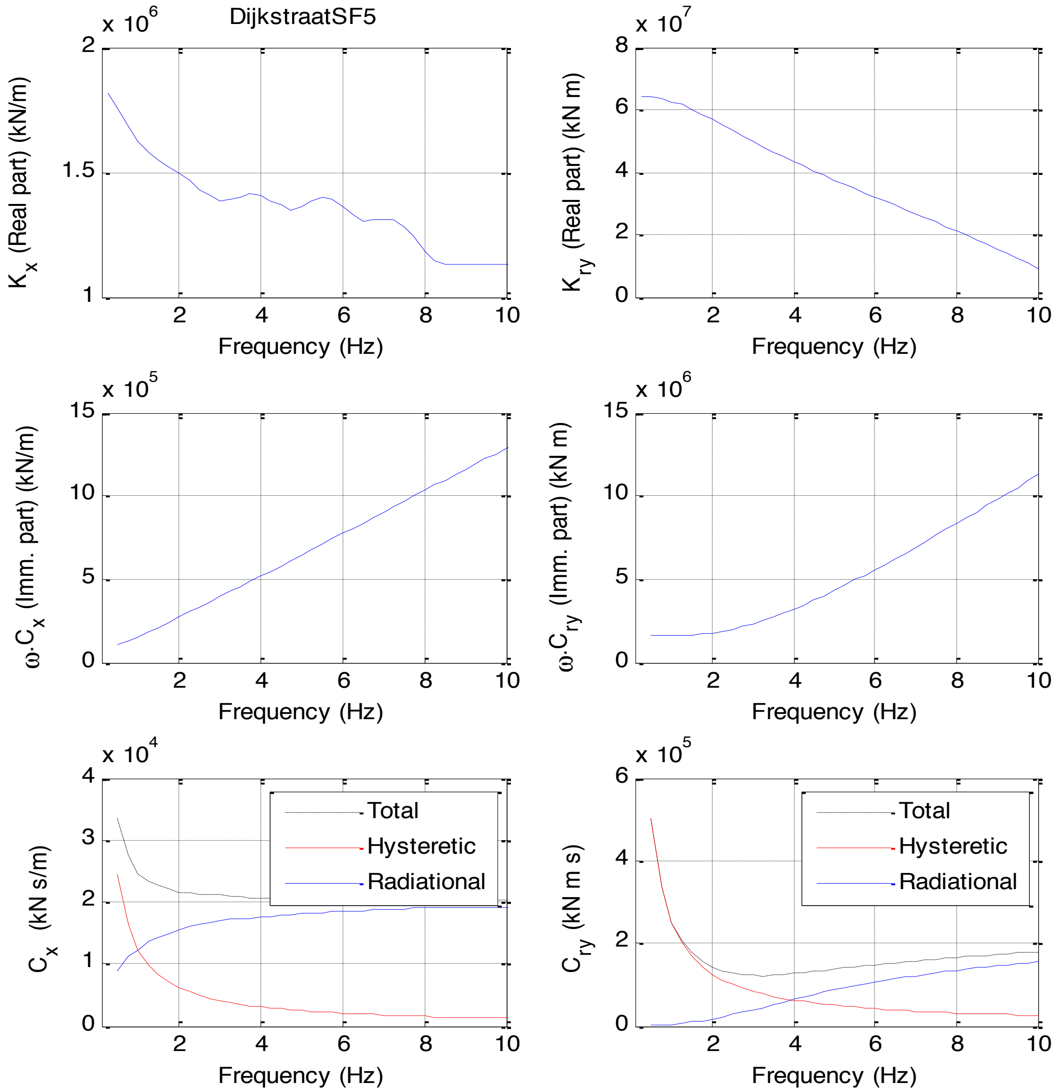

Figure 4.29 Impedance functions for Detached house "Dijkstraat": horizontal translation and rocking – Soil type A, Scaling factor SF5.

4.2.7 Detached house "De Haver"

The scheme of the foundations of the detached "De Haver" index building is shown in Figure 3.11. Impedance functions were evaluated in accordance with the procedure described in section 4.2.2. Table 4.6 summarizes the input parameters used for impedance calculations in DYNA6.1, with four cases being considered because stiffness and damping, as well as horizontal translation and rocking, are evaluated independently. Figure 4.30 shows, for a scaling factor equal to 1, the fitting of the Vs profile obtained considering the limitations of the software DYNA6.1, which considers fixed values of the ratios H/a and $V_{S,in}/V_{S,HS}$ (with the meaning of the symbols described in section 4.2.1).

Table 4.6: Detached house "De haver" - input parameters for DYNA6.1 considering soil type A: soil model and equivalent footing dimensions for different scaling factors.

Detached - De Haver			Stiffness horizontal	Stiffness Rocking	Damping horizontal	Damping rocking
Soil model: Composite medium with linear velocity			L_x (m) 42.1; L_y (m) 45.5; Eq. Dim. (m) 21.9; H_{layer} (m) 44	L_x (m) 16.3; L_y (m) 17.6; Eq. Dim. (m) 8.5; H_{layer} (m) 43	R (m) 10.5; Eq. Dim. (m) 9.3; H_{layer} (m) 46	R (m) 5.15; Eq. Dim. (m) 4.5; H_{layer} (m) 45
ν =0.45	$V_{S,in}$ /$V_{S,HS}$=0.6	γ=18.4 kN/m^3				
PGA (g)	Scaling factor (-)		$V_{S,in}$ (m/s)	$V_{S,in}$ (m/s)	$V_{S,in}$ (m/s)	$V_{S,in}$ (m/s)
0	SF0	1	192	191.4	194.1	193.5
0.05	SF1	0.934	179.3	178.8	181.3	180.8
0.14	SF2	0.840	161.3	160.8	163.0	162.6
0.22	SF3	0.765	146.9	146.4	148.5	148.1
0.29	SF4	0.706	135.5	135.1	137.0	136.6
0.43	SF5	0.602	115.6	115.2	116.8	116.5

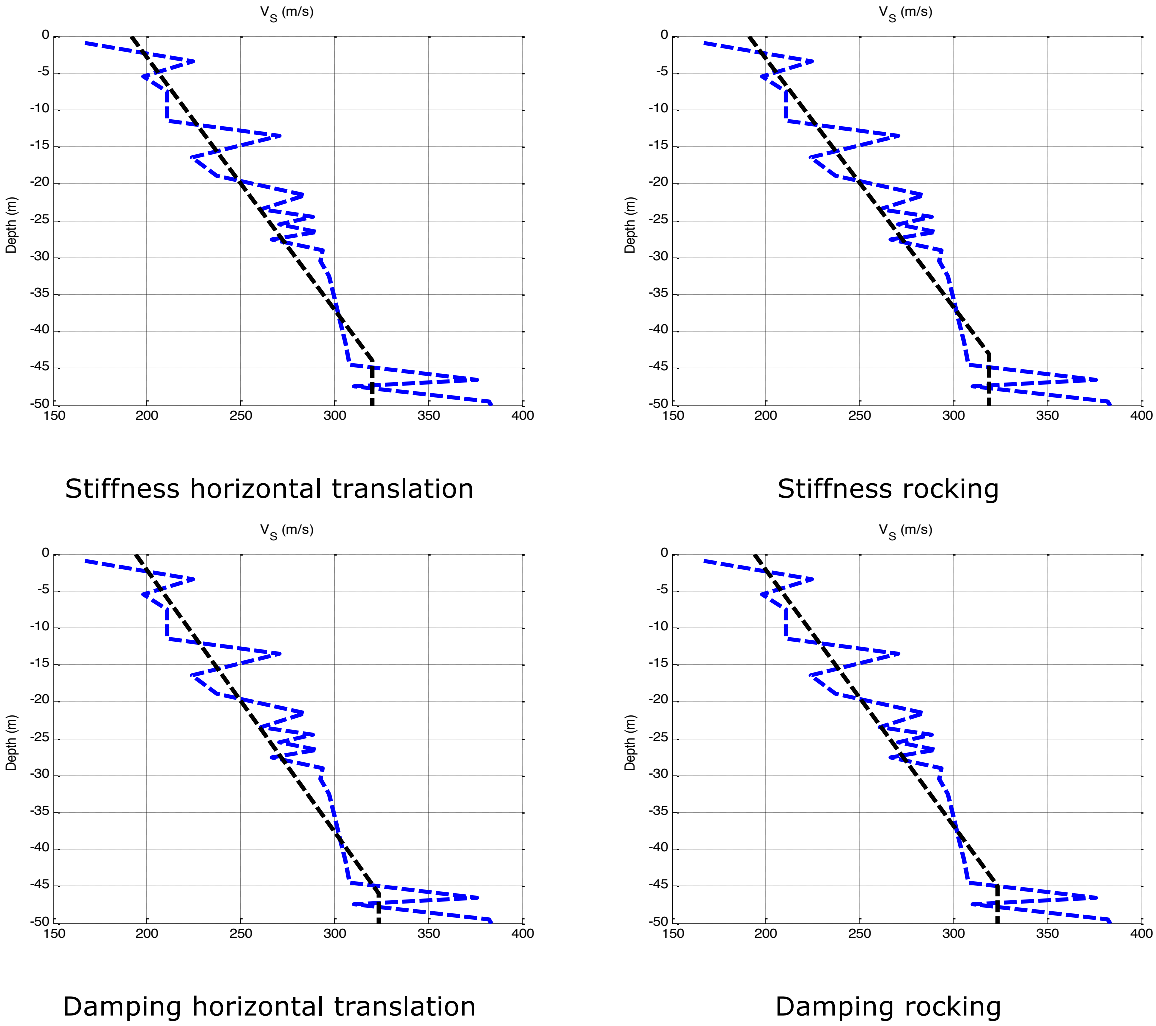

Figure 4.30 Detached house "De Haver": Fitting of the shear wave velocity profile type A using the composite medium (i.e. layer over half-space) depending on the degree of freedom considered (i.e. horizontal translation or rocking) and component (i.e. stiffness and damping) for a scaling factor equal to 1.

The following figures show the impedance functions (in terms of frequency-dependent stiffness and damping) of horizontal translation and rocking considering the soil profile type A, taking into account the five scaling factors summarized in Table 4.1.

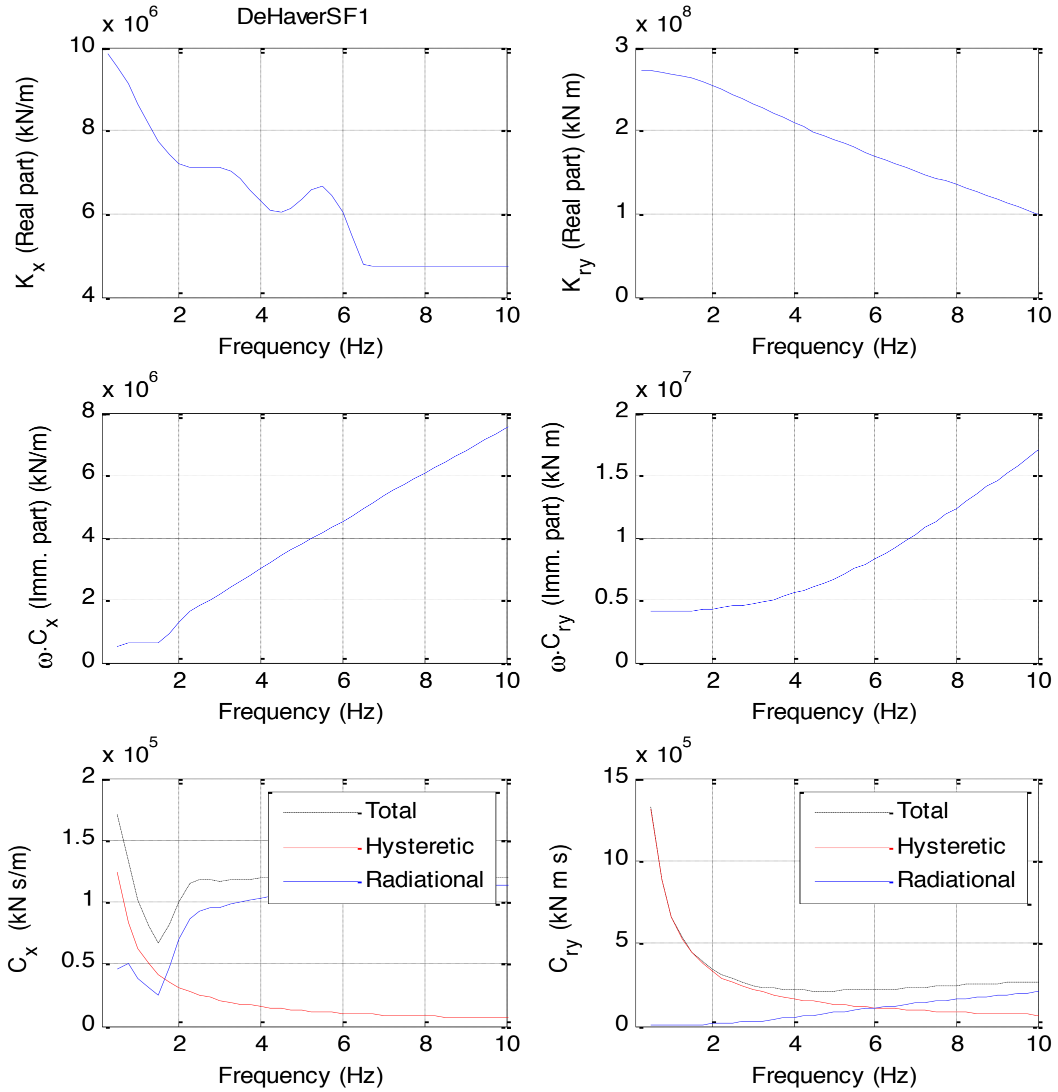

Figure 4.31 Impedance functions for Detached house "De Haver": horizontal translation and rocking – Soil type A, Scaling factor SF1.

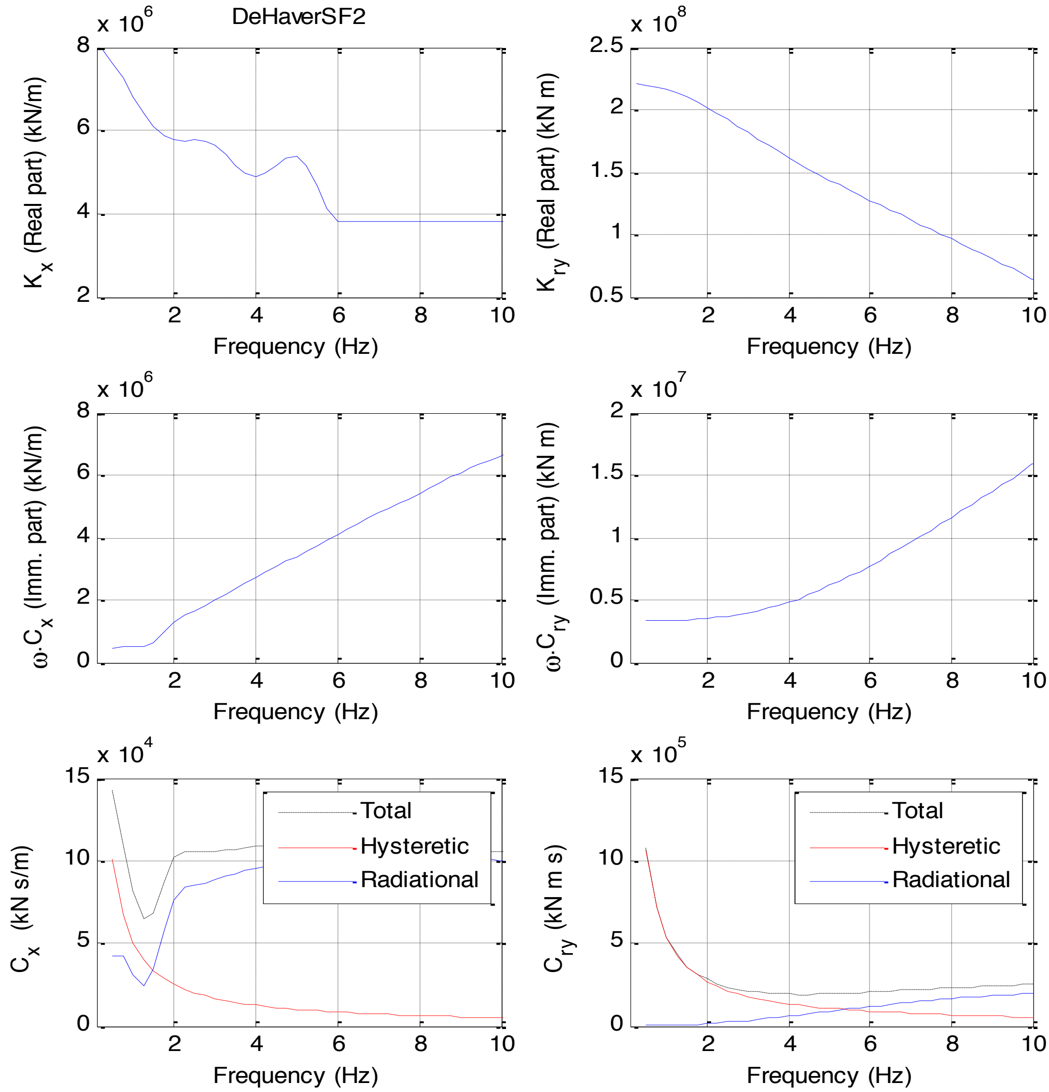

Figure 4.32 Impedance functions for Detached house "De Haver": horizontal translation and rocking - Soil type A, Scaling factor SF2.

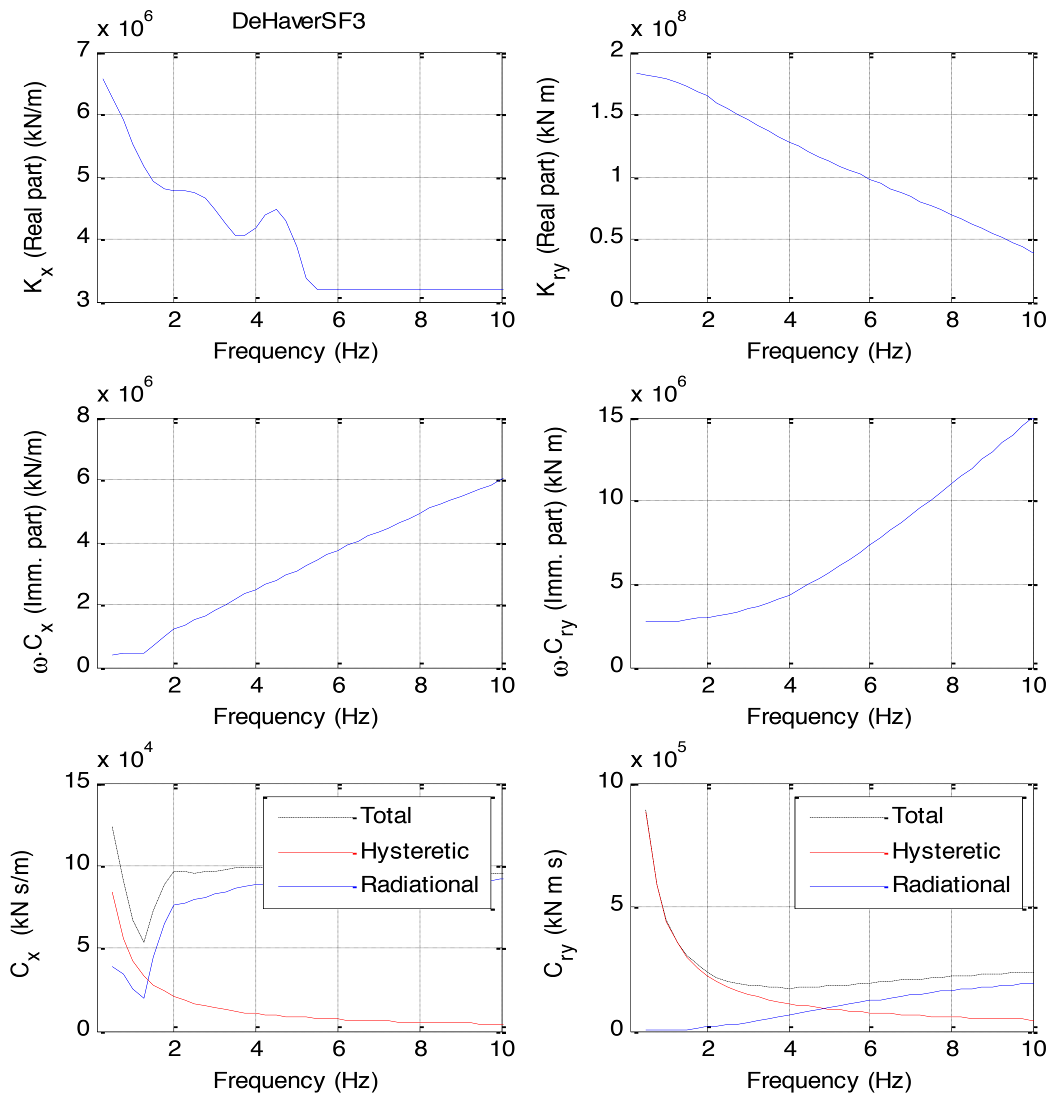

Figure 4.33 Impedance functions for Detached house "De Haver": horizontal translation and rocking – Soil type A, Scaling factor SF3.

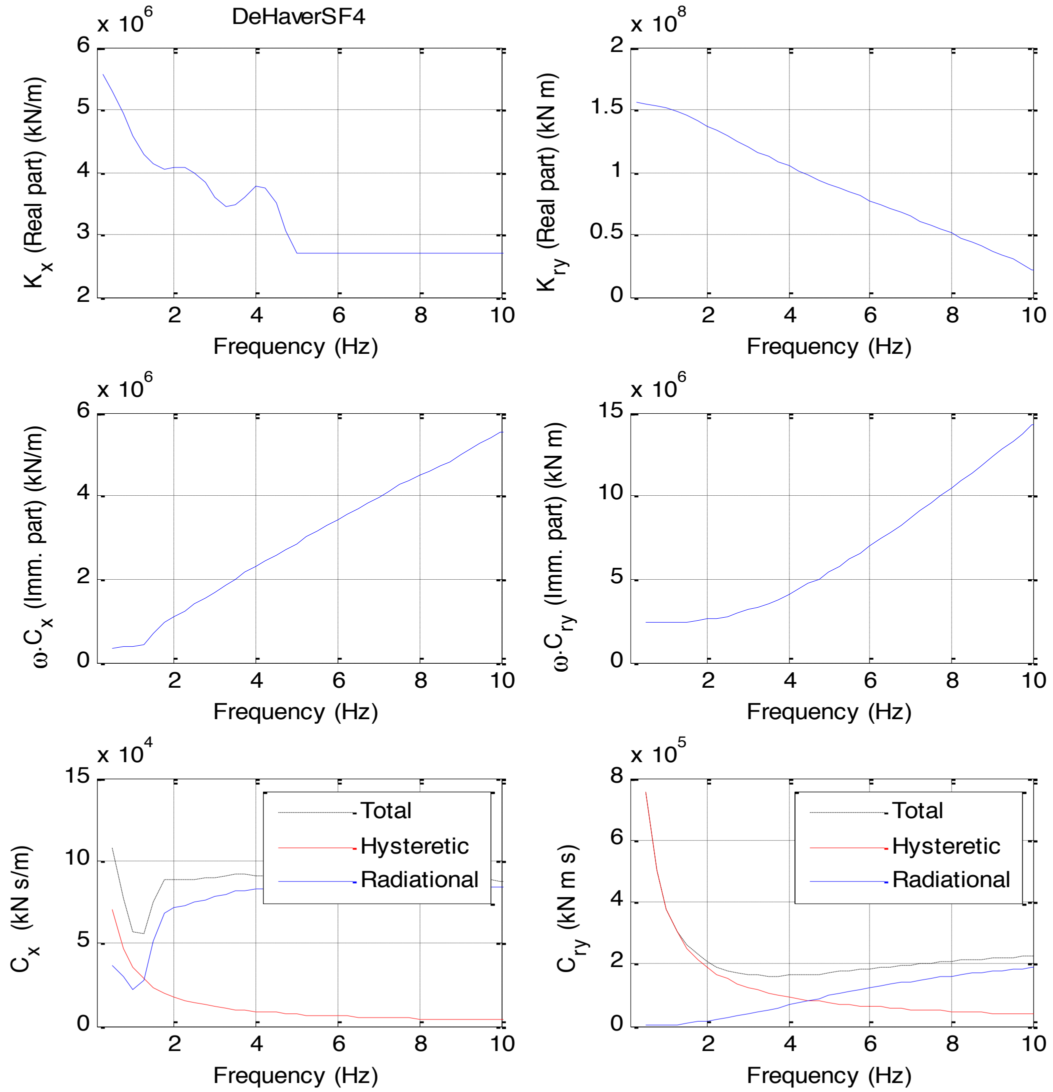

Figure 4.34 Impedance functions for Detached house "De Haver": horizontal translation and rocking – Soil type A, Scaling factor SF4.

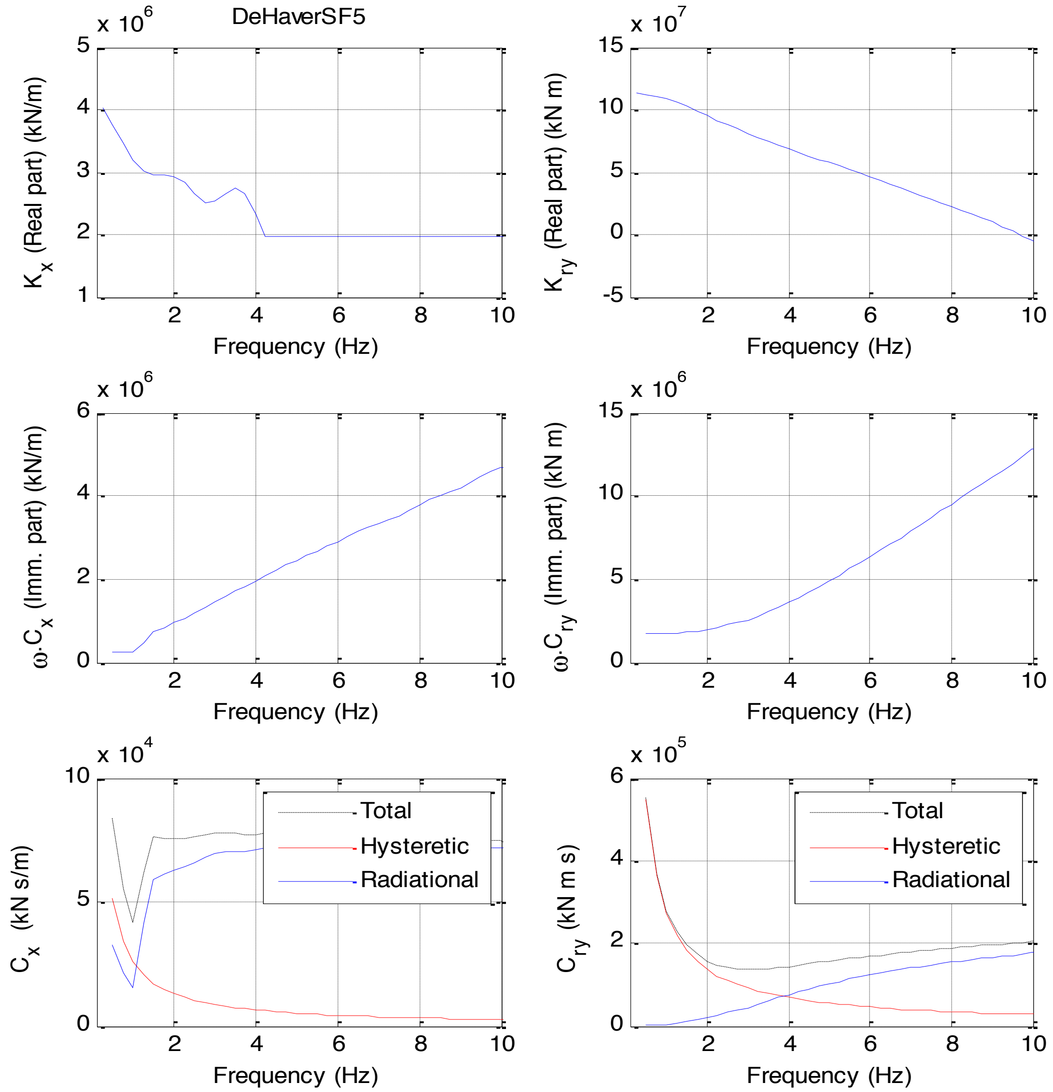

Figure 4.35 Impedance functions for Detached house "De Haver": horizontal translation and rocking – Soil type A, Scaling factor SF5.

4.3 Impedance functions for pile foundations

A typical pile distribution in an Apartment building has been shown in Figure 3.18, whilst the pile foundations typologies considered are described in Section 3.2.1.1. The same building superstructures studied before are considered here, recalling that their foundations feature the same number (67), position and length of piles (16 m). As discussed before, the piles are connected by reinforced concrete (RC) capping beams with height equal to 600 mm, while the width can be 450 mm or 650 mm depending on the beam position (perimeter or internal).

Always as noted before, the index buildings considered differ with respect to the characteristics of piles:

- "K-flat" and "Georg van S" have circular reinforced concrete piles with 45 cm diameter;
- "Drive-in" has square reinforced concrete piles with 25 cm width.

4.3.1 Soil model

For pile foundations, the software DYNA6.1 allows the use of a layered medium. For each stratum, the input parameters are: thickness, shear wave velocity, weight of unit volume, Poisson's coefficient and damping factor. The depth interested by the presence of piles (i.e. 16 m) is subdivided into three layers (namely M1, M2 and M3), while the soil with thickness of 4 m below the pile tip is considered as a base layer (namely M4). The shear wave velocity and the weight for unit volume (γ) of each layer is equal to the average value within the stratum, Table 4.7 summarizes the layers' thicknesses and the resulting V_S and γ values, whereas Figure 4.36 represents the V_S profile, corresponding to soil Type A, of the layered medium considered. For each layer, the Poisson's ratio is taken equal to 0.45 and the material damping coefficient considered is assumed equal to 0.02.

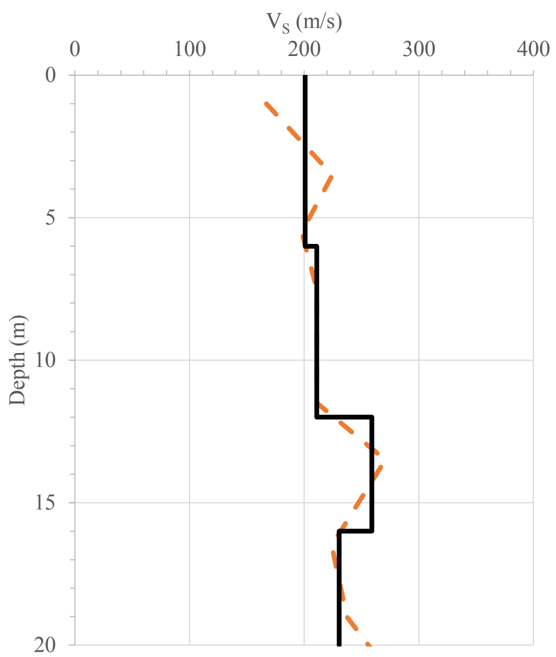

Figure 4.36 V_S profile of the upper 20 m of soil type A (dashed red line) and V_S profile considered for the layered medium used for computation of impedance functions of pile foundations.

Table 4.7: Soil characteristics of the four layers used for computation of impedance functions of pile foundations.

	Thickness (m)	V_S (m/s)	γ (kN/m^3)
M1	6	200.9	18.7
M2	6	211.0	16.7
M3	4	259.1	19.2
M4	4	230.5	18.1

To account for soil nonlinearity, the same approach to define the V_S scaling factors versus PGA described in section 4.2.1 was considered. The average shear strain is evaluated for each layer within the first 20 m of soil type A. Table 4.8 summarizes the layer's number, thickness, stratigraphy and lithology. In the upper 20 m of soil layers, nine different shear modulus degradations curves were considered in site response analysis (Rodriguez-Marek et al., 2017, Kruiver 2019).

Table 4.8: Layering of the upper 20 m of Soil type A used for pile foundations (legend of stratigraphy acronyms: AAOP Anthropogenic deposits; BXWI Boxtel Formation, Wierden Member; BX Boxtel Formation; DR Drente Formation; DRGI Drente Formation, Gieten Member; PE Peelo Formation).

Layer	Thickness (m)	Stratigraphy	Lithology
1	2	AAOP	Fine Sand
2	3	BXWI	Fine Sand
3	1	BX	Clayey sand and sandy clay
4	3	DR	Clayey sand and sandy clay
5	2	DR	Clayey sand and sandy clay
6	1	DRGI	Clayey sand and sandy clay
7	3	PE	Fine Sand
8a	1	PE	Clayey sand and sandy clay
8b	2	PE	Clayey sand and sandy clay
9	2	PE	Clayey sand and sandy clay

Figure 4.37 shows, for different levels of PGA, the G/G_{max} scaling factors evaluated for the average strain levels of the layers within the upper 20 m of the soil type A deposit.

The G/G_{max} scaling factors are converted into V_S scaling factors considering Eq. (4.1). For each layer, the V_S scaling factors were interpolated using an exponential relationship, which are shown in Figure 4.38.

Five PGA levels ranging from 0.05g to 0.43g were considered in the derivation of impedance functions. For these PGA values, the exponential relationships shown in Figure 4.38 were used for the computation of the corresponding V_S scaling factors. Finally, the V_S profiles were scaled considering the mean V_S scaling factors of the four layers (i.e. M1, M2, M3 and M4) identified in Figure 4.36, with the resulting values summarized in Table 4.9.

Table 4.9: V_S scaling factors for soil type A obtained using the exponential relationships shown in Figure 4.38.

Thickness (m)	Layer M1 6m				Layer M2 6m				Layer M3 4m			Layer M4 4m		
	2	3	1		3	2	1		3	1		2	2	
PGA (g)	Layer 1	Layer 2	Layer 3	Mean SF	Layer 4	Layer 5	Layer 6	Mean SF	Layer 7	Layer 8a	Mean SF	Layer 8b	Layer 9	Mean SF
0.05	0.926	0.952	0.960	**0.946**	0.922	0.913	0.902	**0.912**	0.951	0.944	**0.947**	0.939	0.945	**0.942**
0.14	0.821	0.878	0.892	**0.864**	0.797	0.774	0.747	**0.773**	0.869	0.851	**0.860**	0.836	0.852	**0.844**
0.22	0.738	0.818	0.836	**0.797**	0.700	0.668	0.632	**0.667**	0.802	0.775	**0.789**	0.754	0.776	**0.765**
0.29	0.672	0.768	0.790	**0.744**	0.625	0.588	0.546	**0.586**	0.748	0.714	**0.731**	0.689	0.716	**0.703**
0.43	0.558	0.678	0.706	**0.647**	0.498	0.454	0.408	**0.453**	0.651	0.607	**0.629**	0.576	0.609	**0.592**

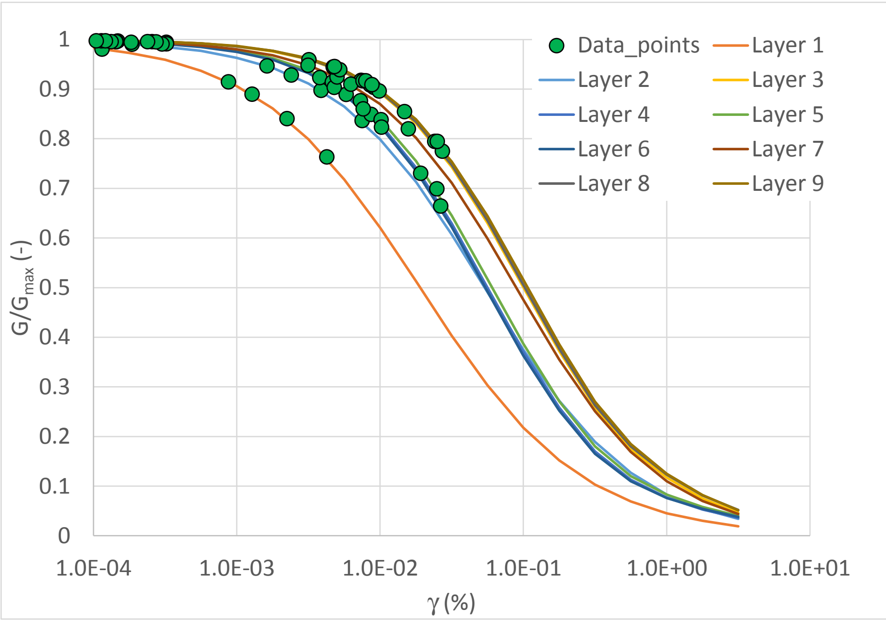

Figure 4.37 G/G_{max} scaling factors obtained from site response analysis for different levels of shear strain in the upper 20 m of soil layers, for the different shear modulus degradation curves considered (Raw results from site response analysis provided by Deltares, 2019).

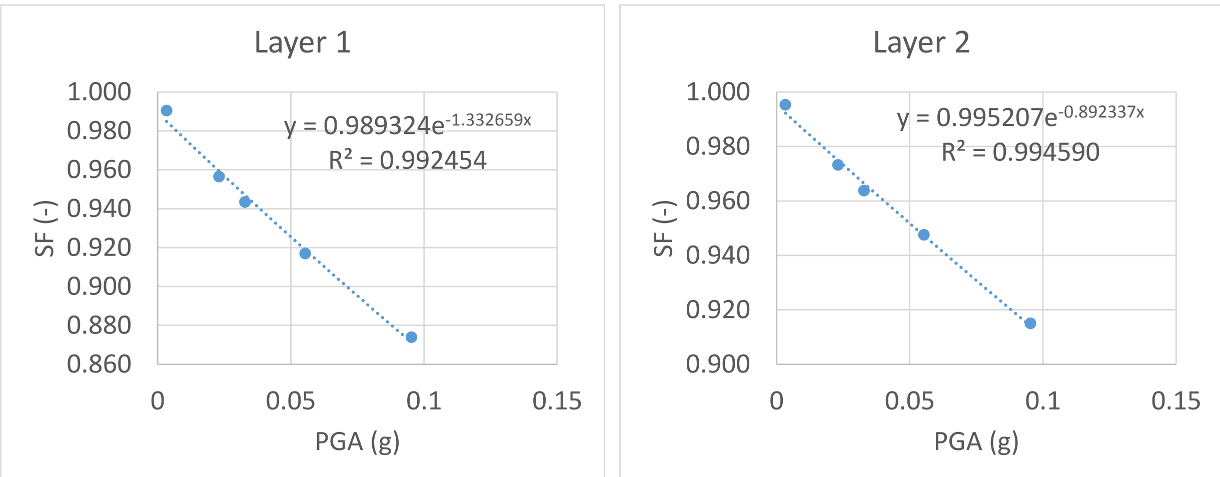

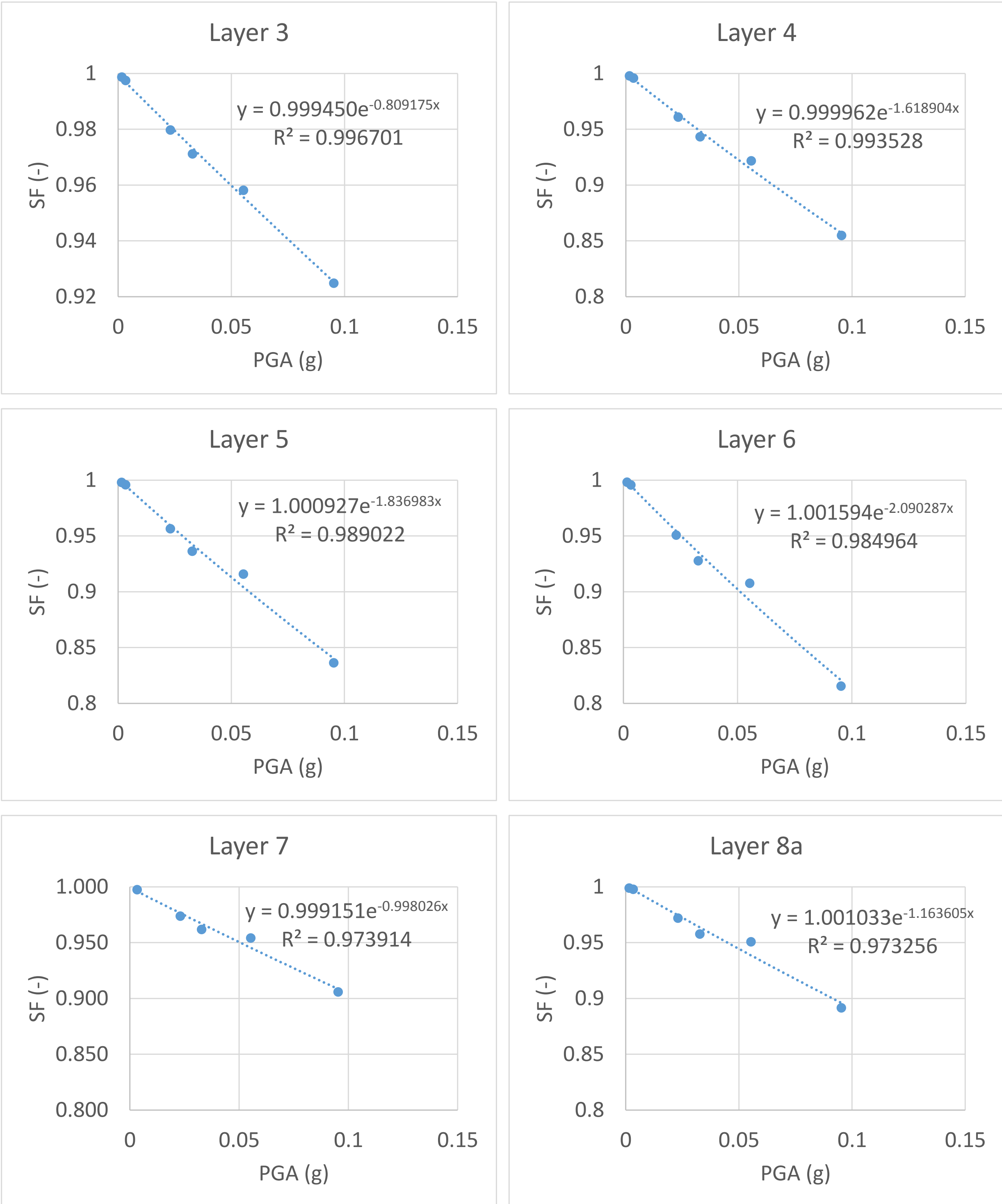
Layer 3
y = 0.999450e^-0.809175x
R² = 0.996701
SF (-)
PGA (g)
Layer 4
y = 0.999962e^-1.618904x
R² = 0.993528
SF (-)
PGA (g)
Layer 5
y = 1.000927e^-1.836983x
R² = 0.989022
SF (-)
PGA (g)
Layer 6
y = 1.001594e^-2.090287x
R² = 0.984964
SF (-)
PGA (g)
Layer 7
y = 0.999151e^-0.998026x
R² = 0.973914
SF (-)
PGA (g)
Layer 8a
y = 1.001033e^-1.163605x
R² = 0.973256
SF (-)
PGA (g)

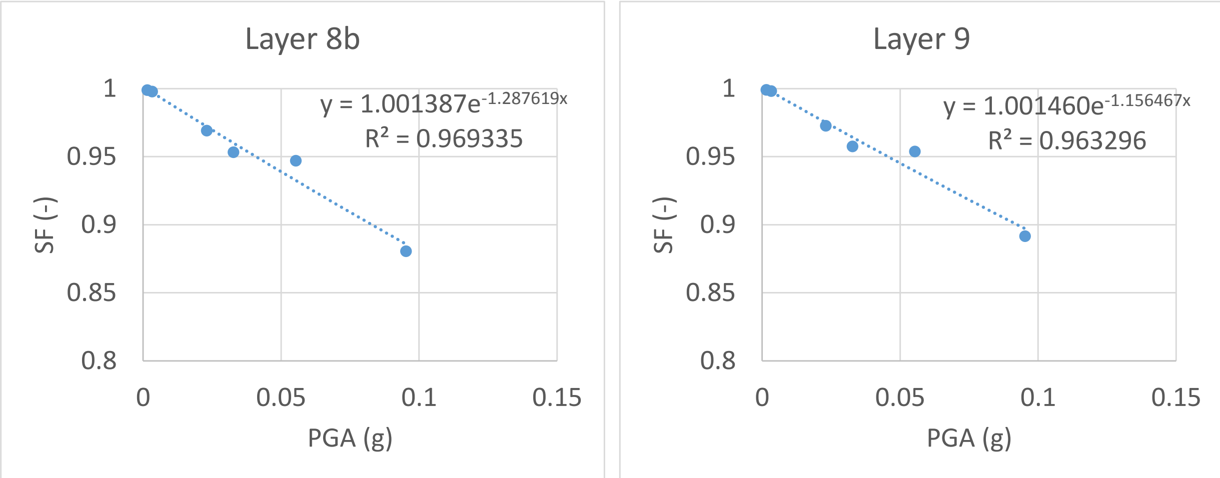

Figure 4.38 Relationships between PGA and V_S scaling factors considering the layers in the upper 20 m of the soil type A.

4.3.2 Procedure for impedance functions calculation

The foundation typology considered for a typical apartment house is constituted by 67 piles connected by cap beams (see Figure 3.19). A detailed description of the foundation characteristics can be found in Section 3.2.1.1. Cap beams for piles aligned in the y-direction are assumed rigid; conversely, in the x-direction the spacing between the beams, about 7.5 m, does not allow considering the rigid hypothesis valid, especially for rocking. For such reason, the resulting behaviour of the whole foundation cannot be considered rigid. To account for this aspect, the impedance functions of the two typical piles alignments (i.e. a perimeter row with 8 piles and an internal row with 11 piles) has been evaluated independently, considering the rigid-massless foundations hypothesis. Afterwards, the total foundation impedance, for different degrees of freedom, was evaluated as the sum of the different rows of piles, namely:

$$3 \cdot K^{*}_{8\,piles} + 4 \cdot K^{*}_{11\,piles} \tag{4.6}$$

Impedance functions were computed considering floating piles and a fixed pile condition at the top. Group effects within each row were incorporated through frequency-dependent pile-to-pile interaction factors. The embedment of the cap foundation was neglected due to its reduced value. For the high-water table level, a Poisson's ratio equal to 0.45 was assumed.

4.3.3 Apartment block "Drive-in"

The scheme of the foundations of the "Drive-in" index building is shown in Figure 3.19. Impedance functions were evaluated in accordance with the procedure described in section 4.3.2. The following figures show the impedance functions (in terms of frequency dependent stiffness and damping) of horizontal translation, rocking and cross swaying-rotational stiffness, considering the soil profile type A and taking into account the five scaling factors summarized in Table 4.9.

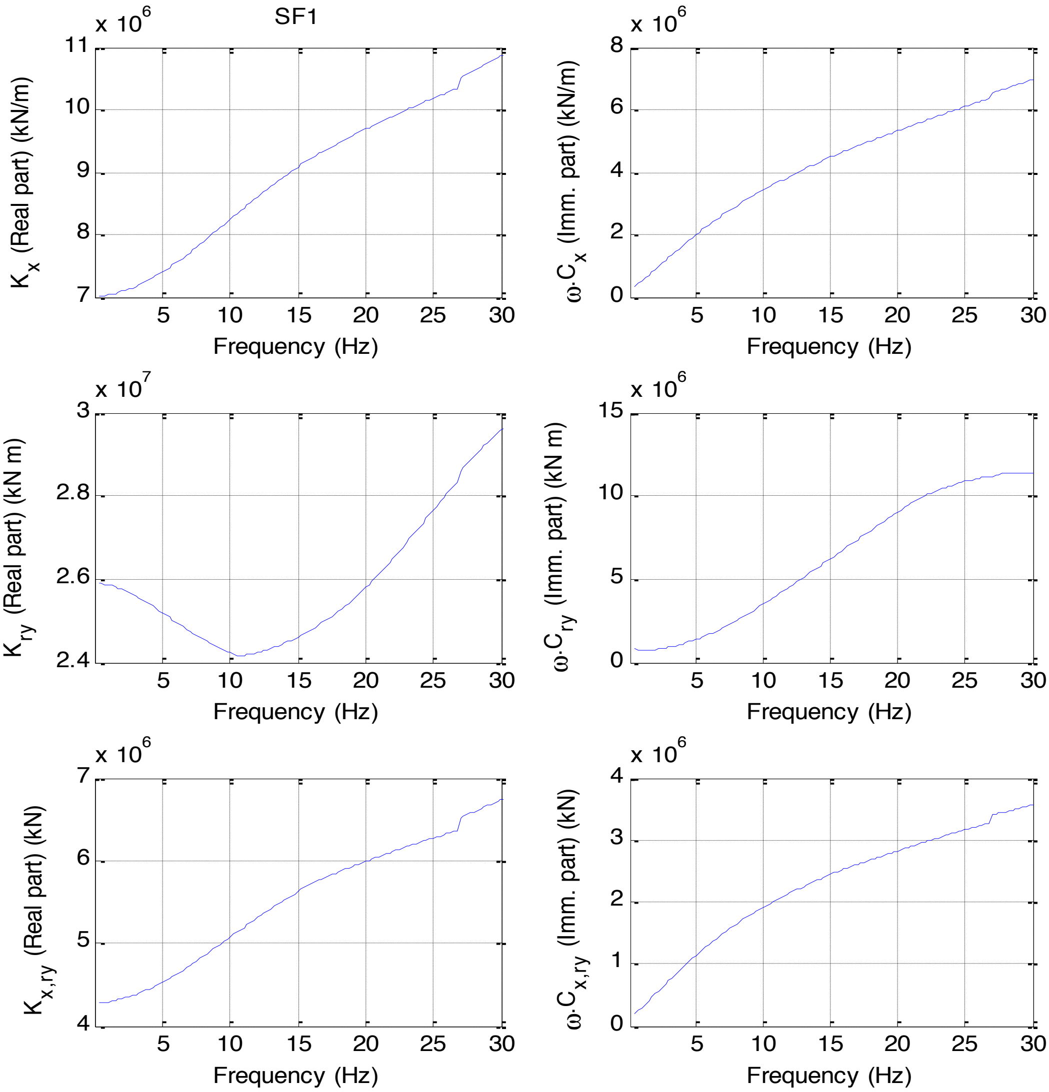

Figure 4.39 Impedance functions for Apartment block "Drive-in" – Fixed head conditions, floating piles: horizontal translation, rocking and coupling term – Soil type A, Scaling factor SF1.

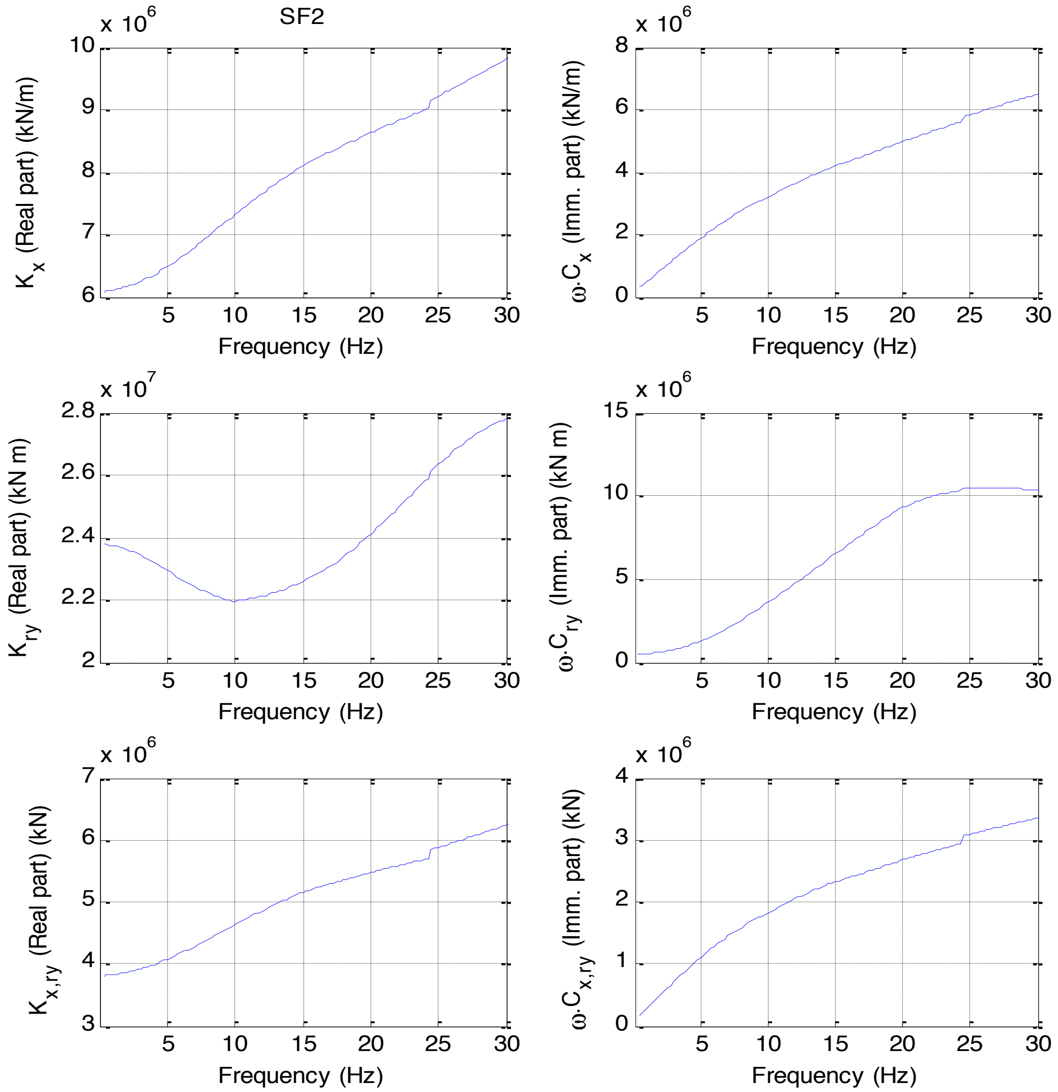

Figure 4.40 Impedance functions for Apartment block "Drive-in" – Fixed head conditions, floating piles: horizontal translation, rocking and coupling term – Soil type A, Scaling factor SF2.

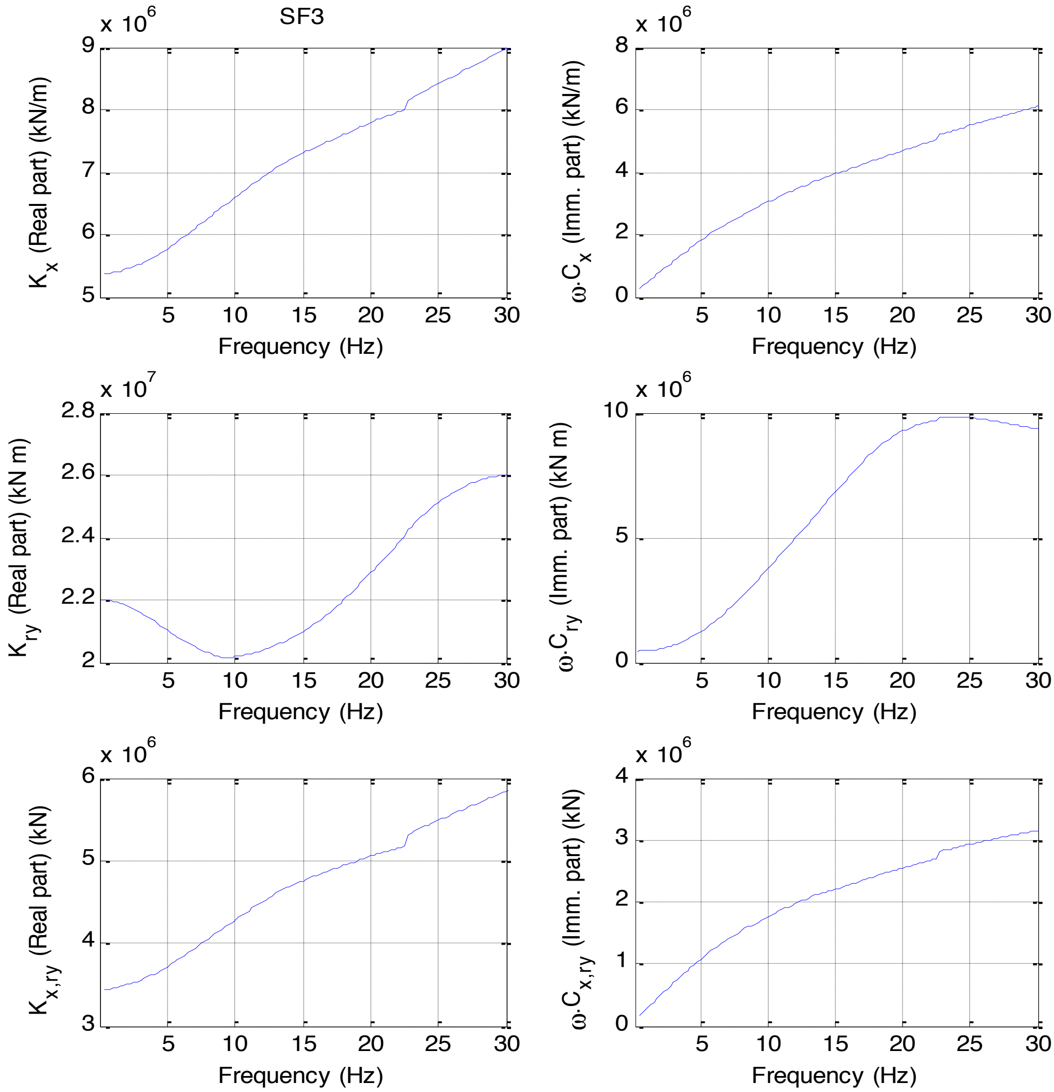

Figure 4.41 Impedance functions for Apartment block "Drive-in" – Fixed head conditions, floating piles: horizontal translation, rocking and coupling term – Soil type A, Scaling factor SF3.

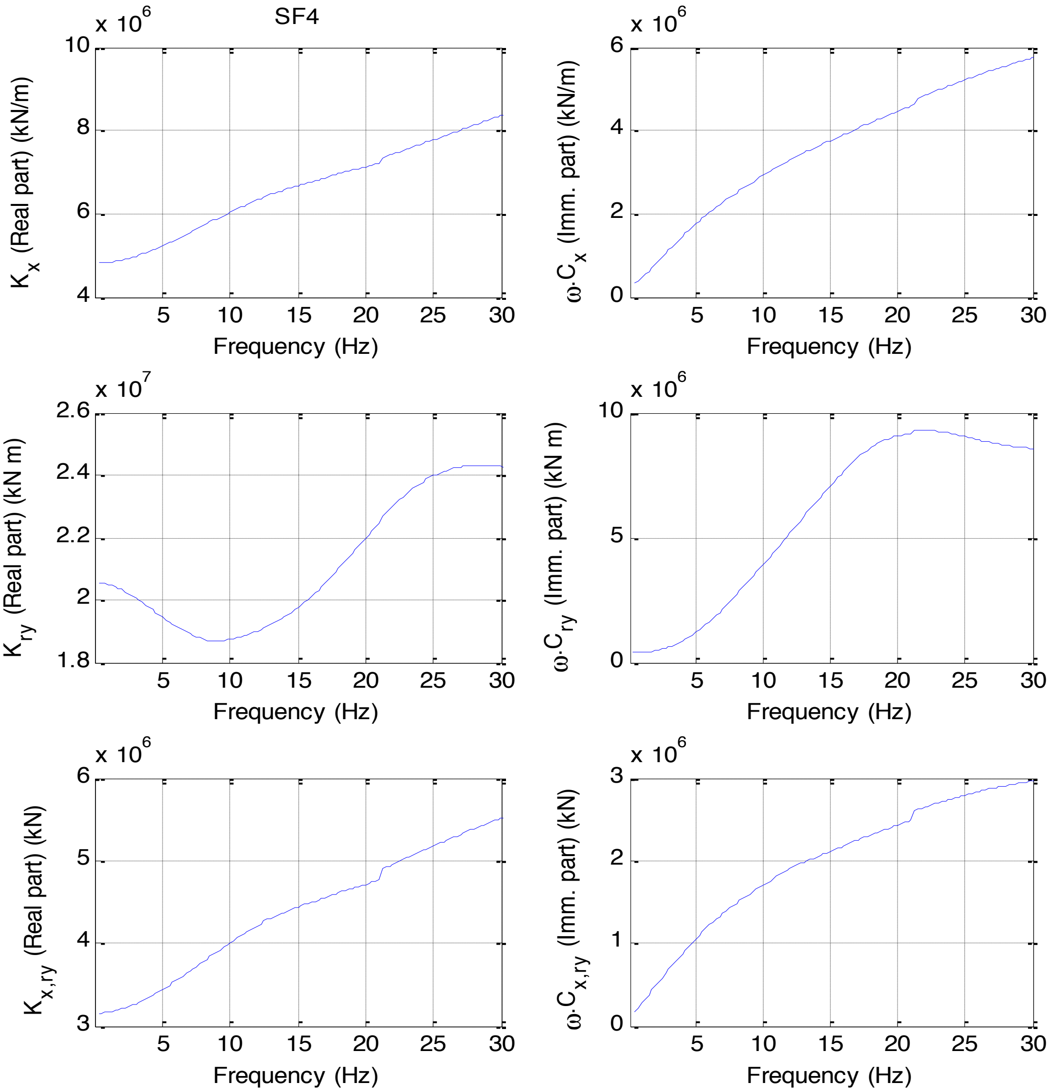

Figure 4.42 Impedance functions for Apartment block "Drive-in" – Fixed head conditions, floating piles: horizontal translation, rocking and coupling term – Soil type A, Scaling factor SF4.

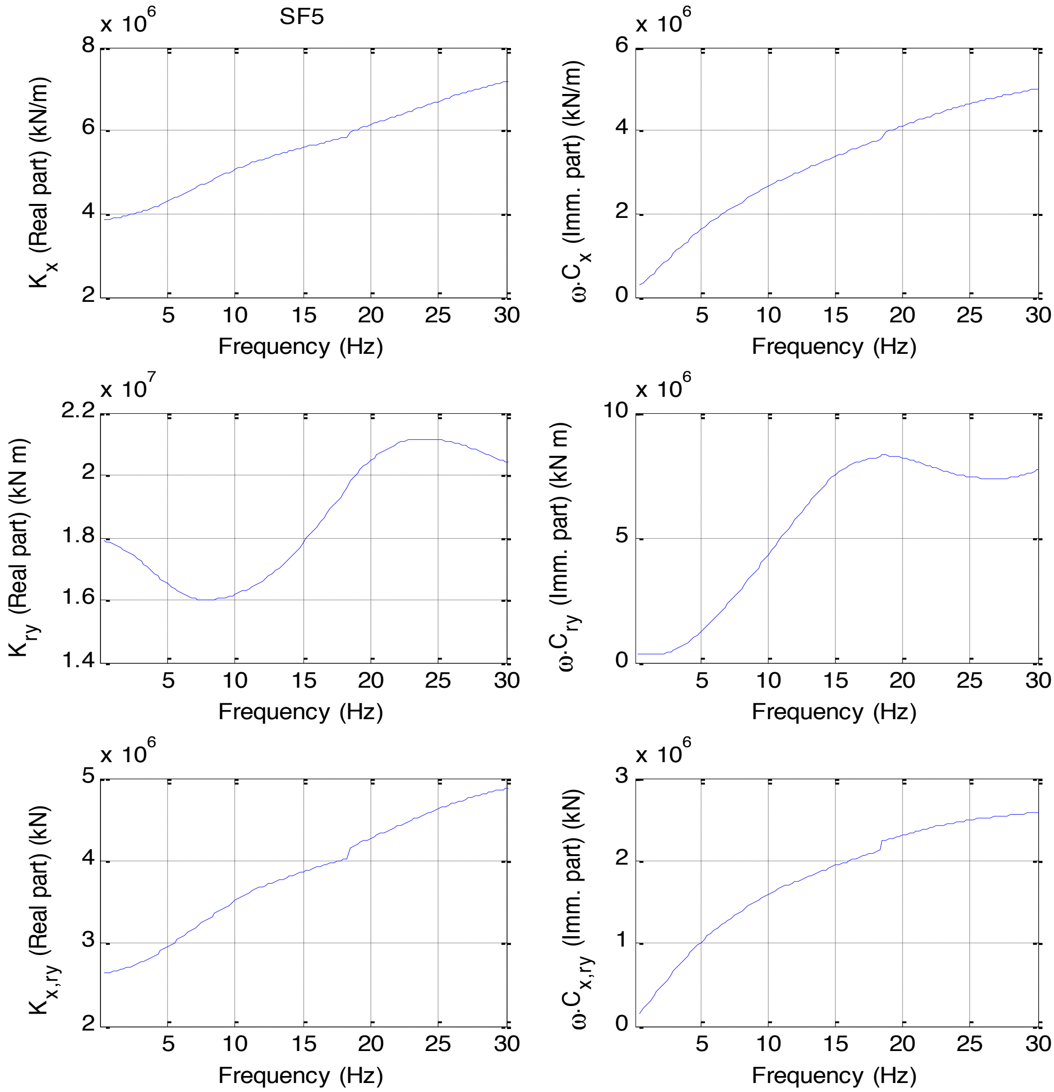

Figure 4.43 Impedance functions for Apartment "Drive-in" on pile foundations – Fixed head conditions, floating piles: horizontal translation, rocking and coupling term – Soil type A, Scaling factor SF5.

4.3.4 Apartment blocks "K-flat" and "Georg Van S"

The scheme of the foundations of the "K-flat" and "Georg van S" index buildings is shown in Figure 3.19. Impedance functions were evaluated in accordance with the procedure described in section 4.3.2. The following figures show the impedance functions (in terms of frequency dependent stiffness and damping) of horizontal translation, rocking and cross swaying-rotational stiffness, considering the soil profile type A and taking into account the five scaling factors summarized in Table 4.9.

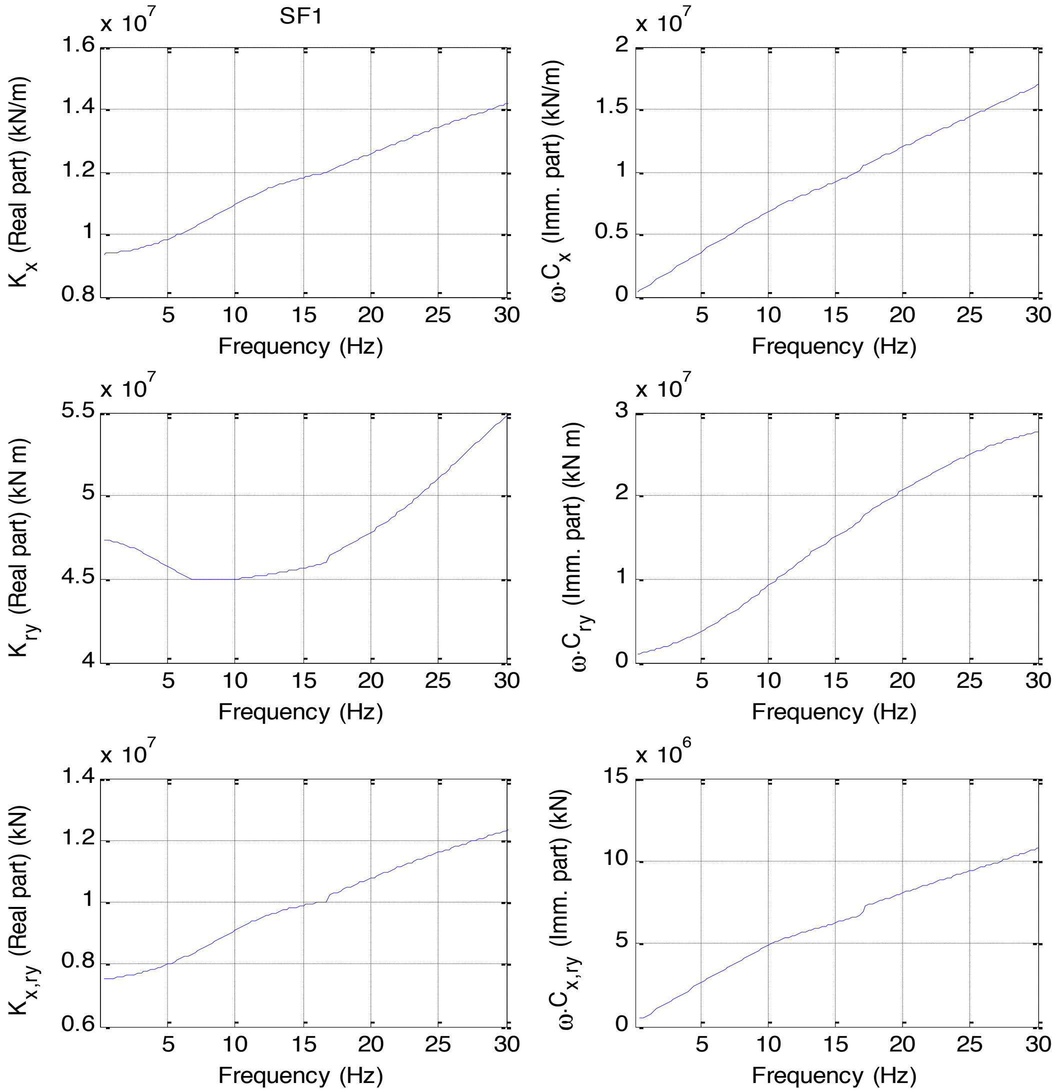

Figure 4.44 Impedance functions for Apartment blocks "K-flat" and "Georg Van S" – Fixed head conditions, floating piles: horizontal translation, rocking and coupling term – Soil type A, Scaling factor SF1.

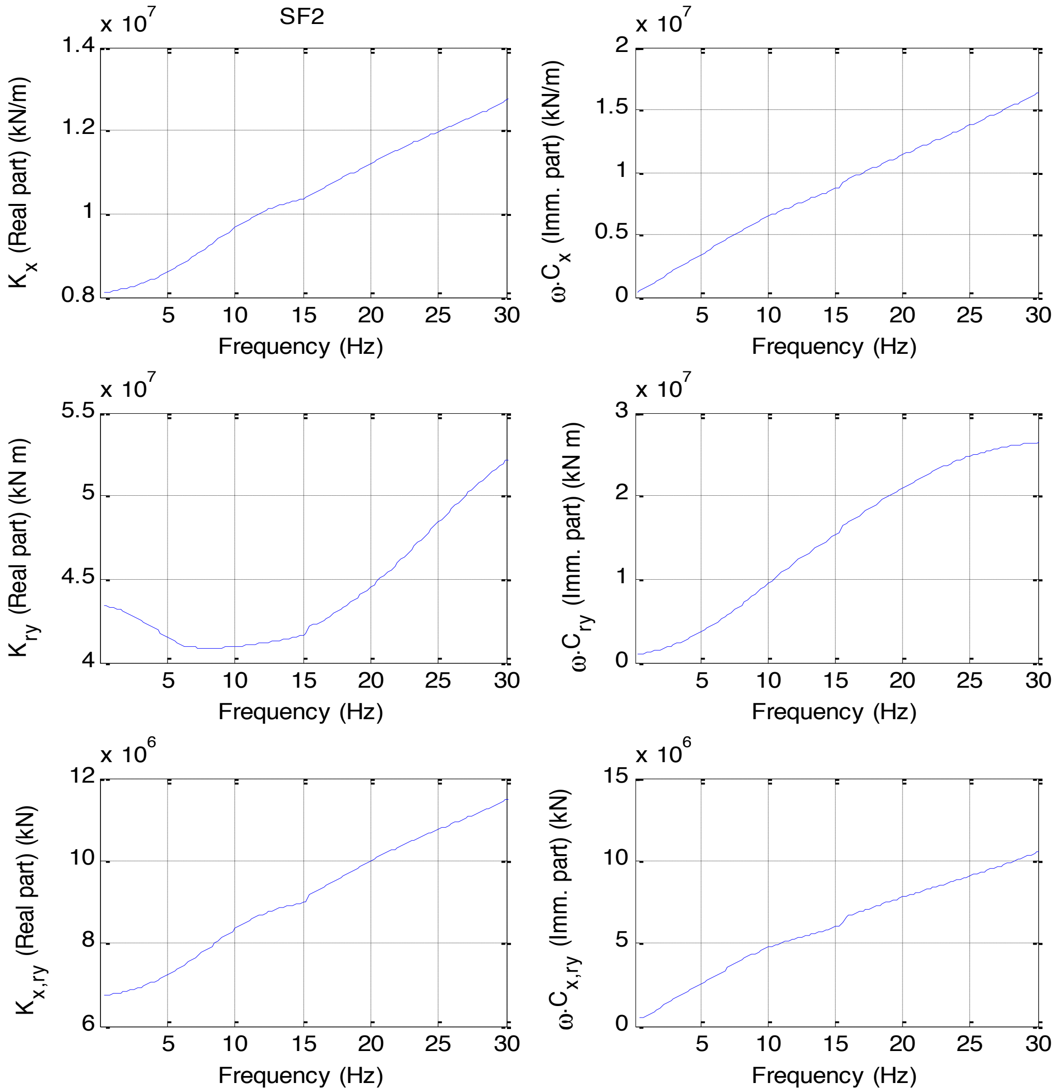

Figure 4.45 Impedance functions for Apartment blocks "K-flat" and "Georg Van S" – Fixed head conditions, floating piles: horizontal translation, rocking and coupling term – Soil type A, Scaling factor SF2.

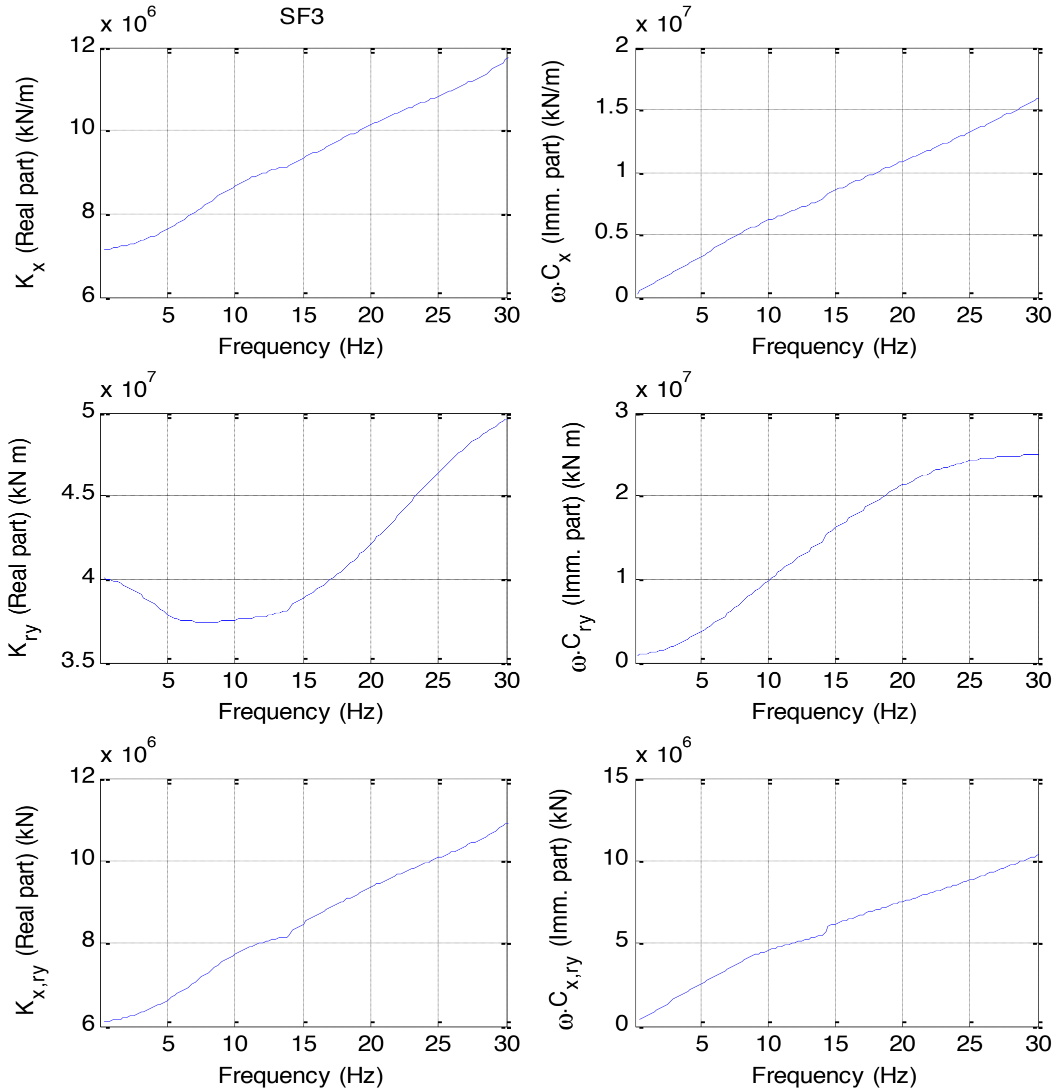

Figure 4.46 Impedance functions for Apartment blocks "K-flat" and "Georg Van S" – Fixed head conditions, floating piles: horizontal translation, rocking and coupling term – Soil type A, Scaling factor SF3.

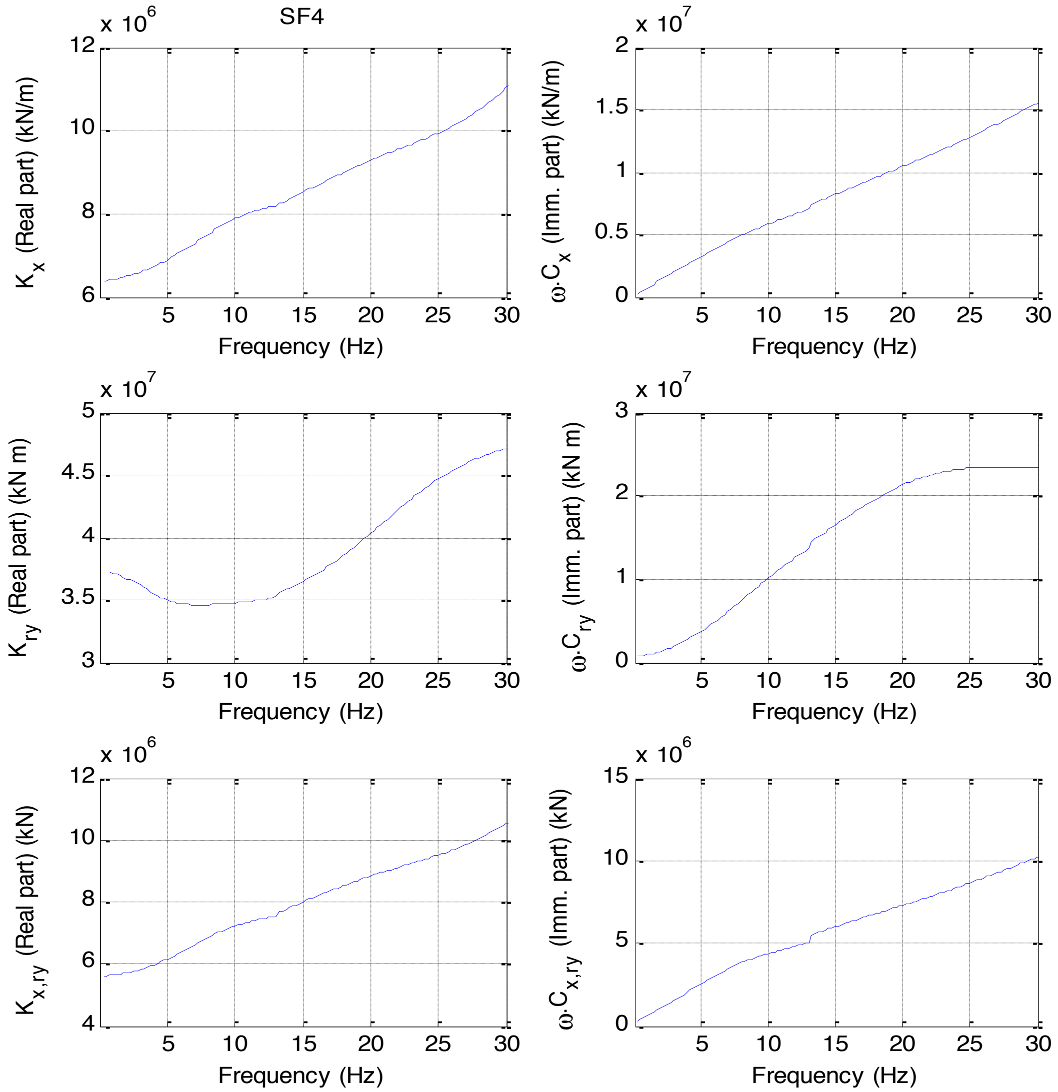

Figure 4.47 Impedance functions for Apartment blocks "K-flat" and "Georg Van S" – Fixed head conditions, floating piles: horizontal translation, rocking and coupling term – Soil type A, Scaling factor SF4.

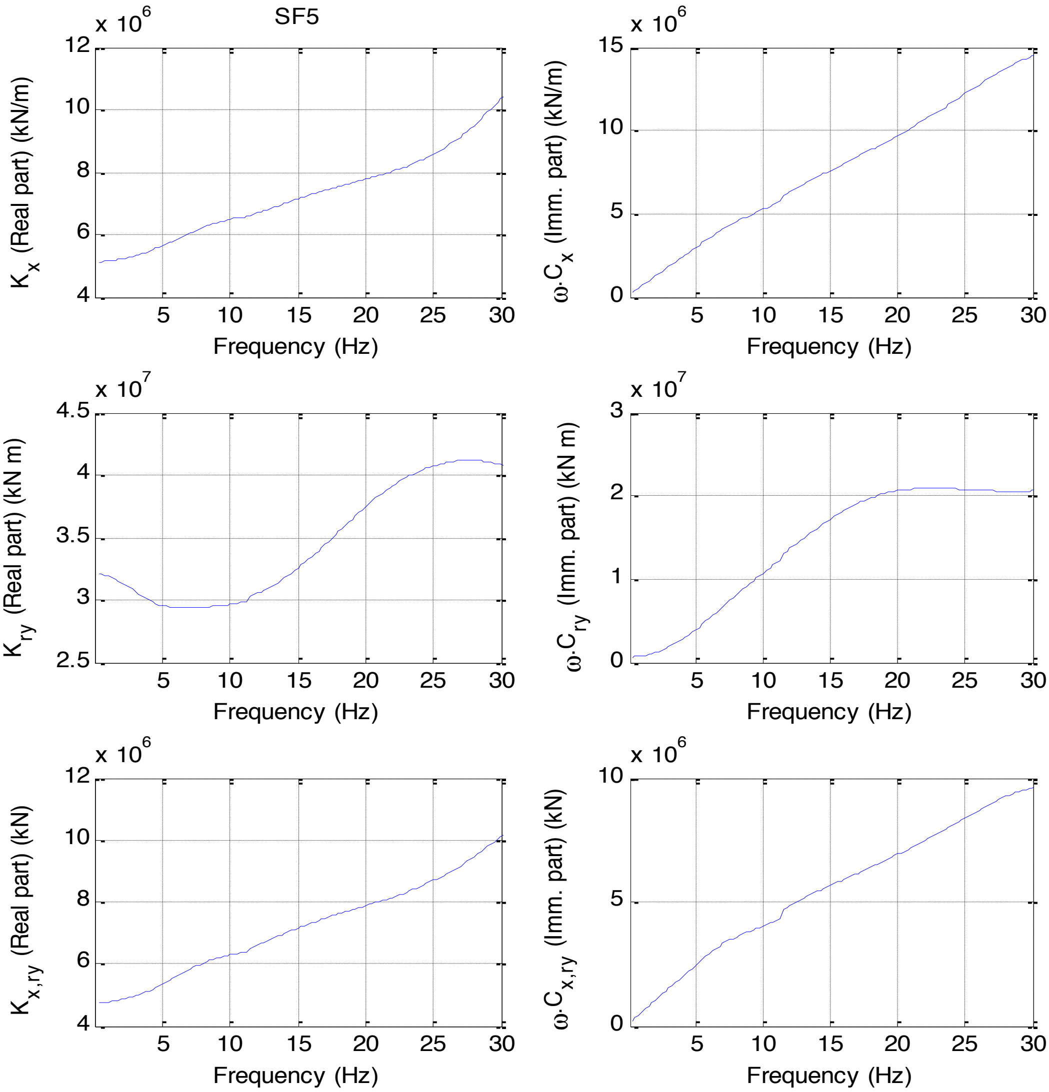

Figure 4.48 Impedance functions for Apartment blocks "K-flat" and "Georg Van S" – Fixed head conditions, floating piles: horizontal translation, rocking and coupling term – Soil type A, Scaling factor SF5.

4.4 One-dimensional frequency-independent model

The first SSI model following the substructure approach in this work is a one-dimensional frequency-independent model, having a lateral spring with stiffness k_x and a dashpot with viscous damping coefficient c_x. The values of the stiffness and viscous damping coefficient were obtained using the fundamental frequency of the fixed-base SDOF model together with the impedance functions derived for the Groningen field. The seismic excitation is input to the system as an acceleration time history, $a(t)$, applied to the fixed support at the base.

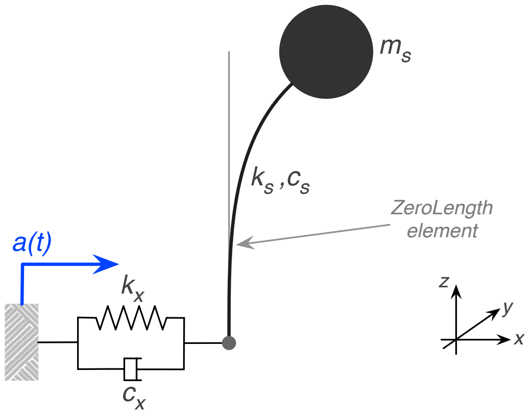

Figure 4.49: The adopted one-dimensional frequency-independent model.

4.4.1 Properties of the SSI elastic 1-D systems for all index buildings

This section summarises the properties of the SSI 1-D systems that were used in the derivation of fragility functions for all index buildings. Such properties were obtained by using the impedance functions presented in Sections 4.2 and 4.3, for footings and piles respectively. Since the computation of these impedances was based on the equivalent macro-element properties, some sets of functions were used for more than one building, characterised by the same equivalent macro-element. However, for each index building a unique set of SSI 1-D properties was derived, because the calibration is based on the building's first natural frequency.

The following tables, from Table 4.10 to Table 4.17, report the retrieved properties of the SSI 1-D systems for terraced, detached and apartment index buildings, in terms of stiffness and damping coefficient, for all five scaling factors considered.

Table 4.10: Properties of the SSI 1-D system for Zijlvest index building.

	SF1	SF2	SF3	SF4	SF5
k_x (kN/m)	7.199E+06	5.710E+06	4.545E+06	3.679E+06	2.575E+06
c_x (ton/s)	8.590E+04	7.693E+04	7.014E+04	6.502E+04	5.613E+04

Table 4.11: Properties of the SSI 1-D system for Kwelder index building.

	SF1	SF2	SF3	SF4	SF5
k_x (kN/m)	2.960E+06	2.383E+06	1.977E+06	1.682E+06	1.223E+06
c_x (ton/s)	2.447E+04	2.204E+04	2.001E+04	1.842E+04	1.580E+04

Table 4.12: Properties of the SSI 1-D system for Badweg index building.

	SF1	SF2	SF3	SF4	SF5
k_x (kN/m)	2.347E+06	1.887E+06	1.592E+06	1.353E+06	9.741E+05
c_x (ton/s)	1.466E+04	1.307E+04	1.191E+04	1.100E+04	9.373E+03

Table 4.13: Properties of the SSI 1-D system for Dijkstraat index building.

	SF1	SF2	SF3	SF4	SF5
k_x (kN/m)	3.650E+06	2.911E+06	2.380E+06	1.991E+06	1.404E+06
c_x (ton/s)	3.408E+04	3.019E+04	2.731E+04	2.506E+04	2.118E+04

Table 4.14: Properties of the SSI 1-D system for De Haver index building.

	SF1	SF2	SF3	SF4	SF5
k_x (kN/m)	4.737E+06	3.834E+06	3.180E+06	2.705E+06	1.969E+06
c_x (ton/s)	1.208E+05	1.077E+05	9.800E+04	8.944E+04	7.540E+04

Table 4.15: Properties of the SSI 1-D system for Drive-in index building.

	SF1	SF2	SF3	SF4	SF5
k_x (kN/m)	7.488E+06	6.576E+06	5.868E+06	5.321E+06	4.394E+06
c_x (ton/s)	6.205E+04	5.911E+04	5.653E+04	5.456E+04	5.020E+04

Table 4.16: Properties of the SSI 1-D system for K-Flat index building.

	SF1	SF2	SF3	SF4	SF5
k_x (kN/m)	9.545E+06	8.295E+06	7.319E+06	6.570E+06	5.302E+06
c_x (ton/s)	1.188E+05	1.133E+05	1.085E+05	1.047E+05	9.733E+04

Table 4.17: Properties of the SSI 1-D system for Georg van S index building.

	SF1	SF2	SF3	SF4	SF5
k_x (kN/m)	9.849E+06	8.607E+06	7.643E+06	6.900E+06	5.647E+06
c_x (ton/s)	1.136E+05	1.085E+05	1.042E+05	1.005E+05	9.423E+04

4.5 Lumped-Parameter Model (LPM)

The second SSI model following the substructure approach in this work is a Lumped-Parameter Model (LPM) accounting for frequency dependence of the impedance functions.

Even though techniques are available to describe frequency dependence of any type through a generalised LPM whose form is not known in advance (Lesgidis et al., 2015), this work adopted the simplest LPM capable of describing approximately, over the frequency range of interest, the features of two components of impedance, namely the translational and rotational terms.

The LPM model proposed by the RINTC Workgroup (2018), which is an extension of the model by Dezi et al. (2009) and Carbonari et al. (2011, 2012, 2018), was taken as a reference. Two variants of such model were implemented, related to shallow and pile foundations, respectively. They are described in Sections 4.5.1 and 4.5.2.

4.5.1 LPM for shallow foundations

For shallow foundations, the model proposed by the RINTC Workgroup was simplified in order to neglect the rocking-sway coupling. The adopted system is shown in Figure 4.50.

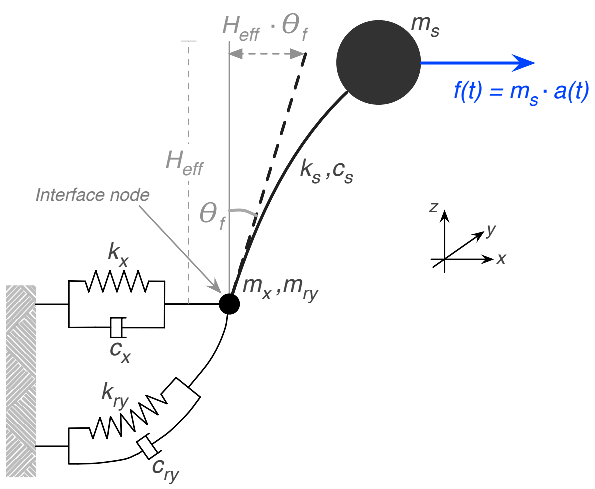

Figure 4.50: The adopted Lumped-Parameter Model for shallow foundations.

The crucial feature of this LPM is the introduction of a translational fictitious (non-physical) mass m_x in the interface node (representing the foundation), linked to the ground by a translational spring (of constant k_x) and by a dashpot (of constant c_x). This system is characterised by a frequency-dependent response to an input and thus allows for an approximate description of the frequency dependence of the impedance. Expressing the equation of motion of the system without the superstructure in the frequency domain, it can be easily seen that the dynamic impedance decreases parabolically ($k_x - m_x \omega^2$) with frequency, whereas the imaginary part increases linearly ($c_x \omega$) with frequency. In case the foundation mass is taken into account, it is added to the fictitious mass in the same node.

In order to model the foundation rotation, the LPM includes a rotational mass m_{ry} in the interface node, linked to the ground by a rotational spring (of constant k_{ry}) and dashpot (of constant c_{ry}).

The soil portion of the LPM is thus characterised by two independent degrees of freedom. The mass matrix takes the form:

$$\mathbf{M} = \begin{bmatrix} M_{11} & M_{12} \\ M_{12} & M_{22} \end{bmatrix} = \begin{bmatrix} m_x & 0 \\ 0 & m_{ry} \end{bmatrix} \quad (4.7)$$

The stiffness and damping matrices, **K** and **C**, are written similarly. The six diagonal terms of the matrices, namely M_{11}, M_{22}, K_{11}, K_{22}, C_{11}, C_{22}, which are coincident with the parameters of the soil portion of the LPM, are obtained by fitting the two components of impedance (i.e., translational and rotational) with parabolic and linear functions for the real and imaginary parts, respectively. Figure 4.51 shows an example of such fit, for a structural SDOF with first natural frequency of 7.6 Hz. As done for the macro-element case, in order to capture the inertial interaction effects between the superstructure and the foundation, the superstructure mass is placed above the ground at the building centroid height, H_{eff}. Similarly, the seismic acceleration, $a(t)$, is input to the system as an inertia force history, $f(t)$, applied to the superstructure mass: this approach properly considers the inertial components in the presence of the structure (structure and foundation masses and their interaction), resulting in a response in terms of relative displacements with respect to the ground motion.

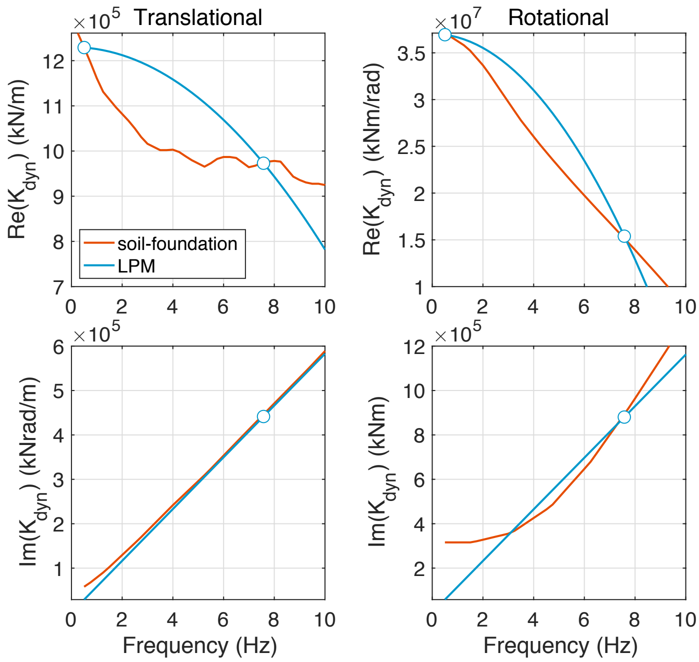

Figure 4.51: Sample fit of real and imaginary parts of two impedance components, in the 0 - 10 Hz frequency range.

4.5.1.1 Properties of the LPM systems for buildings with shallow foundations

This section summarises the properties of the LPM systems that were used in the derivation of fragility functions for shallow foundation index buildings. Such properties were obtained by fitting the impedance functions presented in Section 4.2. Since the computation of these impedances was based on the equivalent macro-element properties, some sets of functions were used for more than one building, characterised by the same equivalent macro-element. However, for each index building a unique set of LPM properties was derived, because the impedance fit is based on the building's first natural frequency.

The following tables, from Table 4.18 to Table 4.22, report the retrieved properties of the LPM systems for all terraced and detached index buildings, in terms of mass, stiffness and damping coefficients, for all five scaling factors considered.

Table 4.18: Properties of the LPM for Zijlvest index building.

	SF1	SF2	SF3	SF4	SF5
m_x (ton)	7.282E+03	5.808E+03	4.999E+03	4.580E+03	3.793E+03
m_{ry} (ton*m^2)	4.740E+05	4.508E+05	4.215E+05	3.950E+05	3.413E+05
k_x (kN/m)	9.709E+06	7.788E+06	6.407E+06	5.406E+06	3.848E+06
k_{ry} (kNm/rad)	7.683E+08	6.216E+08	5.154E+08	4.377E+08	3.172E+08
c_x (ton/s)	8.050E+04	7.207E+04	6.545E+04	6.052E+04	5.207E+04
c_{ry} (ton*m^2/s)	7.059E+04	5.817E+04	4.913E+04	4.249E+04	3.202E+04

Table 4.19: Properties of the LPM for Kwelder index building.

	SF1	SF2	SF3	SF4	SF5
m_x (ton)	2.727E+02	2.209E+02	1.811E+02	1.520E+02	1.069E+02
m_{ry} (ton*m^2)	1.435E+04	1.296E+04	1.190E+04	1.114E+04	9.903E+03
k_x (kN/m)	4.695E+06	3.780E+06	3.123E+06	2.644E+06	1.899E+06
k_{ry} (kNm/rad)	1.329E+08	1.074E+08	8.903E+07	7.585E+07	5.509E+07
c_x (ton/s)	2.414E+04	2.177E+04	1.976E+04	1.819E+04	1.559E+04
c_{ry} (ton*m^2/s)	2.947E+04	2.769E+04	2.624E+04	2.494E+04	2.259E+04

Table 4.20: Properties of the LPM for Badweg index building.

	SF1	SF2	SF3	SF4	SF5
m_x (ton)	2.926E+02	2.403E+02	1.826E+02	1.529E+02	1.135E+02
m_{ry} (ton*m^2)	1.470E+04	1.332E+04	1.216E+04	1.123E+04	9.553E+03
k_x (kN/m)	3.013E+06	2.427E+06	2.006E+06	1.703E+06	1.230E+06
k_{ry} (kNm/rad)	8.948E+07	7.230E+07	5.996E+07	5.107E+07	3.703E+07
c_x (ton/s)	1.452E+04	1.293E+04	1.179E+04	1.088E+04	9.275E+03
c_{ry} (ton*m^2/s)	2.513E+04	2.317E+04	2.152E+04	2.030E+04	1.849E+04

Table 4.21: Properties of the LPM for Dijkstraat index building.

	SF1	SF2	SF3	SF4	SF5
m_x (ton)	2.350E+03	1.998E+03	1.733E+03	1.564E+03	1.222E+03
m_{ry} (ton*m^2)	4.901E+04	4.798E+04	4.749E+04	4.653E+04	4.345E+04
k_x (kN/m)	4.355E+06	3.511E+06	2.900E+06	2.460E+06	1.770E+06
k_{ry} (kNm/rad)	1.550E+08	1.254E+08	1.040E+08	8.853E+07	6.442E+07
c_x (ton/s)	3.402E+04	3.013E+04	2.725E+04	2.501E+04	2.114E+04
c_{ry} (ton*m^2/s)	2.403E+05	1.989E+05	1.702E+05	1.530E+05	1.245E+05

Table 4.22: Properties of the LPM for De Haver index building.

	SF1	SF2	SF3	SF4	SF5
m_x (ton)	1.897E+03	1.509E+03	1.230E+03	1.029E+03	7.140E+02
m_{ry} (ton*m²)	5.448E+04	4.891E+04	4.454E+04	4.118E+04	3.545E+04
k_x (kN/m)	9.530E+06	7.647E+06	6.288E+06	5.305E+06	3.773E+06
k_{ry} (kNm/rad)	2.721E+08	2.199E+08	1.821E+08	1.550E+08	1.125E+08
c_x (ton/s)	1.208E+05	1.077E+05	9.797E+04	8.942E+04	7.538E+04
c_{ry} (ton*m²/s)	2.454E+05	2.310E+05	2.183E+05	2.081E+05	1.887E+05

4.5.2 LPM for pile foundations

For pile foundations, the model proposed by the RINTC Workgroup was implemented "as is", thus accounting for the rocking-sway coupling. The latter is achieved by adding a translational mass, spring and dashpot ($m_{x,ry}$, $k_{x,ry}$, $c_{x,ry}$), connected to the interface node by three rigid links of length h_m, h_k and h_c, respectively. The adopted system is shown in Figure 4.52.

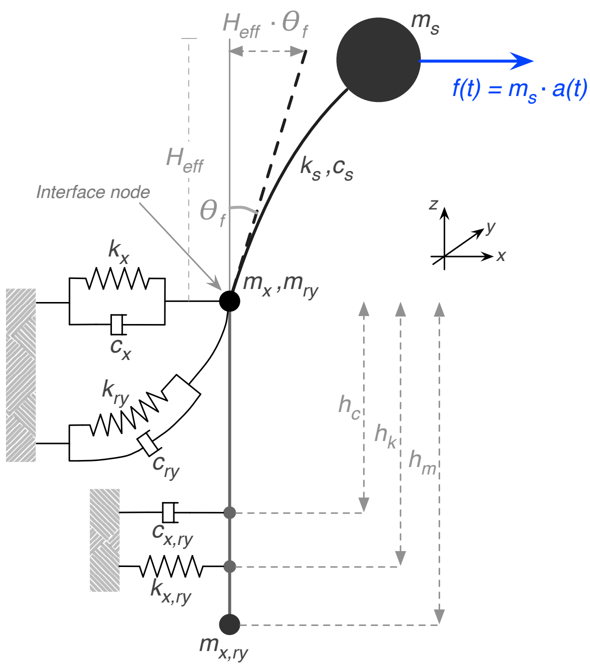

Figure 4.52: The adopted Lumped-Parameter Model for deep foundations.

The soil portion of the LPM is characterised by three degrees of freedom, but only two of them are independent, due to the presence of rigid links. The mass matrix thus takes the form:

$$\mathbf{M} = \begin{bmatrix} M_{11} & M_{12} \\ M_{12} & M_{22} \end{bmatrix} = \begin{bmatrix} m_x + m_{x,ry} & h_m \cdot m_{x,ry} \\ h_m \cdot m_{x,ry} & m_{ry} + h_m^2 \cdot m_{x,ry} \end{bmatrix} \tag{4.8}$$

The stiffness and damping matrices, **K** and **C**, are written similarly. The following relationships hold for mass:

$$\begin{cases} m_{x,ry} = M_{12}/h_m \\ m_x = M_{11} - M_{12}/h_m \\ m_{ry} = M_{22} - h_m \cdot M_{12} \end{cases} \tag{4.9}$$

and similarly for stiffness and damping, for a total of nine equations. Such equations have twelve unknowns and hence the heights h_m, h_k and h_c must be assigned arbitrarily. Since all matrices must be positive definite, nine inequalities must be satisfied. For masses it is possible to write:

$$M_{11} > 0, \quad M_{22} > 0, \quad M_{12}^2 < M_{11} \cdot M_{22} \tag{4.10}$$

and similarly for stiffness and damping. Likewise, the LPM parameters must be positive definite, resulting in further conditions, here reported only for the mass terms:

$$m_{x,ry} > 0, \quad m_x > 0, \quad m_{ry} > 0, \quad h_m > M_{12}/M_{11}, \quad h_m < M_{22}/M_{12} \tag{4.11}$$

The nine terms of the matrices, namely M_{11}, M_{22}, M_{12}, K_{11}, K_{22}, K_{12}, C_{11}, C_{22}, C_{12}, are obtained by fitting the available three components of impedance (translational, rotational and roto-translational) with parabolic and linear functions for the real and imaginary parts, respectively. Figure 4.53 shows an example of such fit, for a structural SDOF with first natural frequency of 5.6 Hz. It can be noted that some components of the real part, in particular the translational and roto-translational, are increasing in the low frequency range. This is somehow expected, since these functions are related not to the single pile but to groups of piles: in this case the impedance is function of the spacing over diameter ratio and can be actually increasing in a given frequency range. For these components, the same parabolic decreasing function had to be adopted for consistency with the employed LPM model, but it was set to be almost constant in order to be as close as possible to the target impedance.

Given the three matrices, the parameters of the soil portion of the LPM are then retrieved by assigning the three heights and using Eq. (4.9) and the inequalities above.

The seismic acceleration, $a(t)$, is input to the system as an inertia force history, $f(t)$, applied to the superstructure mass: this approach properly considers the inertial components in the presence of the structure (structure and foundation masses and their interaction), resulting in a response in terms of relative displacements with respect to the ground motion.

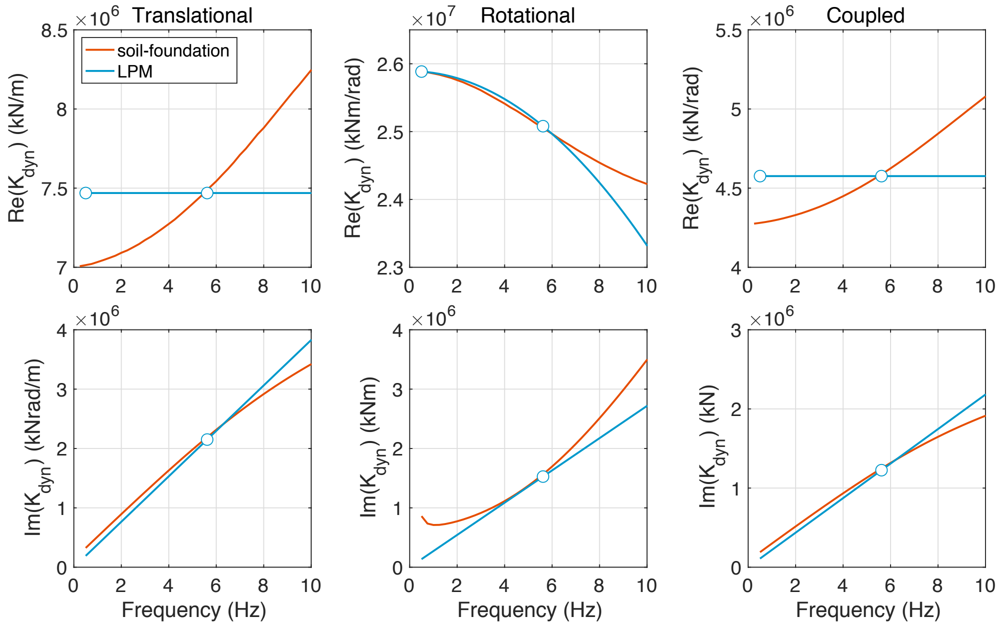

Figure 4.53: Sample fit of real and imaginary parts of three impedance components, in the 0 - 10 Hz frequency range.

4.5.2.1 Properties of the LPM systems for buildings with pile foundations

This section summarises the properties of the LPM systems that were used in the derivation of fragility functions for pile foundation index buildings. Such properties were obtained by fitting the impedance functions presented in Section 4.3.

The following tables, from Table 4.23 to Table 4.25, report the retrieved properties of the LPM systems for all apartment index buildings, in terms of mass, stiffness, damping coefficients and length of rigid links, for all five scaling factors considered.

Table 4.23: Properties of the LPM for Drive-in index building.

	SF1	SF2	SF3	SF4	SF5
m_x (ton)	5.810E-03	5.100E-03	4.540E-03	4.110E-03	3.390E-03
m_{ry} (ton*m²)	6.512E+02	7.806E+02	9.060E+02	1.011E+03	1.214E+03
$m_{x,ry}$ (ton)	2.300E-04	2.100E-04	1.900E-04	1.800E-04	1.500E-04
h_m (m)	16	16	16	16	16
k_x (kN/m)	6.325E+06	5.527E+06	4.907E+06	4.429E+06	3.622E+06
k_{ry} (kNm/rad)	7.587E+06	7.271E+06	6.930E+06	6.588E+06	5.831E+06
$k_{x,ry}$ (kN/m)	1.144E+06	1.032E+06	9.427E+05	8.732E+05	7.532E+05
h_k (m)	4	4	4	4	4
c_x (ton/s)	2.619E+04	2.420E+04	2.249E+04	2.130E+04	1.860E+04
c_{ry} (ton*m²/s)	8.521E+03	4.700E+03	4.124E+03	4.409E+03	7.417E+03
$c_{x,ry}$ (ton/s)	3.473E+04	3.385E+04	3.304E+04	3.231E+04	3.077E+04
h_c (m)	1	1	1	1	1

Table 4.24: Properties of the LPM for K-Flat index building.

	SF1	SF2	SF3	SF4	SF5
m_x (ton)	3.110E-02	2.698E-02	2.376E-02	2.130E-02	1.713E-02
m_{ry} (ton*m^2)	1.935E+03	2.378E+03	2.824E+03	3.232E+03	4.132E+03
$m_{x,ry}$ (ton)	1.650E-03	1.480E-03	1.350E-03	1.240E-03	1.060E-03
h_m (m)	16	16	16	16	16
k_x (kN/m)	7.619E+06	6.565E+06	5.745E+06	5.119E+06	4.066E+06
k_{ry} (kNm/rad)	1.652E+07	1.572E+07	1.488E+07	1.407E+07	1.232E+07
$k_{x,ry}$ (kN/m)	1.925E+06	1.729E+06	1.573E+06	1.449E+06	1.235E+06
h_k (m)	4	4	4	4	4
c_x (ton/s)	2.365E+04	1.980E+04	1.653E+04	2.113E+04	1.592E+04
c_{ry} (ton*m^2/s)	2.819E+04	1.930E+04	1.295E+04	1.596E+04	1.174E+04
$c_{x,ry}$ (ton/s)	9.466E+04	9.295E+04	9.152E+04	8.306E+04	8.097E+04
h_c (m)	1	1	1	1	1

Table 4.25: Properties of the LPM for Georg van S index building.

	SF1	SF2	SF3	SF4	SF5
m_x (ton)	9.470E-03	8.260E-03	7.320E-03	6.600E-03	5.380E-03
m_{ry} (ton*m^2)	1.575E+03	1.873E+03	2.133E+03	2.303E+03	2.498E+03
$m_{x,ry}$ (ton)	5.100E-04	4.600E-04	4.200E-04	3.900E-04	3.400E-04
h_m (m)	16	16	16	16	16
k_x (kN/m)	7.845E+06	6.793E+06	5.980E+06	5.355E+06	4.307E+06
k_{ry} (kNm/rad)	1.532E+07	1.443E+07	1.351E+07	1.262E+07	1.070E+07
$k_{x,ry}$ (kN/m)	2.000E+06	1.809E+06	1.658E+06	1.540E+06	1.335E+06
h_k (m)	4	4	4	4	4
c_x (ton/s)	2.646E+04	2.292E+04	1.990E+04	2.112E+04	1.639E+04
c_{ry} (ton*m^2/s)	3.146E+04	3.034E+04	3.182E+04	3.802E+04	4.700E+04
$c_{x,ry}$ (ton/s)	8.657E+04	8.509E+04	8.379E+04	7.890E+04	7.735E+04
h_c (m)	1	1	1	1	1

5 Impact of SSI on fragility functions

The development of fragility functions for buildings in the Groningen region is beyond the scope of this work and interested readers are instead referred to Crowley et al. (2019). Nonetheless, in order to gain confidence on the results that were obtained using the different SSI methodologies described above, in particular that using the nonlinear macro-element, it was felt to be important to assess how these influenced the fragility functions of the considered buildings.

The obtained fragility curves for the collapse limit state and for the five investigated index buildings on shallow foundations are shown in Figure 5.1. Each subplot displays the curves related to: i) one-dimensional frequency independent model, ii) Lumped Parameter Model, and iii) the nonlinear macro-element. The curve for the fixed-base case is also displayed for reference. It can be noted, in general, that for these buildings with shallow foundations the influence of SSI is small to negligible, and leads the curves to be shifted to the right with respect to the fixed-base case; this means that SSI may have a beneficial effect on the seismic vulnerability of these buildings.

It is also interesting to notice how, for the stiffer and stronger Kwelder detached house, the response of the relatively weak soil plays a more determinant role in the overall fragility of the system, and hence not only the impact of the SSI modelling becomes more evident, but so does also the significance of explicitly considering the nonlinear response of the soil-foundation system.

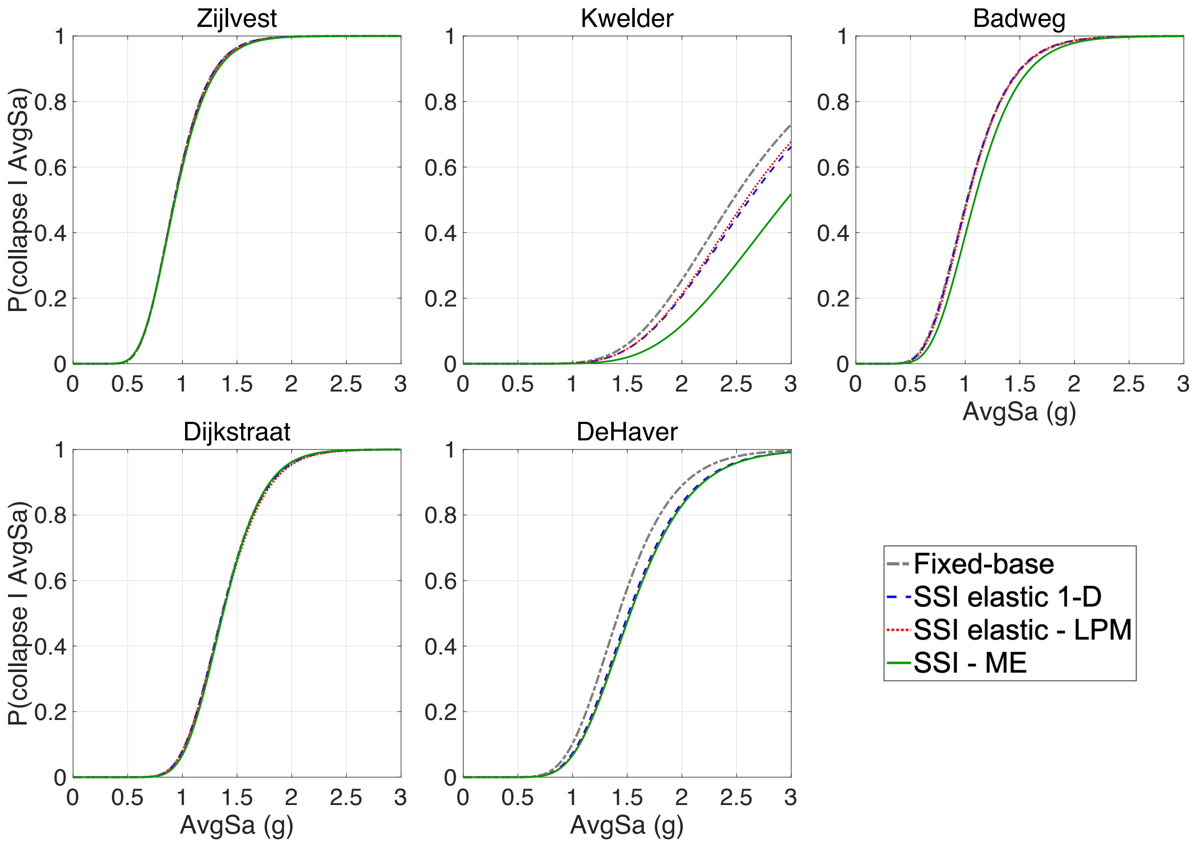

Figure 5.1: Proposed fragility curves for the investigated index buildings on shallow foundations and the different SSI models.

Figure 5.2 presents the obtained collapse fragility curves for the three investigated index buildings on pile foundations. These taller and stronger buildings are more affected by the rocking response of the foundation system, which is visible in the different SSI modelling approaches. A beneficial effect of SSI is also quite visible for the Drive-in and Koeriersterweg buildings, with the fragility curves shifted to the right. Moreover, taking into account the nonlinear response of the foundation system, through the use of the macro-elements, is shown to have a non-negligible influence on the seismic vulnerability of these buildings.

For the GeorgVanS building, a trend opposite to that observed for K-flat, which has similar values of foundation impedances and capacity (and which are larger than the ones of Drive-in), is observed. Being GeorgVanS a stiffer and taller building, it is indeed expected that SSI has a larger influence in its dynamic response, as visible in the elastic SSI fragility curves (which for K-flat coincide instead with the fixed-base case). This effect can also be observed in Drive-in, which is also a stiffer building (albeit not as tall), and for which the elastic SSI fragility functions also deviate from the fixed-base case. One can also note that the SSI 1-D model leads to smaller changes than the LPM one, because it does not include a rocking response, which is dominant for these buildings.

In addition, the period elongation experienced by the GeorgVanS building during its dynamic response proves to be detrimental in terms of SSI effects, as clearly indicated by an LPM fragility curve shifted to the left. Still, the beneficial effect of considering soil nonlinearity in the macro-element model is visible also in this case, with the corresponding fragility curve shifted to the right of the LPM one.

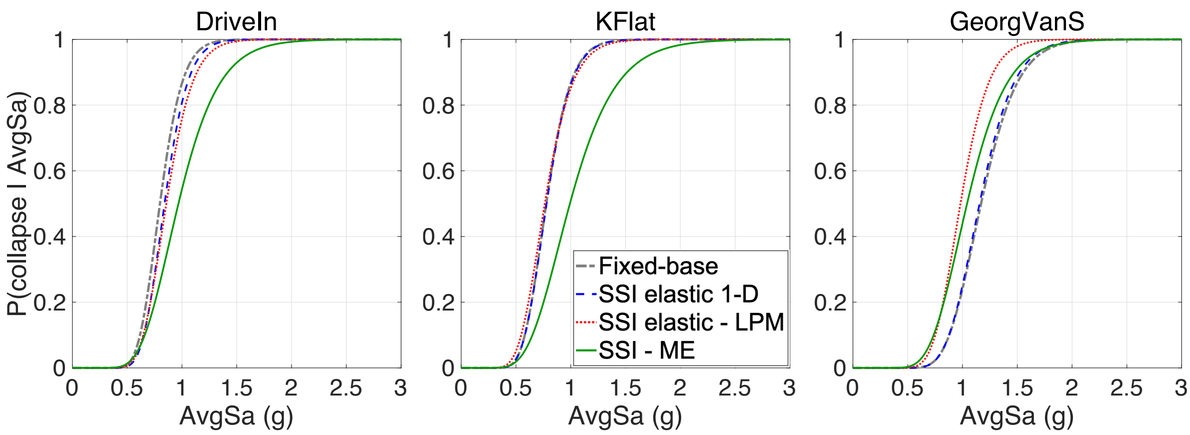

Figure 5.2: Proposed fragility curves for the investigated index buildings on pile foundations and the different SSI models.

Closing remarks

This work described the calibration of an SSI nonlinear macro-element to be used in the development of fragility functions for buildings in the Groningen region. Further, in order to gain confidence on the latter, calibration of two alternative SSI approaches (one-dimensional frequency independent model and Lumped Parameter Model) was also carried out, and the results compared in terms of their impact on fragility functions.

It was shown that the results obtained with the three different models presented similar trends, which is reassuring. In some cases, the nonlinear macro-element led to slight variations in fragility, mostly for stiffer and stronger structures where the response of the relatively weak soil inevitably plays a more determinant role in the overall fragility of the system. This lends further weight to the selection of this approach for the development of the v6 fragility functions.

Considering also that the definition of modelling input for the macro-element case is not so dependent on the development of impedance functions, since its response easily departs from the linear elastic case, this is an SSI methodology that we would recommend for future applications, including parametric studies involving the variation of soil parameters.

Acknowledgements

This work would not have been possible without the precious input of Pauline Kruiver, who kindly provided access to the soil mechanical characterisation data and site response analysis results for the Groningen region.

The fundamental assistance of Stelios Antoniou and Thanasis Farantos on the implementation in SeismoStruct of the nonlinear macro-element is also very gratefully acknowledged.

References

Arup [2015a] *Soil-Structure Interaction for Linear Analysis - Groningen Earthquakes - Structural Upgrading*, Report N. 229746_032.0_REP102. Issue Rev.0.04 | 16 February 2015.

Arup [2015b] *Soil-Structure Interaction for Nonlinear Static Analysis - Groningen Earthquakes - Structural Upgrading*, Report N. 229746_032.0_REP118. Issue Rev.0.02 | 27 February 2015.

Arup [2017] *Typology modelling: Analysis results in support of fragility functions – 2017 batch results*. Report N. 229746_031.0_REP2005. NAM Platform, November 2017.

Arup [2017] *EDB V5 Data Documentation*, Tech. Rep. 229746_052.0_REP2005. NAM Platform, November 2017.

Arup [2019] *Typology modelling: Analysis results in support of fragility functions – 2018-2019 batch results*, June 2019.

Been, K., Jefferies, M.G. [1985] "A state parameter for sands," *Geotechnique*, Vol. 35, No. 2, pp. 99-112.

Bolton, M.D. [1986] "The Strength and Dilatancy of Sands," *Géotechnique*, Vol. 36, No. 1, pp. 65–78.

Bommer, J.J., Dost B., Edwards, B., Kruiver, P.P., Meijers, P., Ntinalexis, M., Polidoro, B., Rodriguez-Marek, A., Stafford, P.J. [2015] *Development of Version 2 GMPEs for response spectral accelerations and significant durations from induced earthquakes in the Groningen field*. NAM Platform, October 2015.

Bommer, J.J., Dost, B., Edwards, B., Stafford, P.J., van Elk, J., Doornhof, D., Ntinalexis, M. [2016] "Developing an application-specific ground motion model for induced seismicity," *Bulletin of the Seismological Society of America*, Vol. 106, No. 1, pp. 158–173.

Bommer, J.J., Stafford, P.J., Edwards, B., Dost, B., van Dedem, E., Rodriguez-Marek, A., Kruiver, P.P., van Elk, J., Doornhof, D., Ntinalexis, M. [2017] "Framework for a ground-motion model for induced seismic hazard and risk analysis in the Groningen gas field, The Netherlands," *Earthquake Spectra*, Vol. 33, No. 2, pp. 481–498.

Bommer, J.J., Dost B., Edwards, B., Kruiver, P.P., Meijers, P., Ntinalexis, M., Rodriguez-Marek, A., Ruigrok, E., Spetzler, J., Stafford, P.J. [2017] *V4 Ground motion model (GMM) for response spectral accelerations, peak ground velocities, and significant durations in the Groningen field – version 2*. NAM Platform, June 2017.

Bommer, J.J., Edwards, B., Kruiver, P.P., Rodriguez-Marek, A., Stafford, P.J., Dost, B., Ntinalexis, M., Ruigrok, E., Spetzler, J. [2018] *V5 ground-motion model for the Groningen Field - revision 1*, NAM Platform, March 2018.

Brinch-Hansen, J.A. [1970] *A revised and extended formula for bearing capacity*. Bulletin N.28, Danish Geotechnical Institute.

British Standard 8002 [2015] *Code of practice for earth retaining structures*. British Standards Institution, UK.

Butterfield, R., Gottardi, G. [1994] "A complete three-dimensional failure envelope for shallow footings on sand," *Géotechnique*, Vol. 44, No. 1, pp. 181–184.

Carbonari, S., Dezi, F., Leoni, G. [2011] "Linear soil–structure interaction of coupled wall–frame structures on pile foundations," *Soil Dynamics and Earthquake Engineering*, Vol. 31, No. 9, pp. 1296-1309.

Carbonari, S., Dezi, F., Leoni, G. [2012] "Nonlinear seismic behaviour of wall-frame dual systems accounting for soil-structure interaction," *Earthquake Engineering & Structural Dynamics*, Vol. 41, No. 12, pp. 1651-1672.

Carbonari, S., Morici, M., Dezi, F., Leoni, G. [2018] "A lumped parameter model for time-domain inertial soil-structure interaction analysis of structures on pile foundations," *Earthquake Engineering & Structural Dynamics*, Vol. 47, No. 11, pp. 2147-2171.

CEN - Comité Européen de Normalisation [2004] *Eurocode 7: Geotechnical design - Part 1: General rules*. ENV 1997:1-1994, 2004.

CEN - Comité Européen de Normalisation [2004] *Eurocode 8: Design of structures for earthquake resistance Part 5: Foundations, retaining structures and geotechnical aspects.* ENV 1998:5-2004.

Chatzigogos, C.T., Figini, R., Pecker, A., Salençon, J. [2011] "A macroelement formulation for shallow foundations on cohesive and frictional soils," *Int. Journal of Numerical and Analytical Methods in Geomechanics*, Vol. 35, No. 8, pp. 902-931.

Correia, A.A. [2011] *A pile-head macro-element approach to seismic design of monoshaft-supported bridges*, Ph.D. Thesis, European School for Advanced Studies in Reduction of Seismic Risk (ROSE School), Pavia, Italy.

Correia, A.A., Pecker, A., Kramer, S.L., Pinho, R. [2012] "A pile-head macro-element approach to seismic design of extended pile-shaft-supported bridges," in *Proceedings of the Second International Conference on Performance-Based Design in Geotechnical Earthquake Engineering*, Taormina (Italy), 28-30 May 2012.

Correia, A.A. [2013] "Recent advances on macro-element modeling: shallow and deep foundations," in *Final workshop of project Compatible soil and structure yielding to improve system performance (CoSSY)*, Oakland, USA.

Correia, A.A., Paolucci, R. [2019] "A 3D coupled nonlinear shallow foundation macro-element for seismic soil-structure interaction analysis," *Earthquake Engineering and Structural Dynamics*, submitted for publication.

Correia, A.A., Pecker, A. [2019] " Nonlinear pile-head macro-element for the seismic analysis of structures on flexible piles," *Bulletin of Earthquake Engineering*, submitted for publication.

Crowley, H., Pinho, R., Polidoro, B., Stafford, P. [2015] *Development of v2 partial collapse fragility and consequence functions for the Groningen field*. NAM Platform, November 2015.

Crowley, H., Pinho, R. [2017] *Report on the v5 fragility and consequence models for the Groningen field*. NAM Platform, November 2017.

Crowley, H., Polidoro, B., Pinho, R., van Elk, J. [2017] "Framework for developing fragility and consequence models for local personal risk," *Earthquake Spectra*, Vol. 33, No. 4, pp. 1325–1345.

Crowley, H., Pinho, R., Cavalieri, F. [2019] *Report on the v6 Fragility and Consequence Models for the Groningen Field*. NAM Platform, March 2019.

Crux Engineering [2014] *Appendix C BV Reports (229746/032.0/REP102)*, 28 Apr 2014.

Cunning, J.C., Robertson, P.K., Sego, D.C. [1995] "Shear wave velocity to evaluate in situ state of cohesionless soils," *Canadian Geotechnical Journal*, Vol. 32, pp. 848-858.

Darendeli, M. (2001). *Development of a new family of normalized modulus reduction and material damping curves*, Ph.D. Thesis, Department of Civil Engineering, University of Texas, Austin, Texas.

Dezi, F., Carbonari, S., Leoni, G. [2009] "A model for the 3D kinematic interaction analysis of pile groups in layered soils," *Earthquake Engineering & Structural Dynamics*, Vol. 38, No. 11, pp. 1281-1305.

Dezi, F., Carbonari, S., Leoni, G. [2010] "Kinematic bending moments in pile foundations," *Soil Dynamics and Earthquake Engineering*, Vol. 30, No. 3, pp. 119-132.

Fear, C.E., Robertson, P.K. [1995] "Estimating the undrained strength of sand: a theoretical framework," *Canadian Geotechnical Journal*, Vol. 32, pp. 859-870.

Figini, R., Paolucci, R., Chatzigogos, C.T. [2012] "A macro-element model for non-linear soil shallow foundation-structure interaction under seismic loads: theoretical development and experimental validation on large scale tests," *Earthquake Engineering and Structural Dynamics*, Vol. 41, No. 3, pp. 475-493.

Gazetas G. [1991] "Foundation vibrations," in *Foundations Engineering Handbook, 2nd edition*, Fang H.Y. (Editor), New York, Van Nostrand Reinholds, pp. 553–593, chapter 15.

GRC - Geotechnical Research Centre of Western Ontario University [2015] *DYNA6.1 – A program for the computation of the response of rigid foundations to all types of dynamic loads*. Ontario, Canada.

Klar, A., Randolph M.F. [2008] "Upper-bound and load–displacement solutions for laterally loaded piles in clays based on energy minimisation," *Géotechnique* , Vol. 58, No. 10, pp. 815-820.

Kramer, S.L. [2007] "Geotechnical Earthquake Engineering," Course Notes, European School for Advanced Studies in Reduction of Seismic Risk (ROSE School), Istituto Universitario di Studi Superiori (IUSS), Pavia, Italy.

Kruiver, P., de Lange, G. [2015] *Geological schematisation of the shallow subsurface of Groningen. For site response to earthquakes for the Groningen gas field. Part I, Part II, Part III.* Deltares. NAM Platform, June 2015.

Kruiver, P.P., Wiersma, A. [2016] *Modification of the geological model for site response at the Groningen field*. Deltares. NAM Platform, June 2016

Kruiver, P.P., Wiersma, A., Kloosteman, F.H., de Lange, G., Korff, M., Stafleu, J., Buscher, F., Harting, R., Gunnink, J.L., [2017a] "Characterisation of the Groningen subsurface for hazard and risk modelling," *Netherlands Journal of Geosciences / Geologie en Mijnbouw*, Vol. 96, No. 5, pp. 215-233.

Kruiver, P.P., van Dedem, E., Romijn, R., de Lange, G., Korff, M., Stafleu, J., Gunnink, J.L., Rodriguez-Marek, A., Bommer, J.J., van Elk, J., Doornhof, D. [2017b] "An integrated shear-wave velocity model for the Groningen gas field, The Netherlands," *Bulletin of Earthquake Engineering*, Vol. 15, No. 9, pp. 3555–3580.

Kruiver, P.P. [2018] *Personal Communications*. Deltares.

Lesgidis, N., Kwon, O.S., Sextos, A. [2015] "A time-domain seismic SSI analysis method for inelastic bridge structures through the use of a frequency-dependent lumped parameter model," *Earthquake Engineering & Structural Dynamics*, Vol. 44, No. 13, pp. 2137-2156.

LSTC—Livermore Software Technology Corporation [2013] *LS-DYNA—a general-purpose finite element program capable of simulating complex problems*. Livermore.

Maljers, D., Stafleu, J., Van der Meulen, M.J., Dambrink, R.M. [2015] "Advances in constructing regional geological voxel models, illustrated by their application in aggregate resource assessments," *Netherlands Journal of Geosciences /Geologie en Mijnbouw*, Vol. 94, pp. 257–270.

Menq, F. Y. [2003] *Dynamic properties of sandy and gravelly soils*, Ph.D. Thesis, Department of Civil Engineering, University of Texas, Austin, Texas.

Meyerhof, G.G. [1953] "The bearing capacity of foundations under eccentric and inclined loads," in *Proceedings of the 3rd International Conference on Soil Mechanics and Foundations Engineering*, Zurich, Vol. 1, pp. 440-445.

Montejo, L.A., Kowalsky, M.J. [2007] *CUMBIA—Set of codes for the analysis of reinforced concrete members*. Technical Report No. IS-07-01, Department of Civil, Construction, and Environmental Engineering. North Carolina University.

Mosayk [2015] *Report on soil-structure interaction (SSI) impedance functions for SDOF systems*. NAM Platform, October 2015.

Mylonakis, G., Gazetas, G. [1998] "Settlement and additional internal forces of grouped piles in layered soil," *Geotechnique*, Vol. 48, No. 1, pp. 55–72.

Mylonakis, G., Nikolaou, S., Gazetas, G. [2006] "Footings under seismic loading: Analysis and design issues with emphasis on bridge foundations," *Soil Dynamics and Earthquake Engineering*, Vol. 26, No. 9, pp. 824-853.

Negussey, D., Wijewickreme, W.K.D., Vaid, Y.P. [1988], "Constant-volume friction angle of granular materials," *Canadian Geotechnical Journal*, Vol. 25, No. 1, pp. 50-55.

Pecker, A., Paolucci, R., Chatzigogos, C., Correia, A.A., Figini, R. [2014] "The role of non-linear dynamic soil–foundation interaction on the seismic response of structures," *Bulletin of Earthquake Engineering*, Vol. 12, No. 3, pp. 1157–1176.

Pianese, G. [2018] *Non-linear effects on the seismic response of buildings with foundation-structure interaction*. Ph.D. Thesis, Politecnico di Milano, Department of Civil and Environmental Engineering, Milano, Italy.

Prearo, C. [2015] *Determination of cyclic resistance of clean sands from cone penetration test based on state parameter*. Ph.D. Thesis. University of Ferrara, Italy.

Randolph, M.F., Wroth, C.P. [1978] "Analysis of deformation of vertically loaded piles," *Journal of Geotechnical Engineering, ASCE*, Vol. 104, No. 12, pp. 1465–1488.

RINTC Workgroup [2018], *Results of the 2015-2017 Implicit seismic risk of code-conforming structures in Italy (RINTC) project*. ReLUIS report, Rete dei Laboratori Universitari di Ingegneria Sismica (ReLUIS), Naples, Italy. Available at http://www.reluis.it/.

Rodriguez-Marek, A., Kruiver, P.P., Meijers, P., Bommer, J.J., Dost, B., van Elk, J., Doornhof, D. [2017] "A Regional Site-Response Model for the Groningen Gas Field," *Bulletin of the Seismological Society of America*, Vol. 107, No. 5, pp. 2067–2077.

Romijn, R. [2017] *Groningen Velocity Model 2017 - Groningen full elastic velocity model*. NAM Platform, September 2017.

Santamarina, J., Cho, G.C. [2001] "Determination of Critical State Parameters in Sandy Soils—Simple Procedure," *Geotechnical Testing Journal*, Vol. 24, No. 2.

Seismosoft, SeismoStruct 2019 [2019] *A computer program for static and dynamic nonlinear analysis of framed structures*. Available at: http://www.seismosoft.com.

Stafleu, J., Maljers, D., Gunnink, J.L., Menkovic, A., Busschers, F.S. [2011] "3D modelling of the shallow subsurface of Zeeland, the Netherlands," *Netherlands Journal of Geosciences*, Vol. 90, No. 4, pp. 293–310.

Stafleu, J., Maljers, D., Busschers, F.S., Gunnink, J.L., Schokker, J., Dambrink, R.M., Hummelman, H.J., Schijf, M.L. [2012] *GeoTOP modellering*. TNO Report 2012-R10991. TNO (Utrecht): 216 pp. Available at www.dinoloket.nl/en/want-know-more.

Stafleu, J., Dubelaar, C.W. [2016] *Product specification Subsurface model GeoTOP*. TNO Report 2016-R10133 v1.3. TNO (Utrecht): 53 pp. Available at www.dinoloket.nl/en/want-know-more.

van der Meulen, M.J., Doornenbal, J.C., Gunnink, J.L., Stafleu, J., Schokker, J., Vernes, R.W., Van Geer, F.C., Van Gessel, S.F., Van Heteren, S., Van Leeuwen, R.J.W., Bakker, M.A.J., Bogaard, P.J.F., Busschers, F.S., Griffoen, J., Gruijters, S.H.L.L., Kiden, P., Schroot, B.M., Simmelink, H.J., Van Berkel, W.O., Van der Krogt, R.A.A., Westerhoff, W.E., Van Daalen, T.M. [2013] "3D geology in a 2D country: perspectives for geological surveying in the Netherlands," *Netherlands Journal of Geosciences / Geologie en Mijnbouw*, Vol. 92, pp. 217–241.

Veletsos, A. S., Wei, Y.T. [1971] "Lateral and rocking vibration of footings," *J. Soil Mech. Found. Div., ASCE*, Vol. 97, pp. 1227-1248.

Veletsos, A.S., Verbic, B. [1973] "Vibration of viscoelastic foundations," *J. Earthquake Engrg. Struct. Dynamics*, Vol. 2, No. 1, pp. 87-102.

Vesic, A.S. [1975] "Bearing capacity of shallow foundations," in *Foundation engineering handbook*. Winterkorn H. F. and Fang H. Y. (Eds): 121-147, New York: van Nostrand Reinhold.

Annex A: A 3D coupled nonlinear shallow foundation macro-element for seismic soil-structure interaction analysis (manuscript by Correia & Paolucci, submitted to Earthquake Engineering and Structural Dynamics)

A 3D COUPLED NONLINEAR SHALLOW FOUNDATION MACRO-ELEMENT FOR SEISMIC SOIL-STRUCTURE INTERACTION ANALYSIS

António A. Correia and Roberto Paolucci

ABSTRACT

During the last two decades, seismic design philosophy has increasingly focused its attention on performance-based design issues related to maximum and residual strains and displacements. However, performance-based earthquake engineering in geotechnical design has its main barrier in the reliable estimation of soil displacements due to the uncertainty on soil properties, its complex and highly nonlinear behaviour and due to the difficulty in assessing soil-structure interaction effects. In order to correctly estimate such displacements, the development of simplified, yet reliable, analysis tools that can be used in seismic design practice is of critical importance.

Macro-element models for shallow foundations are cost-effective tools suitably representing both the nonlinear soil behaviour at near-field and the ground substratum dynamic characteristics at far-field. Hence, all aspects of elastic and inelastic behaviour of the foundation system are encompassed into one computational entity and are described by the behaviour of a single point at the centre of the foundation. No detailed information about the behaviour of the soil mass or individual soil elements is needed nor is available, making the macro-element approach primarily intended to be a design tool. Nevertheless, despite their growing popularity, existing dynamic macro-elements for shallow foundations are not exempt of criticism and improvement: namely, they are not fully consistent and are usually developed for planar loading cases only. For that reason, their innovative concepts and formulations are herein readdressed and further extended.

In this work, a significantly enhanced uplift model is introduced which corrects some inconsistencies of previous approaches. It is based on a nonlinear elastic-uplift response which also considers the cyclic degradation of the contact at the soil/footing interface due to irrecoverable changes in its geometry through a damage model coupled to the inelastic deformations. An improved bounding surface plasticity model is also proposed which builds on the preceding ones in order to reproduce a more general and realistic behaviour, namely in what refers to dynamic loading and unloading/reloading cycles. It includes a new mapping rule for defining the image point and its corresponding directions of plastic deformations, allowing for a better simulation of the evolution of displacements. An innovative cutting-plane type of return mapping algorithm is devised which, unlike previous models, correctly takes into account the simultaneous elastic-uplift and plastic nonlinear responses. Finally, the proposed macro-element formulation is fully applicable to three-dimensional loading cases.

A set of validation analyses is presented, based on results from experimental tests in order to assess and establish the accuracy and capabilities of the proposed model. The encouraging outcome of such validation shows that macro-element models have reached a stage where their application to seismic design is straightforward, leading to a more efficient design and to higher confidence in the predicted structural response. The validation tests are also used for calibrating adequate default values for the small number of parameters of the macro-element.

Keywords: nonlinear macro-element; soil-foundation-structure interaction; shallow foundation; three-dimensional; uplift; bounding surface plasticity.

1. INTRODUCTION

Under earthquake actions, foundation systems are expected to rotate, translate and potentially move vertically (settlement and/or uplift depending on the seismic action and on the structural system). This added flexibility is also related to an added energy dissipation capacity due to soil hysteretic response and due to radiation damping effects. The ensemble of these phenomena is known as soil-structure interaction (SSI) effects, which are well known to be significant for stiff structures on soft soil and negligible for flexible structures on stiff soil.

Typically, the approaches proposed in literature to treat the nonlinear dynamic SSI problems can be broadly divided into direct methods and hybrid methods. Direct methods treat the soil-structure interaction as a global problem, namely with the soil and the structure included within the same numerical model and analysed as a complete system, without decomposing it into subdomains (Lysmer et al., 1975; Prévost, 1999; Anastasopoulos et al., 2011). Analyses with direct methods, such as the finite element method (FEM), are considered to be rigorous and accurate, capable of taking into account foundations of arbitrary complexity, as well as soil heterogeneities and nonlinearities at the foundation level (such as foundation sliding and uplift), but involving exhaustive computational effort and difficulties in the calibration of its parameters, in particular when sophisticated constitutive laws are adopted for the soil behaviour and soil/foundation interface. Hybrid methods have thus been developed as more approachable and less time-consuming analysis, such as the ones based on Winkler and macro-element models. They exploit all the advantages of subdomain decomposition, taking into account the effects of soil heterogeneities and nonlinearities in an approximate way.

Hybrid methods combine the features of both substructure methods and of FEM. Their basic concept is to divide the soil medium into a far-field region and the near-field. The far-field is a domain sufficiently distant from the foundation, and it is governed by the propagation of seismic waves, assuming that nonlinear effects do not occur. It can be modelled by dynamic impedances (Gupta et al., 1980), absorbing boundaries (Bielak and Christiano, 1984), integral equation method (Aubry, 1986), spectral element method (Faccioli et al., 1998), etc. The near-field takes into account all the nonlinearities occurring in the system, as well as all soil heterogeneities. It can be modeled through FEM, Winkler-based models and macro-element models.

In literature, various Winkler-based approaches have been proposed for modelling the rocking response of shallow foundations on either an elastic or inelastic soil medium, and which consider the inelastic actions through the effect of uplift of the foundation (e.g. Wiessing, 1979; Psycharis, 1983; Chopra and Yim, 1984; Yim and Chopra, 1985; Houlsby et al., 2005; Harden et al., 2005; Allotey and El Naggar, 2008; Harden and Hutchinson, 2009). The main advantage of such formulations is that they allow the derivation of a global system response by integration of the local spring responses, which can even be achieved analytically in case the soil behaviour is linear. On the other side, these Beam on Nonlinear Winkler Foundation (BNWF) models are subject to the major limitation of its inability to account correctly for the coupling of vertical, moment and shear deformations of the soil and, in general, its inability to deal with arbitrary computations of loading from vertical and horizontal forces and overturning moments, which is a typical situation during seismic excitation. Besides, difficulties in parameters' calibration and in model discretization (namely spacing between springs) are other critical issues of BNWF approaches.

In the category of hybrid approaches, the macro-element concept has been introduced to model the near-field soil-foundation behaviour by condensing the entire soil-foundation system into a single nonlinear element at the base of the superstructure. Such element aims at reproducing the nonlinear SSI effects taking place at the vicinity of the foundation. The linear response of the soil at the far-field is governed by the propagation of seismic waves and modelled with the concept of dynamic impedances, which, through the use of spring and dashpot elements, represent the global elastic stiffness of the system and the radiation of seismic waves away from the foundation. The general structure of such model is shown in Figure 1.

The macro-element framework has been developed by the earthquake engineering community during the last 20 years, and is now frequently adopted in research studies, because seismic design philosophy has increasingly focused its attention on performance-based design issues related to maximum and residual strains and displacements. These are directly related to the level of structural damage and subsequent repair and strengthening effort, as well as to the evermore important downtime of critical facilities and lifelines. However, performance-based earthquake engineering in geotechnical design has its main barrier in the reliable estimation of soil displacements due to the uncertainty on soil properties, its complex and highly nonlinear behaviour and due to the difficulty in assessing SSI effects. In order to correctly estimate such displacements, the development of simplified, yet reliable, analysis tools that can be used in everyday practice of structural and geotechnical design is of critical importance.

Macro-element models for shallow foundations have previously shown to be a cost-effective and reliable tool for such type of analysis, since they suitably represent both the nonlinear soil behaviour at near-field and the ground substratum dynamic characteristics at far-field, as well as the interaction with the seismic response of the structure. Hence, all aspects of elastic and inelastic behaviour of the foundation system are encompassed into one computational entity and are described by the behaviour of a single point at the centre of the foundation. No detailed information about the behaviour of the soil mass or individual soil elements is needed nor is available, making the macro-element approach primarily intended to be a design tool.

Therefore, the macro-element approach reduces the size of the problem significantly, since the footing and the soil are considered as a single macro-element characterized by six degrees-of freedom (6 DOFs), in the 3D case, whose formulation is based on the resultant forces and displacements. The basic assumption in shallow foundations macro-elements is that the footing is considered as a rigid body, with the main advantage with respect to the BNWF approach being the coupling between all the macro-element DOFs and its definition as a single zero-length link element.

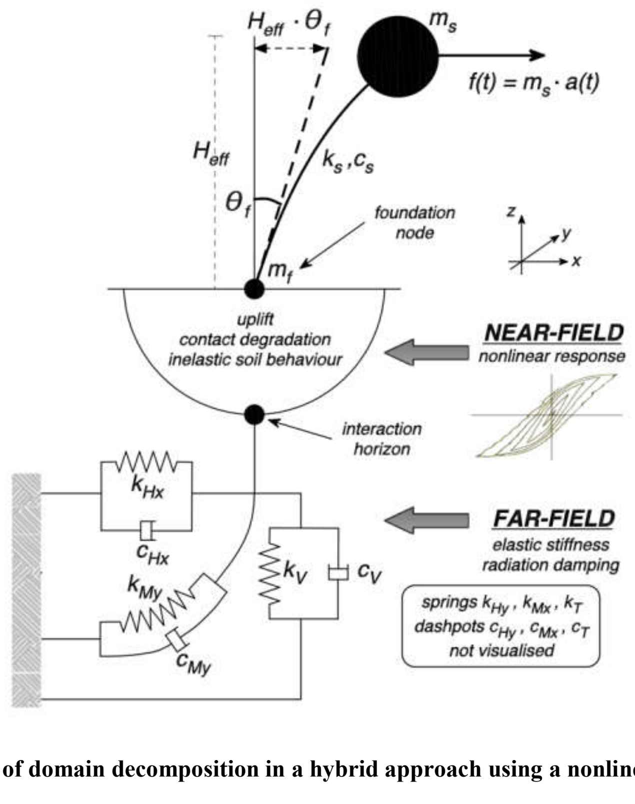

Figure 1. Example of domain decomposition in a hybrid approach using a nonlinear macro-element

The concept of a macro-element to model the nonlinear response of shallow foundations was first developed by Nova and Montrasio (1991). It consisted of an elastoplastic model with isotropic hardening for the entire soil-foundation system during quasi-static monotonic loading. The model, written in terms of generalized force and displacement variables (e.g. Roscoe and Schofield, 1957), was used to predict the vertical settlement of strip footings on sand. In that model, the bearing capacity of the foundation under combined loading was represented as a surface in the space of the resultant forces acting on the foundation (e.g. Salençon, 1990; Butterfield, 1980). The rugby-ball-shaped surface of ultimate loads of the system, shown in Figure 2, was identified as the yield surface of the plasticity model. That model was later extended by Pedretti (1998) and subsequently by di Prisco et al. (2003) to cyclic loading. Based on the isotropic hardening rule of Nova and Montrasio (1991) for the case of virgin loading, they introduced a bounding surface formulation (e.g. Dafalias, 1986) for the case of unloading/reloading that allows obtaining a continuous plastic response of the footing during the loading history.

In parallel, Paolucci (1997) adopted the model by Nova and Montrasio (1991) and its elasto-perfectly plastic formulation for studying the response of simple structures subjected to dynamic loading. This modelling procedure was followed by subsequent works for different soil conditions (clay, loose or dense sand) and different foundation geometries (strip, rectangular, circular shallow foundations), leading to accurate formulations of the ultimate surface, the hardening rule and the flow rule (e.g. Gottardi et al., 1999; Houlsby and Cassidy, 2002; Cassidy et al., 2005).

Cremer et al. (2001, 2002) proposed an original approach by introducing the foundation uplift in the formulation, modelling independently the two sources of footing nonlinearity: uplift and plasticity. Such model considers the coupling between the material and geometrical nonlinearity, as well as their coupling with the response of the superstructure. The model was developed for strip foundations on cohesive soils under seismic loading and adopted a multi-surface plasticity model. However, it was verified that the kinematic and/or isotropic evolution of the inner yield surfaces may become numerically intensive and time consuming, especially for complex geometries of the yield surfaces.

In the last few years, numerous updated macro-element formulations were proposed, as summarized in Table 1. The main features, the experimental benchmarks on which they have been validated, as well as the corresponding references are indicated therein. The plasticity macro-element model proposed by Cremer et al. (2001, 2002) was modified by Grange et al. (2008) and it was tentatively extended to circular footings and three-dimensional loading.

Paolucci et al. (2008) proposed to treat the coupling between uplift and soil yielding using a formulation inspired in damage mechanics. A stiffness degradation model was introduced through a damage parameter using an *ad hoc* analytical expression that takes into account the reduction of soil-footing contact area due to cumulative damage in the soil beneath the footing edges. Shirato et al. (2008b) also presented a macro-element formulation based on an original uplift model included in the Nova and Montrasio (1991) plasticity model.

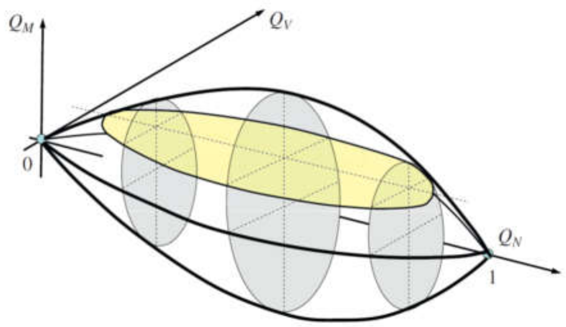

Figure 2. Rugby-ball-shaped surface of ultimate loads in Nova and Montrasio (1991)

Gajan (2006) proposed a contact interface model that allowed tackling the evolution of soil-footing contact area, described through the introduction of a critical contact area ratio parameter. Several contact interface model simulations were carried out and they were compared with large-scale and reduced-scale test results (see Table 1).

Chatzigogos et al. (2009) firstly combined the nonlinear elastic uplift model proposed by Cremer et al. (2001, 2002) with a bounding surface plasticity model for circular footings on cohesive soils under cyclic loading. Then, Chatzigogos et al. (2011) generalized the original formulation presenting a multi-mechanism macro-element model, for both circular and strip shallow foundations. The modelling of the uplift mechanism followed the one proposed by Wolf (1988) and Wolf and Song (2002). This model includes both cohesive and frictional soils, two-dimensional or three-dimensional foundation geometries and interface conditions allowing for foundation uplift or not.

Figini et al. (2012) presented a novel formulation of a macro-element for dynamic analysis of structures lying on shallow foundations. This macro-element combines the main features of the two macro-element models by Paolucci et al. (2008) and Chatzigogos et al. (2011). An uplift-plasticity coupling is now described through the concept of footing effective width, with distinction between transient and permanent reduction of the soil-foundation contact area. Moreover, the vertical mapping rule was introduced in order to better fit the loading path under seismic loading. This macro-element model was carefully validated based on experimental results of three large-size tests (see Table 1).

Nevertheless, despite their growing popularity in the earthquake engineering community, existing dynamic macro-elements for shallow foundations are not exempt of criticism and improvement. Namely, they are not fully consistent and are usually developed for planar loading cases only. Their innovative concepts and formulations, as described by Chatzigogos et al. (2011) and by Figini et al. (2012), are herein readdressed and further extended.

In this work, a significantly enhanced uplift model is introduced which corrects some inconsistencies of previous approaches. It is based on a nonlinear elastic-uplift response which also considers some degradation of the contact at the soil/footing interface due to irrecoverable changes in its geometry. An improved bounding surface plasticity model is also proposed which builds on the preceding ones in order to reproduce a more general and realistic behaviour, namely in what refers to dynamic loading and evolution of displacements. Furthermore, a new cutting-plane type of return mapping algorithm is devised which, unlike the previous models, correctly takes into account the simultaneous elastic-uplift and plastic nonlinear responses. Finally, this superior macro-element formulation is fully applicable to three-dimensional loading cases, thus extending the scope of earlier planar-loading models. Moreover, the proposed macro-element is now also applicable to rectangular footings and not only to strip and circular footings as previous models. Figure 3 schematically represents the type of phenomena intended to be modelled with the macro-element.

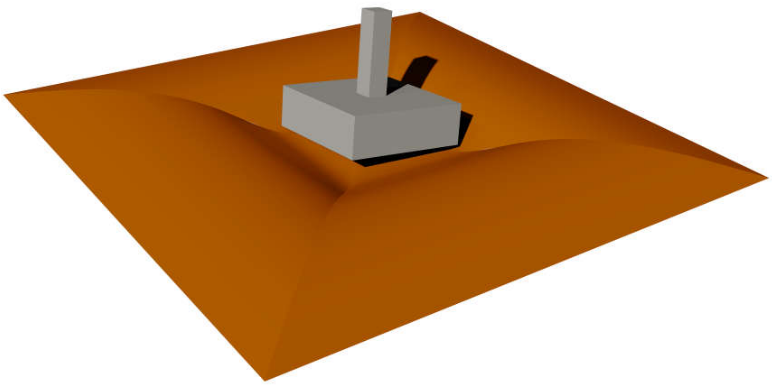

Figure 3. Schematic footing response in 3D case, accounting for uplift, inelasticity and contact degradation

Table 1. Overview of recent macro-element models for shallow foundations

Reference	Main Characteristics	Experimental validations
Grange et al. (2008)	Uplift included into plasticity model. Extension of Cremer et al. (2001, 2002) model to circular footings and 3D loading case	- TRISEE - CAMUS - UCDavis
Paolucci et al. (2008)	Uplift-plasticity coupling though a stiffness degradation model	- PWRI
Shirato et al. (2008b)	Introduction of uplift model in the Nova and Montrasio (1991) plasticity model	- PWRI
Gajan and Kutter (2008)	Evolution of the soil-footing contact area though a contact interface model. Introduction of a critical contact area ratio parameter. Cremer (2001) bounding surface	
Chatzigogos et al. (2011)	Bounding surface plasticity combined with the uplift model by Cremer (2001). Multi-mechanism macro-element (sliding, uplift, plasticity). Radial mapping rule	
Figini et al. (2012)	Bounding surface plasticity combined with Wolf (1988) uplift formulation. Nova and Montrasio (1991) bounding surface. Vertical mapping rule. Uplift-plasticity coupling through a stiffness degradation model	- TRISEE - PWRI - CAMUS
Proposed model	Bounding surface plasticity combined with uplift formulation. Uplift-plasticity coupling through uplift initiation and damage parameter. Evolutionary mapping rule. Approximate extension to 3D behaviour. Implemented in a FEM code available online	- TRISEE - PWRI - CAMUS - UCDavis

After introducing the macro-element formulation, a set of validation analyses is presented. These are based on results from experimental tests in order to assess and establish the accuracy and capabilities of the proposed model. The encouraging outcome of such validation shows that this type of macro-element models has reached a stage where their application to seismic design is straightforward, leading to a more efficient design and to higher confidence in the predicted structural response. The validation tests are also used for calibrating adequate default values for the small number of parameters of the macro-element.

2. MACRO-ELEMENT MODEL

A footing macro-element model is proposed to represent the dynamic behaviour of isolated rigid footings, subjected to three-dimensional inertial loading, from the initial stages of loading up until reaching failure. The proposed macro-element is based on the three major features of the response of footings, namely:

i) Initial elastic response,
ii) Uplift in rocking response,
iii) Failure loading conditions.

The bounding surface plasticity model is used to represent a continuous transition between the initial elastic response and the plastic flow at failure, for monotonic, cyclic and dynamic loading conditions. The uplift phenomenon is represented by a nonlinear elastic model which, however, takes into account and is influenced by the plastic deformation state in the underlying soil.

The failure surface, and all other quantities of interest, will be described in the space of generalised forces or displacements. It should be pointed out that, for dimensional consistency when formulating a plasticity model in the loading space instead of the usual stress space, the generalised forces should either have the same dimensions or be dimensionless. The same applies to the corresponding generalised displacements. Throughout this work, the variables employed in the plasticity formulation are dimensionless, unless explicitly stated otherwise. The normalisation adopted for the macro-element is based on using the footing width, B, and the maximum vertical bearing capacity, N_{max}, as the normalising variables.

The geometry considered herein corresponds to a rigid footing of width B and length L. Considering a planar loading, for simplicity of notation and visualisation, the footing will be subjected to a rocking moment and to both vertical and horizontal forces (M_x, N and H_y respectively), as depicted in Figure 4. The static and kinematic variables are normalised according to expression (1):

$$\boldsymbol{q} = \begin{bmatrix} q_N \\ q_{H_y} \\ q_{M_x} \end{bmatrix} = \begin{bmatrix} \frac{u_z}{B} \\ \frac{u_y}{B} \\ \theta_x \end{bmatrix}, \qquad \boldsymbol{Q} = \begin{bmatrix} Q_N \\ Q_{H_y} \\ Q_{M_x} \end{bmatrix} = \begin{bmatrix} \frac{N}{N_{max}} \\ \frac{H_y}{N_{max}} \\ \frac{M_x}{BN_{max}} \end{bmatrix} \tag{1}$$

where u_z and u_y are the vertical and horizontal displacements of the foundation centre of mass, and θ_x is its rotation.

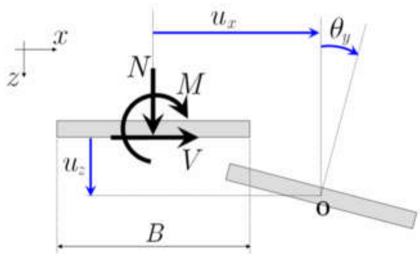

Figure 4. Static and kinematic variables (from Chatzigogos, 2009)

An *additive decomposition* of the total displacements vector is assumed, resulting in its *linear elastic*, *nonlinear elastic (uplift)* and *plastic* components:

$$\boldsymbol{q} = \boldsymbol{q}^{el} + \boldsymbol{q}^{up} + \boldsymbol{q}^{pl} = \boldsymbol{q}^{eu} + \boldsymbol{q}^{pl} = \boldsymbol{q}^{eup} \tag{2}$$

where $\mathbf{q}^{eup}$ is the elastic-uplift-plastic displacement vector and $\mathbf{q}^{eu} = \mathbf{q}^{el} + \mathbf{q}^{up}$ is the elastic-uplift displacement component. The following paragraphs describe the different features of the macro-element formulation.

A generalized stiffness matrix, $\mathbf{K}_{tg}$, relating displacement and load increments and whose elements are normalised, is introduced as follows:

$$\dot{\boldsymbol{Q}} = \mathbf{K}_{tg}\dot{\boldsymbol{q}} \tag{3}$$

2.1 INITIAL ELASTIC RESPONSE

The initial elastic response of isolated rigid footings has been extensively studied through several sophisticated numerical methods, and for the purpose of this macro-element model, the impedances available in literature are deemed to represent such behaviour with sufficient accuracy (e.g. Gazetas, 1991).

The evolution of the footing loading is assumed to obey the rate form of the *elastic constitutive relationships*:

$$\dot{\boldsymbol{Q}} = \boldsymbol{K}^{el}\dot{\boldsymbol{q}}^{el} = \boldsymbol{K}^{el}(\dot{\boldsymbol{q}}^{eu} - \dot{\boldsymbol{q}}^{up}) = \boldsymbol{K}^{el}\left(\dot{\boldsymbol{q}}^{eup} - \dot{\boldsymbol{q}}^{up} - \dot{\boldsymbol{q}}^{pl}\right) \tag{4}$$

In this equation, the dimensionless components of the footing load and displacement vectors are given by expression (1).

The initial elastic stiffness matrix is assumed, with sufficient accuracy, to be constant and diagonal. The terms on the diagonal represent the foundation static impedances, functions of footing geometry and of the soil elastic properties. The diagonal terms in can be determined from standard formulas, while the radiation damping response of the foundations was assumed to be well approximated by frequency-independent dashpot coefficients based on the literature (e.g. Gazetas, 1991).

The elastic displacements are always assumed to be related to the current loading by the initial elastic stiffness matrix, which may be rendered dimensionless, consistently with expression (1), resulting in:

$$\boldsymbol{Q} = \boldsymbol{K}^{el}\boldsymbol{q}^{el}, \qquad \boldsymbol{K}^{el} = \begin{bmatrix} K_{NNn}^{el} & \cdot & \cdot \\ \cdot & K_{HHn}^{el} & \cdot \\ \cdot & \cdot & K_{MMn}^{el} \end{bmatrix} \tag{5}$$

2.2 UPLIFT AND DAMAGE MODELS

There are two mechanisms contributing to a partial detachment between the footing and the soil: i) a gradual degradation of the contact around the edges of the footing due to rocking motion and expressed by a damage parameter, *D*; ii) uplift of the footing for an increasing vertical load eccentricity, *e*. These are discussed in the following paragraphs.

The uplift mechanism model starts from the formulation of Chatzigogos et al. (2011). It is well known that the uplift is a phenomenon of a geometric nature, which leads to a reduction of the soil-footing contact area (Figure 5a), corresponding to a reduction of the foundation elastic-uplift tangent stiffness. Due to its reversibility, the soil-footing contact area is fully recovered once the load eccentricity decreases below the value of uplift initiation, which corresponds to point $(q_{M,o} - Q_{M,o})$ in Figure 5b. The uplift on elastic soil is put in evidence in the moment-rotation plane by a characteristic S-shape curve (Figure 5b).

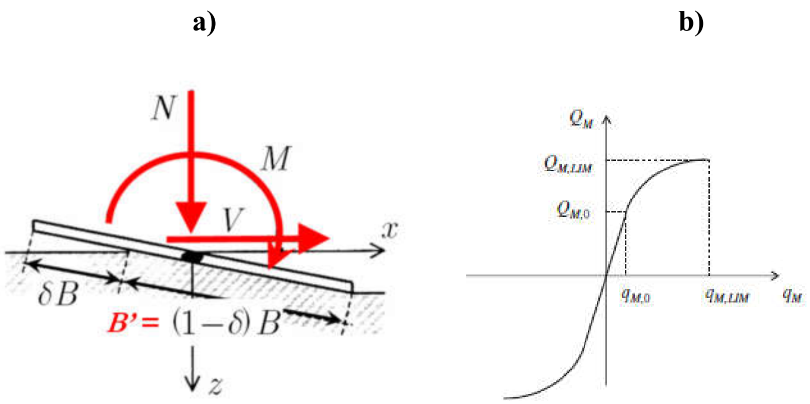

Figure 5. a) Geometric configurations before and after uplift initiation; b) behaviour in the moment-rotation plane ($\mathbf{Q_M - q_M}$) upon foundation uplift on an elastic soil

(a) ***Statics.*** Many interesting results can be obtained by simple statics considerations. For instance, considering the geometric configurations represented in Figure 5, the uplift initiation occurs for a load eccentricity e_o given by:

$$e_0 = \frac{M_0}{N} = \frac{Q_{M0}B}{Q_N} = \frac{B}{2\alpha} \tag{6}$$

The uplift initiation parameter α in expression (6) is only dependent on the assumed stress distribution below the footing and can be determined from simple static considerations. Cremer et al. (2001) considered α equal to 2 for nonlinear stress distributions; Wolf (1988) used a value of α equal to 3 for a linear stress distribution. On the other hand, Chatzigogos et al. (2009) used α equal to 2 or 3 for strip and circular foundations, respectively. In this formulation, the values of α range from 2 to $+\infty$, depending on the assumed stress distribution, as shown in Table 1.

Table 1. Stress distribution below the footing and the corresponding value of uplift initiation parameter ($\boldsymbol{\alpha}$)

Stress distribution below the footing	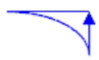	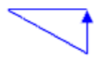	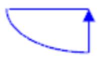	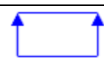
α	2	3	4	$+\infty$
β	2	3/2	4/3	1

The calculation of the reduced base width contact after uplift, B', is related to the parameter δ, that denotes the percentage of footing area being detached from the soil (Figure 5a), as follows:

$$B' = B(1-\delta) \tag{7}$$

B' may also be defined through the contact width parameter, β, as follows:

$$B' = \beta\,(B-2e), \text{ with } e \geq e_o \tag{8}$$

The β values are also summarised in Table 1 as function of the stress distribution below the foundation. It is interesting to note that Wolf (1988) used β equal to 3/2 and Cremer et al. (2001) equal to 2, coherently with the value of α. These expressions show that the uplift initiation and B' are expressed only as function of the stress distribution, overcoming the confusion regarding stress distribution and footing shape of previous approaches (e.g. Chatzigogos et al., 2009).

Considering $e = e_o$ in expression (8), and the definition of e_o in expression (6), it results in:

$$e_o = \frac{\beta - 1}{2\beta} B = \frac{B}{2\alpha} \tag{9}$$

Therefore α and β are linked by:

$$\alpha = \frac{\beta}{\beta - 1} \Leftrightarrow \beta = \frac{\alpha}{\alpha - 1} \tag{10}$$

Consequently, based only on static considerations, the evolution of the rocking moment for the elastic-uplift mechanism can be summarised in the following way:

$$\frac{Q_M}{Q_{Mo}} = \alpha - (\alpha - 1)(1 - \delta) \quad \rightarrow \quad \frac{M}{M_0} = 1 + (\alpha - 1)\ \delta \tag{11}$$

(b) ***Kinematics.*** Based on static and kinematic considerations, namely considering that:

$$\frac{\dot{q}_N^{up}}{\dot{q}_M^{eu}} = -\,\delta/2 \tag{12}$$

for a rotation around the current centre of gravity (*s*) of the uplifted footing (Figure 6), for $\dot{Q}_N = 0$, the increment of generalised forces and displacements at the current centre of gravity (*s*) can be expressed as follows:

$$\begin{cases} \dot{Q}_N = \dot{Q}_N^s \\ \dot{Q}_H = \dot{Q}_H^s \\ \dot{Q}_M = \dot{Q}_M^s + \dot{Q}_N^s \cdot \delta/2 \end{cases} , \qquad \begin{cases} \dot{q}_N^s = \dot{q}_N^{eu} + \dot{q}_M^{eu} \cdot \delta/2 \\ \dot{q}_H^s = \dot{q}_H^{eu} \\ \dot{q}_M^s = \dot{q}_M^{eu} \end{cases} \tag{13}$$

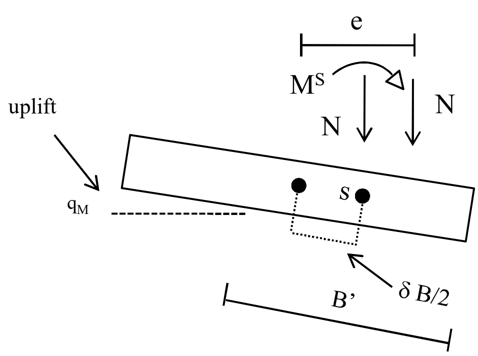

Figure 6. Foundation uplift on an elastic soil: equivalent foundation width B', the point s representing the current centre of gravity of the uplifted footing

(c) ***Diagonal stiffness matrix at the current centre of gravity.*** Assuming that δ is constant during a loading increment, the elastic-uplift constitutive relationship between generalised forces and displacements is written as follows:

$$\begin{cases} \dot{Q}_N^s = K_{NNn}^S \dot{q}_N^s = K_{NNn}^{el}(1 - \delta)\dot{q}_N^s \\ \dot{Q}_H^s = K_{HHn}^S \dot{q}_H^s = K_{HHn}^{el}(1 - \delta)\dot{q}_H^s \\ \dot{Q}_M^s = K_{MMn}^S \dot{q}_M^s = K_{MMn}^{el}(1 - \delta)^3 \dot{q}_M^s \end{cases} \tag{14}$$

This corresponds to a diagonal elastic-uplift stiffness matrix when evaluated with respect to the current centre of gravity (s), and it is the correct interpretation of Wolf's (1988) diagonal matrix approach. When the elastic-uplift tangent stiffness matrix is evaluated at the geometric footing centre, by joining expressions (13) and (14), it thus becomes equal to:

$$\dot{\boldsymbol{Q}} = \boldsymbol{K}^{eu}\dot{\boldsymbol{q}}^{eu}, \qquad \boldsymbol{K}^{eu} = \begin{bmatrix} K_{NNn}(B') & 0 & K_{NMn}(B') \\ 0 & K_{HHn}(B') & 0 \\ K_{MNn}(B') & 0 & K_{MMn}(B') \end{bmatrix} \tag{15}$$

where:

$$\begin{cases} K_{NNn}(B') = K_{NNn}^{el}(1-\delta) \\ K_{HHn}(B') = K_{HHn}^{el}(1-\delta) \\ K_{MM}(B') = K_{MM}^{el}(1-\delta)^3 + K_{NN,n}^{el}(1-\delta)\dfrac{\delta^2}{4} \\ K_{NMn}(B') = K_{MNn}(B') = K_{NN,n}^{el}(1-\delta)\dfrac{\delta}{2} \end{cases} \tag{16}$$

Differently from the Chatzigogos et al. (2009) model, in which the stiffness matrix diagonal terms do not explicitly depend on the reduced base width and they are taken constant in the vertical and horizontal directions, in this macro-element all three diagonal terms are dependent on B', through the percentage of uplifted footing, δ. The latter, as well as the total relation $Q_M = f(q_M^{eu})$, for the case of constant vertical load, can be obtained by integrating expression (15), resulting in:

$$\delta = 1 - \left[\frac{1}{1 + \frac{2}{\alpha - 1}\left(\frac{q_M^{eu}}{q_{Mo}^{eu}} - 1\right)}\right]^{\frac{1}{2}} = 1 - \left[\frac{1}{1 + \frac{2}{\alpha - 1}\left(\frac{\theta}{\theta_0} - 1\right)}\right]^{\frac{1}{2}} \tag{17}$$

Moreover, differently from Figini et al. (2012), in which the second order cross-coupling effects, K_{NM}, are considered by adding the geometric terms in the post-processing phase of the displacement results, herein they are considered throughout the analysis, as a result of kinematic considerations.

Replacing expression (17) in (11), the following elastic-uplift moment-rotation relationship is obtained:

$$\frac{Q_M}{Q_{Mo}} = \alpha - (\alpha - 1)\left[\frac{1}{1 + \frac{2}{\alpha - 1}\left(\frac{q_M^{eu}}{q_{Mo}^{eu}} - 1\right)}\right]^{1/2} \tag{18}$$

This corresponds to the typical S-shaped moment-rotation curve upon uplift response, shown in

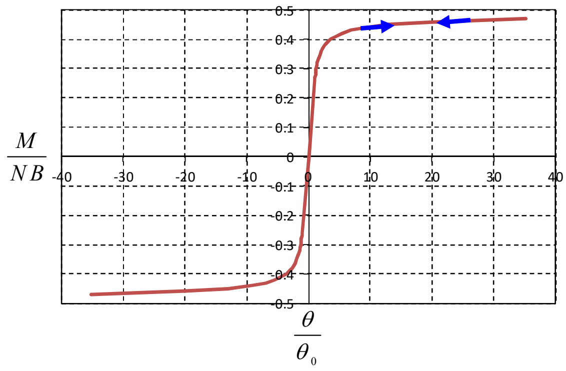

Figure 7. S-shaped moment-rotation response due to uplift phenomenon

It is worth noting that, if $\alpha = 3$, the same expression adopted by Chatzigogos et al. (2011), without a solid basis, is obtained; on the other hand, if $\alpha = 2$, the corresponding expression differs from the one used in Cremer et al. (2001), revealing another inconsistency of previous formulations.

(d) ***Coupling uplift-plasticity and damage model.*** The coupling between footing uplift and soil plasticity is treated based on the Cremer (2001, 2002) formulation, together with the stiffness degradation model introduced by Paolucci (2008) and adopted in Figini et al. (2012). In this formulation, the uplift mechanism is coupled with inelasticity in the soil, through:

- Eccentricity value for uplift initiation – which is no longer constant, as in expression (6), but now interpreted as an evolution towards the one corresponding to a uniform stress distribution with increasing vertical load:

$$e_o = \frac{B\prime}{2\alpha} e^{-\xi Q_N} = \frac{B\prime}{2\alpha_P} \text{with } \alpha_P = \alpha \cdot e^{\xi Q_N} \tag{19}$$

On can note that if $Q_N = 0 \rightarrow \alpha_P = \alpha$; while if $Q_N = 1 \rightarrow \alpha_P \approx 5\,\alpha$ to $12\,\alpha$ for values of ξ between 1.5 and 2.5 (Figini et al, 2012). A value of 1.5 was assumed in this work.

- Damage parameter – which takes into account the "rounding" of the contact surface due to inelastic soil deformations during rocking response, resulting in a decrease of the contact area. The damage parameter in 2D is defined as follows:

$$D = \frac{1 - Q_N}{1 + \frac{1}{d_\theta\, \theta^{pl,cum}}} \tag{20}$$

where D is a function of the vertical load N, of the soil/footing contact degradation parameter due to rocking, d_θ, whereas $\theta^{pl,cum}$ is the cumulative plastic foundation rotation at a specific instant of time. This parameter can be further generalised in order to take into account a possible recovery of the contact due to inelastic settlement:

$$D = \frac{1 - Q_N}{1 + d_u \frac{u_z^{pl,cum}}{B} + \frac{1}{d_\theta\, \theta^{pl,cum}}} \tag{21}$$

In this work d_u was not considered. For the 3D case, separate D_x and D_y are defined.

- Reduction of the effective foundation width, B', taking into account the nonlinear soil behaviour and the uplift:

$$B' = B\,(1-\delta)(1-D) \tag{22}$$

All previous equations can still be used but now using α_{PD} instead of α:

$$\alpha_{PD} = \frac{\alpha_P}{1-D} = \frac{\alpha}{1-D} e^{\xi Q_N} = \alpha_D e^{\xi Q_N} \tag{23}$$

Moreover, due to the coupling between uplift and plasticity, the effective foundation width (22) should now be considered instead of (7) in the elastic-uplift stiffness matrix of expression (16). In this way, the tangent stiffness matrix correctly considers the evolution of the current centre of gravity, and thus of the point of resultant forces, due to both the uplift and damage evolution. It results in a non-symmetric elastic-uplift tangent stiffness matrix with a dependence on the plastic multiplier.

2.3 Failure and Plastic Potential Surfaces

The bounding surface adopted in this macro-element depends on the type of soil and its drainage conditions during a seismic event. Therefore, different 3D failure surfaces are considered for drained and undrained conditions.

The ultimate surface adopted to describe the drained behaviour is a combination of the one described by Butterfield and Gottardi (1994), the one adopted by Nova and Montrasio (1991) and the extension to 3D by Bienen et al. (2006). It thus corresponds to the typical "rugby-ball" shape, extended to the 3D loading space and with an inclination of the ellipse between the horizontal force and the corresponding rotational moment for a given constant vertical force. It is expressed as:

$$\begin{aligned}\left(\frac{Q_{Hx}}{Q_{Hx,max}Q_{NH}}\right)^2 + \left(\frac{Q_{Hy}}{Q_{Hy,max}Q_{NH}}\right)^2 + \left(\frac{Q_{Mx}}{Q_{Mx,max}Q_{NM}}\right)^2 + \left(\frac{Q_{My}}{Q_{My,max}Q_{NM}}\right)^2 \\ + \left(\frac{Q_T}{Q_{T,max}Q_{NH}}\right)^2 + 2C_x \frac{Q_{Hx}}{Q_{Hx,max}Q_{NH}} \frac{Q_{My}}{Q_{My,max}Q_{NM}} \\ - 2C_y \frac{Q_{Hy}}{Q_{Hy,max}Q_{NH}} \frac{Q_{Mx}}{Q_{Mx,max}Q_{NM}} - 1 = 0\end{aligned} \tag{24}$$

where:

$$Q_{NH} = Q_{NM} = [4Q_N(1-Q_N)]^{0.95} \tag{25}$$

for the drained case. The peak values of horizontal forces and moments are always attained at $Q_N = 0.5$. The ellipse inclination factors are herein taken as zero, although they can also be used to reflect the effect of footing embedment.

For undrained loading the ultimate surface (24) is also adopted, but now Q_{NH} reflects the cohesive nature of the soil response at lower values of Q_N:

$$Q_{NH} = 1 - (1-2Q_N)^{10},\ \text{if } 0 \le Q_N < 0.5 \tag{26}$$

This undrained failure surface corresponds to the so-called "scallop" shape, which is represented in Figure 8 in terms of its intersection in the H-N and M-N planes of loading. It is based on the works of Chatzigogos et al. (2007), Ukritchon et al. (1998) and Gourvenec (2007).

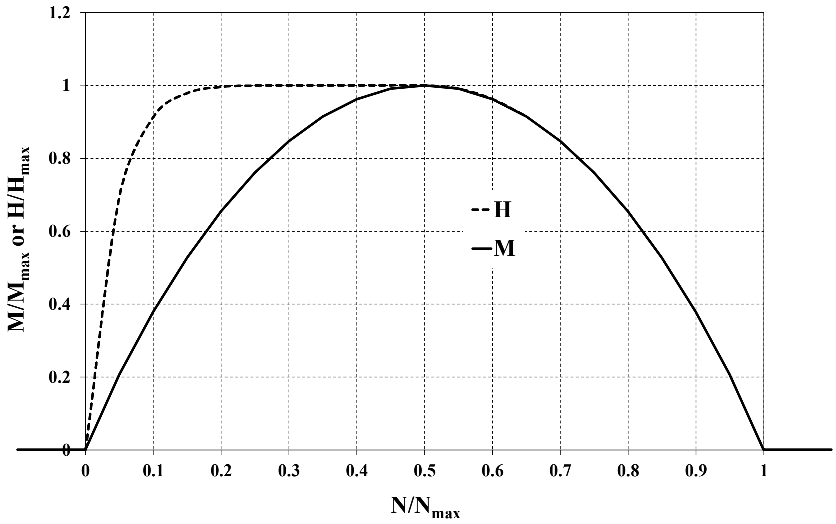

Figure 8. Scallop-shaped failure surface for undrained conditions

The macro-element implementation also considers another undrained loading surface in the case where no uplift is allowed, i.e. with unlimited base suction capacity. This failure surface corresponds to an ellipsoid as the one adopted by Chatzigogos et al. (2009)

Regarding the plastic potential surface, also an ellipsoid centred at the origin is adopted, following the Butterfield and Gottardi (1994) and Bienen et al. (2006) formulations, which implies a non-associative flow rule. This surface is represented by the following expression:

$$\begin{aligned}\left(\frac{Q_{Hx}}{Q_{Hx,max}}\right)^2+\left(\frac{Q_{Hy}}{Q_{Hy,max}}\right)^2+\left(\frac{Q_{Mx}}{Q_{Mx,max}}\right)^2+\left(\frac{Q_{My}}{Q_{My,max}}\right)^2+\left(\frac{Q_{T}}{Q_{T,max}}\right)^2 \\ +2C_x\frac{Q_{Hx}}{Q_{Hx,max}}\frac{Q_{My}}{Q_{My,max}}-2C_y\frac{Q_{Hy}}{Q_{Hy,max}}\frac{Q_{Mx}}{Q_{Mx,max}}+{\chi_g}^2\left({Q_N}^2-{\rho_g}^2\right)=0\end{aligned} \tag{27}$$

where ρ_g is a scale factor for the plastic potential surface to intercept the bounding surface at the current image point and χ_g is a macro-element parameter.

2.4 BOUNDING SURFACE PLASTICITY MODEL

The first important concept in bounding surface plasticity is that the generalised forces are limited by the *bounding surface*:

$$F\left(\overline{\mathbf{Q}},\mathbf{S}\right)=0 \tag{28}$$

where $\overline{\mathbf{Q}}$ is the *image point at the bounding surface* and it is related to the *current loading point*, $\mathbf{Q}$, by a mapping rule, $\overline{\mathbf{Q}}=\mathbf{Map}\left(\mathbf{Q},\mathbf{S}\right)$, satisfying certain conditions (Dafalias, 1986). The image point must always lay on the bounding surface and the generalised forces vector, by definition, always lies on the *loading surface*:

$$f\left(\mathbf{Q},\mathbf{S}\right)=0 \tag{29}$$

The *internal variables*, **S**, present in both (28) and (29), describe the evolution of both surfaces.

The choice of one loading surface over the infinite number of surfaces that pass through the loading point is related to the particular mapping rule chosen. In fact, the loading surface, and its evolution in size and/or position with the loading point variation, is simply a practical way of defining the mapping rule with some kind of physical reasoning. Note that the loading surface may never cross the bounding surface, *i.e.* it is always enclosed by it. This is usually guaranteed by defining the image point as the one having the same unit normal vector to the bounding surface as the unit normal vector to the loading surface at the current loading point. Such a constraint is not absolutely necessary except when the loading point reaches the bounding surface, thus coinciding with the image point.

For simplicity reasons, the loading surface is also usually assumed to have a similar shape to the bounding surface. It shares a lot of properties with the yield surface of classical plasticity. The main difference between the two is that the loading function is always equal to zero, while a yield function can be less or equal to zero. The loading surface moves with the loading point, even upon unloading, while a yield surface represents the maximum extent of previous yielding.

Probably the most successful mapping rule for the image point is the radial projection on the bounding surface (Dafalias, 1986; Borja *et al.*, 2001). The concept of such mapping is discussed in Correia and Pecker (2019), where the bounding surface is centred at $\mathbf{Q}_0^{BS}$ and described by:

$$F\left(\overline{\mathbf{Q}} - \mathbf{Q}_0^{BS}, \mathbf{S}\right) = 0 \tag{30}$$

A *projection centre*, $\mathbf{Q}_P$, is used to project the current loading point on the bounding surface. The mapping rule thus takes the following form:

$$\overline{\mathbf{Q}} = \mathbf{Q} + \mu\left(\mathbf{Q} - \mathbf{Q}_P\right) = \mathbf{Q}_P + (1+\mu)\left(\mathbf{Q} - \mathbf{Q}_P\right) \tag{31}$$

The mapping variable, μ, varies between zero, when $\mathbf{Q} = \overline{\mathbf{Q}}$, and infinity, when $\mathbf{Q} = \mathbf{Q}_P$ (in which case the image point is indeterminate). By imposing that the unit normal vector to the loading surface at the loading point and the unit normal vector to the bounding surface at the image point must coincide, together with the mapping rule (31), one is indirectly defining an appropriate loading surface. Such loading surface is centred at the point $\mathbf{Q}_0^{LS}$ and is defined by the following equation:

$$f\left(\mathbf{Q} - \mathbf{Q}_0^{LS}, \mathbf{S}\right) = F\left(\mathbf{Q} + \mu\left(\mathbf{Q} - \mathbf{Q}_P\right) - \mathbf{Q}_0^{BS}, \mathbf{S}\right) = 0 \tag{32}$$

This loading surface is homologous to the bounding surface and the projection centre $\mathbf{Q}_P$ occupies the same relative position inside both surfaces. It is consequently also called the *homology centre*. In fact, the loading surface represents the *locus* of all loading points $\mathbf{Q}$ with the same value of μ for a given position of the homology centre.

It can be easily shown that, for a loading surface defined as above, all the governing equations of the plasticity problem can be applied indifferently to the bounding surface or to this loading surface instead (see, for instance, Borja *et al.,* 2001). It is noted that μ, in such case, is to be treated similarly to an isotropic hardening parameter for the loading surface.

From (31), the similarity ratio between the bounding and the loading surfaces is given by the following expression:

$$\frac{\left|\overline{\mathbf{Q}} - \mathbf{Q}_P\right|}{\left|\mathbf{Q} - \mathbf{Q}_P\right|} = 1 + \mu = \frac{1}{\delta} \tag{33}$$

where δ is the normalised distance between the loading point and the homology centre with respect to the distance between the latter and the image point. It varies between zero and one and corresponds to the inverse of the loading parameter, λ. This loading parameter varies from infinity to one, when the bounding surface is attained. Further details on these formulations can be found in Correia and Pecker (2019).

In terms of plastic displacements, the role of the plastic potential surface is to define the direction of plastic increments, as well as the magnitude of the plastic modulus, which is dependent on the adopted mapping rule. The mapping rule adopted herein is capable of reproducing both the radial mapping rule, adopted in Chatzigogos et al. (2011) and the constant vertical mapping rule, adopted in Figini et al (2012) in cyclic response, as well as any translational loading, see Figure 9. This is achieved by assuming as the projection centre the loading point before the previous unloading.

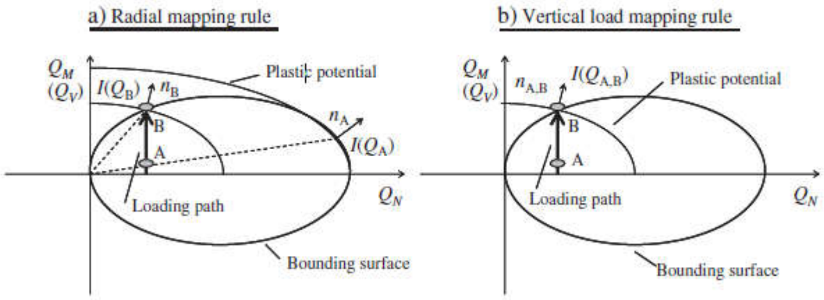

Figure 9. a) Radial mapping rule; b) Vertical load mapping rule (from Figini et al., 2012)

The unit normal vector n_g on the image point is introduced to define the case of the plastic loading, neutral loading and unloading for a given force increment. In case of unloading and neutral loading, the response is elastic. In case of plastic loading, the plastic modulus is defined as:

$$H_{\lambda}^{pl}(Q, \lambda, \lambda_{min}) \begin{cases} H_o^{pl}\, ln\, \lambda \\ H_o^{pl}\, ln[\lambda_{min}(\lambda/\lambda_{min})^{n_{ur}})] \end{cases} \quad (34)$$

where the first expression is valid for virgin loading and the second one is valid for unloading from virgin loading and for reloading inside the maximum loading surface. λ is the abovementioned loading parameter, a scalar quantity that defines the distance between the current state of loading and its image point on the bounding surface, while λ_{min} is the minimum loading parameter achieved during virgin loading.

3. VALIDATION TESTS FOR THE SHALLOW FOUNDATION MACRO-ELEMENT

The macro-element model presented previously was implemented in the structural analysis software SeismoStruct [Seismosoft, 2019]. It requires the definition of 26 input parameters, from which only 3 need to be calibrated. The model parameters along with their definition and suggested values are given in Table 1. They correspond to:

(a) ***2 Geometric parameters.*** The footing dimensions (length, *L*, and width, *B*).

(b) ***12 Elastic impedances parameters.*** The six foundation initial stiffness components, indicated as K_{NN}, $K_{H_xH_x}$, $K_{H_yH_y}$, $K_{M_xM_x}$, $K_{M_yM_y}$, K_{TT}, for vertical, horizontal and rotational directions, respectively, can be evaluated by using formulas from literature (e.g. Gazetas, 1991), or calibrated based on test results. The same applies to the corresponding six equivalent dashpot coefficients for radiation damping representation.

(c) ***6 Strength parameters.*** These characterise the failure surface and are defined as:

-the maximum centred vertical load capacity, N_{max}, that corresponds to the ultimate static bearing capacity of the foundation and can be evaluated by standard superposition formulas (e.g. Brinch-Hansen,1970);

- the maximum base shear capacities, $H_{x,max}$ and $H_{y,max}$, and maximum base moment capacities $M_{x,max}$, $M_{y,max}$, T_{max}, which can be calibrated based either on material properties (e.g. soil friction angle) or on theoretical values.

(d) ***6 Model specific parameters.*** Characterised as follows:

- the choice of bounding surface type is another parameter, which is depending on whether the analysis is drained or undrained. For the drained case, the rugby-ball shape bounding surface is appropriate, while for the undrained case, the scallop shape is the right one;

- the uplift initiation parameter, α, is only dependent on the assumed stress distribution of vertical stresses underneath the foundation. It is not affecting much the results, and is typically taken as 3, which corresponds to assuming a linear distribution of vertical stresses underneath the foundation for the soil at the beginning of the analysis;

- the exponent for loading history in unloading/reloading, n_{UR}, is usually equal to 1, being related to different plastic modulus values for unloading/reloading in comparison to the virgin loading;

- the soil/footing contact degradation parameter, d_{θ}, takes into account the decrease of the contact area due to cumulative inelastic rocking in the damage model and can be evaluated based on experimental results;

- the normalised reference plastic modulus, H_0^{pl}, calibrated based on experimental results;

- and the plastic potential surface parameter, χ_g, also calibrated based on experimental results.

From the above, it turns out that, once the classical elastic and strength parameters for the soil-foundation system are known, a small number of 3 free-parameters remains to be calibrated in the validation process: H_0^{pl}, the normalised reference plastic modulus, χ_g, the plastic potential surface parameter, and d_{θ}, the damage model parameter.

In the following, the influence of those calibration parameters is analysed and a comprehensive validation process against an international experimental dataset is illustrated aiming to investigate the accuracy of the improved macro-element to model the behaviour of shallow foundations during cyclic and seismic loading.

Table 1. Summary of macro-element parameters related to: (i) geometric and elastic parameters; (ii) strength parameters; (iii) model specific parameters

	Symbol	Definition	Suggested Values	
Geometric – Elastic parameter	L, B	footing dimension	geometry	
	K_{NN}	footing initial vertical stiffness	*(i)* estimated based on literature (e.g. Gazetas, 1991); *(ii)*calibrated on experimental results, when available.	
	K_{HH}	footing initial horizontal stiffness in x and y direction		
	K_{MM}	footing initial rotational stiffness in x and y direction		
Strength parameters	N_{max}	Centred vertical bearing capacity	Brinch-Hansen (1970) Vesic (1973) Eurocode8 Butterfield and Gottardi (1994)	
	H_{max}	Maximum base shear capacity along x and y direction		
	M_{max}	Maximum base moment capacity around x and y direction		
	BS	Bounding surface type	1 – rugby-ball shape 2 – scallop shape 3 – ellipsoid shape	
Model specific parameter	α	uplift initiation parameter	static consideration	3
	n_{ur}	exponent for loading history	fixed	1
	d_θ	soil/footing contact degradation	calibrated on experimental results	0.1
	H_0^{pl}	reference plastic modulus ($H_{plo}/N\ K_{NN}$)		0.2-0.4
	χ_g	plastic potential parameter		0.5-2

One database compiles selected data of rocking foundation performance in monotonic and slow cyclic loading (e.g. Hakhamaneshi et al., 2018); the other one summarises selected data of rocking shallow foundation performance in dynamic experiments (e.g. Gavras et al., 2018). The reason for developing these databases was to archive the key experimental results and data of independent test series, including both centrifuge and 1g shake table tests of SDOF-like models on shallow foundations, in a unique and compact form, easy to be used, that allows to better understand the observed response and to compare in a synthetic way the experimental results from different datasets.

Finally, based on this comprehensive validation process against a set of independent experimental results, a reduced set of macro-element parameters for shallow foundations on sand is proposed, which can be used to perform predictive analyses and applications to earthquake engineering analysis.

A set of experimental datasets was selected among those collected in both databases in order to validate the improved macro-element proposed herein:

- large scale cyclic tests carried out in the TRISEE research program (e.g. Faccioli et al., 1998);

- large scale dynamic tests performed at the Japanese Public Work Research Institute (e.g. PWRI, 2007)

- reduced scale centrifuge test performed at the Centre for Geotechnical Modeling (CGM) at the University of Davis, California, carried out in SSG04 research program (e.g. Gajan, 2006; Gajan and Kutter, 2008) and in LJD03 research program (e.g. Deng and Kutter, 2010; Deng et al., 2012).

- in addition to centrifuge tests, results of a large-scale dynamic test, performed in the CAMUS project and not available in the abovementioned databases (e.g. Combescure and Chaudat, 2000; Combescure et al., 2001), have been used for the validation.

Table 2 summarises some relevant information about each test, namely the soil type and relative density, the footing geometry (in terms of length to width ratio, *B/L*, and embedment depth, *D*), superstructure model, loading type, and vertical safety factor, *FS*). The selected dataset varies in model size, testing equipment, superstructure properties, footing shape, supporting soil environment and loading protocol. Both uplifting-dominating response and plastic settlement-dominated response have been investigated by using tests with different initial safety factors for vertical load, ranging from 4 to 30. Ground motion inputs include both cyclic loading of varying amplitude and real or artificial earthquake motions.

Hereafter, a brief description of the setup and load sequence is reported for each test of Table 2, followed by the numerical modelling. A comparison between numerical and experimental results is presented and discussed.

Table 2. Summary of soil, foundation and structural properties for the experimental tests used for calibration

Test series	Test type	Soil Sand Dr[%]	Foundation L/B	 D [m]	Superstructure	Loading	FS
TRISEE	1g	45; 85	1	*1*	-	cyclic	5-7
PWRI	1g	80	1	0,0.05,0.01	-	dynamic	28.5
CAMUS	1g	71	2.62	0	MDOF shear wall	dynamic	4.2
SSG	Centrifuge	80	4.30	0	SDOF shear wall	dynamic	4

3.1 TRISEE CYCLIC TESTS

A programme of large-size, cyclic loading experiments has been carried out in 1997-98, at the ELSA laboratory in ISPRA (Italy) (Negro et al., 1998) within the framework of the European research Project TRISEE (3D Site Effects and Soil-Foundation Interaction in Earthquake and Vibration Risk Evaluation), to investigate the nonlinear interaction between direct foundations and the supporting soil under seismic loading. Figure 5.4 depicts the experimental setup of the TRISEE test. It consists of a rigid caisson (4 m high, 4.6 m wide, 4.6 m long), filled with saturated Ticino river Sand in dense (HD, D_R = 85%) and loose (LD, D_R = 45%) conditions. A steel foundation model (1m x 1m) was placed in the caisson, at the depth of 1m (overburden load: 20 kPa).

A fixed vertical load was imposed by means of a jack (dense sand: 300 kN; loose sand: 100 kN), the resulting static safety factor, evaluated with the classical superposition formula, was found to be about 7 in LD and 5 in HD conditions. Then, a horizontal load was applied at the top of the vertical column of Figure 1. Three distinct loading phases were imposed: (i) small amplitude sinusoidal load-controlled cycles (0.5 Hz frequency); (ii) artificial seismic loading (maximum seismic coefficient H/V=0.20); (iii) cyclic displacement-controlled loading until the collapse of the foundation. Hereafter, a comparison is presented between experimental results from loading phase III in the dense and loose sand strata and the numerical simulations performed by means of the macro-element.

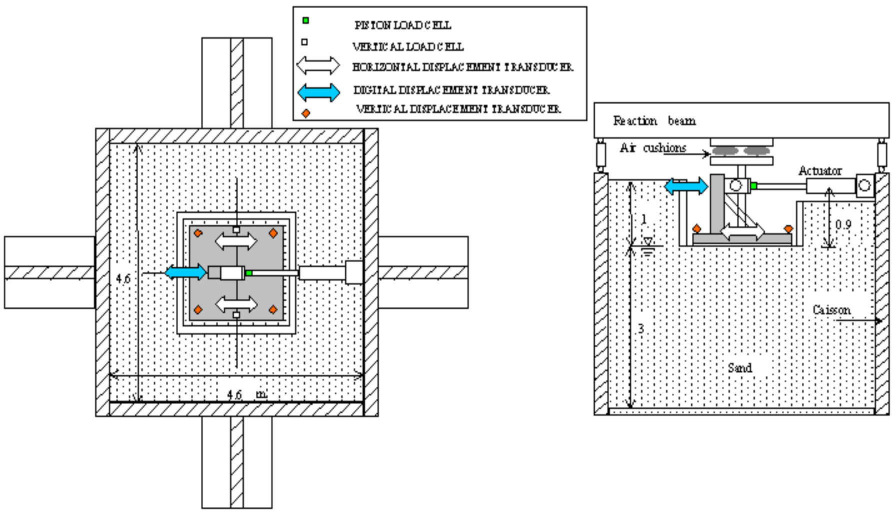

Figure 1. Scheme of the experimental setup of TRISEE tests

The values of macro-element parameters used in the numerical simulations are reported in Table 3, for both HD and LD cases. The foundation impedances values have been calibrated based on the first cycles of phase I experimental results. For the HD case, these values are the same adopted by Figini et al. (2012), while for LD case the values of foundation impedance are close to those used by Grange et al. (2008). The value of static vertical bearing capacity, N_{max}, is set equal to the value reported in the official report of TRISEE experiments. H_{max} and M_{max} are evaluated based on material properties and on theoretical formulae, according to Butterfield and Gottardi (1994), as previously described.

The soil/footing contact damage parameter d_θ was calibrated based on the foundation nonlinear response during the Phase II and III, since it is function of the cumulative plastic rotation. In particular, d_θ is chosen to reproduce the observed moment-rocking loops in terms of energy dissipation, as well as the variation of the elastic rotational stiffness, as discussed in the section on parametric analyses. The plastic modulus H_0^{pl} is determined based on the magnitude of the plastic displacements. Finally, the plastic potential parameter, χ_g, is chosen so that the proportion between the horizontal, vertical and rotational plastic displacements is similar to the experimental one.

Table 3. Macro-element parameters used for the simulation of TRISEE cyclic tests

Phase	B [m]	K_{NN} [MN/m]	K_{HH} [MN/m]	K_{MM} [MN/m]	d_θ [-]	H_0^{pl} [-]	χ_g [-]	N_{max} [MN]
HD-III	1	200	110	70	1	0.2	1	1.5
LD-III	1	30	40	15	0.1	0.2	1.5	0.7

In Figure 2 and Figure 3, the results of the numerical simulations (red lines) are compared with the observed ones (black lines) for Phase III, in both HD and LD conditions, in terms of: (a) moment-rotation cycles; (b) base shear-horizontal displacement cycles; (c) time evolution of rocking angle and (d) time evolution of vertical settlements.

During Phase III, important nonlinearities are developed during this displacement-controlled phase. The HD and LD sets of loops in terms of moment-rocking behaviour are quite different: dense sand shows a more reversible behaviour than loose sand. In particular, the S-shaped curve observed in Figure 2a indicates that the influence of uplift is significant for the HD sand; on the contrary, for LD, only plasticity is developed, with larger energy dissipation (Figure 3a): the foundation on loose sand presents continuously increasing settlements without uplifting (Figure 3d).

The numerical results reproduce satisfactorily the behaviour of the foundation in terms of hysteretic response in HD (Figure 2a, b) and LD (Figure 3a, b). This indicates that the model is able to reproduce correctly both uplift-dominated response (S-shaped curve, HD case in Figure 2a), and the plasticity-dominated response (LD case in Figure 3a). In the moment-rotation plane, the attainment of the strength capacity and the energy dissipation associated with the shape of the hysteresis loops and the stiffness degradation are in good agreement with the observed ones.

The peak and residual rotations are also well estimated in both HD (Figure 2c) and LD (Figure 3c) cases. Moreover, the trend of vertical settlements is well reproduced in terms of shape and amplitude for HD (Figure 2c) and LD (Figure 3c) sand.

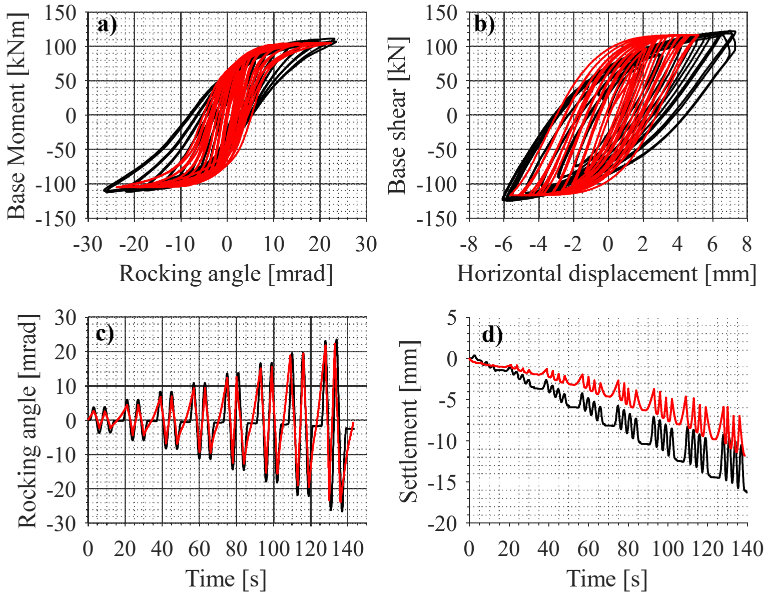

Figure 2. Comparison between numerical simulations (red lines) and experimental results (black lines) of TRISEE Phase III-HD test: a) moment vs. rocking angle; b) base shear vs. horizontal displacement; c) rocking angle history, d) settlement history

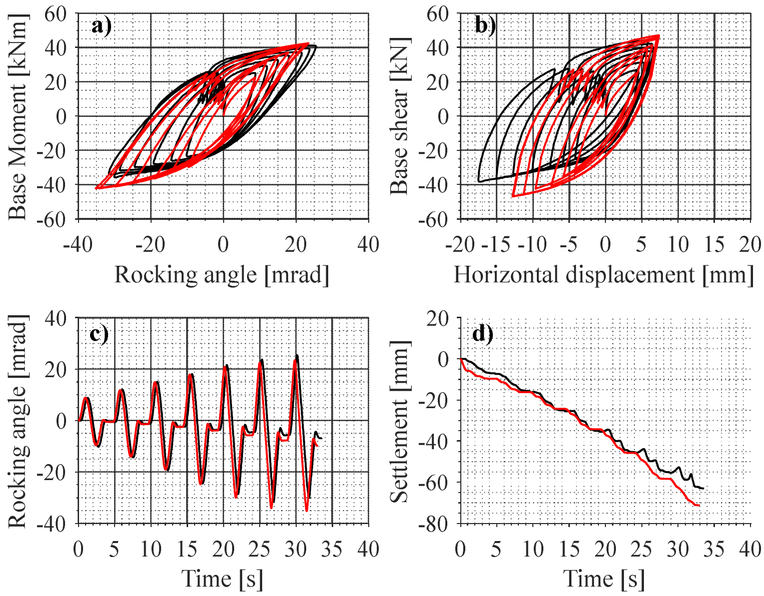

Figure 3. Comparison between numerical simulations (red lines) and experimental results (black lines) of TRISEE Phase III-LD test: a) moment vs. rocking angle; b) base shear vs. horizontal displacement; c) rocking angle history, d) settlement history

3.2 PWRI DYNAMIC TESTS

The PWRI shake table tests (e.g. Shirato et al., 2005,2007; Paolucci et al., 2008) were focused on the performance of a model shallow foundation under realistic seismic loads. A laminar box (2.1 m high and 4 m x 4 m in plan, Figure 4) was placed on the shake table and filled with dry Toyoura sand (with a relative density D_R = 80%, mass density ρ = 1.60 x 10^3 kg/m^3, and an internal friction angle of 42.1°).

Figure 4. Experimental setup of PWRI dynamic tests (after Paolucci et al., 2008)

The test model, located at the centre of the box on the ground level, consists of three main structural components: a steel rack at the top, 5227 N heavy, a 0.5 m sided square foundation block at the bottom, and a short steel beam with I cross-section connecting the two massive blocks. The total height of the model was 0.753 m, while the height of the centre of mass was 0.420 m from the base of the foundation. The total weight of the structural model was 8385 N. The ultimate bearing capacity was evaluated from the available results from monotonic centred vertical loading tests on the model, and is equal to N_{max} = 245 kN. The static safety factor FS = 245/8.385 = 29 is implied. For a more comprehensive and detailed description of the tests, see Paolucci et al. (2008), Shirato et al. (2005,2007).

Hereafter, the experimental results from PWRI shaking table test are compared with the numerical ones for load cases 1-2 and 2-2, corresponding to the seismic inputs shown in Figure 5.

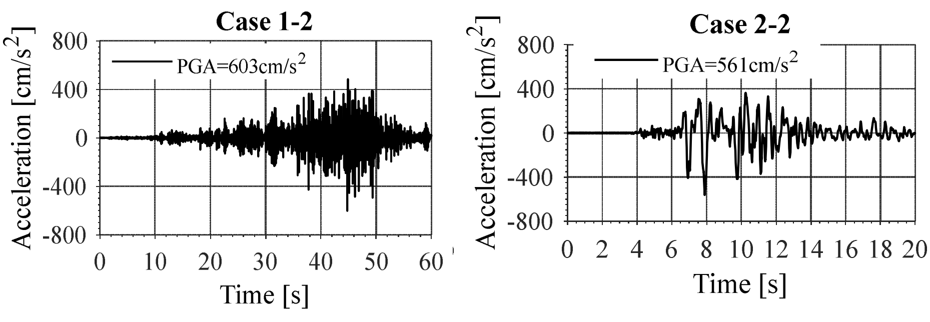

Figure 5. Earthquake records used as input for the PWRI shake table tests

In the numerical analyses, the superstructure was modelled as a SDOF oscillator through an elastic frame element, while the macro-element parameters values are summarised in Table 4. The foundation elastic impedances and damping parameters were set equal to the values calibrated by Paolucci et al. (2008) through the sweep tests and the initial elastic phases of the earthquake excitation. Note that concentrated dashpots at the base of the superstructure were introduced in the model to reproduce the radiation damping. The plastic parameters were calibrated on the experimental results, as explained for the TRISEE experimental tests.

Table 4. Macro-element parameters used for the simulation of PWRI dynamic tests

B	K_{NN}	K_{VV}	K_{MM}	C_{NN}	C_{VV}	C_{MM}	d_θ	H_0^{pl}	χ_g	N_{max}
[m]	[MN/m]	[MN/m]	[MN/m]	[kNs/m]	[kNs/m]	[kNms]	[-]	[-]	[-]	[MN]
0.5	200	110	70	18	16	2	200	0.2	2	0.235

The comparison between experimental (black line) and numerical (red line) results of case 1-2 is shown in Figure 6. From the hysteretic cycles in the moment-rocking angle plot, it is clear that the structure is subjected to a large number of loading cycles, since the input motion consists of a very long duration (more than 60 s) and high-frequency excitation. In spite of this, the large number of loops in the moment vs. rocking plot is adequately reproduced in the simulated response. The attainment of the footing limit moment value, of about 1.5 kNm, from 30 s to 50 s is well captured by the numerical simulations. The large amount of permanent displacements, equal to 30 mrad for the rocking angle and 12 mm for the settlement are correctly predicted by the macro-element model. This represents an important improvement with respect to other simulation attempts of PWRI Case 1-2 (e.g. Shirato et al., 2008b; Paolucci et al., 2008).

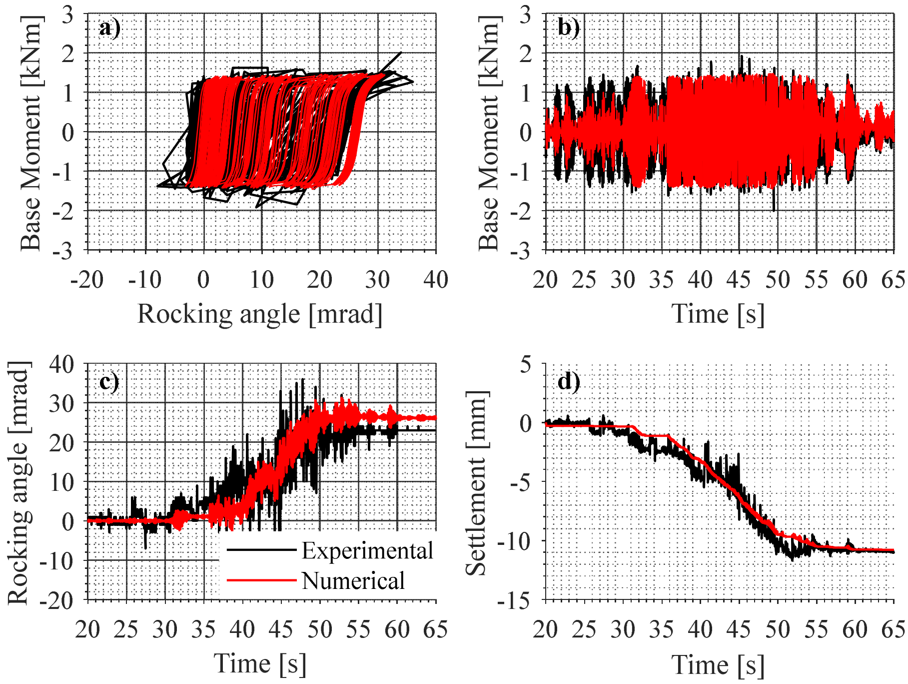

Figure 6. Comparison between experimental results (black lines) and numerical simulations (red lines) of PWRI 1-2 test: a) base moment-rotation hysteretic cycles, b) base moment history, c) rocking angle history, d) evolution of settlements

The experimental and numerical results of case 2-2 are compared in Figure 7. In this case, the experimental behaviour presents a large non-regular shaped cycle, ending with a significant stiffness degradation, which is promptly recovered after one oscillation (black line). On the contrary, the numerical response in terms of hysteretic behaviour appears to be more regular (red line), and not capable of reproducing the largest hysteretic cycle of the response, observed around 10.5 s.

On the other hand, the history of the foundation base moment is well captured by the numerical simulation. Moreover, the evolution in time of the rotation and settlement are in satisfactory agreement with the observed one, although the peak rotation is underestimated (30 mrad against 55 mrad). The uplift model allows to predict the evolution of vertical settlement in reasonable agreement, both in magnitude and in shape, while the residual settlement, around 2 mm, is well reproduced by the numerical simulation.

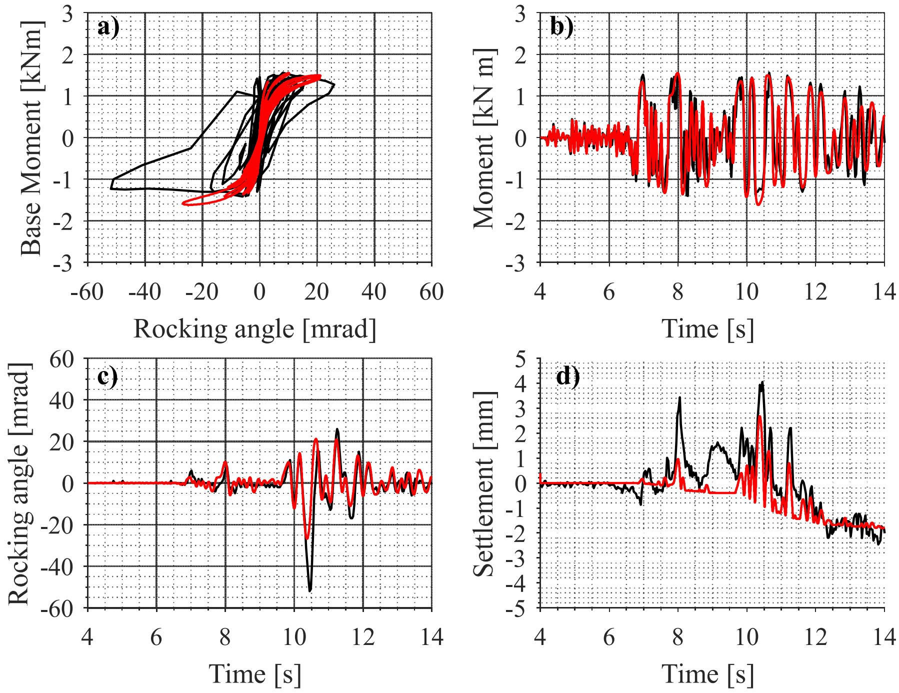

Figure 7. Comparison between experimental results (black lines) and numerical simulations (red lines) of PWRI 2-2 test: a) base moment-rotation hysteretic cycles, b) base moment history, c) rocking angle history, d) evolution of settlements

Figini et al. (2012) have also simulated the PWRI tests. Their results were improved in this simulation, particularly in terms of: (a) the moment-rotation hysteretic response – the present macro-element is able to predict more accurately the number of loops and the energy dissipation; (b) settlement prediction – this model is able to follow the trend of vertical settlements in time, with a good prediction of the permanent displacements at the end of the excitation, while in Figini et al. (2012) the history of vertical settlements is not well captured except for the initial phase of the shaking.

3.3 CAMUS DYNAMIC TESTS

A series of seismic tests on reinforced concrete (RC) shear wall structures were performed at CEA within the Camus Research Project between 1996 and 1999. One of the 1:3 scaled specimens, CAMUS IV, is of interest for the validation of the macro-element. The specimen consists of two parallel 5-floor RC walls, without openings, connected by 6 floor slabs and with a total mass of 36 tonnes. While the previous specimens were tested as fixed base wall buildings, the CAMUS IV model stands on a 40-cm-deep sand layer (with a relative density D_R = 71%, a friction angle of 35° and a dry unit weight of 16.1 kN/m^3) with two strip foundations (2.1 m x 0.8 m, Figure 8). For more details about the setup description and processing of the experimental data, see Combescure and Chaudat (2000) and Combescure et al. (2001). A series of increasing intensity seismic tests were performed, with the acceleration inputs of interest for this work reproduced in Figure 9.

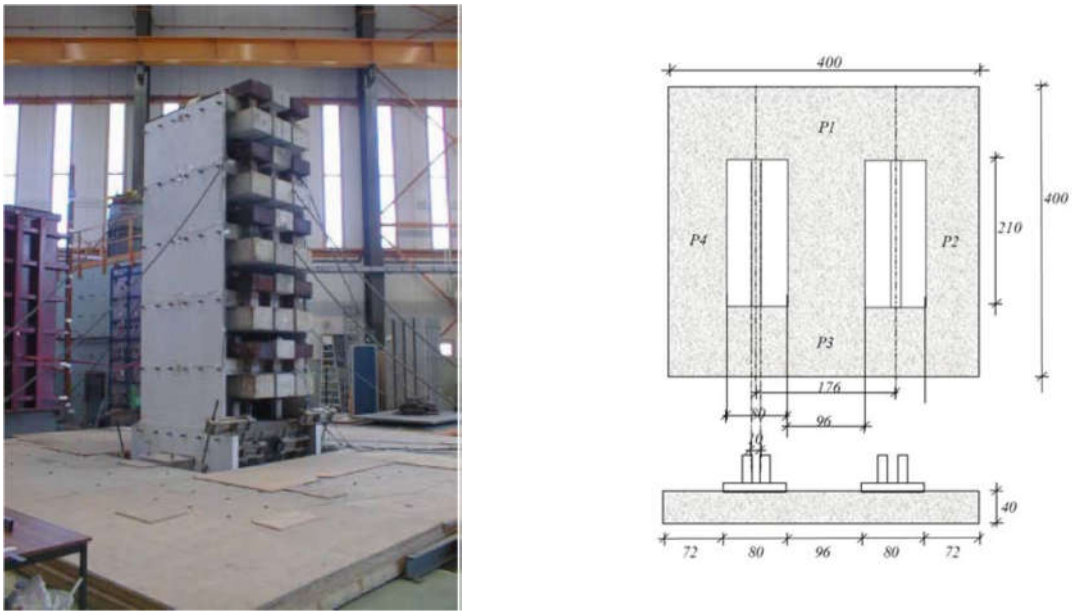

a) **b)**

Figure 8. a) General view of the CAMUS experimental setup; (b) dimensions of the sand box and of the two footings for the CAMUS IV specimen (after Combescure and Chaudat, 2000)

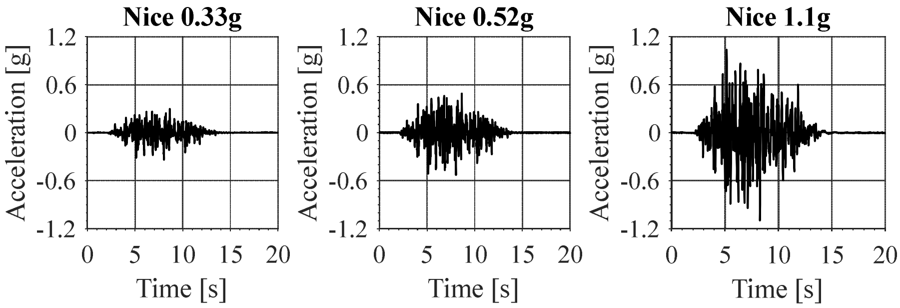

Figure 9. Input signals used for the numerical simulation of CAMUS IV tests: Nice 0.33 g, 0.52 g and 1.1 g

In the numerical simulation of CAMUS IV tests, only one of the two shear walls was considered, similarly to Cremer et al. (2001) and Figini et al. (2012). It was modelled as a MDOF elastic cantilever beam, with lumped masses at each floor. The total mass of the wall including the foundation is about 19.3 tonnes. In the numerical simulations, Rayleigh damping was considered for the superstructure, to achieve a damping ratio ξ = 2% at frequencies close to the fundamental frequency of the structure, which has also been used in Combescure et al. (2001) and Figini et al. (2012).

The macro-element parameters used for the simulation of CAMUS IV tests are summarised in Table 5 for the three events of Figure 9. The foundation static bearing capacity N_{max} was taken equal to the value used by Cremer et al. (2001), 0.8 MN, corresponding to a static factor of safety FS≅4. The foundation elastic impedances were set equal to those reported in Figini et al. (2012) for Nice 0.33 g and Nice 0.52 g tests; these values were calibrated based on the first cycles of the force-displacement curves of the Nice 0.05 g test. Note that the elastic rotation stiffness for the Nice 1.1 g test is reduced with respect to the previous cases to take into account the degradation of dynamic characteristics of the specimen, as reported in Combescure and Chaudat (2000). The footing dashpot coefficients, reported in Table 5, are equal to the ones considered by Grange (2008). The parameters of the surface of ultimate loads are calibrated based on the Nice 0.52 g test, in which the loads reach their limit values. The plastic parameters were calibrated based on the experimental results, as described for the TRISEE test simulations.

Table 5. Macro-element parameters used for the simulation of CAMUS IV dynamic tests

Input	B	K_{NN}	K_{VV}	K_{MM}	C_{NN}	C_{VV}	C_{MM}	d_θ	H_0^{pl}	χ_g	N_{max}
[g]	[m]	[MN/m]	[MN/m]	[MN/m]	[kNs/m]	[kNs/m]	[kNms]	[-]	[-]	[-]	[MN]
0.33 0.52	2.1	230	50	160	200	110	280	10	0.4	0.5	0.8
1.1	2.1	230	50	140	200	110	280	0.1	0.4	1	0.8

The comparison between the numerical simulation for Nice 0.33 g and the experimental results is shown in Figure 10. As can be observed, the simulated results are in very good agreement with the observed foundation response. Namely, the hysteretic behaviour of the foundation, governed mainly by uplift, is well-reproduced by the macro-element. In what concerns the foundation rotations and settlements, they are very well predicted, both in magnitude and in shape throughout the duration of the excitation. Likewise, the displacements at the top of the structure agree in both results.

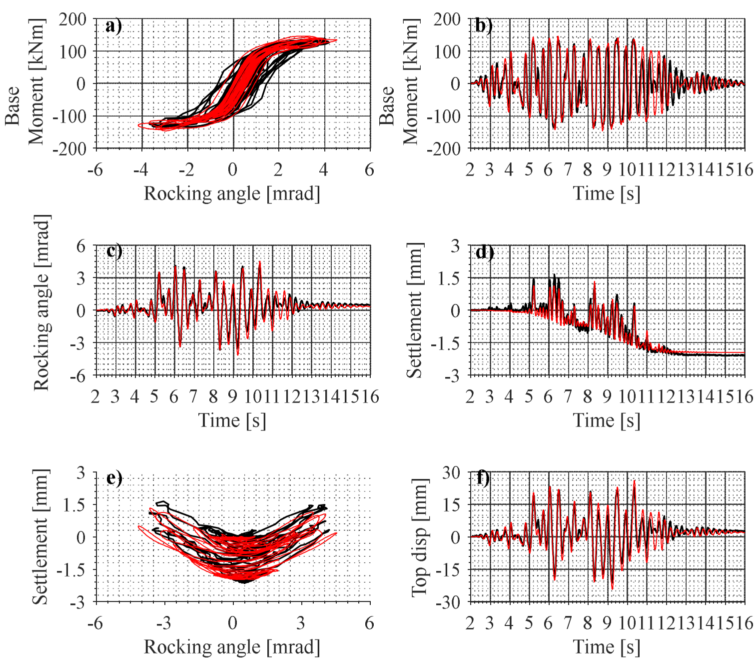

Figure 10. Comparison between experimental results (black lines) and numerical simulations (red lines) of CAMUS IV test for Nice 0.33 g: a) base moment-rotation hysteretic cycles, b) base moment history, c) rocking angle history, d) evolution of settlements; e) settlement vs. rocking angle; f) evolution of top displacement

Regarding the results for seismic input Nice 0.52 g, they are depicted in Figure 11. The uplift-plasticity coupling is well reproduced by the S-shape curves and area of the loops in the moment-rotation response. The moment of uplift initiation is captured accurately, as well as the limit moment level, when the surface of ultimate loads is reached and the plastic displacement flow is produced. The history of base moment is also very well followed, similarly to the vertical settlement and rocking angle evolutions, which are very close to the experimental ones. These results highlight the capacity of the macro-element model to reproduce accurately the coupling between the uplift and plasticity.

Finally, the numerical results for input Nice 1.1 g are compared with the observed response in Figure 12. Differently from the previous cases, in which the S-shape of hysteretic behaviour was observed, in this case the moment-rotation response is more complex and not symmetric, reaching much larger values of the rotation. There are large and irregularly shaped cycles, ending with significant stiffness degradation. Although the numerical model does not fit this trend completely, namely not capturing the change in stiffness that characterises the largest cycle, the overall response of the foundation is qualitatively captured, both in terms of base moment history and in terms of foundation displacements. Moreover, the accumulation of residual footing rotations (Fig.5.19c) is satisfactorily simulated, as well as the evolution of vertical settlements. Regarding the structural response, the simulated top displacement is in good agreement with the experimental one.

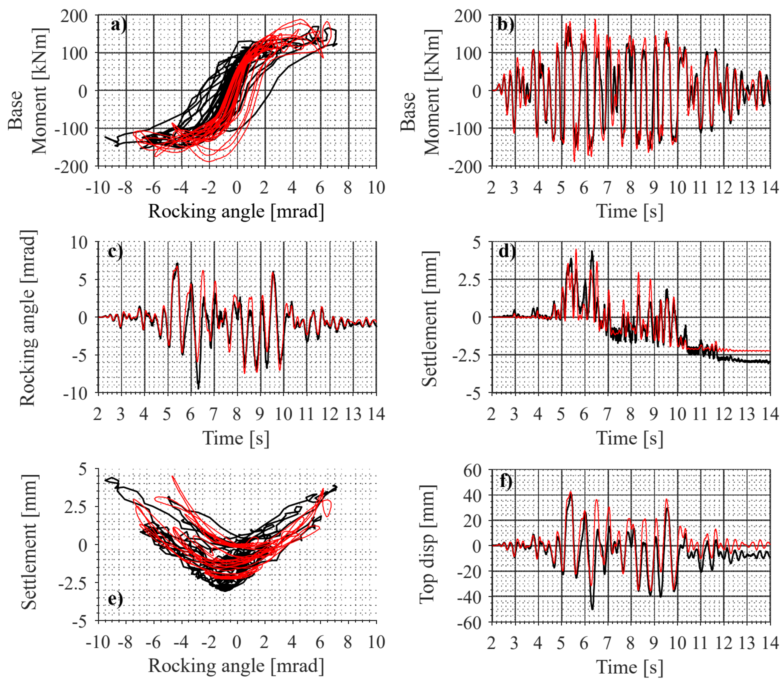

Figure 11. Comparison between experimental results (black lines) and numerical simulations (red lines) of CAMUS IV test for Nice 0.52 g: a) base moment-rotation hysteretic cycles, b) base moment history, c) rocking angle history, d) evolution of settlements; e) settlement vs. rocking angle; f) evolution of top displacement

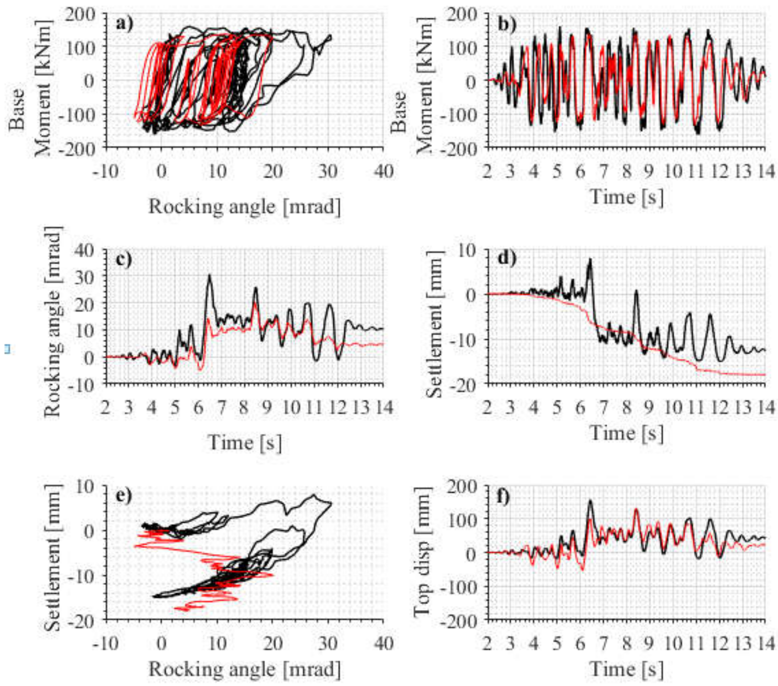

Figure 12. Comparison between experimental results (black lines) and numerical simulations (red lines) of CAMUS IV test for Nice 1.1 g: a) base moment-rotation hysteretic cycles, b) base moment history, c) rocking angle history, d) evolution of settlements; e) settlement vs. rocking angle; f) evolution of top displacement

3.4 SSG04 Centrifuge Tests

Gajan et al. (2005) and Gajan and Kutter (2008) conducted a test programme of centrifuge experiments, subjected both to slow lateral cyclic loading and to dynamic base shaking, aiming at better understand the behaviour of buildings on shallow foundations under large nonlinear loadings and soil stresses representative of field conditions. The experiments have been conducted in a 9.1 m radius centrifuge at 20 g centrifuge acceleration.

The centrifuge test programme consisted of seven series of tests, including 40 models tested under different loading conditions. Such tests were performed to study the effects of footing dimensions, depth of embedment, initial static vertical factor of safety and soil type on the nonlinear soil-foundation response. Figure 13 represents the model container and the experimental setup for different tests. Hereafter, the focus is on the dynamic loading test, denoted as SSG04, and also shown in Figure 13. A soil bed (4.0 m depth) of dry Nevada sand (with relative density, D_R = 80% and friction angle of 42°, estimated experimentally from the observed ultimate vertical load) was prepared inside a rigid container (1.75 m x 0.90 m x 0.53 m, in model dimensions). Scaling laws for centrifuge modelling were described in detail in Kutter (1995).

The structural configuration includes double shear-walls, connected by a rigid floor (Figure 13). The total mass of the prototype wall structure, in aluminium, is equal to 36.8 tonnes per footing and height of the centre of gravity equal to 5.3 m. Each wall is connected to a strip foundation (with length, L = 2.8 m; width, B = 0.65 m; embedment, D = 0 m).

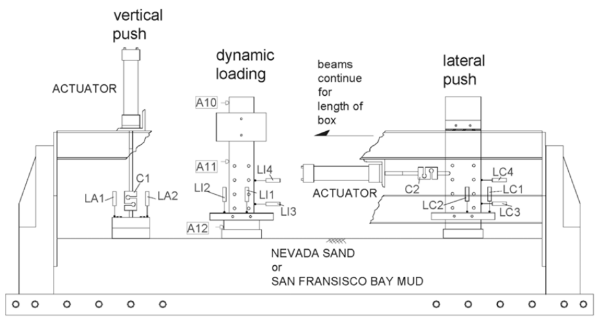

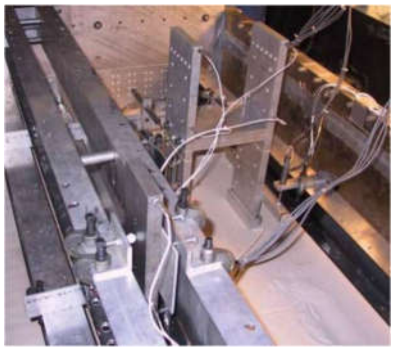

Figure 13. Model container and experimental setups for different tests (left). Experimental setup and instrumentation for SSG04 dynamic base shaking tests (right) (after Gajan, 2006)

The base acceleration, applied in the direction of the longer dimension, corresponds to tapered cosine cycles with increasing amplitude and predominant frequency of about 1.2 Hz and with higher frequency accelerations superimposed. Different peak base accelerations were obtained by scaling up or down the base soil acceleration, simultaneously maintaining the same frequency in dynamic shaking tests. Figure 14 shows three acceleration histories, with increasing amplitude, from 0.12 g to 0.90 g, selected for the numerical simulation of SSG04 centrifuge tests.

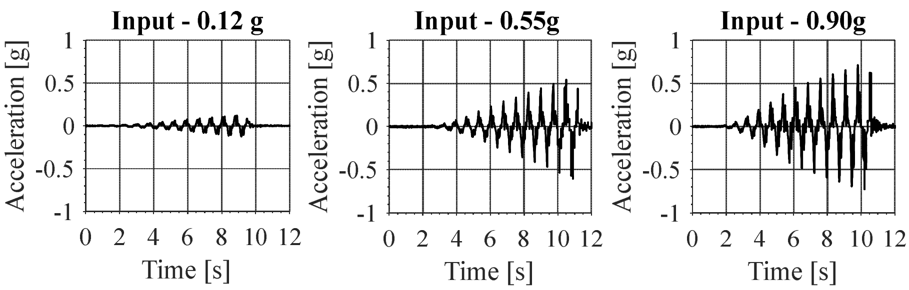

Figure 14. Input signals used for the numerical simulation of SSG04 tests, with amplitudes of 0.12 g to 0.90 g

The shear wall was modelled as a cantilever beam, similarly to Gajan (2006). The values of the macro-element parameters are reported in Table 6, for the 0.12 g, 0.55 g and 0.90 g inputs. The elastic foundation impedance values, in the vertical and in the horizontal directions, are available in Gajan (2006) and used in this work, whereas the initial elastic rotational stiffness was calibrated on the first cycles of the moment-rocking response observed at the beginning of the smallest magnitude shaking, with peak acceleration equal to 0.12 g. The maximum vertical bearing capacity value was set equal to that reported in Gajan (2006). The macro-element parameters characterising the plastic response, were calibrated to the experimental results but trying to maintain as many parameters as possible constant throughout the different simulations.

Table 6. Macro-element parameters used for the simulation of SSG04 dynamic tests

Input [g]	B [m]	K_{NN} [MN/m]	K_{VV} [MN/m]	K_{MM} [MN/m]	C_{NN} [kNs/m]	C_{VV} [kNs/m]	C_{MM} [kNms]	d_θ [-]	H_0^{pl} [-]	χ_g [-]	N_{max} [MN]
0.12	2.8	560	150	520	200	100	200	10	0.2	0.5	1.4
0.55	2.8	560	150	520	200	100	200	0.1	0.2	1.70	1.4
0.90	2.8	560	150	520	200	100	200	0.1	0.2	1.70	1.4

Figure 15 shows the comparisons of the simulated and observed responses for the 0.12 g test. For the smallest magnitude shaking, even though the mobilised moment does not reach the moment capacity, the moment-rotation hysteretic loops show an onset of nonlinear behaviour and energy dissipation, which is reasonably well-captured by the numerical results. The evolution of foundation rotations and of vertical settlements is in good agreement with the observed one.

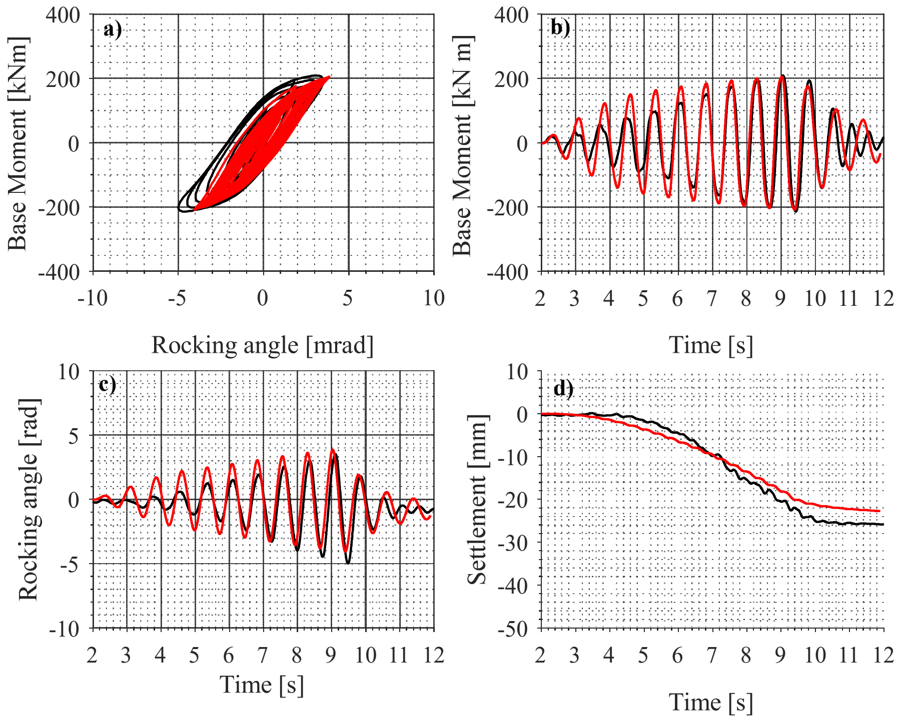

Figure 15. Comparison between experimental results (black lines) and numerical simulations (red lines) of SSG04 for the 0.12 g input: a) base moment-rotation hysteretic cycles, b) base moment history, c) rocking angle history, d) evolution of settlements

The comparison between the macro-element response and the experimental results for the test with 0.55 g is represented in Figure 16. The foundation dynamic response is dominated by soil plasticity, as can be observed by the significant area of the hysteretic loops. Although the numerical simulation shows a stiffer response than the observed one, the overall hysteretic behaviour is reasonably well reproduced, capturing the moment capacity and the size of the loops. On the contrary, the shear-horizontal displacement relationship fails in reproducing the observed response. The experimental response shows a significant nonlinear behaviour, which is not well represented in the macro-element model response; hence the degradation of the shear stiffness is not captured, producing an underestimation of the horizontal displacements. This is likely related to the larger estimated value of the maximum horizontal capacity, based on the value of the soil-friction angle, which prevents a more significant plastic response. However, the evolution of the simulated foundation deformations correlates reasonably well with the experimental ones, especially in terms of general shape. The predicted residual settlements are slightly larger than the observed ones, while the history of rocking angle follows reasonably well the observed one. Moreover, the evolution of the drift is reproduced reasonably well.

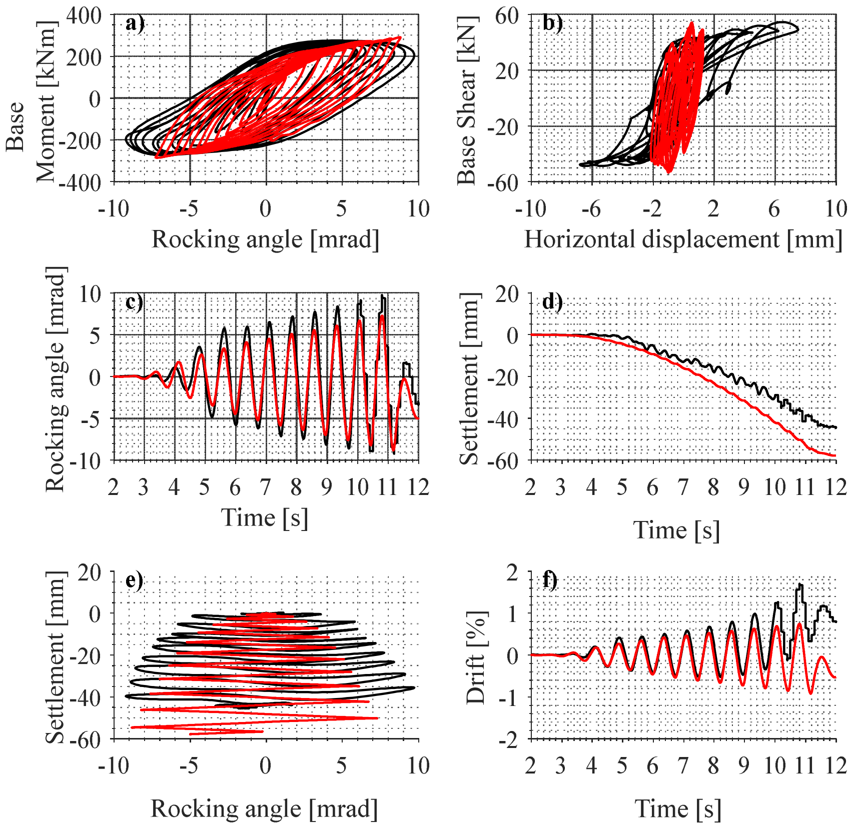

Figure 16. Comparison between experimental results (black lines) and numerical simulations (red lines) of SSG04 for the 0.55 g input: a) base moment-rotation hysteretic cycles, b) base shear-horizontal displacement cycles, c) rocking angle history, d) evolution of settlements; e) settlement vs. rocking angle; f) evolution of drifts

The numerical results of 0.90 g test are now compared with the observed ones in Figure 17, for the foundation response and structural response. The experimental results show that the footing rocks through larger amplitude rotations, showing more permanent settlements as the shaking intensity increases. The foundation hysteretic loops show unsymmetrical behaviour and a permanent tilt at the end of the shaking. This observed behaviour is well predicted by the numerical simulations. The moment capacity and the degradation of rotational stiffness with increasing amplitude of rotation are captured satisfactorily in the model. On the contrary, as previously also pointed out for the 0.55 g input, the shear-horizontal behaviour does not fit the observed one. The simulated evolution of foundation displacements, in terms of rocking angle and vertical settlements, is consistent with the experimental results: the amount of permanent rotation and vertical settlement is very well reproduced, showing almost equal residual values.

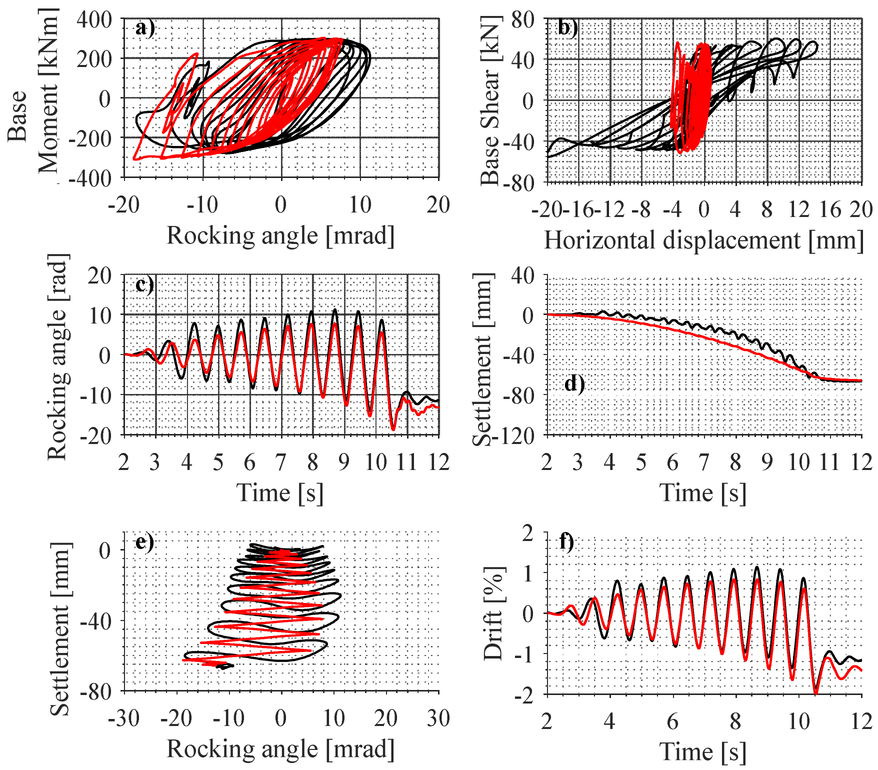

Figure 17. Comparison between experimental results (black lines) and numerical simulations (red lines) of SSG04 for the 0.90 g input: a) base moment-rotation hysteretic cycles, b) base shear-horizontal displacement cycles, c) rocking angle history, d) evolution of settlements; e) settlement vs. rocking angle; f) evolution of drifts

Although some discrepancies in the predicted hysteretic responses were detected, these results can be considered very satisfactory, proving the capacity to predict foundation displacements under a very high level of seismic input. This can be appreciated if one considers the performance of the available simulation results carried out by Gajan (2006). The improvements of the present modelling approach are visible in the moment-rocking response simulation, and in the settlement-rotation diagram.

3.5 Variability of Macro-Element Parameters

Parameters calibration is a significant aspect to be considered in order for the macro-element model to be used for practical applications. For this purpose, the attention was focused on the three discussed parameters, the soil/ footing contact degradation parameter, d_θ, the reference plastic modulus, H_0^{pl} and the plastic potential, χ_g, which are specific of this macro-element and cannot be related in a straightforward way to the elastic or strength parameters of the soil-foundation system. The objective is to find a default set of values that ensures an overall good performance of the model.

It should be noted that the PWRI macro-element parameters are not considered in this discussion, since the d_θ value used in PWRI simulations differs significantly from the values adopted in other tests. The main difference with respect to the other cases is that the most severe PWRI tests are based on the combination of a very high static safety factor (FS = 30) and very large levels of seismic excitation that may have induced a significant degradation of the contact surface of the soil and the foundation, thus requiring an extremely large d_θ for a proper simulation of the experimental results.

From the previous analyses, it can be seen that the parameter that presents a significant variability for the various tests is the footing/soil contact degradation parameter, d_θ, ranging from 0.1 to 10; while the plastic potential parameters varies from 0.5 to 2. The reference plastic modulus values set in each independent test are quite similar, changing from 0.2 to 0.4.

The reference plastic modulus, H_0^{pl} *.*

The reference plastic modulus, H_0^{pl}, is related to the magnitude of plastic displacements: a lower value is associated to larger plastic displacements. It can be observed that H_0^{pl} = 0.4 occurs only for the CAMUS IV tests (for 0.33 g and 0.55 g case) that have shown a uplift-dominated response. On the other hand, a value of 0.2 is found for the plastic-dominated response (e.g. TRISEE HD, TRISEE LD, SSG04).

The plastic potential parameter, χ_g*.*

Focusing on the χ_g parameter, it is one of the parameters used for the plastic potential formulation. Changing χ_g values, the direction of the normal to plastic potential changes. Figure 18 shows the variability of χ_g as a function of the permanent vertical displacement normalised by the foundation length, *δ/L*.

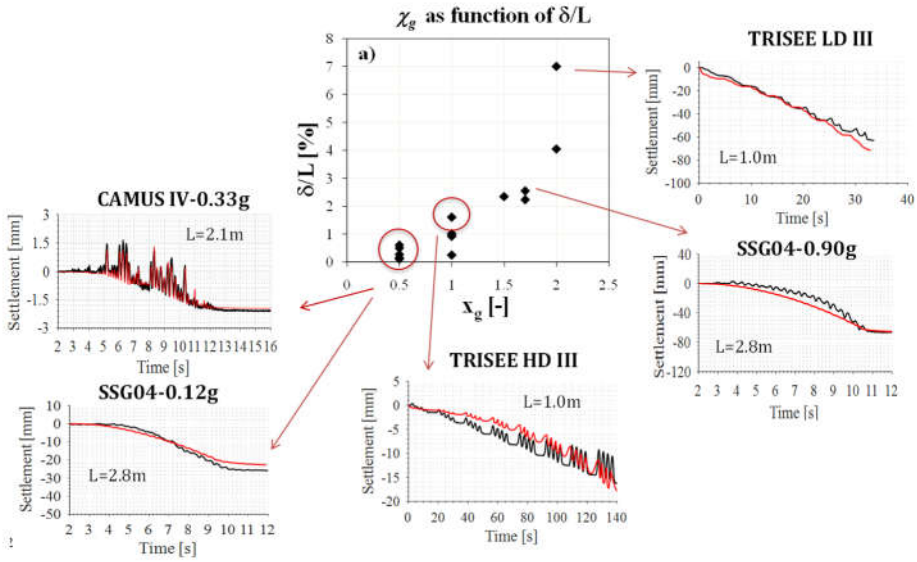

Figure 18. Variability of the plastic potential parameter χ_g as function of the normalised vertical displacement, δ/L. The time evolution of settlements is also displayed for five selected case: CAMUS IV 0.33 g and SSG04 0.12 g for χ_g=0.5 (left); TRISEE HD III for χ_g=1 (centre); TRISEE LD III and SSG04 0.90 g for χ_g=2 (right)

It can be observed that:

- χ_g = 0.5 is found for numerical simulations of experimental test characterised by residual settlement δ/L< 0.5, for example, during the CAMUS IV test and during the SSG04 test with a small level of input acceleration (0.12g);

- χ_g~ 2 is used for the experimental tests in which the foundations experience significant permanent settlement (6.5% for cyclic TRISEE LD; 2.5% for dynamic SSG04).

- 0.5 <χ_g< 2 is detected in case the δ/L varies from 0.5% to 1.5% (e.g. CAMUS IV for 1.1 g).

The effect of the χ_g values on the numerical response can be also observed in Figure 19. The black line represents the observed response during SSG04 test, for 0.55 g input, in terms of the history of settlements. The coloured lines correspond to different values of χ_g, varying from 0.5 to 2. The trend observed can be explained as follows: when a low value of χ_g is adopted, the normal to the plastic potential surface is mainly directed along the vertical axis (related to the rotation component of plastic displacement); on the contrary, when a high value is adopted, the normal is mainly directed along the horizontal axis, that implies higher values of vertical settlement.

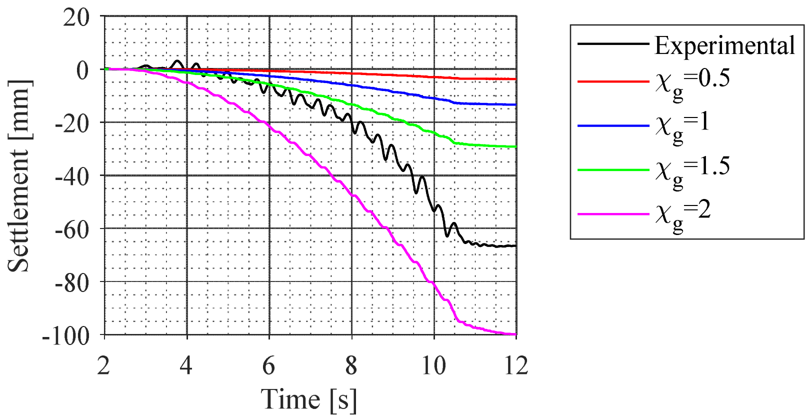

Figure 19. Effect of plastic potential parameter, χ_g, on the numerical results in terms of history of vertical settlement

The footing/soil contact degradation parameter, d_θ.

From the previous analyses, it can be seen that the parameter that presents the most significant variability is the footing/soil contact degradation parameter, ranging between 0.1 and 10. It is worth noting that such variability can be detected only for dense sand cases, while for the low density cases (e.g. TRISEE LD, D_R = 45%), it is equal to 0.1.

The damage parameter is a function of the cumulative plastic rotations and it has been introduced in the macro-element formulation to define the damage function *D*, that takes into account the reduction of the contact between the footing and the soil due to irrecoverable downward movement of soil beneath the foundation induced by foundation rotations during load cycles.

It can be observed that within the macro-element formulation, a small value of d_θ leads to a more plastic response with wider hysteresis loops, whereas a large value produces the nonlinear elastic response where the uplift is the predominant mechanism, with low energy dissipation.

In order to provide a practical rule to define its value, for example depending on the FS, a set of parametric simulations were carried out, considering two different values of FS, equal to 5 and 15 respectively. The structural model consists of a square footing with length 7.5 m, on sand with a friction angle of 33.5°, shear modulus of 90 MPa and Poisson's ratio of 0.3 (e.g. Sotiriadis et al., 2017). The corresponding footing bearing capacity under pure vertical load was 40 MN. The initial stiffness properties of the footing are estimated based on standard formulas for a square foundation. In the numerical simulations, the model is characterised by the same bearing capacity of the foundation, and by two values of the vertical loads to achieve the two different FS values. A quasi-static cyclic displacement loading (in terms of rotation) is applied in one direction with increasing amplitude. The results, in terms of hysteretic response, are displayed in Figure 20: the moment-rocking foundation response is indicated by a red line for d_θ = 0.1 and by a blue line for d_θ = 10. As can be observed, the influence of d_θ is apparent for low FS systems where plasticity seems to play a more significant role. On the contrary, systems with a larger FS, where uplift response is dominant, exhibit minor or practically no hysteretic damping.

Based on the validation process, as well as on this independent analysis, it can be concluded that: in case of uplift- dominated response (e.g. higher value of FS), or in case of linear response (e.g. in case of small shaking amplitude), the effects of d_θ are negligible; in case of plastic-dominated response (e.g. low values of FS), the suggested reference value should be 0.1.

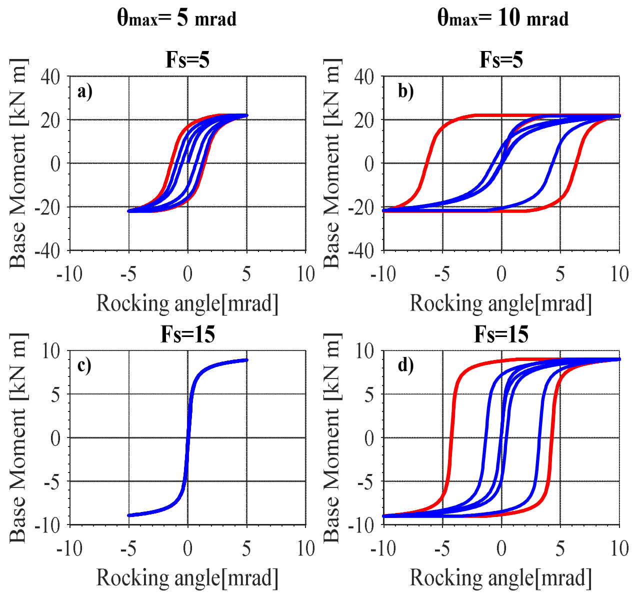

Figure 20. Numerical results in terms of moment vs. rocking angle, obtained by considering two different initial safety factors, FS= 5 and FS= 15, and setting d_θ= 0.1 (red line) and d_θ= 10 (blue line)

The results of the simulations confirm that the d_θ parameter does not affect the results in case of: almost linear foundation response; uplift-dominated response.

On the contrary, the different values of χ_g parameter produce significant variation in the response. As explained previously, this difference is expected, since it is related to the plastic displacement flow, when the surface of ultimate loads is reached. As a practical rule, it can be assumed that: χ_g = 2 for plastic-settlement dominated response, that reasonably occurs in case of loose sand; χ_g = 0.5 for uplift-dominated response, that reasonably occurs in the case of dense sand.

To conclude, the robustness of the model is supported by the relatively limited set of parameters to be calibrated. For predictive analyses using the macro-element, and considering shallow foundations on sand, the following rules can be suggested: for elastic and strength parameters, use the relationships proposed in literature; for model specific parameters, use the parameters of the nonlinear macro-element discussed above, as a summary of the previous validation experience. It is worth underlining that the proposed reference parameter set for sand with different relative density does not depend neither on elastic nor on the strength soil parameters. The dependence on the elastic properties of soil material is implicitly accounted for in the parameters of the dynamic impedance, while the soil strength is implicitly accounted for in the static bearing capacity, N_{max}.

4. CONCLUSIONS

This paper dealt with the numerical modelling of nonlinear foundation behaviour and its interaction with the superstructure. An innovative and efficient pile-head macro-element was presented that is capable of accurately describing the main features of the dynamic response of rigid isolated footings. It was based on the three fundamental characteristics of the footing response: linear elastic behaviour at low levels of loading; uplift evolution and its effects on the rocking behaviour; and failure conditions.

The improved macro-element model builds upon the well-consolidated concepts and formulations of previous models. Nevertheless, it incorporates some major improvements, namely addressing inconsistencies regarding the formulation of the participating mechanisms, such as the soil-footing geometric (uplift) and material (soil plasticity) nonlinearities. Moreover, this macro-element introduces a significantly enhanced uplift model, based on a nonlinear elastic uplift response which also considers some degradation of the contact at the soil/footing interface due to irrecoverable changes in its geometry. An improved bounding surface plasticity model is adopted in order to reproduce a more general and realistic material nonlinear behaviour, which correctly takes into account the simultaneous elastic-uplift and plastic nonlinear responses. Another original feature of this model is represented by its implementation in a finite element code and its extension to three-dimensional cases.

The macro-element was extensively validated against results of experimental tests, including both large-scale and reduced-scale tests. The good, and in some cases excellent, agreement between simulated and observed response of foundation subjected to different shaking inputs demonstrates that the numerical model is able to qualitatively and quantitatively reproduce the experimental behaviour, also when the dynamic nonlinear soil-foundation behaviour plays a dominant role. The prediction of foundation displacements fits very well the experimental results.

The proposed macro-element was tested on the selected cyclic and dynamic experimental datasets covering a wide range of variations of geometries, structures and soil properties. Both uplifting-dominating response and plastic settlement-dominated response were investigated by using tests with different initial safety factor for vertical load, ranging from 4 (CAMUS and SSG04) to 30 (PWRI). In all experiments, the foundation sand presented a different relative density (from 45% in TRISEE LD to 85% in TRISEE HD). Loading inputs included both cyclic loading of varying amplitude and real or artificial earthquake motions of moderate and strong intensity (e.g. the maximum input acceleration varies from 0.12 g (SSG04 test) to 1.1 g (CAMUS). The remarkable agreement achieved between the numerical results and observed response gives an important indication on the robustness and accuracy of the macro-element model.

The numerical model was able to qualitatively and quantitatively reproduce with satisfactory accuracy the experimental behaviour, also for the case in which very intense input motions are used (e.g. CAMUS 1.1g, SSG04 0.90 g). Even in the case of very high excitation (e.g. PWRI), the macro-element model seems to be adequate, since it captures the overall hysteretic response and the residual settlements and rotation. In the opposite scenario, when the maximum footing rotation is limited to about 20 mrad, the numerical model provides very good results (e.g. TRISEE LD; SSG04 for 0.90 g input).

In conclusion, macro-element models have by now reached a very satisfactory level of sophistication and the required maturity to undertake a systematic work of parameter calibration. Furthermore, in order for them to be of use for the practicing engineer, such calibration effort should eventually lead to a database associating specific macro-element models and sets of parameters to specific foundation configurations and soil conditions.

It was therefore another main achievement of the model validation and parametric analyses to define a default set of macro-element parameter values that ensures an overall good performance of the model. The practical indications regarding the selection of the parameters were provided, related to: (i) geometric and elastic parameters; (ii) strength parameters; (iii) model specific parameters. The limited number of model specific parameters (3) to be defined is a key aspect that may favour the practical use of this model either for application in design or for parametric studies.

REFERENCES

Allotey, N., El Naggar, M.H. [2008] "Generalized dynamic Winkler model for nonlinear soil-structure interaction analysis," *Canadian Geotechnical Journal*, Vol. 45, pp. 560-573.

Anastasopoulos, I., Gelagoti F., Kourkoulis R., Gazetas, G. [2011] "Simplified Constitutive Model for Simulation of Cyclic Response of shallow foundations: Validation against Laboratory Tests," *Journal of Geotechnical and Geoenvironmental Engineering*, Vol. 137, No. 12.

Bienen, B., Byrne, B.W., Houlsby, G.T., Cassidy, M.J. [2006] "Investigating six-degree-of-freedom loading of shallow foundations on sand," *Géotechnique*, Vol. 56, No. 6, pp. 367-379.

Borja, R.I., Lin, C.H., Montáns, F.J. [2001] "Cam-Clay plasticity, Part IV: Implicit integration of anisotropic bounding surface model with nonlinear hyperelasticity and ellipsoidal loading function," *Computer Methods in Applied Mechanics and Engineering*, Vol. 190, pp. 3293-3323.

Butterfield, R., Gottardi, G. [1994] "A complete three-dimensional failure envelope for shallow footings on sand," *Géotechnique*, Vol. 44, No. 1, pp. 181-184.

Chatzigogos, C.T., Pecker, A., Salençon, J. [2007] "Seismic bearing capacity of a circular footing on a heterogeneous cohesive soil," *Soils and Foundations*, Vol. 47, No. 4, pp. 783-797.

Chatzigogos, C.T., Pecker, A., Salençon, J. [2009] "Macroelement modeling of shallow foundations," *Soil Dynamics and Earthquake Engineering*, Vol. 29, No. 5, pp. 765-781.

Chatzigogos, C.T., Figini, R., Pecker, A., Salençon, J. [2011] "A macroelement formulation for shallow foundations on cohesive and frictional soils," *International Journal for Numerical and Analytical Methods in Geomechanics*, Vol. 35, No. 8, pp. 902-931.

Correia, A.A., Pecker, A. [2019] "Nonlinear pile-head macro-element for the seismic analysis of structures on flexible piles," submitted to *Bulletin of Earthquake Engineering*.

Cremer, C., Pecker, A., Davenne, L. [2001] "Cyclic macro-element for soil-structure interaction: material and geometrical non-linearities," *International Journal for Numerical and Analytical Methods in Geomechanics*, Vol. 25, No. 13, pp. 1257-1284.

Cremer, C., Pecker, A., Davenne, L. [2002] "Modelling of nonlinear dynamic behaviour of a shallow strip foundation with macro-element," *Journal of Earthquake Engineering*, Vol. 6, No. 2, pp. 175-211.

Dafalias, Y.F. [1986] "Bounding surface plasticity. I: Mathematical foundation and hypoplasticity," *Journal of Engineering Mechanics*, Vol. 112, No. 9, pp. 966-987.

Figini, R., Paolucci, R., Chatzigogos, C.T. [2012] "A macro-element model for non-linear soil-shallow foundation-structure interaction under seismic loads: theoretical development and experimental validation on large scale tests," *Earthquake Engineering and Structural Dynamics*, Vol. 41, No. 3, pp. 475-493, DOI: 10.1002/eqe.1140.

Gajan, S., [2006] "Physical and numerical modeling of nonlinear cyclic load-deformation behavior of shallow foundations supporting rocking shear walls, *Ph.D. Thesis*, University of California, Davis, USA.

Gajan, S., Kutter, B.L. [2008] "Capacity, settlement, and energy dissipation of shallow footings subjected to rocking," *Journal of Geotechnical and Geoenvironmental Engineering*, Vol. 135, No. 3, pp. 407–420.

Gavras, A.G., Kutter, B.L., Hakhamaneshi, M., Gajan, S., Tsatsis, A.,Sharma, K., Kouno, T., Deng, L., Anastasopoulos, I., Gazetas, G., Variam, K.A. [2018] "FoRDy: Rocking Shallow Foundation Performance in DynamicExperiments".

Gazetas, G. [1991] "Foundation vibrations," *Foundation Engineering Handbook*, 2nd Ed., Fang, H.Y. (Ed.), pp. 553-593, Van Nostrand Reinhold, New York, USA.

Grange, S., Kotronis, P., Mazars, J. [2008] "A macro-element for a circular foundation to simulate 3D soil-structure interaction," *Int. Journal for Num. and Analytical Meth. In Geomechanics*, Vol. 32, pp 1205-1227.

Gourvenec, S. [2007] "Shape effects on the capacity of rectangular footings under general loading," *Géotechnique*, Vol. 57, No. 8, pp. 637-646.

Hakhamaneshi, M., Kutter, B.L., Gavras, A.G., Gajan, S., Tsatsis, A., Liu, K., Sharma, Pianese, G., Kouno, T., Deng, L., Paolucci, R., Anastasopoulos, I., Gazetas, G. [2018] "FoRCY: Rocking Foundation Performance in SlowCyclic and Monotonic Experiments".

Harden, C.W., Hutchinson, T. C. [2009] "Beam-on-nonlinear-Winkler-foundation modeling of shallow, rocking-dominated footings," *Earthquake Spectra*, Vol. 25, No. 2, pp 277-300.

Lysmer, J., Udaka, T., Tsai C.F. [1975] FLUSH: a computer program for approximate 3-D analysis of soil-structure interaction problems. EERC Report 75-30, University of California, Berkeley, USA.

Nova, R., Montrasio, L. [1991] "Settlements of shallow foundations on sand," *Géotechnique*, Vol. 41, No. 2, pp. 243-256.

Paolucci, R. [1997] "Simplified evaluation of earthquake-induced permanent displacements of shallow foundations," *Journal of Earthquake Engineering*, Vol. 1, No. 3, pp. 563-579.

Paolucci, R., Shirato, M., Yilmaz, M. T. [2008] "Seismic behaviour of shallow foundations: Shaking table experiments vs. numerical modeling," *Earthquake Engineering and Structural Dynamics*; Vol. 37, pp 577-595.

Prévost, J.H. [1999] *Dynaflow*.

Salençon, J. [1990] "An introduction to the Yield Design Theory and its applications to Soil Mechanics," *European Journal of Mechanics A/Solids*, Vol. 9, No. 5, pp. 477-500.

Seismosoft [2019] *SeismoStruct 2019 – A computer program for static and dynamic nonlinear analysis of framed structures*, available at: http://www.seismosoft.com.

Shirato, M., Kouno, T., Asai, R., Nakatani, S., Fukui, J., Paolucci, R. [2008a] "Large-scale experiments on nonlinear behaviour of shallow foundations subjected to strong earthquakes," *Soils and Foundations*, Vol. 48, No. 5, pp. 673–692.

Shirato, M., Paolucci, R., Kouno, T., Nakatani, S., Fukui, J., Nova, R., di Prisco, C. [2008b] "Numerical simulations of model tests of pier-shallow foundation systems subjected to earthquake loads using an elasto-uplift-plastic macro element," *Soils and Foundations*, Vol. 48, No. 5, pp. 693-711.

Sotiriadis, D., Correia, A.A., Sullivan, T.J. [2017] "Accounting for soil-structure interaction in the seismic design of RC wall structures on shallow foundations", *16th World Conference on Earthquake Engineering (16WCEE)*, Santiago, Chile.

Ukritchon, B., Whittle, A.J., Sloan, S.W. [1998] "Undrained limit analyses for combined loading of strip footings on clay," *Journal of Geotechnical and Geoenvironmental Engineering*, Vol. 124, No. 3, pp. 265-276.

Annex B: Nonlinear pile-head macro-element for the seismic analysis of structures on flexible piles (manuscript by Correia & Pecker, submitted to Bulletin of Earthquake Engineering)

NONLINEAR PILE-HEAD MACRO-ELEMENT FOR THE SEISMIC ANALYSIS OF STRUCTURES ON FLEXIBLE PILES

António A. Correia and Alain Pecker

ABSTRACT

Performance-based design (PBD) procedures require accurate estimates of both maximum and residual displacements in structural systems. Macro-element models are already proven tools for designing structures on shallow foundations according to PBD, since they represent a very cost-effective solution in terms of balance between physical behaviour, simulation accuracy and computational cost. This work extends the macro-element approach to the analysis of laterally loaded pile-shafts and soil-pile-structure interaction. The lateral response of the entire soil-pile system to seismic actions is thus condensed at the pile-head, being represented by a zero-length element located at the base of the columns and subjected to the foundation input motion.

The macro-element model is presented, based on the three fundamental features of the response of laterally loaded piles: initial elastic behaviour, gap opening/closure effects and failure conditions. These three characteristic behaviours are all made compatible by using an inelastic model which accounts for the evolution from initial nonlinear elastic behaviour to full plastic flow at failure. Such inelastic model is based on a bounding surface plasticity theory formulation that ensures a smooth transition from the initial elastic pile-head response up to nonlinear behaviour and collapse.

In order to validate the macro-element, its response is compared with numerical results from advanced simulations of pile lateral behaviour and with load tests on real piles.

Keywords: macro-element; soil-pile-structure interaction; pile-head; lateral response; gap; bounding surface plasticity.

1. INTRODUCTION

Recent tendencies in seismic design procedures call for an accurate determination of maximum and residual displacements of structural systems, thus requiring efficient design tools for analysing the nonlinear seismic performance of structures. While macro-element approaches have proven to be adequate for performance-based design of shallow foundations (*e.g.* Figini *et al*. [2012]), there are no equivalent simplified tools for the analysis of deep foundations. This work aims at broadening the scope of such method to the seismic design of extended pile-shaft-supported bridges. Figure 1 depicts alternative models for analysing the lateral response of piles, either by using the concept of experimentally determined *p-y* curves or by using a pile-head condensation of the response as adopted in the model proposed herein.

The pile-head macro-element may be regarded as a lumped model located at the base of the superstructure which intends to represent the behaviour of the entire soil-foundation system. With the aim of realistically simulating the seismic response of a structure, nonlinear cyclic behaviour has to be considered not only for the superstructure but also for both the foundation and the supporting soil. The main sources of nonlinearity for laterally loaded piles have been shown to be related to soil and pile inelastic response, including gap opening and closure. Only when these effects are fully captured, one can carry out a performance-based assessment of the structure [Correia, 2011].

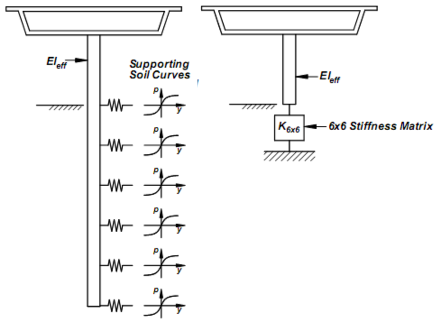

Figure 1. Alternative analysis models for laterally loaded extended pile-shaft supports in bridges (Hutchinson et al. [2002])

The basic idea of the pile-head macro-element is to replace the full description of the soil and pile kinematic, static and constitutive behaviour, in the continuum mechanics sense, by the corresponding generalised force and displacement quantities. In fact, while constitutive formulations are usually conceived using stress and strain tensors, in this work we are concerned instead with generalised forces and displacements. These kinematic and static quantities are related through the inelastic constitutive relationships that compose the core of the macro-element. They may be based on any viscoelastic-plastic model, after reformulating it in terms of those generalised entities.

The shallow foundation macro-element developed by Cremer *et al*. [2001, 2002] adopted a multi-surface plasticity model. However, it was verified that the kinematic and/or isotropic evolution of the inner yield surfaces may become numerically intensive and time consuming, especially for complex geometries of the yield surfaces. On the other hand, bounding surface plasticity models have already been successfully adopted in shallow foundation macro-element formulations [Chatzigogos, 2007; Chatzigogos *et al.*, 2009, 2010; Figini, 2010; Figini *et al.*, 2012]. One such model is adopted herein and presented in the following section, together with the fundamental features of the response related to initial elastic behaviour, gap opening/closure effects and failure conditions.

2. MACRO-ELEMENT MODEL

A pile-head macro-element model is proposed to represent the lateral behaviour of single vertical piles, subjected to a horizontal load and a moment, from the initial stages of loading up until reaching failure. The effects of vertical loading are not directly considered in this model except for its influence on the plastic moment of the pile cross-section. Otherwise, it is considered that the upper zone of the soil profile, until the depth at which the plastic hinge will form, only contributes to the lateral load resistance. The vertical load is assumed to be transferred to the surrounding soil below that depth, where there is no influence of gap opening.

A saturated soil deposit is considered and, upon seismic motion, is assumed to be impervious. The soil is thus considered to have undrained behaviour since the aim of the macro-element is to simulate the pile response under seismic actions, or short-term cyclic loads, and the Tresca failure criterion is assumed to be valid. Figure 2a represents two simplified geotechnical scenarios considered in this study, in terms of undrained shear strength (S_u) distribution along the depth of the soil deposit: constant or linear. Figure 2b illustrates the characteristic soil response for a laterally loaded long pile, namely: a soil passive wedge failure at shallow depths and flow-around failure at larger depths, with a possible gap formation at the back of the pile.

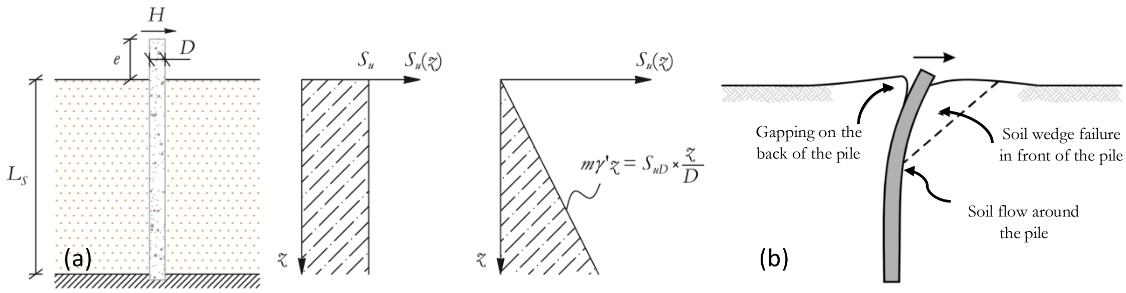

Figure 2. Simplified (a) geotechnical scenarios and (b) soil response for pile-head lateral loading

It seems natural to consider, in the context of a bounding surface plasticity model, the failure surface presented in Correia *et al.* [2019] as the limit yield surface for laterally loaded piles in the space of generalised forces. It should be pointed out that, for dimensional consistency when formulating a plasticity model in the loading space instead of the usual stress space, the generalised forces should either have the same dimensions or be dimensionless. The same applies to the corresponding generalised displacements. Throughout this work, the variables employed in the plasticity formulation are dimensionless, unless explicitly stated otherwise. The normalisation adopted for the macro-element is based on using the pile diameter, D, and the pile yield moment, M_y, as the normalising variables.

The proposed macro-element is based on the three major features of the behaviour of laterally loaded piles, namely:

i) Initial elastic response,
ii) Gap opening and closure,
iii) Failure loading conditions.

The bounding surface plasticity model is used to represent a continuous transition between the initial elastic response and the plastic flow at failure, for monotonic as well as cyclic pile-head loading conditions. The gapping behaviour is represented by a nonlinear elastic model which, however, takes into account and is influenced by the plastic deformation state in the surrounding soil.

An *additive decomposition* of the displacement rate in its *elastic*, *gap* and *plastic* components is considered:

$$\dot{\mathbf{q}}^{egp} = \dot{\mathbf{q}}^{el} + \dot{\mathbf{q}}^{gap} + \dot{\mathbf{q}}^{pl} = \dot{\mathbf{q}}^{eg} + \dot{\mathbf{q}}^{pl} \tag{1}$$

where $\dot{\mathbf{q}}^{egp}$ is the elastic-gap-plastic displacement rate and $\dot{\mathbf{q}}^{eg} = \dot{\mathbf{q}}^{el} + \dot{\mathbf{q}}^{gap}$ is the elastic-gap displacement rate. The following paragraphs describe the macro-element model characteristics and how each of these displacement components is computed.

2.1 Initial Elastic Response

The initial elastic lateral response of single piles has been extensively studied through several sophisticated numerical methods, as reviewed in Correia [2011]. For the purpose of this macro-element model, the pile-head impedances available in literature are deemed to represent such behaviour with sufficient accuracy.

Within the scope of this work, the expressions of the pile-head static stiffnesses presented in EC 8 – Part 5 [2003], for the simplified soil profiles consisting of either constant shear wave velocity, V_S, a linearly increasing one with depth, or a parabolically increasing one with depth are used. Other authors also proposed approximate expressions for the pile-head stiffness coefficients in different simplified soil profiles [Randolph, 1981; Davies and Budhu, 1986; Budhu and Davies, 1987, 1988; Gazetas, 1991]. Several numerical methods have also been proposed for the determination of the elastic response of laterally loaded piles in more complex soil profiles, which may be used in order to obtain the corresponding pile-head stiffnesses. Note that, in the macro-element framework, these stiffness coefficients, and hence the soil Young's modulus at the depth of one diameter, E_{SD}, and the pile Young's modulus, E_p, are deemed to represent the initial elastic response and not an equivalent-linear or effective stiffness state.

The evolution of the pile-head loading is assumed to obey the rate form of the *elastic constitutive relationships*:

$$\dot{\mathbf{Q}} = \mathbf{K}^{el}\,\dot{\mathbf{q}}^{el} = \mathbf{K}^{el}\left(\dot{\mathbf{q}}^{eg} - \dot{\mathbf{q}}^{gap}\right) = \mathbf{K}^{el}\left(\dot{\mathbf{q}}^{egp} - \dot{\mathbf{q}}^{gap} - \dot{\mathbf{q}}^{pl}\right) \tag{2}$$

In this equation, the dimensionless components of the pile-head load and displacement vectors and of the initial elastic symmetric stiffness matrix are given by:

$$\begin{aligned}
\mathbf{Q} &= \begin{bmatrix} H_n \\ M_n \end{bmatrix} = \begin{bmatrix} HD/M_y \\ M/M_y \end{bmatrix} \\
\mathbf{K}^{el} &= \begin{bmatrix} K_{HHn} & K_{HMn} \\ K_{MHn} & K_{MMn} \end{bmatrix} = \begin{bmatrix} \dfrac{K_{HH} D^2}{M_y} & \dfrac{K_{HM} D}{M_y} \\ \dfrac{K_{HM} D}{M_y} & \dfrac{K_{MM}}{M_y} \end{bmatrix} \\
\mathbf{q} &= \begin{bmatrix} u_n \\ \theta_n \end{bmatrix} = \begin{bmatrix} u/D \\ \theta \end{bmatrix}
\end{aligned} \tag{3}$$

The subscript n in these variables stands for normalised or dimensionless.

2.2 Gapping Behaviour

Gap opening and closure in laterally loaded piles is a very complex behaviour and it has considerable influence on the response of a single pile, as discussed in Correia *et al.* [2019], particularly for the soil profile with constant S_u. For that case, during a monotonic loading application a gap will develop on the back of the pile. The failure mechanism used herein predicts that it will reach a depth corresponding to the active soil wedge depth at failure conditions, which is also the depth at which the plastic hinge will form on the pile.

For the soil profile with linear S_u, instead, no gap opening was predicted for the failure mechanism in Correia *et al.* [2019] and numerical simulations clearly show that the gap influence for this particular soil profile is of much less significance. Nevertheless, a gap will certainly develop for cyclic loading conditions, which are not considered in yield design theory, due to the increasing plastic deformations in the surrounding soil and the progressive soil heave in front of the pile.

Based on results from other authors and on numerical simulations presented later, a gap evolution model is proposed here. A first important note is that the initial horizontal stress state around the pile was found to have only a very small influence on the gap behaviour and is thus disregarded in this model.

Despite expression (2) being similar in form to the one used in plasticity theories, this model assumes that the elastic-gap displacement components, $\mathbf{q}^{eg}$, have a nonlinear elastic and non-dissipative behaviour. Hence, no irreversible components of displacement exist when plasticity is not considered. This is successfully simulated by considering that the same tangent stiffness is valid for both loading and unloading. However, when plasticity is present, it will affect the gapping behaviour and this interaction must, therefore, be taken into account. The following expression formalises the rate form of the *nonlinear elastic constitutive relationship*:

$$\dot{\mathbf{Q}} = \mathbf{K}^{eg}\,\dot{\mathbf{q}}^{eg} \tag{4}$$

The *elastic-gap stiffness matrix*, $\mathbf{K}^{eg}$, varies during loading application. It is computed, in a simplified manner, as the inverse of a weighted average of the initial elastic flexibility matrix and a flexibility matrix considering an open gap on both the front and the back of the pile. The latter is obtained as described in the following paragraph.

(a) ***Flexibility matrix with full gap around the pile.*** This corresponds to the limit case where a full gap has developed, on both the front and back of the pile, up to a depth z_{gap}. It remains permanently open due to irreversible deformations of the soil surrounding the pile. Figure 3 describes the variables of interest for this situation. It is assumed that the pile is long enough below depth z_{gap} so that the "flexible pile" stiffnesses, defined in (3), may be used as if the pile head was at such depth. Moreover, it is assumed that the soil and pile moduli of deformation correspond to the initial ones below that depth, while an effective stiffness to yield is considered for the pile length above it. This portion of the pile behaves as a cantilever on a deformable foundation. A statically equivalent loading at depth z_{gap} to the pile-head loading is given by:

$$\begin{cases} H^* = H \\ M^* = M + H z_{gap} \end{cases} \Leftrightarrow \quad \mathbf{Q}^* = \begin{bmatrix} H_n^* \\ M_n^* \end{bmatrix} = \begin{bmatrix} 1 & 0 \\ z_{gap,n} & 1 \end{bmatrix} \begin{bmatrix} H_n \\ M_n \end{bmatrix} = \mathbf{ZQ} \tag{5}$$

The conjugate relationship for the pile-head displacements derives directly from Figure 4 and is expressed by:

$$\begin{cases} u = u^* + \theta^* z_{gap} + u_p \\ \theta = \theta^* + \theta_p \end{cases} \Leftrightarrow \quad \mathbf{q} = \begin{bmatrix} u_n \\ \theta_n \end{bmatrix} = \begin{bmatrix} 1 & z_{gap,n} \\ 0 & 1 \end{bmatrix} \begin{bmatrix} u_n^* \\ \theta_n^* \end{bmatrix} + \begin{bmatrix} u_{p,n} \\ \theta_{p,n} \end{bmatrix} = \mathbf{Z}^T \mathbf{q}^* + \mathbf{q}_p \tag{6}$$

In this expression, $\mathbf{q}_p$ is the pile cantilever contribution for the total deformation above depth z_{gap}. The pile displacements at depth z_{gap} are only due to soil flexibility and are expressed as:

$$\mathbf{q}^* = \begin{bmatrix} u_n^* \\ \theta_n^* \end{bmatrix} = \mathbf{F}^{el} \begin{bmatrix} H_n^* \\ M_n^* \end{bmatrix} = \mathbf{F}^{el} \begin{bmatrix} 1 & 0 \\ z_{gap,n} & 1 \end{bmatrix} \begin{bmatrix} H_n \\ M_n \end{bmatrix} = \mathbf{F}^{el}\,\mathbf{ZQ} \tag{7}$$

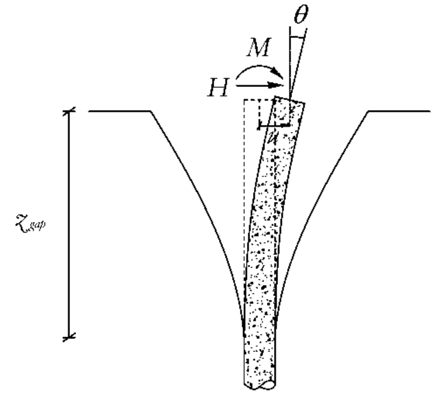

Figure 3. Permanent full gap up to depth z_{gap}

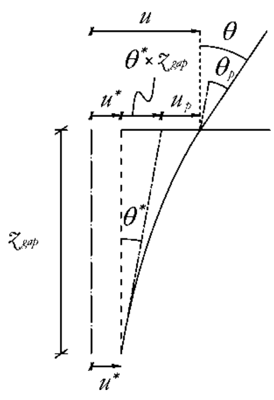

Figure 4. Transmission of displacements from depth z_{gap} to the pile-head

where $\mathbf{F}^{el}$ is the static pile-head flexibility matrix for a long pile, given by:

$$\mathbf{F}^{el} = \begin{bmatrix} f_{uH,n} & f_{uM,n} \\ f_{\theta H,n} & f_{\theta M,n} \end{bmatrix} = \frac{1}{K_{HHn} K_{MMn} - K_{HMn}^{2}} \begin{bmatrix} K_{HHn} & -K_{HMn} \\ -K_{MHn} & K_{MMn} \end{bmatrix} = \left(\mathbf{K}^{el}\right)^{-1} \tag{8}$$

On the other hand, the pile cantilever effective flexibility contribution to the total displacement is:

$$\mathbf{q}_p = \begin{bmatrix} u_{p,n} \\ \theta_{p,n} \end{bmatrix} = \frac{1}{\left(E_p I_p\right)_{eff,n}} \begin{bmatrix} \frac{z_{gap,n}^{3}}{3} & \frac{z_{gap,n}^{2}}{2} \\ \frac{z_{gap,n}^{2}}{2} & z_{gap,n} \end{bmatrix} \begin{bmatrix} H_n \\ M_n \end{bmatrix} = \mathbf{F}_P \mathbf{Q} \tag{9}$$

By replacing (9) and (7) into expression (6), one finally obtains the formula for the total pile-head displacements with a full gap around the pile:

$$\mathbf{q} = \begin{bmatrix} u_n \\ \theta_n \end{bmatrix} = \left(\mathbf{Z}^T \mathbf{F}^{el} \mathbf{Z} + \mathbf{F}_p\right)\mathbf{Q} = \left(\mathbf{K}_{2sides}^{gap}(z_{gap})\right)^{-1} \mathbf{Q} \tag{10}$$

The rate form of this relationship is assumed to produce the same tangent stiffness, which corresponds to ignoring a possible variation of the gap depth during the application of a load increment.

(b) ***Gap behaviour during virgin loading phase.*** Following the reasoning presented thus far, during virgin loading phase the elastic-gap stiffness matrix will decrease progressively as the gap depth increases. For a given gap depth, the elastic-gap stiffness matrix, relating the pile-head loading rate to the rate of displacements according to (4), is assumed to be computed by the following expression:

$$\left(\mathbf{K}^{eg}\right)^{-1} = \left(\mathbf{K}_{1side}^{gap}(z_{gap})\right)^{-1} = \left[\frac{1}{2}\left(\mathbf{K}^{el}\right)^{-1} + \frac{1}{2}\left(\mathbf{K}_{2sides}^{gap}(z_{gap})\right)^{-1}\right] \tag{11}$$

According to (11), the elastic-gap flexibility matrix with a gap opening on the back of the pile equals the average of the initial elastic flexibility matrix and the elastic flexibility matrix corresponding to the case of a full gap opening around the pile down to the current gap depth.

On the other hand, the current gap depth value indirectly relates the gapping and plastic behaviours. In fact, in this model, it is considered that the maximum gap depth equals the soil wedge depth, z_w, obtained for the failure mechanism through yield design theory [Correia *et al.*, 2019]. Furthermore, it is assumed that the current gap depth is inversely proportional to the loading parameter, λ, which varies between $+\infty$ and 1 and is inversely proportional to the distance from the current loading point to the failure surface. The gap depth evolution is thus governed by the following relation:

$$z_{gap} = \frac{z_w}{\lambda^\beta} \tag{12}$$

In this expression, $\beta > 0$ is a calibration parameter that affects the gap depth rate of growth with loading evolution. Note that the asymptotic behaviour of z_{gap} respects the limiting conditions of being zero for the initial state, where $\lambda = +\infty$, and being equal to z_w at failure, where $\lambda = 1$.

(c) ***Gap behaviour during unloading/reloading phases.*** It is assumed that the elastic-gap tangent stiffness varies according to (11) and (12), similarly to the virgin loading case. Therefore, detachment and re-attachment on opposite sides of the soil/pile interface is considered in the gapping model.

Moreover, since irreversible plastic displacements occur in the surrounding soil mass and the soil presents an increased stiffness upon unloading, an accumulated cyclic gap opening is considered. This corresponds to an increasing minimum gap depth, $z_{gap}^{\min}$, which is not closed during subsequent loading cycles. It is assumed that this value depends on the cumulative plastic dimensionless displacement, $u_{cum,n}^{pl}$, according to the following law:

$$z_{gap} = \frac{z_w}{\lambda^\beta} \geq z_{gap}^{\min} = z_{gap}^{\max}\left(1 - e^{-\eta\, u_{cum,n}^{pl}}\right) \tag{13}$$

In this expression, $\eta > 0$ is the second calibration parameter of the macro-element model, while $z_{gap}^{\max}$ is the maximum gap depth attained in previous loadings, corresponding to the loading parameter $\lambda_{\min}$:

$$z_{gap}^{\max} = \frac{z_w}{(\lambda_{\min})^\beta} \tag{14}$$

On the other hand, (13) may be used to determine the value of the loading parameter corresponding to the unloading point at which the minimum gap depth is attained:

$$\lambda_{z_{gap}^{\min}} = \left(\frac{z_w}{z_{gap}^{\min}}\right)^{1/\beta} \tag{15}$$

Inside the loading surface corresponding to this loading parameter value, *i.e.* for $\lambda > \lambda_{z_{gap}^{\min}}$, there is a swift evolution between the elastic-gap stiffness related to a gap open on one side of the pile, defined in (11), and the stiffness related to an open gap on both sides, obtained by (10). This evolution is expressed by the following relation:

$$\left(\mathbf{K}^{eg}\right)^{-1} = \left[\frac{\lambda_{z_{gap}^{\min}}}{\lambda}\left(\mathbf{K}_{1side}^{gap}(z_{gap}^{\min})\right)^{-1} + \left(1 - \frac{\lambda_{z_{gap}^{\min}}}{\lambda}\right)\left(\mathbf{K}_{2sides}^{gap}(z_{gap}^{\min})\right)^{-1}\right] \tag{16}$$

These expressions are valid for both unloading and reloading.

2.3 Failure Surface for Laterally Loaded Piles

The bounding surface in the macro-element model proposed hereafter corresponds to the failure surface for laterally loaded piles. Since there is no evidence showing that non-associative behaviour should be considered, associative plasticity will be used and the bounding surface will act simultaneously as the plastic potential surface. Hence, it is important to define this surface as accurately as possible and preferably by using a simple and smooth function to represent it. The failure surface adopted in this work is the one derived in Correia *et al.* [2019], which satisfies those requirements.

No axial load effects are considered in this macro-element formulation and, consequently, the failure surface is defined in the loading space of the pile-head horizontal force and moment only. Furthermore, as already mentioned, a planar loading is assumed.

A "rounded" approximate failure surface was proposed in Correia *et al.* [2019], which is based on the so-called superellipse. This corresponds to a generalisation of the common ellipse. Supposing a superellipse centred at the point (H_c, M_c), with a horizontal axis length $H_{u,e=0}$ and a vertical axis length M_y, which is also superimposed to a distortion of its shape, $\gamma < 0$, this approximate failure surface can be expressed as:

$$\left| \frac{\overline{H} - H_c}{H_{u,e=0}} - \gamma \frac{\overline{M} - M_c}{M_y} \right|^{n_H} + \left| \frac{\overline{M} - M_c}{M_y} \right|^{n_M} = 1 \tag{17}$$

The positive exponents n_H and n_M control the curvature of the sides of the superellipse and should be ≥ 2 so that no corners arise. If both exponents equal two, the common ellipse is retrieved.

Figure 5 represents such distorted superellipse configuration, centred at the origin ($H_c = M_c = 0$), with its parameters calibrated in order to fit the failure surface for the linear S_u soil profile obtained in Correia *et al.* [2019]. It provides a good approximation to the failure surface resulting from the failure mechanism optimisation. A distorted superellipse will be used hereafter as the failure surface for the macro-element.

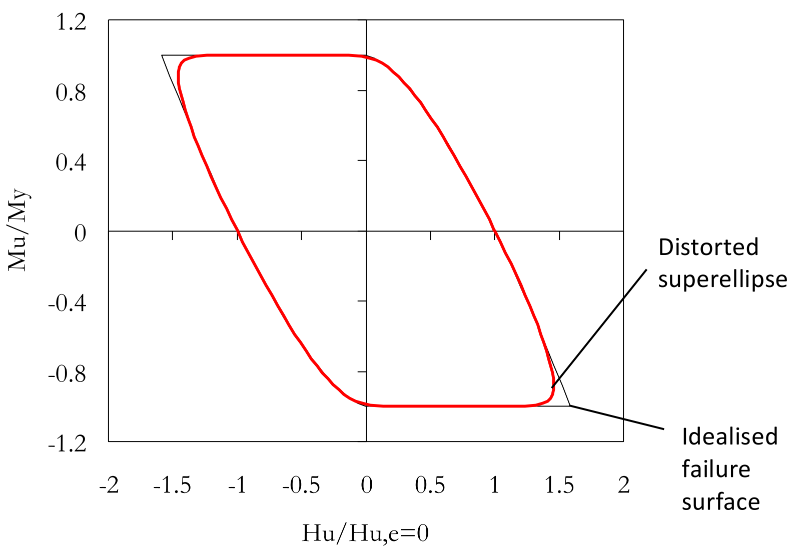

Figure 5. Distorted superellipse configuration for linear S_u

2.4 Bounding Surface Plasticity Model

The first important concept in bounding surface plasticity is that the generalised forces are limited by the *bounding surface*:

$$F\left(\overline{\mathbf{Q}}, \mathbf{S}\right) = 0 \tag{18}$$

where $\overline{\mathbf{Q}}$ is the *image point at the bounding surface* and it is related to the *current loading point*, $\mathbf{Q}$, by a mapping rule, $\overline{\mathbf{Q}} = \mathbf{Map}(\mathbf{Q},\mathbf{S})$, satisfying certain conditions [Dafalias, 1986]. The image point must always lay on the bounding surface and the generalised forces vector, by definition, always lies on the *loading surface*:

$$f(\mathbf{Q},\mathbf{S}) = 0 \tag{19}$$

The *internal variables*, $\mathbf{S}$, present in both (18) and (19), describe the evolution of both surfaces.

The choice of one loading surface over the infinite number of surfaces that pass through the loading point is related to the particular mapping rule chosen. In fact, the loading surface, and its evolution in size and/or position with the loading point variation, is simply a practical way of defining the mapping rule with some kind of physical reasoning. Note that the loading surface may never cross the bounding surface, *i.e.* it is always enclosed by it. This is usually guaranteed by defining the image point as the one having the same unit normal vector to the bounding surface as the unit normal vector to the loading surface at the current loading point. Such a constraint is not absolutely necessary except when the loading point reaches the bounding surface, thus coinciding with the image point.

For simplicity reasons, the loading surface is also usually assumed to have a similar shape to the bounding surface. It shares a lot of properties with the yield surface of classical plasticity. The main difference between the two is that the loading function is always equal to zero, while a yield function can be less or equal to zero. The loading surface moves with the loading point, even upon unloading, while a yield surface represents the maximum extent of previous yielding. Figure 6 exemplifies these concepts for a radial mapping rule and circular surfaces.

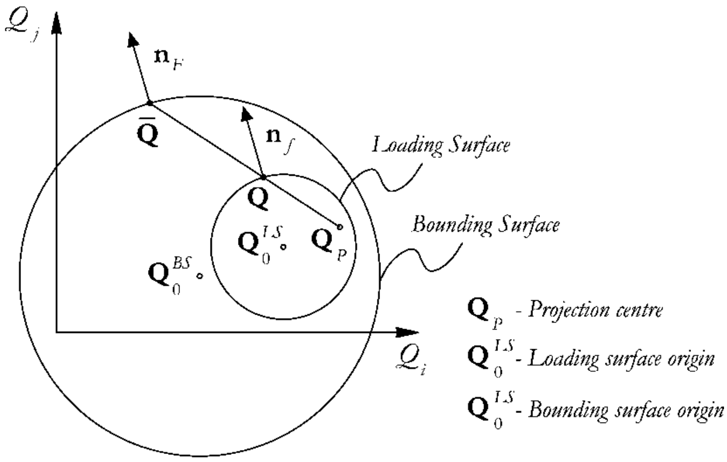

Figure 6. Radial mapping rule in bounding surface plasticity

Probably the most successful mapping rule for the image point is the radial projection on the bounding surface [Dafalias, 1986; Borja *et al.*, 2001]. The concept of such mapping is shown in Figure 6, where the bounding surface is schematically shown as a circle of centre $\mathbf{Q}_0^{BS}$ and described by:

$$F\left(\overline{\mathbf{Q}} - \mathbf{Q}_0^{BS}, \mathbf{S}\right) = 0 \tag{20}$$

A *projection centre*, $\mathbf{Q}_P$, is used to radially project the current loading point on the bounding surface. The radial mapping rule thus takes the following form:

$$\overline{\mathbf{Q}} = \mathbf{Q} + \mu\left(\mathbf{Q} - \mathbf{Q}_P\right) = \mathbf{Q}_P + (1+\mu)\left(\mathbf{Q} - \mathbf{Q}_P\right) \tag{21}$$

The mapping variable, μ, varies between zero, when $\mathbf{Q}=\overline{\mathbf{Q}}$, and infinity, when $\mathbf{Q}=\mathbf{Q}_P$ (in which case the image point is indeterminate). By imposing that the unit normal vector to the loading surface at the loading point and the unit normal vector to the bounding surface at the image point must coincide, together with the mapping rule (21), one is indirectly defining an appropriate loading surface. Such loading surface is centred at the point $\mathbf{Q}_0^{LS}$ and is defined by the following equation:

$$f\left(\mathbf{Q}-\mathbf{Q}_0^{LS},\mathbf{S}\right)=F\left(\mathbf{Q}+\mu\,(\mathbf{Q}-\mathbf{Q}_P)-\mathbf{Q}_0^{BS},\mathbf{S}\right)=0 \tag{22}$$

This loading surface is homologous to the bounding surface and the projection centre $\mathbf{Q}_P$ occupies the same relative position inside both surfaces. It is consequently also called the *homology centre*. In fact, the loading surface represents the *locus* of all loading points $\mathbf{Q}$ with the same value of μ for a given position of the homology centre.

It can be easily shown that, for a loading surface defined as above, all the governing equations of the plasticity problem can be applied indifferently to the bounding surface or to this loading surface instead (see, for instance, Borja *et al.* [2001]). It is noted that μ, in such case, is to be treated similarly to an isotropic hardening parameter for the loading surface.

From (21), the similarity ratio between the bounding and the loading surfaces is given by the following expression:

$$\frac{\left|\overline{\mathbf{Q}}-\mathbf{Q}_P\right|}{\left|\mathbf{Q}-\mathbf{Q}_P\right|}=1+\mu=\frac{1}{\delta} \tag{23}$$

where δ is the normalised distance between the loading point and the homology centre with respect to the distance between the latter and the image point. It varies between zero and one.

In the following, our attention will be focused on the simplest of the radial mapping rules, which will prove to be most helpful for the rest of the work. Firstly, a monotonic loading is considered. Afterwards, cyclic behaviour is analysed.

2.4.1 Radial mapping from the origin

If one considers that both the bounding and loading surfaces are centred at the origin of the loading space, the homology centre will consequently also be positioned at that point:

$$\mathbf{Q}_0^{BS}=\mathbf{Q}_0^{LS}=\mathbf{Q}_P=\mathbf{0} \tag{24}$$

Hence, the simplest of the mapping rules results:

$$\overline{\mathbf{Q}}=(1+\mu)\,\mathbf{Q}=\frac{1}{\delta}\,\mathbf{Q}=\lambda\,\mathbf{Q} \tag{25}$$

The *loading parameter* λ, equal to $1+\mu$, decreases from infinity to one as the loading vector increases from zero until it reaches the bounding surface. It will be used to represent the similarity ratio for this particular mapping rule. Moreover, the bounding surface will be assumed to maintain its shape and size all the time. Hence, one can represent the self-similar bounding and loading surfaces by the following expressions:

$$\begin{aligned} &F\left(\overline{\mathbf{Q}}\right)=0 \\ &f\left(\mathbf{Q},\lambda\right)=F\left(\lambda\mathbf{Q}\right)=0 \end{aligned} \tag{26}$$

It is clear from the above, that the loading parameter represents the scale factor of the bounding surface relative to the loading surface. More importantly, it represents the isotropic hardening parameter of the current yield/loading surface.

The plastic displacements' evolution is described by the *plastic flow rule*:

$$\dot{\mathbf{q}}^{pl} = \dot{\gamma}\,\mathbf{n}_g \tag{27}$$

where the *unit normal vector to the plastic potential surface*, $\mathbf{n}_g$, defines the direction of the plastic displacements' increments. The *plastic multiplier or consistency parameter*, $\dot{\gamma}$, is greater than zero only when plastic deformation occurs, and is identical to zero otherwise.

The evolution of the internal variables or hardening parameters is defined by the *hardening rule*, which in this case can be expressed as a scalar hardening rule of the following type:

$$\dot{\lambda} = \dot{\gamma}\,\bar{\lambda}\left(\mathbf{Q},\lambda\right) \tag{28}$$

The *hardening function* $\bar{\lambda}$ needs to be completely defined in classical plasticity theory context. However, one of the differences towards bounding surface plasticity is that the latter uses a direct definition of the *plastic modulus* instead. Hence, a full explicit description of $\bar{\lambda}$ is not required, as seen below.

The so-called *consistency condition* in bounding surface plasticity enforces that the image point must always lie on the bounding surface, allowing the computation of the plastic multiplier value [Correia, 2011]. It implies that:

$$\begin{aligned}
\dot{F}\left(\overline{\mathbf{Q}}\right) &= \partial_{\overline{\mathbf{Q}}}F\left(\overline{\mathbf{Q}}\right)\cdot\dot{\overline{\mathbf{Q}}} = \\
&= \partial_{\overline{\mathbf{Q}}}F\cdot\partial_{\mathbf{Q}}\overline{\mathbf{Q}}\cdot\dot{\mathbf{Q}} + \dot{\lambda}\,\partial_{\overline{\mathbf{Q}}}F\cdot\partial_{\lambda}\overline{\mathbf{Q}} = \\
&= \nabla F\cdot\lambda\mathbf{I}\cdot\dot{\mathbf{Q}} + \dot{\lambda}\,\nabla F\cdot\mathbf{Q} = \\
&= \lambda\,\nabla F\cdot\dot{\mathbf{Q}} + \dot{\gamma}\bar{\lambda}\,\nabla F\cdot\mathbf{Q} = 0
\end{aligned} \tag{29}$$

The notation can be simplified using the following definitions:

$$\begin{aligned}
\nabla F &= \partial_{\overline{\mathbf{Q}}}F \\
\mathbf{n}_F &= \frac{\nabla F}{\left|\nabla F\right|}
\end{aligned} \tag{30}$$

where $\mathbf{n}_F$ is the *unit normal vector to the bounding surface*.

The *plastic modulus at the current loading point*, H^{pl}, for this mapping rule, is now defined as:

$$H^{pl}\left(\mathbf{Q},\lambda\right) = -\frac{\dot{\lambda}}{\lambda\left|\nabla F\right|\dot{\gamma}}\nabla F\cdot\mathbf{Q} = -\frac{\bar{\lambda}}{\lambda}\left(\mathbf{n}_F\cdot\mathbf{Q}\right) \tag{31}$$

And, using expression (29) and the mapping rule for the image point, the plastic multiplier becomes:

$$\dot{\gamma} = \frac{1}{\overline{H}^{pl}}\left(\mathbf{n}_F\cdot\dot{\overline{\mathbf{Q}}}\right) = \frac{1}{H^{pl}}\left(\mathbf{n}_F\cdot\dot{\mathbf{Q}}\right) \tag{32}$$

In bounding surface theory, the plastic modulus at the current loading point, H^{pl}, is obtained by a function depending only on the distance between the loading and image points. This function must respect some limiting behaviours, namely:

i) When the distance becomes zero and the loading point coincides with the image point, the plastic modulus must be equal to $\overline{H}^{pl}$,
ii) During elastic behaviour the plastic modulus function must be infinite,
iii) In between the above limits, the plastic modulus must be monotonically decreasing.

According to the *a priori* definition of the plastic modulus, the evolution of the hardening parameters is now constrained by the scalar expression (31). Therefore, in bounding surface plasticity, the hardening rule does not have to be completely defined as in (28).

The bounding surface adopted in the macro-element model presents no hardening since it represents a failure surface. Hence, the plastic modulus when the yield/loading surface reaches it is equal to zero. An example of a simple plastic modulus in the macro-element context is the one used by Chatzigogos [2007] and Chatzigogos *et al.* [2009, 2010] for monotonic loading of shallow foundations:

$$H^{pl}(\lambda) = H_0^{pl} \ln \lambda \tag{33}$$

This expression, where H_0^{pl} is a constant coefficient for calibration, correctly starts at infinity for zero loading and tends to zero as the loading point reaches the bounding surface. It will also be used in the pile-head macro-element.

The distorted superellipse, as defined by Equation (17), is used to represent the bounding, loading, and plastic potential surfaces. Moreover, the parameters specified in Correia *et al.* [2019] are adopted for the constant S_u and the linear S_u soil profiles.

This macro-element model thus assumes a radial mapping from the origin for virgin loading in order to define the image point on the bounding surface. For the planar loading considered and using dimensionless variables, the bounding surface corresponding to (17) is defined by:

$$F\left(\overline{H}_n, \overline{M}_n\right) = \left| \frac{\overline{H}_n}{H_{un,e=0}} - \gamma \overline{M}_n \right|^{n_H} + \left| \overline{M}_n \right|^{n_M} - 1 = 0 \tag{34}$$

The corresponding self-similar yield/loading surface is described by:

$$f\left(H_n, M_n, \lambda\right) = F\left(\lambda H_n, \lambda M_n\right) = \left| \frac{\lambda H_n}{H_{un,e=0}} - \gamma \lambda M_n \right|^{n_H} + \left| \lambda M_n \right|^{n_M} - 1 = 0 \tag{35}$$

In the context of return mapping procedures for solving plasticity problems, the evolution of the loading parameter λ is determined by inverting expression (31).

In order to determine the plastic displacement components, the gradient of the bounding surface at the image point must be derived:

$$\nabla F\left(\overline{H}_n, \overline{M}_n\right) = \partial_{\overline{\mathbf{Q}}} F\left(\overline{H}_n, \overline{M}_n\right) = \begin{bmatrix} \partial_{\overline{H}_n} F \\ \partial_{\overline{M}_n} F \end{bmatrix} \tag{36}$$

These gradient components are given by:

$$
\begin{aligned}
&\partial_{\overline{H}_n} F = \frac{n_H}{H_{un,e=0}} \left| \frac{\overline{H}_n}{H_{un,e=0}} - \gamma\, \overline{M}_n \right|^{n_H - 1} sign\left(\frac{\overline{H}_n}{H_{un,e=0}} - \gamma\, \overline{M}_n \right) \\
&\partial_{\overline{M}_n} F = -n_H\, \gamma \left| \frac{\overline{H}_n}{H_{un,e=0}} - \gamma\, \overline{M}_n \right|^{n_H - 1} sign\left(\frac{\overline{H}_n}{H_{un,e=0}} - \gamma\, \overline{M}_n \right) + \\
&\qquad + n_M \left| \overline{M}_n \right|^{n_M - 1} sign\left(\overline{M}_n \right)
\end{aligned}
\tag{37}
$$

In the following sections, particular aspects of the cyclic response in this model are analysed, and the return mapping algorithms for solving the plasticity problem are exposed.

2.4.2 Cyclic Response

As presented so far, the radial mapping model predicts inelastic behaviour while loading but an elastic response for unloading. This produces an unrealistic behaviour upon partial unloading/reloading cycles, since the corresponding stress-strain loops are not closed [Dafalias, 1986]. Chatzigogos *et al.* [2009, 2010], for instance, used such model for their shallow foundation macro-element. It has a reloading behaviour slightly different from the initial loading one, which is represented by expression (33). They assume a less plastic response during reloading relative to the initial loading response:

$$
H^{pl}\left(\lambda, \lambda_{\min}\right) = H_0^{pl} \ln\left[\left(\frac{\lambda}{\lambda_{\min}} \right)^{n_R} \lambda \right] \tag{38}
$$

where $\lambda_{\min} < \lambda$ is the minimum value of the loading parameter attained during virgin loading and the constant exponent n_R controls the difference between the loading and reloading stiffnesses. Nevertheless, this will produce a similar behaviour to the one pointed out by Dafalias [1986]. While such model may represent sufficiently well the response of a shallow foundation for cyclic vertical loading, for moment and/or horizontal loading it would be desirable that the response would also be inelastic while unloading. For cyclic soil behaviour and cyclic pile lateral response the same applies.

A more realistic behaviour is obtained, as shown later, by assuming that, upon unloading, there is a discrete relocation of the projection centre to the point of load reversal. This was idealised and implemented by the author, but it had been already proposed by several authors, as early as Mróz and Zienkiewicz [1984] or Borja *et al.* [2001].

Figure 7 represents the concept of this cyclic model. Assuming radial mapping from the origin for virgin loading, the initial loading surface grows, centred at the origin, until the load reversal point is reached. The plastic modulus may be assumed to evolve according to an expression like (33). Upon unloading, the homology centre is relocated to the load reversal point and a second loading surface originates within the first one, both surfaces remaining in contact at such point.

In order to avoid over-shooting phenomena, it is suggested that the plastic modulus now varies between infinity and the plastic modulus at the moment of load reversal, which is attained when the second loading surface expands to the point it becomes identical to the initial one. When this happens, the homology centre has reached the origin and the second loading surface vanishes. The first one becomes active again, with radial mapping from the origin once more.

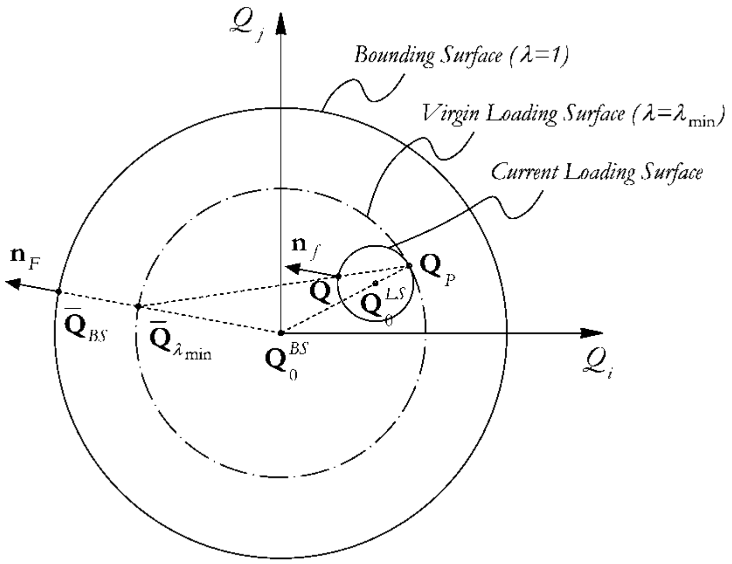

Figure 7. Evolution of loading surface and homology centre for cyclic behaviour

It is noted that the suggested plastic modulus variation with the evolution of the second loading surface corresponds to making a double projection of the loading point. The load reversal point is used to project the current loading point on the initial loading surface and the first projection centre, the origin, is used to project this first image point into the bounding surface. The plastic modulus may then be computed according to:

$$H^{pl}\left(\delta_1,\delta_2\right)=H_0^{pl}\left[\ln\frac{1}{\delta_1}+\ln\left(\frac{1}{\delta_2}\right)^{n_{UR}}\right] \tag{39}$$

In (39), $\delta_1 = 1/\lambda_{min}$ is the similarity ratio between the first loading and the bounding surfaces, while δ_2 is the similarity ratio between the second and the first loading surfaces and n_{UR} is a calibration constant.

If more than two loading surfaces are created by successive load reversals of decreasing amplitude, the same process is repeated internally to each loading surface. An increasingly higher number of projection centres and loading surfaces are then successively created, and multiple radial mapping operations are performed in order to obtain the image point and the plastic modulus. Expression (39) may be easily generalised for such case. Dafalias [1986] mentions that the concept of generating new loading surfaces at each load reversal and the corresponding rule for their hierarchical elimination can be traced back to the work by Phillips [1972].

The cyclic features adopted for the macro-element follow these concepts of discrete relocation of the homology centre upon load reversals, with the subsequent generation of new loading surfaces. The behaviour was described as being similar to a multi-yield surface kinematic plasticity formulation, with the sequential creation of loading surfaces and the continuous evolution of the plastic modulus.

There are, however, three main changes to the aforementioned description. The first is that only a limited number of loading surfaces is accepted to co-exist in a cyclic loading with decreasing amplitude, so as to limit computational effort and memory requirements. This limit was chosen to be two, for the analyses presented in this work. Hence, in a given moment, the formulation considers: the bounding surface; the outer loading surface corresponding to virgin loading and to the minimum value attained by the loading parameter, λ_{min}; and a possible loading surface corresponding to unloading or reloading inside the latter one.

It should be noted that, by setting this limit, overshooting is only formally prevented at the virgin loading surface and not in an inner unloading/reloading cycle. However, this was deemed to represent a good compromise between accuracy and complexity in the formulation. Numerical tests have shown that no significant overshooting problem occurs.

A second change is concerned with the evolution of the homology centre when unloading or reloading. This point, together with the centre of the current loading surface and the current loading point are deemed to always being aligned in the same line centred at the origin, as represented in Figure 8. This feature leads to a gradual evolution of the homology centre location if the load eccentricity changes. Nevertheless, it always corresponds to a common point between the current loading surface and the previous one, although not necessarily the point of load reversal anymore. It is noted that, if the load eccentricity is constant, the two approaches coincide.

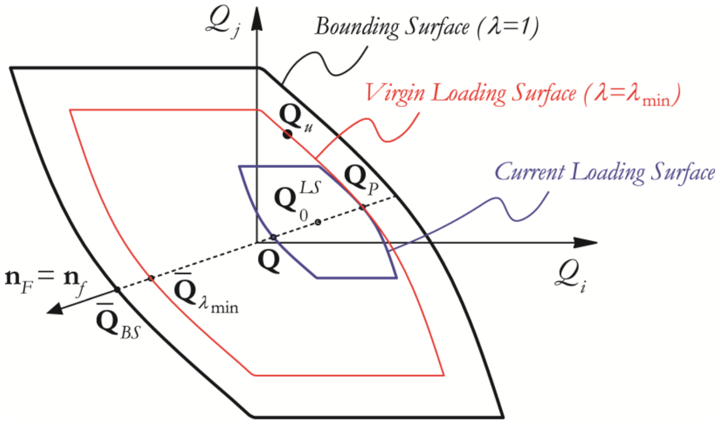

Figure 8. Evolution of homology centre during unloading

The third change is that, although formally there is a relocation of the homology centre and the generation of a new loading surface upon a load reversal, in practical terms the approach used in this formulation is different. In fact, it is easier to keep track of the current loading point, and of the size of the active loading surface, by using a concentric loading surface, *i.e.* centred at the origin, than to use a non-concentric loading surface. This concentric current loading surface is easily defined, and its evolution is computed similarly to the evolution of the virgin loading surface. However, the plastic modulus now is computed through expression (39), considering the current unloading/reloading state. Figure 9 represents the conceptual differences in the approaches.

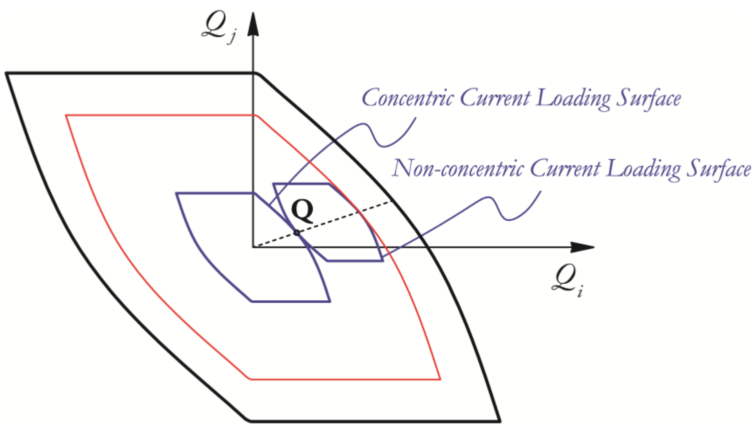

Figure 9. Concentric vs. non-concentric current loading surface

Hence, the current loading surface is always defined by expression (35) and it presents isotropic hardening/softening. It evolves with the current loading point, always centred at the origin, from being a vanishing elastic nucleus at the origin when the loading starts up to the outermost loading surface corresponding to the virgin loading state. Upon unloading, this current loading surface softens isotropically and the image point at the bounding surface is located at the opposite side. It is pointed out that, for the loading surface to be able to soften, the plastic multiplier $\dot{\gamma}$ may now assume negative values.

The following paragraphs clarify and summarise the plastic modulus computation for the three possible loading states.

(a) ***Virgin loading state.*** For this loading state, the simplest of the mapping rules is applied in order to define the image point at the bounding surface. It is represented in Figure 10 and it is defined in expression (25). As already mentioned before, the loading parameter λ decreases gradually from infinity to one. The plastic modulus value is therefore assumed to be given by:

$$H^{pl} = H_0^{pl} \ln \frac{1}{\delta} = H_0^{pl} \ln \lambda \tag{40}$$

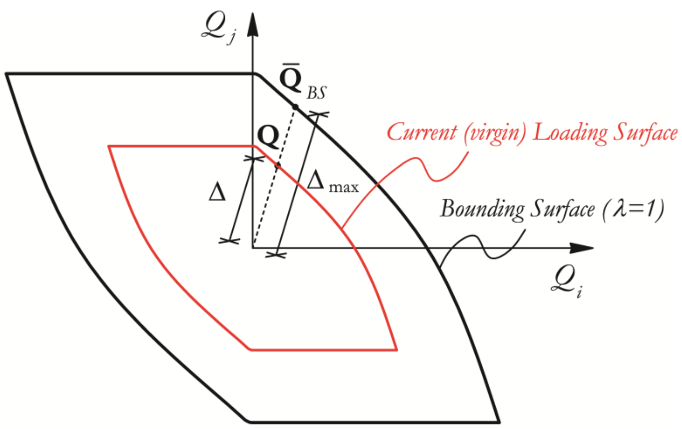

Figure 10. Image point and plastic modulus computation for the virgin loading case

(b) ***Unloading state.*** In the most general case of unloading state, which is unloading from a previous reloading state, one must consider the bounding surface, the current loading surface, the outermost loading surface attained during virgin loading and the loading surface passing through the load reversal point for unloading. These are depicted in Figure 11. The image point at the bounding surface is now defined as:

$$\overline{\mathbf{Q}}_{BS} = -\lambda \, \mathbf{Q} \tag{41}$$

where λ is the current loading parameter. The image point at the outermost loading surface attained during virgin loading is computed as:

$$\overline{\mathbf{Q}}_{\lambda_{\min}} = \frac{1}{\lambda_{\min}} \overline{\mathbf{Q}}_{\mathbf{BS}} = -\frac{\lambda}{\lambda_{\min}} \mathbf{Q} \tag{42}$$

On the other hand, the homology centre is defined as:

$$\mathbf{Q}_P = -\frac{1}{\lambda_U} \overline{\mathbf{Q}}_{\mathbf{BS}} = \frac{\lambda}{\lambda_U} \mathbf{Q} \tag{43}$$

where λ_U is the loading parameter associated to the load reversal point for unloading.

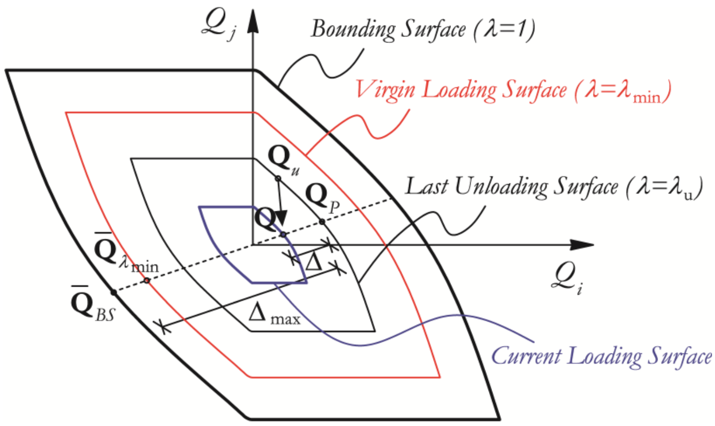

Figure 11. Image point and plastic modulus computation for the unloading case

For this case, the distances from the homology centre, $\mathbf{Q}_P$, to the image point at the outermost loading surface attained during virgin loading, $\overline{\mathbf{Q}}_{\lambda_{min}}$, and to the loading point, $\mathbf{Q}$, are given by:

$$\Delta_{max} = \left|\overline{\mathbf{Q}}_{\lambda_{min}} - \mathbf{Q}_P\right| = \left(\frac{1}{\lambda_U} + \frac{1}{\lambda_{min}}\right)\left|\overline{\mathbf{Q}}_{BS}\right|$$
$$\Delta = \left|\mathbf{Q} - \mathbf{Q}_P\right| = \left(\frac{1}{\lambda_U} - \frac{1}{\lambda}\right)\left|\overline{\mathbf{Q}}_{BS}\right| \tag{44}$$

Hence, the normalised distance δ between the loading point and the homology centre with respect to the distance between the latter and the image point $\overline{\mathbf{Q}}_{\lambda_{min}}$ corresponds to the ratio:

$$\delta = \frac{\Delta}{\Delta_{max}} = \frac{\dfrac{1}{\lambda_U} - \dfrac{1}{\lambda}}{\dfrac{1}{\lambda_U} + \dfrac{1}{\lambda_{min}}} = \frac{\lambda_{min}}{\lambda}\,\frac{\lambda - \lambda_U}{\lambda_{min} + \lambda_U} \tag{45}$$

It should be pointed out that this expression, for the similarity ratio between the non-concentric current loading surface and the concentric loading surface corresponding to λ_{min}, is only valid until the loading point unloads to zero. If the load point continues to move on the same direction, it becomes a reloading state. The plastic modulus during unloading is computed through an expression equivalent to the one presented in expression (39):

$$H^{pl} = H_0^{pl}\left[\ln\lambda_{min} + \ln\left(\frac{1}{\delta}\right)^{n_{UR}}\right] =$$
$$= H_0^{pl}\left[\ln\lambda_{min} + n_{UR}\ln\left(\frac{\lambda}{\lambda_{min}}\,\frac{\lambda_{min} + \lambda_U}{\lambda - \lambda_U}\right)\right] \tag{46}$$

Immediately after the load reversal, $\lambda = \lambda_U$, $\delta = 0$ and the plastic modulus is infinite, as expected. At the point of zero loading, λ is infinite, $\delta = \lambda_{min}/(\lambda_U + \lambda_{min})$ and the plastic modulus will be equal to $H_0^{pl}\left[\ln\lambda_{min} + n_{UR}\ln((\lambda_{min} + \lambda_U)/\lambda_{min})\right]$.

(c) ***Reloading state.*** The macro-element behaviour during reloading after unloading is very similar to the one exposed above for the unloading state. Hence, one still needs to consider the bounding surface, the current loading surface, the outermost loading surface attained during virgin loading and, now, the loading surface passing through the load reversal point for reloading. There are, however, two possible reloading states that must be analysed, as represented in Figure 12. A parameter that allows distinguishing between both situations is:

$$r = sign\left(\mathbf{Q}_U \cdot \mathbf{Q}\right) \tag{47}$$

This parameter is either 1 or -1. If it is positive, the reloading is in the same direction of the loading at the previous load reversal point for unloading. Otherwise, the unloading reached the point of zero loading and continued reloading from zero in the same direction, *i.e.* opposite to the previous load reversal point for unloading.

The image points at the bounding surface and at the outermost loading surface attained during virgin loading are now computed as:

$$\overline{\mathbf{Q}}_{BS} = \lambda\,\mathbf{Q} \tag{48}$$

$$\overline{\mathbf{Q}}_{\lambda_{\min}} = \frac{1}{\lambda_{\min}}\overline{\mathbf{Q}}_{\mathbf{BS}} = \frac{\lambda}{\lambda_{\min}}\mathbf{Q} \tag{49}$$

On the other hand, the homology centre definition now depends on r and is given by:

$$\mathbf{Q}_P = \frac{r}{\lambda_R}\overline{\mathbf{Q}}_{\mathbf{BS}} = \frac{\lambda r}{\lambda_R}\mathbf{Q} \tag{50}$$

where λ_R is the loading parameter associated to the load reversal point for reloading. It is pointed out that $\lambda_R = \lambda_U$ if $r = -1$.

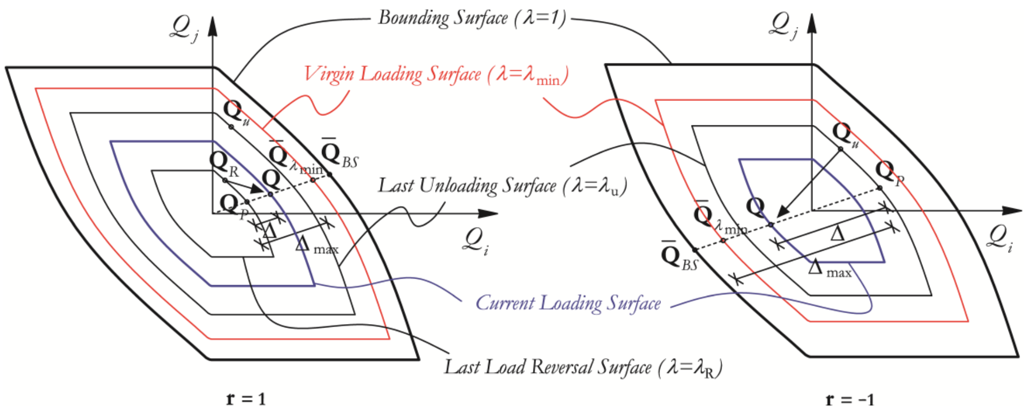

Figure 12. Image point and plastic modulus computation for the two reloading cases

For the reloading case, the distances $\Delta_{\max}$ and Δ and the normalised distance δ are computed as:

$$\begin{aligned}\Delta_{\max} &= \left|\overline{\mathbf{Q}}_{\lambda_{\min}} - \mathbf{Q}_P\right| = \left(\frac{1}{\lambda_{\min}} - \frac{r}{\lambda_R}\right)\left|\overline{\mathbf{Q}}_{BS}\right| \\ \Delta &= \left|\mathbf{Q} - \mathbf{Q}_P\right| = \left(\frac{1}{\lambda} - \frac{r}{\lambda_R}\right)\left|\overline{\mathbf{Q}}_{BS}\right|\end{aligned} \tag{51}$$

$$\delta = \frac{\Delta}{\Delta_{\max}} = \frac{\dfrac{1}{\lambda} - \dfrac{r}{\lambda_R}}{\dfrac{1}{\lambda_{\min}} - \dfrac{r}{\lambda_R}} = \frac{\lambda_{\min}}{\lambda}\,\frac{\lambda_R - r\lambda}{\lambda_R - r\lambda_{\min}} \tag{52}$$

The corresponding plastic modulus during reloading is given by:

$$
\begin{aligned}
H^{pl} &= H_0^{pl}\left[\ln\lambda_{\min} + \ln\left(\frac{1}{\delta}\right)^{n_{UR}}\right] = \\
&= H_0^{pl}\left[\ln\lambda_{\min} + n_{UR}\ln\left(\frac{\lambda}{\lambda_{\min}}\frac{\lambda_R - r\lambda_{\min}}{\lambda_R - r\lambda}\right)\right]
\end{aligned}
\tag{53}
$$

For $r = 1$, δ will vary between zero, when $\lambda = \lambda_R$, and one, when $\lambda = \lambda_{\min}$. The plastic modulus will be respectively equal to infinite and to $H_0^{pl}\ln\lambda$. On the other hand, for $r = -1$, δ will vary between $\lambda_{\min}/(\lambda_U + \lambda_{\min})$, when λ is infinite, and one, when $\lambda = \lambda_{\min}$. The plastic modulus will be respectively equal to the one obtained for unloading, at the transition point from unloading to reloading, and to $H_0^{pl}\ln\lambda$.

When the outermost loading surface attained during virgin loading is reached, the virgin loading state is activated again. The plastic modulus is continuous at that point, although the rate of its evolution is discontinuous.

2.4.3 Return Mapping Algorithm

The previous paragraphs have thoroughly presented the constitutive relationships for the macro-element in terms of generalised forces and displacements. The problem now arises of determining, for a given generalised displacements history, the corresponding evolution of the generalised forces. This is accomplished by integrating the rate form of the constitutive equations.

Exact analytical solutions for the classical plasticity evolution problem are only available for the simplest elastic-plastic problems [Prévost, 1987]. The first exact solution was obtained by Krieg and Krieg [1977] for the case of isotropic elastic-perfectly plastic Von Mises model. Despite exact solutions have been developed over the years for other plasticity models, the more complex ones have no analytical solution. Moreover, the exact solutions, although error-free, are computationally too slow to be used in practice. Hence, all elastic-plastic problems are numerically implemented with some error. Explicit one-step forward Euler schemes should not be considered due to their inherent error accumulation characteristics. Iterative schemes using some form of predictor or trial elastic step followed by a plastic corrector step should be used instead. The plastic consistency is restored in the plastic corrector step through a return mapping algorithm. It involves an integration which is usually performed using a backward Euler scheme, an implicit one requiring iterations. The global solution is strongly affected by the accuracy, stability and computational efficiency of such algorithms [Prévost, 1987].

A general framework for developing consistent, accurate and stable return mapping algorithms was formulated by Simo and co-workers [Simo and Ortiz, 1985; Simo and Taylor, 1985; Ortiz and Simo, 1986; Simo and Hughes, 1998; Ortiz and Martin, 1989]. The most successful of the return mapping algorithms in classical plasticity are the closest point projection and the cutting plane algorithms. They both apply to the case of a general yield condition, flow rule and hardening law.

The closest point projection algorithm relies on an implicit backward Euler integration scheme, the normality to the yield and plastic potential surfaces is enforced at the final – and unknown – state, and the consistency condition is solved using Newton's method. The algorithm is consistent with the constitutive relations to be integrated (i.e., first-order accurate), unconditionally stable and achieves a quadratic convergence rate. It can be exactly linearized in closed form, leading to a consistent algorithmic tangent moduli matrix. It requires, however, the computation of the second-order derivatives of both the yield and plastic potential surfaces, which may prove to be exceedingly laborious or even impossible for complex plasticity models [Ortiz and Simo, 1986; Prévost, 1987; Simo and Hughes, 1998].

On the other hand, the cutting plane algorithm is an efficient and simpler procedure, which bypasses the need for computing such second-order derivatives. In this algorithm the return mapping is defined iteratively. At each iteration, the plastic corrector problem is integrated about the current values of the state variables by an explicit procedure in order to satisfy the linearized version of the consistency condition. As such, the normality to the yield and plastic potential surfaces is enforced at the initial – and known – state. This algorithm is consistent but only conditionally stable and it cannot be exactly linearized in closed form. Hence, a consistent algorithmic tangent moduli matrix cannot be obtained for this case. Nevertheless, it also achieves a quadratic convergence rate for the update [Ortiz and Simo, 1986; Prévost, 1987; Simo and Hughes, 1998].

In view of the fact that the macro-element comprises two nonlinear mechanisms – gapping and inelasticity –, a modified version of the usual return mapping algorithms is required. A cutting plane algorithm is preferred, instead of a closest point projection one, since there is no sufficient information on the yield and plastic potential surfaces so as to consider correctly their second derivatives.

Moreover, given that the elastic-gap constitutive relationships, expressed through expression (4), relate directly the elastic-gap displacements and forces without separating both components, a simpler version of the cutting plane algorithm is devised. This is based on a Newton-Raphson iterative scheme, which is described in the following paragraphs.

(a) ***Predictor or trial elastic-gap step.*** An initial trial elastic-gap step is computed by freezing the plastic flow. Considering all state variables known at load step *N*, the input for the next step is the increment of total displacements:

$$\mathbf{q}_{N+1}^{egp} = \mathbf{q}_N^{egp} + \Delta\mathbf{q}_{N+1}^{egp} \tag{54}$$

The trial values of the relevant state variables are:

$$\begin{cases} \mathbf{q}_{N+1}^{eg,trial} = \mathbf{q}_N^{eg} + \Delta\mathbf{q}_{N+1}^{egp} \\ \mathbf{q}_{N+1}^{pl,trial} = \mathbf{q}_N^{pl} \end{cases} \qquad \mathbf{K}_{N+1}^{eg,trial} = \mathbf{K}_N^{eg} \qquad \lambda_{N+1}^{trial} = \lambda_N \tag{55}$$

The trial vector of generalised forces is coherently given by:

$$\mathbf{Q}_{N+1}^{trial} = \mathbf{Q}_N + \mathbf{K}_{N+1}^{eg,trial}\,\Delta\mathbf{q}_{N+1}^{egp} \tag{56}$$

If the loading point corresponds to a load reversal point, this trial elastic-gap state is correct. Hence this is a nonlinear elastic unloading or reloading step. The analysis parameters are updated, namely, the loading parameter through solving equation (35) and the elastic-gap stiffness matrix through expression (11) or (16).

Otherwise, a return mapping or corrector phase is required. As predictor step, the initial state is computed with the current tangent stiffness and no plastic flow or hardening:

$$\mathbf{Q}_{N+1}^{(0)} = \mathbf{Q}_N \qquad \begin{cases} \mathbf{q}_{N+1}^{egp(0)} = \mathbf{q}_N^{eg} \\ \mathbf{q}_{N+1}^{eg(0)} = \mathbf{q}_N^{eg} \\ \mathbf{q}_{N+1}^{pl(0)} = \mathbf{q}_N^{pl} \end{cases} \qquad \begin{cases} \mathbf{K}_{N+1}^{egp(0)} = \mathbf{K}_N^{egp} \\ \mathbf{K}_{N+1}^{eg(0)} = \mathbf{K}_N^{eg} \end{cases} \qquad \begin{cases} \Delta\gamma_{N+1}^{(0)} = 0 \\ \lambda_{N+1}^{(0)} = \lambda_N \end{cases} \tag{57}$$

The vector of generalised forces for the first iteration thus corresponds to:

$$\mathbf{Q}_{N+1}^{(1)} = \mathbf{Q}_{N+1}^{(0)} + \Delta\mathbf{Q}_{N+1}^{(0)} = \mathbf{Q}_{N+1}^{(0)} + \mathbf{K}_{N+1}^{egp(0)} \left(\mathbf{q}_{N+1}^{egp} - \mathbf{q}_{N+1}^{egp(0)} \right) \tag{58}$$

In order to iteratively update the remaining state variables associated to this generalised forces' vector, a corrector phase is implemented which depends on whether the loading point is inside or outside the bounding surface.

(b) ***Corrector step inside the bounding surface.*** The vector of generalised displacements at iteration *k* can be obtained as the sum of its components:

$$\begin{aligned} &\mathbf{Q}_{N+1}^{(k)} = \mathbf{K}^{el} \left(\mathbf{q}_{N+1}^{egp(k)} - \mathbf{q}_{N+1}^{gap(k)} - \mathbf{q}_{N+1}^{pl(k)} \right) \Leftrightarrow \\ &\Leftrightarrow \mathbf{q}_{N+1}^{egp(k)} = \left(\mathbf{K}^{el} \right)^{-1} \mathbf{Q}_{N+1}^{(k)} + \mathbf{q}_{N+1}^{gap(k)} + \mathbf{q}_{N+1}^{pl(k)} \Leftrightarrow \\ &\Leftrightarrow \mathbf{q}_{N+1}^{egp(k)} = \mathbf{q}_{N+1}^{el(k)} + \mathbf{q}_{N+1}^{gap(k)} + \mathbf{q}_{N+1}^{pl(k)} = \mathbf{q}_{N+1}^{eg(k)} + \mathbf{q}_{N+1}^{pl(k)} \end{aligned} \tag{59}$$

The corresponding elastic-gap displacements are obtained through the elastic-gap constitutive relationships, while the plastic displacements are updated using the flow rule. Using an explicit integration scheme for these variables, one obtains:

$$\mathbf{q}_{N+1}^{eg(k)} = \mathbf{q}_{N+1}^{eg(k-1)} + \Delta\mathbf{q}_{N+1}^{eg(k-1)} = \mathbf{q}_{N+1}^{eg(k-1)} + \left(\mathbf{K}_{N+1}^{eg(k-1)} \right)^{-1} \Delta\mathbf{Q}_{N+1}^{(k-1)} \tag{60}$$

$$\mathbf{q}_{N+1}^{pl(k)} = \mathbf{q}_{N+1}^{pl(k-1)} + \Delta\mathbf{q}_{N+1}^{pl(k-1)} = \mathbf{q}_{N+1}^{pl(k-1)} + \Delta\gamma_{N+1}^{(k-1)} \mathbf{n}_{g,N+1}^{(k-1)} \tag{61}$$

The discrete version of the hardening law, using also an explicit update, leads to:

$$\begin{aligned} \lambda_{N+1}^{(k)} &= \lambda_{N+1}^{(k-1)} + \Delta\lambda_{N+1}^{(k-1)} = \lambda_{N+1}^{(k-1)} + \Delta\gamma_{N+1}^{(k-1)} \bar{\lambda}_{N+1}^{(k-1)} = \\ &= \lambda_{N+1}^{(k-1)} - \Delta\gamma_{N+1}^{(k-1)} \frac{\lambda_{N+1}^{(k-1)} H_{N+1}^{pl(k-1)}}{\mathbf{n}_{F,N+1}^{(k-1)} \cdot \mathbf{Q}_{N+1}^{(k-1)}} \end{aligned} \tag{62}$$

Up to this point, all variables used were already known from the previous step. In order to compute the new value of the plastic multiplier, Newton's method is now applied to both the displacement residue and the yield condition. The current displacement residue is defined as:

$$\mathbf{R}_{N+1}^{(k)} = \mathbf{q}_{N+1}^{egp} - \mathbf{q}_{N+1}^{egp(k)} = \mathbf{q}_{N+1}^{egp} - \mathbf{q}_{N+1}^{eg(k)} - \mathbf{q}_{N+1}^{pl(k)} \tag{63}$$

It is now imposed that the linearized prediction for the updated displacement residue should be zero:

$$\mathbf{R}_{N+1}^{(k+1)} \approx \mathbf{R}_{N+1}^{(k)} - \left(\mathbf{K}_{N+1}^{eg(k)} \right)^{-1} \Delta\mathbf{Q}_{N+1}^{(k)} - \Delta\gamma_{N+1}^{(k)} \mathbf{n}_{g,N+1}^{(k)} = \mathbf{0} \tag{64}$$

Solving this equation for the increment of generalised forces, one finds:

$$\Delta\mathbf{Q}_{N+1}^{(k)} = \mathbf{K}_{N+1}^{eg(k)} \left(\mathbf{R}_{N+1}^{(k)} - \Delta\gamma_{N+1}^{(k)} \mathbf{n}_{g,N+1}^{(k)} \right) \tag{65}$$

The linearization of the discrete consistency condition gives:

$$\begin{aligned} F_{N+1}^{(k+1)} &\approx F_{N+1}^{(k)} + \nabla F_{N+1}^{(k)} \cdot \left(\lambda_{N+1}^{(k)} \Delta\mathbf{Q}_{N+1}^{(k)} + \Delta\lambda_{N+1}^{(k)} \mathbf{Q}_{N+1}^{(k)} \right) = \\ &= F_{N+1}^{(k)} + \nabla F_{N+1}^{(k)} \cdot \left(\lambda_{N+1}^{(k)} \mathbf{K}_{N+1}^{eg(k)} \mathbf{R}_{N+1}^{(k)} \right) + \\ &\quad - \Delta\gamma_{N+1}^{(k)} \nabla F_{N+1}^{(k)} \cdot \left(\lambda_{N+1}^{(k)} \mathbf{K}_{N+1}^{eg(k)} \mathbf{n}_{g,N+1}^{(k)} \right) + \\ &\quad - \Delta\gamma_{N+1}^{(k)} \left| \nabla F_{N+1}^{(k)} \right| \lambda_{N+1}^{(k)} H_{N+1}^{pl(k)} = 0 \end{aligned} \tag{66}$$

Finally, the plastic multiplier increment corresponds to:

$$\Delta\gamma_{N+1}^{(k)} = \frac{F_{N+1}^{(k)} + \lambda_{N+1}^{(k)} \nabla F_{N+1}^{(k)} \cdot \mathbf{K}_{N+1}^{eg(k)} \mathbf{R}_{N+1}^{(k)}}{\left|\nabla F_{N+1}^{(k)}\right| \lambda_{N+1}^{(k)} \left(H_{N+1}^{pl(k)} + \mathbf{n}_{F,N+1}^{(k)} \cdot \mathbf{K}_{N+1}^{eg(k)} \mathbf{n}_{g,N+1}^{(k)} \right)} = \\ = \frac{F_{N+1}^{(k)} + \nabla F_{N+1}^{(k)} \cdot \mathbf{K}_{N+1}^{eg(k)} \left(\mathbf{q}_{N+1}^{egp} - \mathbf{q}_{N+1}^{egp(k)} \right)}{\left|\nabla F_{N+1}^{(k)}\right| \lambda_{N+1}^{(k)} \left(H_{N+1}^{pl(k)} + H_{N+1}^{el(k)} \right)} \tag{67}$$

At this point, the vector of generalised forces may be updated with the increment given by expression (65) and the iterative process may be repeated from expressions (59) to (67), until the displacement residue and the bounding surface function are smaller than a given tolerance.

(c) ***Corrector step outside the bounding surface.*** When the loading point is outside the bounding surface this problem reduces to a classical plasticity one, where the bounding surface behaves as the yield surface. Expressions (59)-(61) and (63)-(65), of the corrector step inside the bounding surface, remain unaltered. The loading parameter, λ, is now constant and equal to one and the elastic-gap stiffness matrix is given by:

$$\mathbf{K}_{N+1}^{eg} = \mathbf{K}_{1side}^{gap} (z_{gap} = z_w) \tag{68}$$

The linearization of the discrete consistency condition now results in:

$$F_{N+1}^{(k+1)} \approx F_{N+1}^{(k)} + \nabla F_{N+1}^{(k)} \cdot \Delta\mathbf{Q}_{N+1}^{(k)} = 0 \tag{69}$$

Replacing expression (65) in this one and solving for the incremental plastic multiplier leads to:

$$\Delta\gamma_{N+1}^{(k)} = \frac{F_{N+1}^{(k)} + \nabla F_{N+1}^{(k)} \cdot \mathbf{K}_{N+1}^{eg} \mathbf{R}_{N+1}^{(k)}}{\nabla F_{N+1}^{(k)} \cdot \mathbf{K}_{N+1}^{eg} \mathbf{n}_{g,N+1}^{(k)}} = \\ = \frac{F_{N+1}^{(k)} + \nabla F_{N+1}^{(k)} \cdot \mathbf{K}_{N+1}^{eg} \left(\mathbf{q}_{N+1}^{egp} - \mathbf{q}_{N+1}^{egp(k)} \right)}{\left|\nabla F_{N+1}^{(k)}\right| H_{N+1}^{eg(k)}} \tag{70}$$

Similarly to the previous case, the iterative process is repeated until the displacement residue and the bounding surface function are smaller than a given tolerance.

(d) ***Tangent stiffness matrix.*** If one wished to update the global tangent stiffness matrix, the consistent algorithmic tangent moduli matrix would be computed through:

$$\Delta\mathbf{Q}_{N+1} = \mathbf{K}^{el} \left(\Delta\mathbf{q}_{N+1}^{egp} - \Delta\mathbf{q}_{N+1}^{gap} - \Delta\mathbf{q}_{N+1}^{pl} \right) \tag{71}$$

However, there is no explicit algorithmic formula for the increments $\Delta\mathbf{q}_{N+1}^{gap}$ and $\Delta\mathbf{q}_{N+1}^{pl}$. Consequently, as already mentioned, such consistent matrix cannot be determined and it has to be replaced by the continuum tangent moduli matrix corresponding to the last converged state.

Hence, considering $\mathbf{K}_{N+1}^{eg}$ and $\mathbf{n}_{g,N+1}$ to be defined at the last converged state, expression (71) may be developed as:

$$\Delta\mathbf{Q}_{N+1} = \mathbf{K}^{el} \left(\Delta\mathbf{q}_{N+1}^{egp} - \Delta\mathbf{q}_{N+1}^{gap} - \Delta\mathbf{q}_{N+1}^{pl} \right) = \\ = \mathbf{K}_{N+1}^{eg} \left(\Delta\mathbf{q}_{N+1}^{egp} - \Delta\mathbf{q}_{N+1}^{pl} \right) = \\ = \mathbf{K}_{N+1}^{eg} \left(\Delta\mathbf{q}_{N+1}^{egp} - \Delta\gamma_{N+1} \mathbf{n}_{g,N+1} \right) \tag{72}$$

The incremental consistency condition is given by:

$$\begin{aligned}\Delta F_{N+1} &= \nabla F_{N+1} \cdot \left(\lambda_{N+1}\, \Delta \mathbf{Q}_{N+1} + \Delta\lambda_{N+1}\, \mathbf{Q}_{N+1} \right) = \\ &= \nabla F_{N+1} \cdot \left(\lambda_{N+1}\, \mathbf{K}^{eg}_{N+1}\, \Delta \mathbf{q}^{egp}_{N+1} \right) + \\ &\quad - \Delta\gamma_{N+1}\, \nabla F_{N+1} \cdot \left(\lambda_{N+1}\, \mathbf{K}^{eg}_{N+1}\, \mathbf{n}_{g,N+1} \right) + \\ &\quad - \Delta\gamma_{N+1} \left| \nabla F_{N+1} \right| \lambda_{N+1}\, H^{pl}_{N+1} = 0\end{aligned} \tag{73}$$

Replacing (72) in (73), the plastic multiplier is computed as:

$$\begin{aligned}\Delta\gamma_{N+1} &= \frac{\mathbf{n}_{F,N+1} \cdot \mathbf{K}^{eg}_{N+1}\, \Delta \mathbf{q}^{egp}_{N+1}}{H^{pl}_{N+1} + \mathbf{n}_{F,N+1} \cdot \mathbf{K}^{eg}_{N+1}\, \mathbf{n}_{g,N+1}} = \\ &= \frac{\mathbf{n}_{F,N+1} \cdot \mathbf{K}^{eg}_{N+1}\, \Delta \mathbf{q}^{egp}_{N+1}}{H^{pl}_{N+1} + H^{eg}_{N+1}}\end{aligned} \tag{74}$$

Finally, replacing the plastic multiplier expression in (72) defines the continuum tangent moduli matrix:

$$\begin{aligned}\Delta \mathbf{Q}_{N+1} &= \left[\mathbf{K}^{eg}_{N+1} - \frac{\left(\mathbf{K}^{eg}_{N+1}\, \mathbf{n}_{g,N+1} \right) \otimes \left((\mathbf{K}^{eg}_{N+1})^T\, \mathbf{n}_{F,N+1} \right)}{H^{pl}_{N+1} + H^{eg}_{N+1}} \right] \Delta \mathbf{q}^{egp}_{N+1} = \\ &= \mathbf{K}^{egp}_{N+1}\, \Delta \mathbf{q}^{egp}_{N+1}\end{aligned} \tag{75}$$

Instead of using for $\mathbf{n}_{g,N+1}$ the values corresponding to the last converged state, one can also compute secant values based on the iterative procedure of the previous increment. In fact, one can assume that, after r iterations, the increment of plastic displacements is given by:

$$\Delta \mathbf{q}^{pl}_{N+1} = \mathbf{q}^{pl}_{N+1} - \mathbf{q}^{pl}_{N} = \sum_{k=1}^{r} \Delta\gamma^{(k)}_{N+1}\, \mathbf{n}^{(k)}_{g,N+1} = \Delta\gamma_{N+1}\, \mathbf{n}_{g,N+1} \tag{76}$$

which defines an equivalent increment for the plastic multiplier and an equivalent normal unit vector to the plastic potential surface.

3. VALIDATION TESTS FOR PILE-HEAD MACRO-ELEMENT

The macro-element model presented previously was implemented in the structural analysis software SeismoStruct [Seismosoft, 2019]. It requires the definition of the following 15 input parameters: D, K_{HH}, K_{MM}, K_{HM}, $H_{u,\,e=0}$, M_y, n_H, n_M, γ, z_w, $\left(E_p I_p\right)_{eff}$, β, η, H^{pl}_0 and n_{UR}. Only the last four of these parameters must be calibrated, since all the remaining ones are computed directly through expressions developed in the literature [*e.g.* Gazetas, 1991; Correia *et al.*, 2019].

Amongst the four calibration parameters, two of them are related to monotonic response – β and H^{pl}_0, and the other two are related to cyclic behaviour – η and n_{UR}. Alternatively, two of the parameters are related to the gapping behaviour – β and η, and the other two are related to the plasticity model – H^{pl}_0 and n_{UR}. The parameters β, H^{pl}_0 and n_{UR} are always positive, while η can also be equal to zero if no residual gap opening is considered.

In the following, the influence of those four calibration parameters is analysed and several validation tests for the macro-element are performed by comparing its response both to numerical results obtained with OpenSees [McKenna *et al.*, 2000] and to real lateral load tests on piles.

3.1 INFLUENCE OF MACRO-ELEMENT CALIBRATION PARAMETERS

In order to test the influence of the four macro-element calibration parameters, a soil profile with constant $S_u = 80$ kPa is considered. The shear wave velocity is assumed to be $V_S = 200$ m/s and the Poisson's ratio is taken equal to 0.5. It is further assumed that the pile has a diameter $D = 1$ m and above-ground height equal to $e = 5$ m, corresponding to the load eccentricity. Table 1 and Table 2 summarise all assumed input parameters' values. The effective flexural stiffness of the pile cross-section is the one corresponding to yield, as suggested by Priestley *et al.* [2007].

Table 1. Pre-determined geometric and elastic macro-element parameters

D [m]	K_{HH} [MN/m]	K_{MM} [MNm/rad]	K_{HM} [MN/rad]	z_w [m]	$(E_pI_p)_{eff}$ [MNm^2]
1.00	647	1343	-544	1.24	580

Table 2. Pre-determined failure surface parameters

$H_{u,e=0}$ [kN]	M_y [kNm]	n_H	n_M	γ
1834	3200	8.435	2.000	-0.597

The most important of the macro-element calibration parameters is the reference plastic modulus value, H_0^{pl}, which determines the relative amount of irreversible displacements occurring during monotonic loading. For convenience, it is defined relatively to the dimensionless component of the initial elastic stiffness matrix for horizontal displacement, *i.e.* the normalised value H_0^{pl} / K_{HHn} is used. The effect of this variable is shown in Figure 13, where the pile-head response is plotted in terms of displacement, with $\beta = 1$.

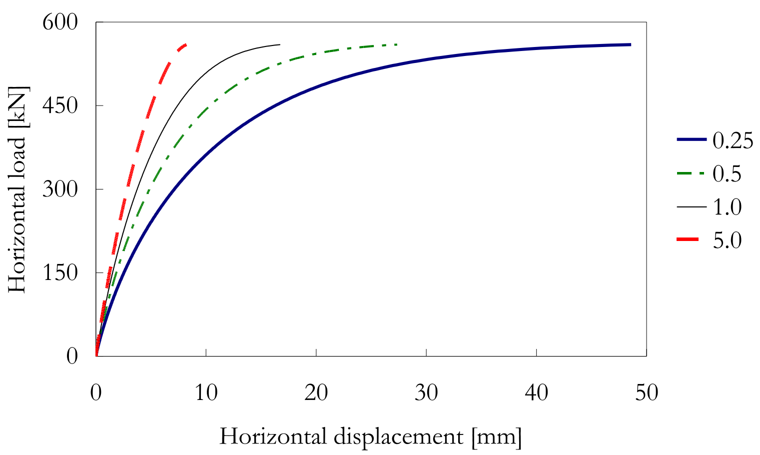

Figure 13. Influence of the normalised reference plastic modulus (H_0^{pl}/K_{HHn}) on the pile-head displacement

This normalised reference plastic modulus has a very significant effect on the amount of irreversible displacements. As its value increases, the response will tend to become more similar to an elastic-perfectly plastic one. As it decreases, more nonlinear behaviour and irreversible displacements are expected to occur for lower values of the loading parameter.

On the other hand, the gap evolution parameter, β, has a much less significant influence on the response of the macro-element. It mainly affects the quasi-elastic stiffness evolution at low levels of displacement. Such effect is clear in Figure 14, where the pile-head response is again plotted in terms of displacement, now with $H_0^{pl} / K_{HHn} = 1$.

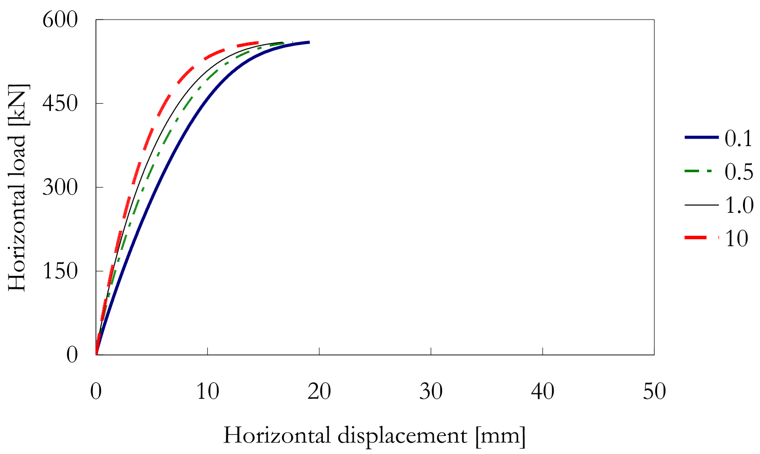

Figure 14. Influence of gap evolution parameter β on the pile-head displacement

Regarding cyclic behaviour, the significant influence of the unloading/reloading exponent, n_{UR}, is shown in Figure 15, with $\eta = 0$. It can be seen that this parameter controls the amount of plastic response upon unloading/reloading. When it equals one, the cyclic response to a given load follows Masing's rule, *i.e.* it is symmetric. For other values it may increase or reduce the irreversible displacements, depending on if its value is smaller or higher than one, respectively. It should be noted that upon completing a full cycle to a given load level, the same displacement of the monotonic response is always attained, for $\eta = 0$.

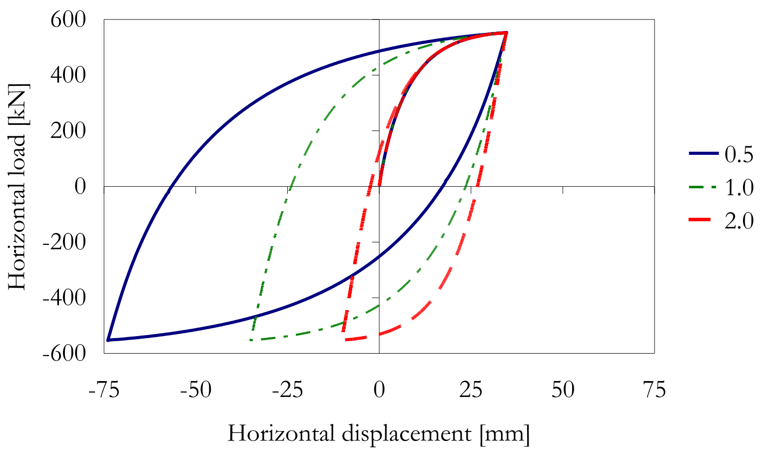

Figure 15. Influence of unloading/reloading exponent n_{UR} on the pile-head displacement

This parameter can alternatively be interpreted as controlling the amount of hysteretic damping of the macro-element response.

The residual gap parameter, if different than zero, always increases the amount of displacement upon unloading/reloading to the same load with opposite sign. This can be clearly seen in Figure 16, where $n_{UR} = 1$.

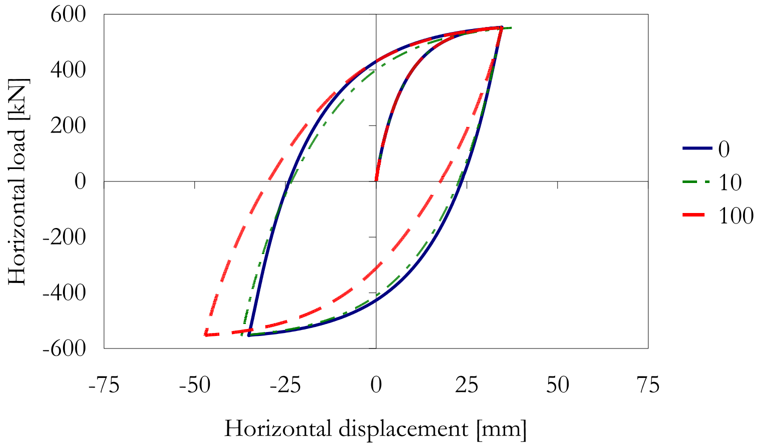

Figure 16. Influence of residual gap parameter η on the pile-head displacement

The residual gap parameter has a smaller influence on the overall response than n_{UR}, and its value can be conjugated with the latter one, if $n_{UR} > 1$, in order to produce a quasi-symmetric cyclic response with different amounts of hysteretic damping. If $n_{UR} < 1$, on the other hand, the response can never be symmetric.

A comparison of the responses for a symmetric loading cycle and for asymmetric loading cycle with the same limits but containing several unload/reload inner cycles was also performed. The corresponding response, purely for illustrative purposes, is presented in Figure 17.

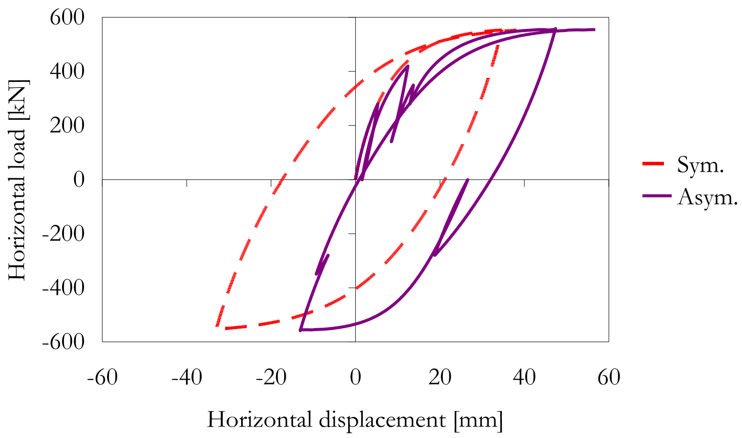

Figure 17. Asymmetric loading history displacement response

3.2 Comparison with Finite Element Results

The response of the macro-element will now be calibrated and compared to numerical simulations performed with OpenSeesPL [Lu *et al.*, 2011], which is a graphical user interface for OpenSees [McKenna *et al.*, 2000] dedicated to solid finite element analysis of piles. Static, cyclic and dynamic analyses of a laterally loaded pile with $D = 1$ m were performed. The pile-column had an above-ground height of $e = 5$ m. Two different soil profiles were considered: (i) a soil profile with constant $S_u = 80$ kPa, shear wave velocity $V_S = 200$ m/s and a depth $L_S = 15$ m; (ii) a soil profile with a linearly increasing S_u with depth. The latter had an undrained shear strength constant of proportionality $m = 0.25$, a depth $L_S = 30$ m and assumed that the maximum soil shear modulus was related to the undrained strength by $G_{\max} = 1100\ S_u$.

The soil model used a multi-yield surface plasticity formulation according to Elgamal *et al.* [2003], assuming that the Von Mises failure surface was attained for an octahedral shear strain of 10%. The soil was modelled as being fully saturated and with a very low permeability, thus having an undrained behaviour for all practical purposes. Moreover, a tension cut-off was considered for both the soil domain and the soil-pile interface layer [Correia, 2011].

(a) ***Soil profile with constant Su.*** The horizontal load-displacement response obtained with solid finite elements for a pushover analysis in undrained conditions is shown in Figure 18, for various types of soil and pile behaviour. One can observe that gapping effects are limited in the linear elastic range of response but become significant with increasing load level.

Figure 19 presents the three-dimensional soil mesh in its deformed configuration for a monotonic pushover with full nonlinear response with gapping. At this load level, close to failure, it is interesting to note the very limited dimension of the soil region contributing to the response.

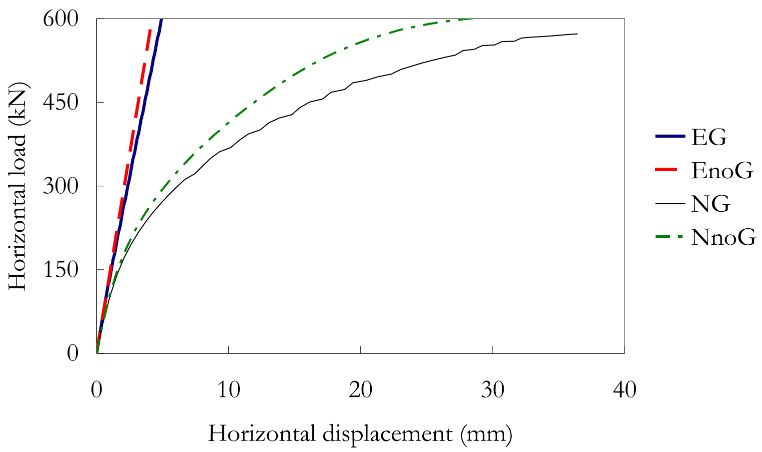

Figure 18. Pushover curves for the constant S_u soil profile with: elastic behaviour with gapping (EG), and without gapping (EnoG), full nonlinear response with gapping (NG) and without gapping (NnoG)

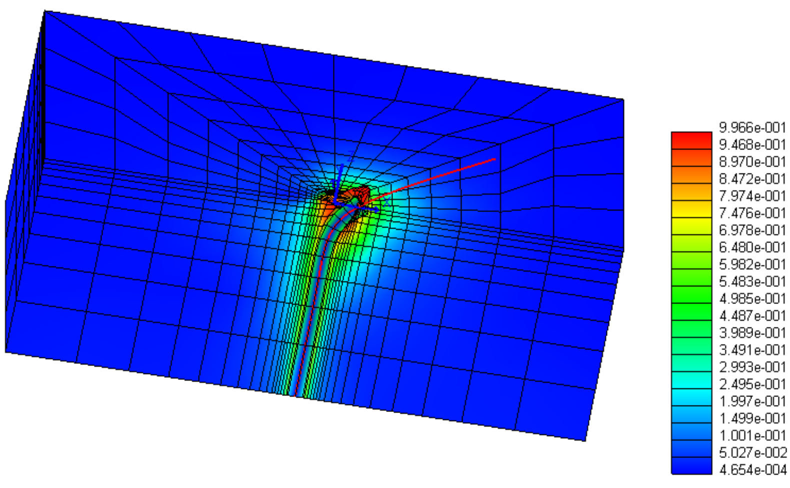

Figure 19. Deformed mesh and stress ratio contour

Figure 20 illustrates the similar responses obtained in a fully coupled dynamic analysis, with simulation of the pore pressure variations in rapid loading conditions, and the results obtained in static analyses with equivalent dry soil conditions.

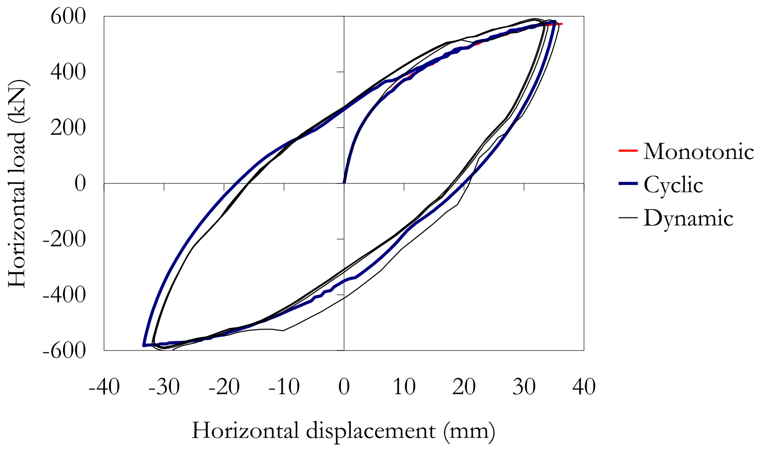

Figure 20. Load-displacement response for the constant S_u soil profile for monotonic, cyclic and dynamic loading conditions and undrained behaviour

The macro-element parameters are now calibrated in order to reproduce the results obtained with solid finite elements. For the simulations performed with this soil profile, the macro-element properties are the ones indicated in Table 1 and Table 2. In order to calibrate the remaining four macro-element parameters, the following approach is employed:

i) The gap evolution parameter, β, is calibrated using the simulation results with elastic soil and pile response but including gapping behaviour. Moreover, the pile initial elastic flexural stiffness is considered, E_pI_p, instead of the effective one, and a very large value is considered for H_0^{pl} so that no plastic displacements occur before the bounding surface is attained,

ii) Afterwards, the full nonlinear monotonic results are considered for calibrating the reference plastic modulus H_0^{pl},

iii) Finally, cyclic nonlinear results are used to calibrate simultaneously η and n_{UR} with the purpose of replicating both the symmetric response obtained for cyclic loading and the amount of hysteretic damping evidenced by solid finite element simulations.

This methodology was applied using the solid finite element results for pile-head displacement. Table 3 presents the values obtained for the macro-element calibration parameters. The comparison of macro-element response with the one obtained by solid finite elements is presented in Figure 21 and Figure 22, in terms of pile-head displacement both for monotonic and cyclic loading.

Table 3. Calibration results for macro-element parameters

β	η	$\frac{H_0^{pl}}{K_{HHn}}$	n_{UR}
4	45	0.30	1.30

Before even discussing the calibration results, attention must be pointed out to the fact that the initial elastic stiffnesses computed by the approximate expressions from literature give very good results for this case.

More important, however, for the objectives of this work, is the fact that the failure conditions predicted by the results obtained with the yield design theory parametric study from Correia [2019] are correct. In fact, it can be clearly seen in Figure 21 that the maximum horizontal load obtained in the numerical simulation with solid finite elements is very similar to the one predicted by the superellipse failure surface based on those parametric study results. Furthermore, the slight under-prediction of the failure load by the macro-element may be attributed to the fact that OpenSeesPL [Lu *et al.*, 2011] uses Von Mises failure criterion, while the macro-element is using the values obtained with Tresca failure criterion. As previously mentioned, the difference in both criteria may reach about 15% for a plane strain mechanism.

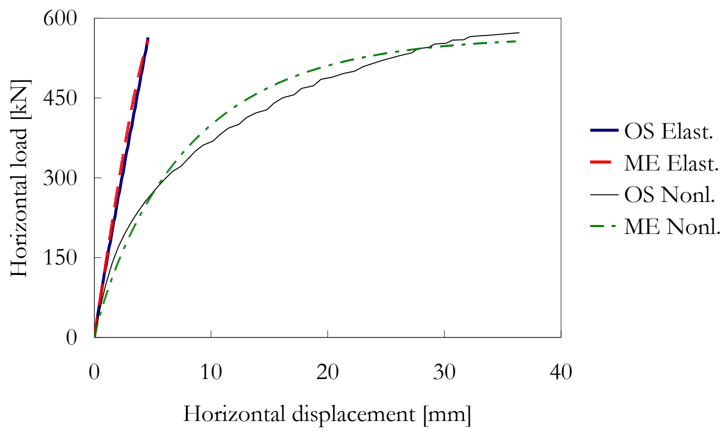

Figure 21. Comparison of Macro-Element (ME) vs. OpenSeesPL (OS) pile-head monotonic load-displacement response, for constant S_u soil profile and for both elastic and nonlinear behaviour

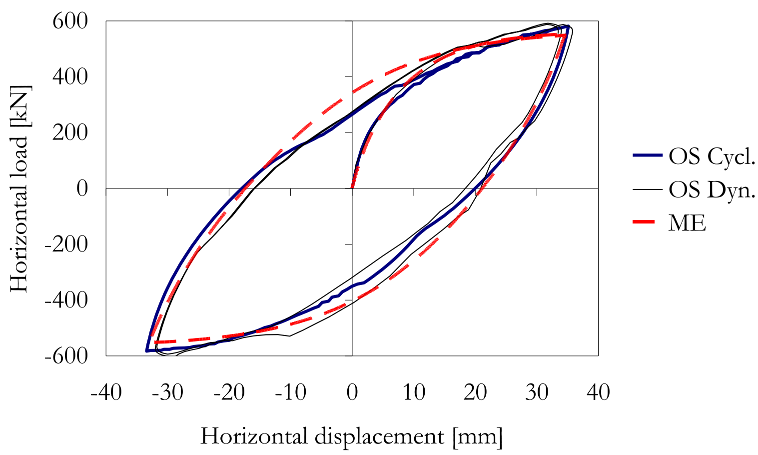

Figure 22. Comparison of Macro-Element (ME) vs. OpenSeesPL (OS) pile-head cyclic load-displacement response, for constant S_u soil profile

By applying the abovementioned calibration methodology to the displacement response, one can validate the behaviour of the macro-element by verifying that it adequately reproduces the overall response obtained with solid finite elements. Furthermore, and probably more important as a validation result, the response in terms of pile-head rotation is also adequately reproduced. In fact, for monotonic loading, with either elastic or nonlinear response, the results are at least as accurate as the ones used for calibrating the macro-element. For cyclic loading, albeit a slightly higher hysteretic damping obtained in the cyclic response of the macro-element, the results are also very satisfactory.

(b) ***Soil profile with linear Su.*** Starting with the results obtained with OpenSeesPL [Lu *et al.*, 2011], they follow closely what was obtained for the previous soil profile. However, two important differences arise: (i) gapping has a much-reduced influence; (ii) the overall flexibility is extremely larger. These observations can be verified in the pushover results of Figure 23.

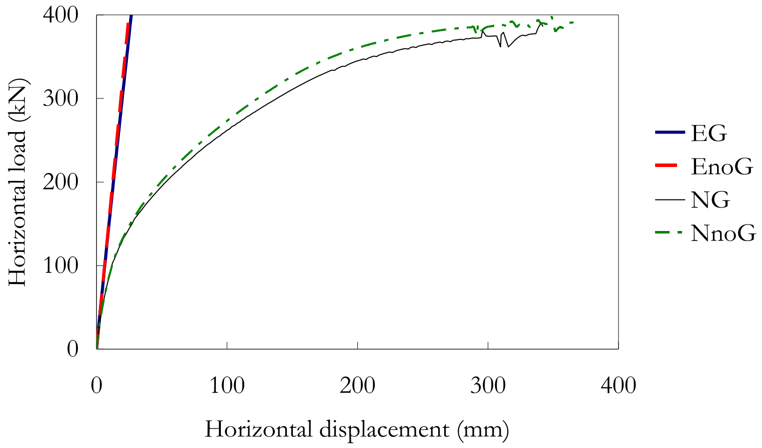

Figure 23. Pushover curves for the linear S_u soil profile with: elastic behaviour with gapping (EG), and without gapping (EnoG), full nonlinear response with gapping (NG) and without gapping (NnoG)

It is interesting to note that albeit the virtual failure mechanism for this soil profile considered no contribution from gapping Correia [2019], it influences slightly the results both in terms of strength and stiffness. Hence, in the macro-element analyses this gapping influence will be considered also for this soil profile. The macro-element properties are now the ones indicated in Table 4 and Table 5.

The calibration of the macro-element parameters was performed as proposed for the other soil profile and the results are presented in Table 6. Both parameters associated with cyclic response were found to give good results having the same values than before.

Table 4. Pre-determined geometric and elastic macro-element parameters

D [m]	K_{HH} [MN/m]	K_{MM} [MNm/rad]	K_{HM} [MN/rad]	z_w [m]	$(E_pI_p)_{eff}$ [MNm^2]
1.00	72.9	744.2	-168.5	3.86	580

Table 5. Pre-determined failure surface parameters

$H_{u,e=0}$ [kN]	M_y [kNm]	n_H	n_M	γ
642.2	3200	7.040	2.000	-0.667

Table 6. Calibration results for macro-element parameters

β	η	$\frac{H_0^{pl}}{K_{HHn}}$	n_{UR}
12	45	0.12	1.30

The comparison in terms of pile-head displacement for both monotonic and cyclic loading of the macro-element response with the one obtained by solid finite elements is shown in Figure 24 and Figure 25.

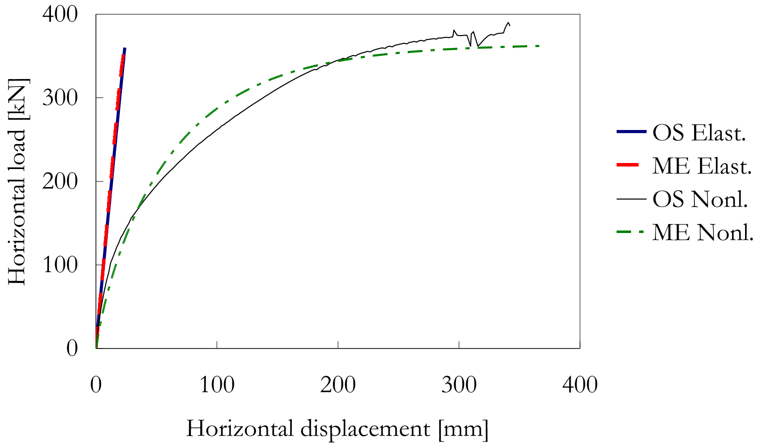

Figure 24. Comparison of Macro-Element (ME) vs. OpenSeesPL (OS) pile-head monotonic load-displacement response, for linear S_u soil profile and for both elastic and nonlinear behaviour

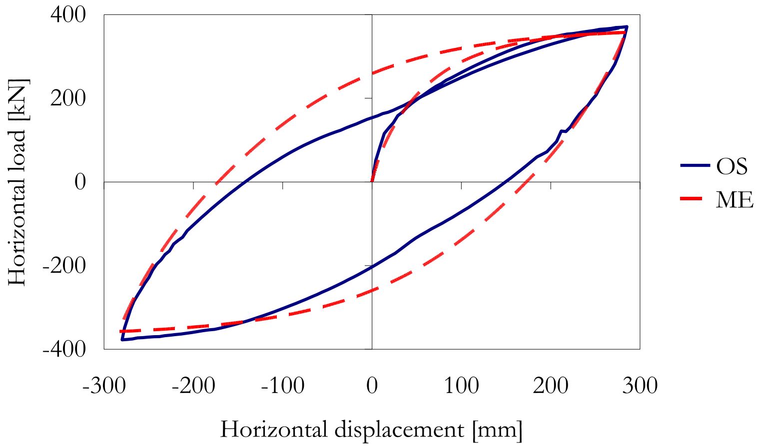

Figure 25. Comparison of Macro-Element (ME) vs. OpenSeesPL (OS) pile-head cyclic load-displacement response, for linear S_u soil profile

The same conclusions drawn for the other soil profile apply in this case. One may verify once more that the initial stiffnesses and the failure load are adequately predicted by the approximate expressions presented in this thesis. It is also clear that the response in terms of displacement, used for calibration purposes, is well replicated by the macro-element analyses. On the other hand, the response in terms of pile-head rotation, used for validation effects, is again properly reproduced.

3.3 COMPARISON WITH *UCLA* PILE TESTS

In a report by Stewart *et al.* [2007] a series of full scale cyclic large deflection lateral load tests of drilled shaft foundations were described. They performed three tests with reinforced concrete circular piles of the same diameter, $D = 0.61$ m (2 ft), in both a flagpole and a fixed-head configuration, as well as in a nine-pile group arrangement. The first two tests will be considered here for assessing the macro-element capabilities. The last two tests are further described and analysed in Lemnitzer *et al.* [2010].

The site conditions at the depth range of interest correspond roughly to an *OC* silty clay with undrained shear strength of about S_u = 187 kPa (3900 psf). Despite the water table was at large depths, due to the high saturation levels of the surficial layers and the high loading rate during the test, undrained soil behaviour was assumed. The initial undrained soil modulus of deformation was taken as E_S = 335 MPa (7000 ksf) and, with a Poisson's ratio of 0.5, the maximum soil shear modulus was assumed to be G = 112 MPa. A soil unit weight of 19 kN/m^3 was measured.

(a) ***Flagpole test.*** This free-head pile was subjected to a lateral force only, at a height of e = 4.06 m (13'4''). It had a below-ground length of L_P = 7.62 m (25 ft). A cyclic displacement history was imposed at the top of the column. Three cycles were performed at each displacement level. The displacement levels corresponded to multiplying a predicted yield displacement of 50.8 mm (2 in) by the following factors: $^1/_8$, ¼, ½, ¾, 1, 1 ¼, 1 ½, 2, 3, 4, 6, 8.

Figure 26 represents the experimental load-deflection response. These results clearly show a strength degradation effect for repeated cycles at the same displacement level. Nevertheless, there seems to be some influence of creep deformations on these plots, evidenced by the decrease of strength at maximum load conditions for each cycle and displacement level.

Given the cross-sectional properties indicated in the aforementioned reports, the nominal pile yield moment corresponds to M_y = 510 kNm. The horizontal failure load obtained by the predictive expression in Correia [2019] is equal to 121 kN, which agrees well with the experimental results. Once more, pre-determined macro-element parameters are computed through the expressions presented in Correia [2019] and are summarised in Table 7 and Table 8.

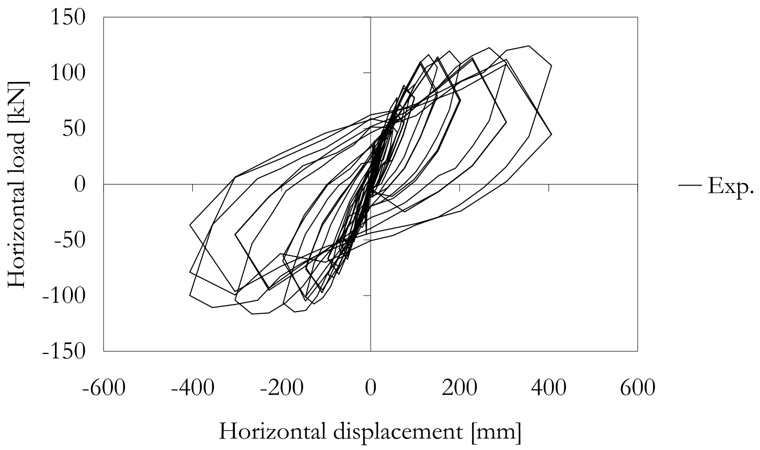

Figure 26. Experimental load vs. top displacement response for the flagpole test (after Stewart *et al.* [2007])

Table 7. Pre-determined geometric and elastic macro-element parameters

D [m]	K_{HH} [MN/m]	K_{MM} [MNm/rad]	K_{HM} [MN/rad]	z_w [m]	$(E_pI_p)_{eff}$ [MNm^2]
0.61	573	362	-264	0.25	54.7

Table 8. Pre-determined failure surface parameters

$H_{u,e=0}$ [kN]	M_y [kNm]	n_H	n_M	γ
792	510	8.435	2.000	-0.597

Regarding the macro-element calibration parameters, it was found that the gapping behaviour had little influence on the results due to the shallow wedge geometry. Consequently, the default values were adopted for β and η. The remaining macro-element parameters, related to inelastic monotonic, H_0^{pl}, and cyclic, n_{UR}, response, were calibrated to the values shown in Table 9.

Table 9. Calibration results for macro-element parameters

β	η	$\frac{H_0^{pl}}{K_{HHn}}$	n_{UR}
1	0	0.3	0.25

Figure 27 illustrates the monotonic response of the macro-element in comparison to the cyclic load-displacement results. The monotonic curve correctly envelopes the cyclic results and the maximum horizontal load is correctly predicted.

Figure 28 represents the macro-element response for three load cycles at the maximum displacement level of the experimental test. The strength degradation with subsequent cycles appears to be correctly captured. Experimental hysteretic loops are somewhat thinner than the macro-element ones at low loading levels, but the overall loop area seems to be similar. It should be mentioned that the plastic hinge in the experimental test formed deeper than expected by the failure mechanism theoretical results (where $z_h = z_w$). If the passive wedge depth is increased accordingly, the macro-element hysteretic loops tend to get thinner, although the gap influence was not large in this test as already mentioned.

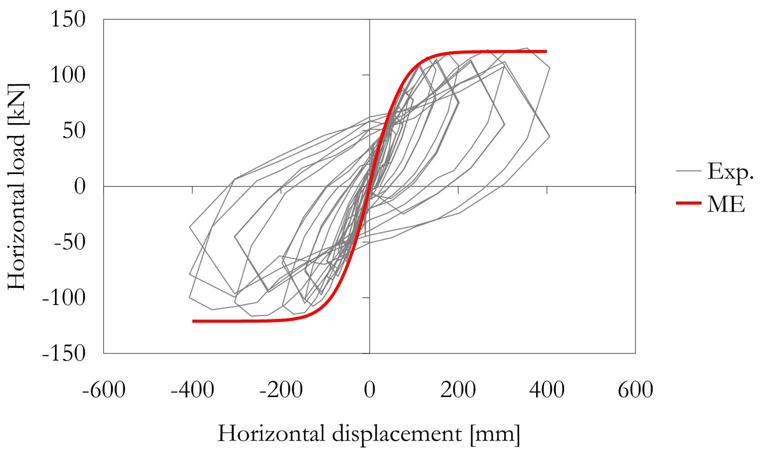

Figure 27. Comparison of Macro-Element (ME) monotonic vs. flagpole cyclic (Exp.) load-displacement results

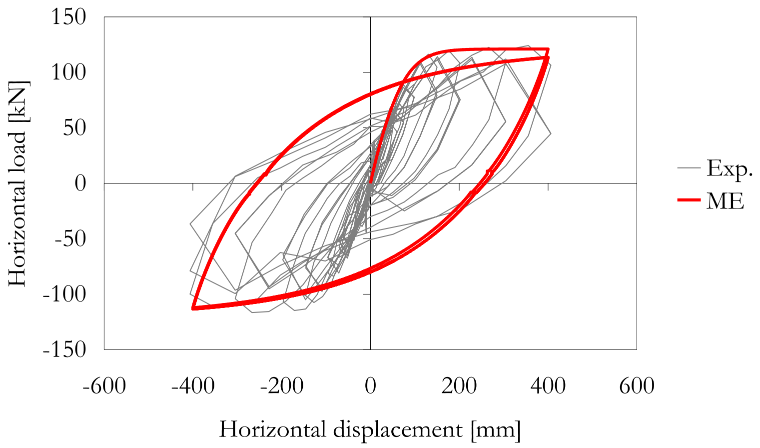

Figure 28. Comparison of Macro-Element (ME) vs. flagpole (Exp.) cyclic load-displacement results at maximum displacement level

Finally, Figure 29 represents the full cyclic response of the macro-element in comparison to the experimental one. The overall response seems to agree very well, both in terms of strength and stiffness.

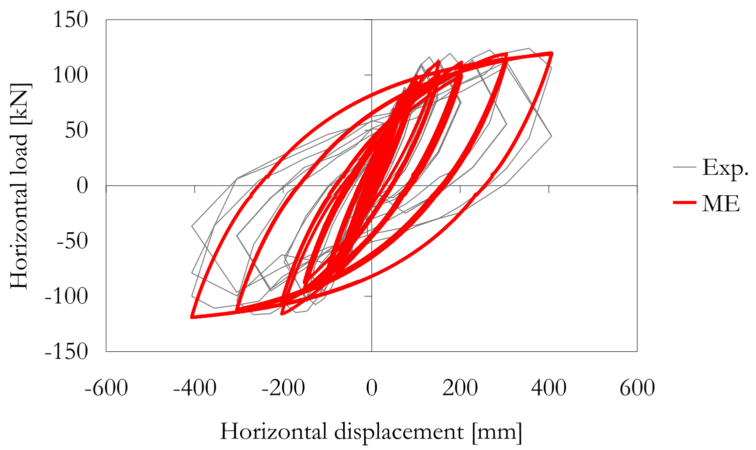

Figure 29. Comparison of Macro-Element (ME) vs. flagpole (Exp.) cyclic load-displacement results

(b) ***Fixed-head test.*** The fixed-head pile was subjected to a lateral force and a moment restraining the pile-head rotation. The load eccentricity is thus negative and with undefined value, since it varies with the loading evolution depending on the pile-head rotational and off-diagonal stiffness. The geometry of the fixed-head pile is the same as the flagpole one. Also, a proportional cyclic displacement history was imposed at the pile head, with the difference that the predicted yield displacement is now 12.7 mm (0.5 in).

The material properties of this reinforced concrete pile are slightly different from the flagpole ones, resulting in a nominal pile yield moment of M_y = 600 kNm. This implies a different ultimate load for zero eccentricity condition, now equal to $H_{u,\ e=0}$ = 868 kN. All remaining macro-element parameters are the same, except the gap maximum depth z_w. The predictive equation derived for this variable depends on the load eccentricity Correia [2019]. Since this is undetermined and since that equation was not calibrated to negative eccentricity values, there is no easy way to determine z_w but to perform an optimisation analysis with yield design theory.

A constant value of z_w = 1.50 m was considered based on previous optimisation results. However, this value is expected to vary during a load cycle, according to the changing load eccentricity. It should be recognized that the macro-element is not fully adapted to analyse fixed-head piles and that it needs further adjustments for that purpose. Nevertheless, a monotonic analysis was performed and compared to the experimental results, as depicted in Figure 30.

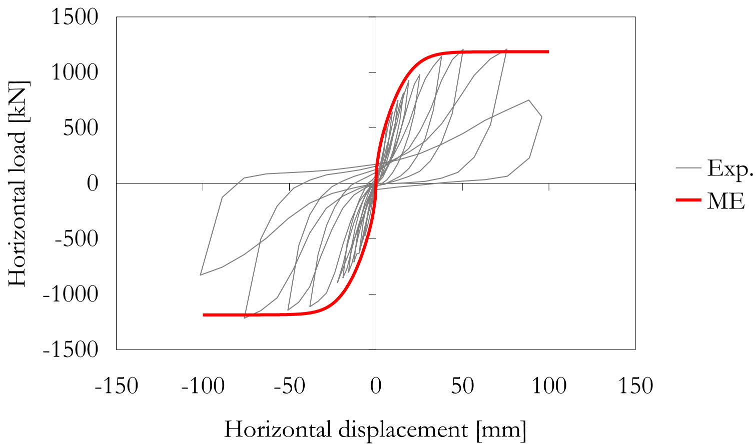

Figure 30. Comparison of Macro-Element (ME) monotonic vs. fixed-head pile cyclic (Exp.) load-displacement results

It is very encouraging to verify that, despite the abovementioned problems, a very good prediction of the cyclic results envelope is obtained. Attention is pointed to the fact that only the first cycle for each displacement level is represented in the previous plot, since it was not possible to obtain the full experimental load-displacement results. It is also noted that the experimental results for this test are very different from the flagpole ones: there is a clear pinching effect on the cyclic loop. In the last displacement level, failure of the pile was attained, resulting on the significant strength degradation observed in the load-deflection curve. This failure is evidently not perceived with the macro-element analysis.

4. CONCLUSIONS

An innovative and efficient pile-head macro-element was presented that is capable of accurately describing the main features of lateral cyclic behaviour for flexible single piles. It was based on the three fundamental characteristics of pile lateral response: linear elastic behaviour at low levels of loading; gapping evolution and its effects on pile stiffness; and failure conditions.

Elastic-gap evolution behaviour was considered through a nonlinear elastic model, which in turn was related to the failure mechanism characteristics. Transition from initial elastic behaviour to plastic flow conditions at failure was appropriately modelled by using a bounding surface plasticity formulation. Such model accounts for the irreversible nature of pile behaviour from initial loading up to collapse, but also for unloading/reloading hysteresis characteristics.

The macro-element parameters are largely based on fundamental response characteristics which are appropriately predicted by either existing calibrated expressions or by predictive relationships developed in previous chapters. It turns out that, from the initial set of 15 macro-element parameters, only four of them need to be calibrated, for given site and pile properties, through comparison with more complex numerical models or to lateral load tests on real piles. A procedure was suggested for successive individual calibration of those four parameters by using simple numerical results.

Finally, advanced nonlinear analyses of laterally loaded piles, using solid finite elements, were carried out and their results were exposed and interpreted, namely in what refers to the gapping influence. Afterwards, successful calibration and validation of the macro-element response was achieved for a set of different existing results, both numerical and experimental. This very satisfactory behaviour rewarded the effort put on the development of such analysis tool and encourages its continued development for more complex soil conditions and behaviour.

REFERENCES

Borja, R.I., Lin, C.H., Montáns, F.J. [2001] "Cam-Clay plasticity, Part IV: Implicit integration of anisotropic bounding surface model with nonlinear hyperelasticity and ellipsoidal loading function," *Computer Methods in Applied Mechanics and Engineering*, Vol. 190, pp. 3293-3323.

Budhu, M., Davies, T.G. [1987] "Nonlinear analysis of laterally loaded piles in cohesionless soils," *Canadian Geotechnical Journal*, Vol. 24, pp. 289-296.

Budhu, M., Davies, T.G. [1988] "Analysis of laterally loaded piles in soft clays," *Journal of Geotechnical Engineering*, Vol. 114, No. 1, pp. 21-39.

Chatzigogos, C.T. [2007] "Comportement sismique des fondations superficielles: vers la prise en compte d'un critère de performance dans la conception," *PhD Thesis*, École Polytechnique, Palaiseau, France.

Chatzigogos, C.T., Pecker, A., Salençon, J. [2009] "Macroelement modeling of shallow foundations," *Soil Dynamics and Earthquake Engineering*, Vol. 29, No. 5, pp. 765-781.

Chatzigogos, C.T., Figini, R., Pecker, A., Salençon, J. [2010] "A macroelement formulation for shallow foundations on cohesive and frictional soils," *International Journal for Numerical and Analytical Methods in Geomechanics*, Vol. 35, No. 8, pp. 902-931.

Correia, A.A. [2011] "A pile-head macro-element approach to seismic design of monoshaft-supported bridges," *PhD Thesis*, ROSE School, IUSS Pavia, Italy.

Correia, A.A., Pecker, A. [2019] "Failure mechanism for laterally loaded flexible piles based on yield design theory," submitted to *Géotechnique*.

Cremer, C., Pecker, A., Davenne, L. [2001] "Cyclic macro-element for soil-structure interaction: material and geometrical non-linearities," *International Journal for Numerical and Analytical Methods in Geomechanics*, Vol. 25, No. 13, pp. 1257-1284.

Cremer, C., Pecker, A., Davenne, L. [2002] "Modelling of nonlinear dynamic behaviour of a shallow strip foundation with macro-element," *Journal of Earthquake Engineering*, Vol. 6, No. 2, pp. 175-211.

Dafalias, Y.F. [1986] "Bounding surface plasticity. I: Mathematical foundation and hypoplasticity," *Journal of Engineering Mechanics*, Vol. 112, No. 9, pp. 966-987.

Davies, T.G., Budhu, M. [1986] "Non-linear analysis of laterally loaded piles in heavily overconsolidated clays," *Géotechnique*, Vol. 36, No. 4, pp. 527-538.

EC8 – Part 5 [2003] *Eurocode 8: Design of structures for earthquake resistance – Part 5: Foundations, retaining structures and geotechnical aspects*, EN 1998-5:2004, European Committee for Standardization (CEN), Belgium.

Elgamal, A., Yang, Z., Parra, E., Ragheb, A. [2003] "Modeling of cyclic mobility in saturated cohesionless soils," *International Journal of Plasticity*, Vol. 19, pp. 883-905.

Figini, R. [2010] "Non-linear dynamic soil-structure interaction: application to seismic analysis and design of structures on shallow foundations," *PhD Thesis*, Politecnico di Milano, Milan, Italy.

Figini, R., Paolucci, R., Chatzigogos, C.T. [2012] "A macro-element model for non-linear soil-shallow foundation-structure interaction under seismic loads: theoretical development and experimental validation on large scale tests," *Earthquake Engineering and Structural Dynamics*, Vol. 41, No. 3, pp. 475-493, DOI: 10.1002/eqe.1140.

Gazetas, G. [1991] "Foundation vibrations," *Foundation Engineering Handbook*, 2nd Ed., Fang, H.Y. (Ed.), pp. 553-593, Van Nostrand Reinhold, New York, USA.

Hutchinson, T.C., Boulanger, R.W., Chai, Y.H., Idriss, I.M. [2002] "Inelastic seismic response of extended pile shaft supported bridge structures," *Report PEER 2002/14*, Pacific Earthquake Engineering Research Center, University of California, Berkeley, USA.

Krieg, R.D., Krieg, D.B. [1977] "Accuracies of numerical solution methods for the elastic-perfectly plastic model," *Journal of Pressure Vessel Technology*, Vol. 99, No. 4, pp. 510-515.

Lemnitzer, A., Khalili-Tehrani, P., Ahlberg, E.R., Rha, C., Taciroglu, E., Wallace, J.W., Stewart, J.P. [2010] "Nonlinear efficiency of bored pile group under lateral loading," *Journal of Geothechnical and Geoenvironmental Engineering*, Vol. 136, No. 12, pp. 1673-1685.

Lu, J., Elgamal, A., Yang, Z. [2011] *OpenSeesPL: 3D lateral pile-ground interaction*, available at http://www.soilquake.net/openseespl, University of California, San Diego, USA.

McKenna, F., Fenves, G.L., Scott, M.H., Jeremic, B. [2000] *OpenSees: Open system for earthquake engineering simulation*, available at http://opensees.berkeley.edu, Pacific Earthquake Engineering Research Center, University of California, Berkeley, USA.

Mróz, Z., Zienkiewicz, O.C. [1984] "Uniform formulation of constitutive equations for clays and sands," *Mechanics of Engineering Materials*, Desai, C.S., Gallagher, R.H. (Eds.), pp. 415-449, John Wiley and Sons, Chichester, UK.

Ortiz, M., Martin, J.B. [1989] "Symmetry-preserving return mapping algorithms and incrementally extremal paths: a unification of concepts," *International Journal for Numerical Methods in Engineering*, Vol. 28, No. 8, pp. 1839-1853.

Ortiz, M., Simo, J.C. [1986] "An analysis of a new class of integration algorithms for elastoplastic constitutive relations," *International Journal for Numerical Methods in Engineering*, Vol. 23, No. 3, pp. 353-366.

Phillips, A. [1972] "On rate-independent continuum theories of graphite and their experimental verification," *Nuclear Engineering and Design*, Vol. 18, pp. 203-211.

Prévost, J.H. [1987] "Modeling the Behavior of Geomaterials," *Course Notes*, Short-Course on Nonlinear Soil Mechanics and Dynamic Soil-Structure Interaction, Zace Services Ltd., Lausanne, Switzerland.

Priestley, M.J.N., Calvi, G.M., Kowalsky, M.J. [2007] *Displacement-Based Seismic Design of Structures*, IUSS Press, Pavia, Italy.

Randolph, M.F. [1981] "The response of flexible piles to lateral loading," *Géotechnique*, Vol. 31, No. 2, pp. 247-259.

Seismosoft [2019] *SeismoStruct 2019 – A computer program for static and dynamic nonlinear analysis of framed structures*, available at: http://www.seismosoft.com.

Simo, J.C., Hughes, T.J.R. [1998] *Computational Inelasticity*, Springer, New York, USA.

Simo, J.C., Ortiz, M. [1985] "A unified approach to finite deformation elastoplastic analysis based on the use of hyperelastic constitutive equations," *Computer Methods in Applied Mechanics and Engineering*, Vol. 49, No.2, pp. 221-245.

Simo, J.C., Taylor, R.L. [1985] "Consistent tangent operators for rate independent elasto-plasticity," *Computer Methods in Applied Mechanics and Engineering*, Vol. 48, No.1, pp. 101-118.

Stewart, J.P., Taciroglu, E., Wallace, J.W., Ahlberg, E.R., Lemnitzer, A., Rha, C., Khalili-Tehrani, P., Keowen, S., Nigbor, R.L., Salamanca, A. [2007] "Full scale cyclic large deflection testing of foundation support systems for highway bridges. Part I: Drilled shaft foundations" *Report UCLA SGEL-01*, Structural and Geotechnical Engineering Laboratory, University of California, Los Angeles, USA.